



# LAWOFS

## 2019

LATIN AMERICAN WORKSHOP  
ON OPTICAL FIBER SENSORS

# PROCEEDINGS

## Latin American Workshop on Optical Fiber Sensors

17 – 19 July 2019 – Rio de Janeiro, Brazil

**Editors:**

**José Luís Fabris (UTFPR)**

**Maria Aparecida Gonçalves Martinez (CEFET/RJ)**

**Maria Thereza Miranda Rocco Giraldi (IME)**

ISBN 978-85-92987-02-2



Sociedade Brasileira  
de Micro-ondas  
e Optoeletrônica

2019

# PROCEEDINGS

## Latin American Workshop on Optical Fiber Sensors – 2019

### Editors:

José Luís Fabris (UTFPR)

Maria Aparecida Gonçalves Martinez (CEFET/RJ)

Maria Thereza Miranda Rocco Giraldi (IME)

SBMO, São Caetano do Sul - Brazil

2019



## Proceedings

### Latin American Workshop on Optical Fiber Sensors – 2019

Copyright Sociedade Brasileira de Micro-ondas e Optoeletrônica. Abstracting is permitted with credit to the source. Downloading, copying, reprinting or reproduction for personal use is permitted with proper credit to the authors and publisher. Other requests should be addressed to Sociedade Brasileira de Micro-ondas e Optoeletrônica, Praça Mauá 1, 09580-900 São Caetano do Sul, Brazil; e-mail: [sbmo@sbmo.org.br](mailto:sbmo@sbmo.org.br)

#### **Dados internacionais de Catalogação na Publicação**

Ficha catalográfica elaborada pela Biblioteca Central do CEFET/RJ

L357 Latin America Workshop on Optical Fiber Sensors (2. : 2019 : São Caetano do Sul, SP)

Proceedings of Latin America Workshop on Optical Fiber Sensors, SBMO, Brazil, July 17-19 2019 / editors: José Luís Fabris, Maria Aparecida Gonçalves Martinez, Maria Thereza Miranda Rocco Giraldi. – 2nd ed. – São Caetano do Sul, SP : SBMO, 2019. 153p. : il. (algumas color.) , graf. , tabs.

ISBN: 978-85-92987-02-2

Inclui bibliografias.

1. Detectores ópticos. 2. Microondas. 3. Engenharia eletrônica. I. Fabris, José Luís (Ed.). II. Martinez, Maria Aparecida Gonçalves (Ed.). III. Giraldi, Maria Thereza Miranda Rocco (Ed.). IV. Sociedade Brasileira de Micro-ondas e Optoeletrônica. V. Título.

CDD 621.381542

Elaborada pela bibliotecária Mariana Oliveira CRB-7/5929

Agência Brasileira do ISBN

ISBN 978-85-92987-02-2



9 788592 987022

## **Steering Committee**

### **Conference Chair**

Prof. Maria Thereza Rocco Giraldi Instituto Militar de Engenharia, Brazil

### **Conference Co-Chair**

Prof. Maria Aparecida Martinez CEFET-RJ, Brazil

### **Members**

Prof. Andrés Pablo López Barbero Universidade Federal Fluminense, Brazil  
Prof. Arthur Braga Pontifical Catholic University of Rio de Janeiro, Brazil  
Prof. Juan Hernandez-Cordero UNAM, Mexico  
Dr. Alexis Mendez MCH Engineering, LLC, USA  
Prof. Ricardo Olivares Universidad Tecnica Federico Santa María, Chile  
Prof. Pedro Torres Universidad Nacional de Colombia – Medellin

## **Local Organizing Committee**

### **Members**

Prof. Maria Aparecida Martinez CEFET-RJ, Brazil  
Prof. Maria Thereza Rocco Giraldi Instituto Militar de Engenharia, Brazil  
Prof. Carolina V S Borges CEFET-RJ, Brazil  
Prof. Hypolito José Kalinowski Universidade Federal Fluminense, Brazil

## **Technical Program Committee**

Prof. José Fabris Federal University of Technology – Parana – **TPC Chair**  
Dr. Alexandre Bessa Universidade Federal de Juiz de Fora  
Prof. Jean Carlos Cardozo da Silva Federal University of Technology – Paraná  
Dr. Cristiano Cordeiro State University of Campinas, UNICAMP  
Prof. Eduardo Fontana Universidade Federal de Pernambuco  
Prof. Marcos Franco Instituto de Estudos Avançados, CTA  
Prof. Ricardo Kamikawachi Federal University of Technology – Paraná  
Prof. Marcia Muller Federal University of Technology – Paraná  
Prof. Aleksander Paterno - Santa Catarina State University  
Prof. Maria José Pontes - Universidade Federal do Espírito Santo  
Prof. Josemir Santos - University of Sao Paulo  
Prof. Vinicius Nunes Henrique Silva Universidade Federal Fluminense  
Dr. Marcelo Soto - Universidad Técnica Federico Santa María  
Dr. Luiz Carlos Guedes Valente Ouro Negro AS  
Dr. Gloria Margarita Varón Durán - Universidad Nacional de Colombia  
Prof. Marcelo Werneck - COPPE, Universidade Federal do Rio de Janeiro  
Prof. Joao Weyl Costa - Universidade Federal do Pará - UFPA

## Realization



Sociedade Brasileira  
de Micro-ondas  
e Optoeletrônica



Universidade  
Federal  
Fluminense



CEFET/RJ



## Sponsor

**THORLABS**

## Financial Support





## FOREWORD

The success attained by the 24<sup>th</sup> International Conference on Optical Fiber Sensors - OFS24, held in Curitiba from September 28<sup>th</sup> until October 2<sup>nd</sup>, 2015, surfaced the strong interest of Latin America's and Brazilian scientific communities in the optical fiber sensors area. Following the trend, the Brazilian Society for Microwaves and Optoelectronics (SBMO) decided to organize the Latin American Workshop on Optical Fiber Sensors (LAWOFS).

LAWOFS is proposed to take place every three years, coinciding with the intervals of the OFS conference series. The first edition, LAWOFS 2016 was co-located with MOMAG 2016 in Porto Alegre, Brazil. The 2019 Edition will take place in Rio de Janeiro from July 17<sup>th</sup> until 19<sup>th</sup>, 2019.

The Workshop proposes to engage research groups from Brazil and Latin America to debate on new concepts, technologies and applications of optical fiber sensing with the focus on intense interaction among the participants in order to enhance future collaborations in R&D projects.

LAWOFS2019 selected papers, reviewed by the Technical Program Committee members, will address mainly physical and chemical optical sensors based on fiber Bragg grating technology. Besides special fibers, long period fiber Bragg grating, interferometric and distributed sensors and signal processing techniques for sensing interrogation will also be discussed. The applications areas include biomedical, energy, food processing industry, transportation and environmental quality.

Prof. Maria Thereza Miranda Rocco Giraldi

Prof. Maria Aparecida Gonçalves Martinez

Prof. José Luís Fabris

*LAWOFS 2019 Organizers*

## Second Latin American Workshop on Optical Fiber Sensors-2019: Program

	Wednesday, July 17	Thursday, July 18	Friday, July 19
8:50 - 10:00	Registration	Oral Session 3	Oral Session 6
10:00 - 10:30	Coffee break 1 & Registration		
10:30 - 11:00	Opening Session	Coffee break 3	Coffee break 5
11:00 - 12:00	Invited Talk 1	Invited Talk 2	Round table
12:00 - 13:30	Lunch 1	Lunch 2	Lunch 3
13:30 - 15:10	Oral Session 1	Oral Session 4	Oral Session 7
15:10 - 15:40	Coffee break 2	Coffee break 4	Coffee break 6
15:40 - 16:00	Oral Session 2	Oral Session 5	Closing Session
16:00 - 17:20			
17:20 - 19:00			
19:00 - 21:00		Workshop Dinner	

### Wednesday, July 17

Wednesday, July 17 8:50 - 10:00

Registration

Wednesday, July 17 10:00 - 10:30

Coffee break 1 & Registration

Wednesday, July 17 10:30 - 11:00

Opening Session

Chairs: Dr. Maria Thereza Rocco Giraldi

Dr. Maria Aparecida Martinez,

Wednesday, July 17 11:00 - 12:00

### Invited Talk 1

Optical Fiber Sensors: A 40-Year Retrospective

**Prof. ALEXIS MENDEZ - MCH ENGINEERING - USA**

Chairs: Dr. Maria Aparecida Martinez

Dr. Maria Thereza Rocco Giraldi

Wednesday, July 17 12:00 - 13:30

### Lunch 1

Wednesday, July 17 13:30 - 15:10

### Oral Session 1

Physical Sensors - 1

Chair: Dr. José L Fabris

#### **13:30 *A Temperature-Compensated FBG Sensor Interrogator***

[Gustavo Mattos](#), [Alex Dante](#), [Regina Allil](#), [Cesar Carvalho](#) and [Marcelo Werneck](#)

In this paper, we present a closed-loop interrogation system for temperature compensation of FBG sensors in measurements of AC voltage. In the proposed system, a filter FBG tracks a sensing FBG under temperature variation. Experimental results show that the proposed system allows for stable measurements of AC voltage in a delta T of 20 °C.

#### **13:50 *Optical Technology for Remote Monitoring of Leakage Current in Isolators of 500-kV Transmission Lines***

[Daniel Sá de Oliveira](#), [Marcelo Werneck](#), [Regina Allil](#), [Alex Dante](#) and [Cesar Carvalho](#)

PAPER REMOVED DUE TO AUTHOR NO-SHOW AT THE WORKSHOP

#### **14:10 *Humidity Monitoring in Acidic Sewer Environments Using Fibre Bragg Grating-based Sensors***

[Matthias Fabian](#), [Heriberto Bustamante](#), [Louisa Vorreiter](#), [Bruno Rente](#), [Miodrag Vidakovic](#), [Ye Chen](#), [Tong Sun](#) and [Kenneth Grattan](#)

Innovative fibre Bragg grating-based sensors have been designed and implemented to monitor reliably the relative humidity and temperature in the challenging harsh, corrosive environment of a working sewer. The robustness and long-term performance of the sensor system has been demonstrated through an extensive 2-month field test, showing excellent performance with no major signs of deterioration.

**14:30 *Strain Measurements for a Magnetostrictive Material Using Fiber Bragg Gratings***

[Oscar Sosa Puerto](#), [Christian Camilo Cano](#) and [Gloria Margarita Varón Durán](#)

Magnetostrictive materials change their crystal network structure properties due to an external magnetic field action. These changes also affect a macroscopic property such as their physical dimension. Optical fiber Bragg gratings could be used to monitor any elongation in a piece of a magnetostrictive material, mainly because of their complete electromagnetic immunity. In this paper, we present the design and complete characterization of the system that uses a Helmholtz coil to produce a controlled magnetic field that is applied to a sample of the magnetostrictive material. Current results include a characterization for both strain and temperature sensitivity of the FBGs to be used.

**14:50 *Macrobending SMS Fiber-Optic Arc Sensor Using Fixed Curvature Radius***

[Jesse Werner Costa](#), [Maria Thereza Rocco Giraldi](#) and [Marcos A. R. Franco](#)

A simple and high sensitivity fiber-optic arc sensor based on single mode-multimode-single mode (SMS) structure is reported. The output power intensity of SMS bend sensors may increase or decrease with the rise of curvature, depending on Multimodal Interference (MMI) conditions. In order to avoid slope inversions due to wide range bend applications, it is possible to choose a fixed curvature radius and let MMI effects happen due to arc variation, as demonstrated with experimental tests. Absolute output power peak sensitivity of 35.82 dB/m is reported.

Wednesday, July 17 15:10 - 15:40

Coffee break 2

Wednesday, July 17 15:40 - 17:20

Oral Session 2

Chemical Sensors

Chair: Dr. Hypolito J. Kalinowski

**15:40 *External Refractive Index Sensitivity Enhancement of a Long Period Grating by Graphene Oxide Overlay***

[Kasun Dissanayake](#), [Bruno Rente](#), [Tong Sun](#), [Kenneth Grattan](#), [Leonardo Binetti](#), [Lourdes Alwis](#) and [Souvik Ghosh](#)

In this paper, an external refractive index sensor is presented based on a graphene oxide coated long period grating. Graphene oxide was coated on the fibre surface using a drop casting technique. Wavelength shift sensitivity was improved by 43% compared to the response of a bare long period grating against external refractive index.

**16:00 *Development of a Solid Substrate for Surface Enhanced Raman Spectroscopy***

[Felipe Hornung](#), [Marcia Muller](#) and [José L Fabris](#)

In this work, a solid substrate for Surface Enhanced Raman Spectroscopy was developed and characterized. The interaction of silver nanoparticles with the probe molecule rhodamine 6G was compared for both liquid and solid substrates. Parameters of the solid substrate were optimized for use with an optical fiber Raman spectrometer.

**16:20 *Optical Sensor to Monitor the Fermentation Process of Beers Based on Etched Fibre Bragg Gratings***

[Vicente Oliveira](#), [Vinicius Nunes Henrique Silva](#), [Andrés Pablo López Barbero](#), [Fernando Peixoto](#), [Leandro Sphaier](#) and [Jean Kuhne](#)

In this paper, it is presented preliminary results in the development of a sensor to monitor the fermentation process of beers in real time based on Etched Fibre Bragg Gratings (EFBG). The experiments show that these sensors are extremely responsive to the density variations, which makes them useful for the monitoring beer fermentation.

#### **16:40 *Optical Fiber Bragg Grating Sensors for Temperature Measurements in the Hyperthermia Treatment***

[Nicolas Ospina Mendivelso](#), [Juan Coronel-Rico](#), [Hector Fabian Guarnizo](#), [Christian Camilo Cano](#) and [Gloria Margarita Varón Durán](#)

The hyperthermia is a treatment consisting in raising the temperature of a part of or the whole body above normal (usually between 35 °C and 45 °C) for a defined period of time using microwave radiation as an adjuvant for the treatment of tumors. However, the use of conventional sensors (thermocouples, thermistors, RTD) presents interference issues linked to the microwave energy scattering that can affect surrounding tissues of the body. The goal of these proposal is to give a proof of concept of the feasibility of using an optical fiber based temperature measurement system taking advantage of the transparency of optical fiber materials when facing microwave energy. This means no undesired reflections or scattering inside the body. In this stage of the work a gelatin phantom was built in order to measure the temperature reached when it is irradiated using a 2.45 GHz and 800 W microwave source. From these results can be inferred a linear relation between the temperature reached and the irradiation time, it is given a proof of concept of real time measurement for hyperthermia applications.

#### **17:00 *Fiber Bragg Grating Coated with Diphenylalanine Nanotubes for Methanol Vapor Detection***

[Ricardo Kamikawachi](#), [Bruno Cunha](#), [Raquel Corotti](#), [Rafael Barreto](#) and [André Conceição](#)

In this work, etched fiber Bragg gratings (EFBG) coated with diphenylalanine nanotubes (DNT) are studied for methanol vapor detection. The DNT morphology is characterized by Scanning Electron Microscopy and the temperature transition is determinate by Small-Angle X-Ray Scattering technique. After the phase transition, a significant increase in wavelength shift can be observed.

Thursday, July 18

Thursday, July 18 8:50 - 10:30

### Oral Session 3

Signal Processing for Sensing

Chair: Dr. Gloria Margarita Varón Durán

#### **8:50 *Interrogation of Long-Period Grating Temperature Sensor Using Fiber Bragg Gratings and Artificial Neural Network***

[Marco Aurélio Jucá](#) and [Alexandre dos Santos Bessa](#)

Considering the increasingly wide application of optical fiber sensors, this paper aims to present an alternative form of interrogation without the use of an optical spectrum analyzer or any other high-cost devices. The sensor studied here is a long-period grating being used to measure temperature. The interrogator is composed of optical filters and photodetectors whose responses are processed by a suitably trained artificial neural network. Results show that this technique enables effective interrogation of a range limited only by the optical bandwidth of the light source.

### **9:10 Adaptive Data Compression Method for Distributed Temperature Sensors**

[Luis Silva](#), [Jorge Samatelo](#), [Marcelo Segatto](#) and [Maria Jose Pontes](#)

This paper presents a new method of adaptive data compression for DTS systems that preserve the curve profile, spatial resolution and temperature resolution of the sensor. The approach allows compressing the data at a compression ratio of 2.65x, saving 62.3% of the hard disk memory, and reducing the processing time of the generated data.

### **9:30 Study on the Best Reflection Spectra of FBGs for Dynamic Sensing**

[Talitha Trovão](#), [Alex Dante](#), [Juan D Lopez](#), [Cesar Carvalho](#), [Regina Allil](#) and [Marcelo Werneck](#)

This paper presents a study of FBG reflection spectrum for application in dynamic measurements, such as AC current and voltage. In this work, we show the best reflection spectra of two FBGs employed in a twin-grating interrogation technique that guarantees the best linearity levels possible in the response of the dynamic measurement sensor.

### **9:50 LPG Spectrum Estimation Using Neural Networks and Temperature Modulated FBG Array**

[Felipe O Barino](#) and [Alexandre dos Santos Bessa](#)

This work proposes a novel approach to Long Period Fiber Grating (LPFG) interrogation involving power measurements to estimate the transmission spectra. The aim of this work is to develop a cheap alternative to the Optical Spectrum Analyzer. To accomplish this task a temperature modulated Fiber Bragg Gratings array was used. Accuracy close to half input spectrum resolution was obtained.

### **10:10 A Simple Optoelectronic Load Cell**

[Camila Moura](#), [Lorena Jeranoski](#), [Pedro Lima](#), [Fernando Castaldo](#), [Valmir de Oliveira](#) and [Hypolito J. Kalinowski](#)

In this work, an optical load cell was developed based on the intensity light variation get as a distance function between a light emitting diode (LED) and a FC-PC multimode optical fiber connector. The load cell is composed by a spring return and mass displacement system. The optical system consists of a LED in the infrared band whose emission is directed to a FC-PC multimode optical cord (MMF 62.5/125) , at another end of the optical cord the power was applied to a phototransistor. The resulting current in the phototransistor was amplified in a two-stage transimpedance circuit using general purpose operational amplifier. The voltage response was correlated to the value of the load applied to the system. Four tests were carried out, in which they exchanged the springs for return and loads intensities. Through the tests, the transducer's calibration curves were done. The optical load cell shown in this work was developed for the cost reduction purpose and the reasonableness simple solution.

Thursday, July 18 10:30 - 11:00

Coffee break 3

Thursday, July 18 11:00 - 12:00

Invited Talk 2

Distributed Brillouin Fibre Sensing: From Fundamentals to Advanced Techniques

**Prof. MARCELO SOTO - UTFSM - Chile**

Chair: Dr. José L Fabris

Thursday, July 18 12:00 - 13:30

Lunch 2

Thursday, July 18 13:30 - 15:10

Oral Session 4

Physical Sensors - 2

Chair: Dr. Marcelo Werneck

**13:30 *Study of Core Diameter Mismatch Based Optical Fiber Sensors for Salinity and Temperature***

[Tanushree Selokar](#) and [Maria Thereza Rocco Giraldi](#)

In this paper it is presented core diameter mismatch structured devices that use multimode interference technique as optical fiber sensors. Singlemode-MultimodeSinglemode (SMS) and Singlemode-Multimode-Singlemode-Multimode-Singlemode (SMSMS) configurations are used for measurement of refractive index (RI) and temperature. The best sensitivity achieved for RI measurements is obtained with the SMS sensor: 273.63 nm/RIU. For temperature sensing, the best sensitivity attained is accomplished using the SMSMS sensor: 312.75 pm/°C.

**13:50 *Multi-parameter Non-Invasive Monitoring of Lithium-Ion Batteries Using Fibre Bragg Gratings***

[Bruno Rente](#), [Matthias Fabian](#), [Tong Sun](#) and [Kenneth Grattan](#)

The integration of Fibre Bragg Gratings (FBG) into the body of Lithium-Ion battery cells, for measuring both their strain and temperature to achieve better overall condition monitoring is reported. Sufficient data have thus been gathered to develop an appropriate model for the prediction and thus the prevention of battery failure.

**14:10 *Fabrication of a Flexible Tactile Sensing System with Macro-Bend Optical Fiber Sensors***

[Diogo Lugarini](#), [Vinicius Carvalho](#), [Marcos Aleksandro Kamizi](#), [José L Fabris](#) and [Marcia Muller](#)

Fabrication steps of a sensing system composed of four optical fiber macro-bend sensors embedded in silicone sheet are described. Sensing ability was tested by individually applying loads from 0.0 kg to 3.0 kg on the sheet surface. Preliminary results show the system ability of detecting loads applied in areas not coinciding with the sensors positions.

**14:30 *Experimental and Simulated Curvature Analysis in Structure Based on Core Diameter Mismatch***

[Felipe Takeda](#), [Victor Rodrigues Cardoso](#), [Cindy Fernandes](#), [Joao Weyl Costa](#) and [Maria Thereza Rocco Giraldi](#)

In this paper study of multimodal interferences in optical fiber curvature sensor is presented. The sensor consist of a Mach-Zender interferometer based in Core Diameter Mismatch technique. The analysis provided a numerical model of adjustment by the diameter in the multimode section with the purpose of acquiring better linear results.

**14:50 *Fabrication of Arc-Induced Long Period Fiber Grating with Opposite Point-by-point Modulation***

[Felipe Delgado](#), [Deivid Campos](#), [Thiago Coelho](#) and [Alexandre dos Santos Bessa](#)

We demonstrate the fabrication of an arc-induced long period fiber grating (LPFG) with opposite point-by-point modulation. The produced LPFG exhibited low polarization dependent loss (PDL) and a linear torsion sensitivity up to 0.197 nm/(rad/m), which is higher than that of the traditional arc-induced LPFGs

Thursday, July 18 15:10 - 15:40

Coffee break 4

Thursday, July 18 15:40 - 17:20

Oral Session 5

Electromagnetic & Special fiber sensors

Chair: Dr. Maria José Pontes

**15:40 *Optical Current Sensor Based on Magnetostrictive Composites***

Juan D Lopez, Alex Dante, Talitha Trovão, Roberto Mok, Cesar Carvalho, Regina Allil, Fabricio Borghi and Marcelo Werneck

This paper presents a novel compact fiber-optic current sensor (FOCS) based on magnetostrictive composites that employ only 1 gram of Terfenol-D. Finite element method (FEM) simulations supported the design and construction of two versions of FOCS, which were capable to measure on a.c. current from 200 to 800 Arms in laboratory.

**16:00 *Analysis of Magnetic Field Sensor Based on Intermodal Interference Using Tapered Square No-Core Fiber***

Wilson Morais, Jr. and Maria Thereza Rocco Giraldi

This paper presents the computational implementation of a magnetic field sensor model, based on the principle of intermodal interference using a taper with square section in an optical fiber. Simulations were performed varying its constructive dimensions in order to analyze the influence of them in the sensor performance.

**16:20 *Electromagnetic Contactor Core Temperature and Dynamic Strain Evaluation Using Fiber Bragg Gratings***

Cesar Tapia, Jorge Luis Roel Ortiz, Uilian José Dreyer and Kleiton Sousa

This paper presents the dynamic strain and temperature measurements for a electromagnetic contactor core using the Fiber Bragg Grating (FBG). These measurements are used to predict future preventative maintenance of this device. The temperature variation is approximately 76 °C. In the steady state, for dynamic strain measurement, the fundamental frequency is 120 Hz.

**16:40 *Influence of Gold Nanoparticles Film on the Sensitivity of Long Period Fiber Grating***

Robsson Pereira Dias, Carla Klimpovuz, Marcela Oliveira, José L Fabris and Marcia Muller

The responses of three coated and uncoated long period gratings to the refractive index of the surroundings are compared. Gratings operate at the visible spectral range close to the plasmon resonance band of gold nanoparticles. Sensitivity increase up to 85.2% was achieved after coating the grating.

**17:00 *D-shaped Photonic Crystal Fiber Biosensor for Glucose Concentration Using a Graphene-Sheet***

[Amanda F Romeiro](#), [Patrick Gaia](#), [Markos Cardoso](#), [Anderson Silva](#) and [Joao Weyl Costa](#)

We design a graphene-based D-shaped photonic crystal fiber refractive index sensor to detect changes in the levels of glucose concentration. Its sensing performance is theoretically analyzed using the Finite Element Method (FEM). The sensor has an average sensitivity of 2560.6 nm/RIU when we vary the glucose concentration from 0 to 200g/l.

Thursday, July 18 19:00 - 21:00

Workshop Dinner

Friday, July 19

Friday, July 19 8:50 - 10:30

Oral Session 6

Chemical & Special fiber sensors

Chair: Dr. Marcelo A. Soto

**8:50 *Plastic Fiber Optic for Ultrasensitive Gas Detector Applications***

[Meysam Keley](#), [Juan D Lopez](#), [Alex Dante](#), [Talitha Trovão](#), [Roberto Mok](#), [Pedro Henrique Romualdo](#), [Fabricio Borghi](#), [Cesar Carvalho](#), [Regina Allil](#) and [Marcelo Werneck](#)

In the present study, an ultrasensitive hydrogen sulfide sensor is developed via functionalization of U-shaped Plastic optical fiber. The results of the sensor demonstrate low response time and full recovery while exposed to a gas mixture containing 200ppm concentration of measurand.

**9:10 *Rehabilitation Tools on Biomedical Using Fiber Bragg Grating Sensors***

[Alessandra Kalinowski](#), [José Galvão](#), [Talita Paes De Bastos](#), [Eduardo Dureck](#), [Uilian José Dreyer](#), [Carlos Zamarreño](#), [Cicero Martelli](#) and [Jean Carlos Cardozo da Silva](#)

PAPER REMOVED DUE TO AUTHOR NO-SHOW AT THE WORKSHOP

**9:30 *Etched Fiber Bragg Gratings Functionalized with PCDTBT:PDI Thin Film for Ammonia Detection***

[Jean Kuhne](#), [Anderson Gavim](#), [Paula Rodrigues](#), [Bruno Torres](#), [Andréia Macedo](#), [Jeferson de Deus](#) and [Ricardo Kamikawachi](#)

The functionalization of an etched fiber Bragg grating with a drop casted thin film improved the sensor sensitivity to ammonia vapors. The film was obtained from a solution of a perylene derivative along with the copolymer PCDTBT, in chlorobenzene. The resulting sensor detects ammonia vapors ranging from 27 to 6954 ppm, at room temperature.

**9:50 *Hole-Assisted Helically Twisted Twin-Core Fiber Coupler***

[Juan E Úsuga](#), [William M Guimarães](#) and [Marcos A. R. Franco](#)

Coupling characteristics of helically twisted twin-core fibers with hole-assisted structure were numerically evaluated. It was observed the increase of coupling beat length with the increase of twist rate, and it was confirmed the effectiveness of hole-assisted guidance to loss reduction. The proposed twisted fiber, with 66 mm length, works as a circular polarization splitter.

#### **10:10 *Fiber Specklegram Analysis for Monitoring Evaporation Inside a Capillary-like Optical Fiber***

[Thiago D Cabral](#), [Luiz da Silva](#), [Eric Fujiwara](#) and [Cristiano MB Cordeiro](#)

A liquid filled capillary-like fiber sensor for monitoring the evaporation rate of the filling liquid through fiber specklegram analysis is proposed and evaluated. Experimental data shows a clear relation between the specklegram shift over time and evaporation, prospectively allowing the assessment of multiple parameters of the liquid by modeling evaporation in a capillary.

Friday, July 19 10:30 - 11:00

[Coffee break 5](#)

Friday, July 19 11:00 - 12:00

[Round table](#)

Optical Fiber Sensors: Markets & Products

**Dr. Ed Mendoza - Redondo Optics**

**Dr. Alexis Mendez - MHC Engineering**

**Dr. João Batista Rosolem - Fundação CPqD**

Chair: Dr. Hypolito J. Kalinowski

Friday, July 19 12:00 - 13:30

[Lunch 3](#)

Friday, July 19 13:30 - 15:10

[Oral Session 7](#)

Field applications & Sensor development

Chair: Dr. Josemir Coelho Santos

**13:30 *Fibre Bragg Grating Based Sensor System for Pantograph - Overhead Line Interface Condition Monitoring During Electrified Train Operation***

[Miodrag Vidakovic](#), Tong Sun, Ye Chen, Matthias Fabian, Kenneth Grattan, Matt Askill, Lee Brun, Rod Fawcett, Peter Dearman and Simon Warren

Efficient current collection and monitoring railway current-collecting pantographs is one of the key challenges for railway sector in electrical train operation. Fibre Bragg grating (FBG) sensors integrated into a pantograph are used to provide accurate contact force and contact location measurements at the crucial pantograph-overhead line (OHL) interface. Data collected during field trials are reported in the paper.

**13:50 *Optical Current Transducer Metrological Characterization for Current Transformer on Site Calibration***

[Marcelo Costa](#)

This paper presents metrological characterization of an optical current transducer solution for high voltage current transformers on site calibration. In metrological tests, from 150 A to 1700 A, ratio errors were between  $\pm 0.1\%$  and phase errors were between  $\pm 5'$ . Although the good results, some strategies are suggested for uncertainty improvement in field application.

**14:10 *Evaluation of Coupling to Symmetric and Asymmetric Cladding Modes in Long-Period Fiber Gratings***

[Felipe Delgado](#), Renato Luiz, Daniel D. Silveira and Alexandre dos Santos Bessa

We analyze the influence of coupling to symmetric and asymmetric cladding modes in arc-induced Long-Period Fiber Gratings for temperature and strain sensing. The origin of this difference in energy coupling is related to the fabrication process of these gratings and depends on the electric arc discharge conditions, which modulates the refractive index and geometry of the optical fiber. Finally, results demonstrate the performance of different cladding modes excited in arc-induced LPPGs to temperature and strain applications and, in addition, indicate which coupling might be appropriate to certain sensing applications.

**14:30 *Inertial Compensation in an Electrified Railway Pantograph Condition Monitoring System Using FBG-based Accelerometers***

[Ye Chen](#), Miodrag Vidakovic, Matthias Fabian, Tong Sun, Kenneth Grattan, Matt Askill and Lee Brun

This paper presents the results from an assessment of dynamic force inertial compensation, obtained using two Fibre Bragg Grating (FBG)-based accelerometers integrated into a railway current-collecting pantograph, allowing more accurate measurement of contact force and contact location are presented. In the tests carried out, a high level of transfer function accuracy in the monitoring of dynamic contact force was achieved.

**14:50 *Optical Fiber Sensor for Carbon Dioxide Measurement Using Tapered Long Period Grating***

[Manuella Oliveira](#), Alexandre dos Santos Bessa, Felipe Delgado, Marco Aurélio Jucá, Daniel Discini, Thiago Coelho and Renato Luiz

This paper presents the development of a refractive index (RI) sensing methodology for measuring CO<sub>2</sub> concentration in environments considering the temperature effect. We propose and demonstrate the modulated tapered Long Period Gratings to enhance the RI sensitivity of the sensor. The results show it is possible to measure the CO<sub>2</sub> considering the temperature cross-sensitivity effect.

Friday, July 19 15:10 - 15:40

Coffee break 6

Friday, July 19 15:40 - 16:00

Closing Session

Chairs: Dr. Maria Aparecida Martinez

Dr. Maria Thereza Rocco Giraldi

# Proceedings of the Latin American Workshop on Optical Fiber Sensors

LAWOFS 2019 – Rio de Janeiro, Brazil

## Summary

**Wednesday, July 17 13:30 - 15:10**

Session 1

Physical Sensors

Chair: José L Fabris

13:30 A Temperature-Compensated FBG Sensor Interrogator	1
Gustavo Mattos, Alex Dante, Regina Allil, Cesar Carvalho and Marcelo Werneck	
13:50 Optical Technology for Remote Monitoring of Leakage Current in Isolators of 500-kV Transmission Lines – PAPER NOT INCLUDED IN PROCEEDINGS DUE TO AUTHOR NO SHOW	
Daniel Sá de Oliveira, Marcelo Werneck, Regina Allil, Alex Dante and Cesar Carvalho	
14:10 Humidity Monitoring in Acidic Sewer Environments Using Fibre Bragg Grating-based Sensors	5
Matthias Fabian, Heriberto Bustamante, Louisa Vorreiter, Bruno Rente, Miodrag Vidakovic, Ye Chen, Tong Sun and Kenneth Grattan	
14:30 Strain Measurements for a Magnetostrictive Material Using Fiber Bragg Gratings	10
Oscar Sosa Puerto, Christian Camilo Cano and Gloria Margarita Varón Durán	
14:50 Macrobending SMS Fiber-Optic Arc Sensor Using Fixed Curvature Radius	14
Jesse Werner Costa, Maria Thereza Rocco Giralddi and Marcos A. R. Franco	

## **Wednesday, July 17 15:40 - 17:20**

### Session 2

#### Chemical Sensors

Chair: Hypolito J. Kalinowski

15:40 External Refractive Index Sensitivity Enhancement of a Long Period Grating by Graphene Oxide Overlay 18

Kasun Dissanayake, Bruno Rente, Tong Sun, Kenneth Grattan, Leonardo Binetti, Lourdes Alwis and Souvik Ghosh

16:00 Development of a Solid Substrate for Surface Enhanced Raman Spectroscopy 22

Felipe Hornung, Marcia Muller and José L Fabris

16:20 Optical Sensor to Monitor the Fermentation Process of Beers Based on Etched Fibre Bragg Gratings 27

Vicente Oliveira, Vinicius Nunes Henrique Silva, Andrés Pablo López Barbero, Fernando Peixoto, Leandro Sphaier and Jean Kuhne

16:40 Optical Fiber Bragg Grating Sensors for Temperature Measurements in the Hyperthermia Treatment 31

Nicolas Ospina Mendivelso, Juan Coronel-Rico, Hector Fabian Guarnizo, Christian Camilo Cano and Gloria Margarita Varón Durán

17:00 Fiber Bragg Grating Coated with Diphenylalanine Nanotubes for Methanol Vapor Detection 36

Ricardo Kamikawachi, Bruno Cunha, Raquel Corotti, Rafael Barreto and André Conceição

## **Thursday, July 18 8:50 - 10:30**

### Session 3

#### Signal Processing for Sensing

Chair: Gloria Margarita Varón Durán

8:50 Interrogation of Long-Period Grating Temperature Sensor Using Fiber Bragg Gratings and Artificial Neural Network 41

Marco Aurélio Jucá and Alexandre dos Santos Bessa

9:10 Adaptive Data Compression Method for Distributed Temperature Sensors	45
Luis Silva, Jorge Samatelo, Marcelo Segatto and Maria Jose Pontes	
9:30 Study on the Best Reflection Spectra of FBGs for Dynamic Sensing	50
Talitha Trovão, Alex Dante, Juan D Lopez, Cesar Carvalho, Regina Allil and Marcelo Werneck	
9:50 LPG Spectrum Estimation Using Neural Networks and Temperature Modulated FBG Array	55
Felipe O Barino and Alexandre dos Santos Bessa	
10:10 A Simple Optoelectronic Load Cell	59
Camila Moura, Lorena Jeranoski, Pedro Lima, Fernando Castaldo, Valmir de Oliveira and Hypolito J. Kalinowski	

#### **Thursday, July 18 13:30 - 15:10**

##### Session 4

##### Physical Sensors

Chair: Marcelo Werneck

13:30 Study of Core Diameter Mismatch Based Optical Fiber Sensors for Salinity and Temperature	64
Tanushree Selokar and Maria Thereza Rocco Giraldi	
13:50 Multi-parameter Non-Invasive Monitoring of Lithium-Ion Batteries Using Fibre Bragg Gratings	69
Bruno Rente, Matthias Fabian, Tong Sun and Kenneth Grattan	
14:10 Fabrication of a Flexible Tactile Sensing System with Macro-Bend Optical Fiber Sensors	73
Diogo Lugarini, Vinicius Carvalho, Marcos Aleksandro Kamizi, José L Fabris and Marcia Muller	
14:30 Experimental and Simulated Curvature Analysis in Structure Based on Core Diameter Mismatch	78
Felipe Takeda, Victor Rodrigues Cardoso, Cindy Fernandes, Joao Weyl Costa and Maria Thereza Rocco Giraldi	
14:50 Fabrication of Arc-Induced Long Period Fiber Grating with Opposite Point-by-point Modulation	83
Felipe Delgado, Deivid Campos, Thiago Coelho and Alexandre dos Santos Bessa	

## Thursday, July 18 15:40 - 17:20

### Session 5

#### Electromagnetic & Special fiber sensors

Chair: Maria Jose Pontes

- 15:40 Optical Current Sensor Based on Magnetostrictive Composites 87  
Juan D Lopez, Alex Dante, Talitha Trovão, Roberto Mok, Cesar Carvalho, Regina Allil, Fabricio Borghi and Marcelo Werneck
- 16:00 Analysis of Magnetic Field Sensor Based on Intermodal Interference Using Tapered Square No-Core Fiber 91  
Wilson Morais, Jr. and Maria Thereza Rocco Giraldi
- 16:20 Electromagnetic Contactor Core Temperature and Dynamic Strain Evaluation Using Fiber Bragg Gratings 96  
Cesar Tapia, Jorge Luis Roel Ortiz, Uilian José Dreyer and Kleiton Sousa
- 16:40 Influence of Gold Nanoparticles Film on the Sensitivity of Long Period Fiber Grating 101  
Robsson Pereira Dias, Carla Klimpovuz, Marcela Oliveira, José L Fabris and Marcia Muller
- 17:00 D-shaped Photonic Crystal Fiber Biosensor for Glucose Concentration Using a Graphene-Sheet 106  
Amanda F Romeiro, Patrick Gaia, Markos Cardoso, Anderson Silva and Joao Weyl Costa

## Friday, July 19 8:50 - 10:30

### Session 6

#### Chemical & Special fiber sensors

Chair: Marcelo A. Soto

- 8:50 Plastic Fiber Optic for Ultrasensitive Gas Detector Applications 111  
Meysam Keley, Juan D Lopez, Alex Dante, Talitha Trovão, Roberto Mok, Pedro Henrique Romualdo, Fabricio Borghi, Cesar Carvalho, Regina Allil and Marcelo Werneck

9:10 Rehabilitation Tools on Biomedical Using Fiber Bragg Grating Sensors – PAPER NOT INCLUDED  
IN PROCEEDINGS DUE TO AUTHOR NO SHOW

Alessandra Kalinowski, José Galvão, Talita Paes De Bastos, Eduardo Dureck, Uilian José Dreyer,  
Carlos Zamarreño, Cicero Martelli and Jean Carlos Cardozo da Silva

9:30 Etched Fiber Bragg Gratings Functionalized with PCDTBT:PDI Thin Film for Ammonia  
Detection 116

Jean Kuhne, Anderson Gavim, Paula Rodrigues, Bruno Torres, Andréia Macedo, Jeferson de Deus  
and Ricardo Kamikawachi

9:50 Hole-Assisted Helically Twisted Twin-Core Fiber Coupler 121

Juan E Úsuga, William M Guimarães and Marcos A. R. Franco

10:10 Fiber Specklegram Analysis for Monitoring Evaporation Inside a Capillary-like Optical Fiber  
126

Thiago D Cabral, Luiz da Silva, Eric Fujiwara and Cristiano MB Cordeiro

## Friday, July 19 13:30 - 15:10

Session 7

Field applications & Sensor development

Chair: Josemir Coelho Santos

13:30 Fibre Bragg Grating Based Sensor System for Pantograph - Overhead Line Interface  
Condition Monitoring During Electrified Train Operation 131

Miodrag Vidakovic, Tong Sun, Ye Chen, Matthias Fabian, Kenneth Grattan, Matt Askill, Lee Brun,  
Rod Fawcett, Peter Dearman and Simon Warren

13:50 Optical Current Transducer Metrological Characterization for Current Transformer on Site  
Calibration 136

Marcelo Costa, Angela Costa Santa Brigida, Cledson Santana Lopes Goncalves and Joao Weyl  
Costa

14:10 Evaluation of Coupling to Symmetric and Asymmetric Cladding Modes in Long-Period Fiber  
Gratings 140

Felipe Delgado, Renato Luiz, Daniel D. Silveira and Alexandre dos Santos Bessa

14:30 Inertial Compensation in an Electrified Railway Pantograph Condition Monitoring System  
Using FBG-based Accelerometers 144

Ye Chen, Miodrag Vidakovic, Matthias Fabian, Tong Sun, Kenneth Grattan, Matt Askill and Lee Brun

14:50 Optical Fiber Sensor for Carbon Dioxide Measurement Using Tapered Long Period Grating

148

Manuella Oliveira, Alexandre dos Santos Bessa, Felipe Delgado, Marco Aurélio Jucá, Daniel Discini, Thiago Coelho and Renato Luiz

# A Temperature-Compensated FBG Sensor Interrogator

Gustavo Marques Mattos<sup>1,2</sup>, Alex Dante<sup>1</sup>, Regina Célia da Silva Barros Allil<sup>1</sup>,  
Cesar Cosenza Carvalho<sup>1</sup> and Marcelo Martins Werneck<sup>1</sup>

<sup>1</sup>Photonics and Instrumentation Laboratory, Electrical Engineering Program, COPPE,  
Federal University of Rio de Janeiro, Brazil, <sup>2</sup>gusmmattos@gmail.com

**Abstract:** In this paper, we present a closed-loop interrogation system for temperature compensation of FBG sensors in measurements of AC voltage. In the proposed system, a filter FBG tracks a sensing FBG under temperature variation. Experimental results show that the proposed system allows for stable measurements of AC voltage in a  $\Delta T$  of 20 °C.

## 1. Introduction

Optical fiber sensors (OFS) have been making an enormous impact on modern instrumentation and measurement systems due to excellent properties of optical fibers. Some types of OFS that have been popularized in recent decades are those based on Fiber Bragg gratings (FBGs). In the electric power systems industry, they are particularly used for the monitoring of voltage of high-voltage transmission lines, as reported by [1-8].

However, in order to avoid measurement errors, the interrogation system of an FBG-based sensor should separate the cross-sensitivity between temperature and strain, such as demonstrated in [2]. In [4], temperature compensation was performed by controlling the sensor temperature with the actuation of a thermoelectric cooler (TEC). In [7], this same technique was employed but without using a temperature sensor. In Dante *et al.* [2] work, a piezoelectric actuator was used instead of a TEC.

In this work, we report the development of an optoelectronic interrogation system for FBG sensors employing a twin grating interrogation technique, which allows temperature compensation of sensors, applied to measurement of AC variables, such as current and voltage using a TEC as an actuator. The developed system was tested in laboratory for high-voltage measurements with induced temperature variations.

## 2. Fundamentals of FBG

An FBG is formed by periodic modulations of the refractive index in a portion of the optical fiber core written with ultraviolet (UV) radiation. When a broadband light source (BLS) illuminates this fiber, part of the light is reflected by the FBG with a characteristic spectrum profile centered at  $\lambda_B$ , the Bragg wavelength. Its sensitivity as a function of strain and temperature is given by

$$\frac{\Delta\lambda_B}{\lambda_B} = (1 - \rho_e)\epsilon_z + (\alpha + \eta)\Delta T \quad (1)$$

where  $\rho_e$  is the photoelastic coefficient, which is dependent on the material of the fiber core,  $\epsilon_z$  is the longitudinal mechanical stress applied to the FBG,  $\alpha$  is the coefficient of thermal expansion of the fiber and  $\eta$  is the thermo-optical coefficient, which is related to the change in the refractive index of the fiber core by temperature variations.

## 3. Materials and Methods

### 3.1. The Twin Grating Interrogation Technique

Several types of FBG-based sensors for AC voltage and current have been described in the literature [1,2-4,6]. The most popular interrogation techniques for FBG sensors rely on high-speed interferometry, such as those employed by commercial FBG interrogators. However, those techniques are preferred when a broad spectrum must be covered because they have low accuracies, whereas interrogation systems based on the twin-grating technique [2,5] may provide subpicometric resolutions [2,3,7]. This is due to the great sensitivity they can achieve, depending on the transducer, e. g., piezoelectric for high-voltage sensors [1,5,6,8] and Terfenol-D for current sensors [3,8].

In the twin grating interrogation technique, the spectrum reflected by an FBG works as a light source to another FBG. The light reflected from this second FBG is the overlapping area of both FBGs spectra. This optical signal is converted into photocurrent. Then a transimpedance amplifier can convert it to voltage levels, easily read by an oscilloscope or microcontroller. If there is a change in the convolution between the two spectra, the optical

power will change, meaning that there was a relative shift of the FBGs. In case of the need to measure only mechanical strain, temperature variations must be compensated.

### 3.2. Interrogation Independent of Temperature Variations

In order to compensate for temperature shifts on the sensing-FBG, a closed-loop optical power control was implemented [2,7]. Fig. 1(a) shows that, given the sensing and the filter FBGs spectra (red and blue curves, respectively) at the initial instant and at the temperature  $T_0$ , they are superimposed and the black hatched area is the optical power reflected that is guided to the photodetector. The dashed line represents the AC displacement of the sensing-FBG spectrum due to the high-voltage application.

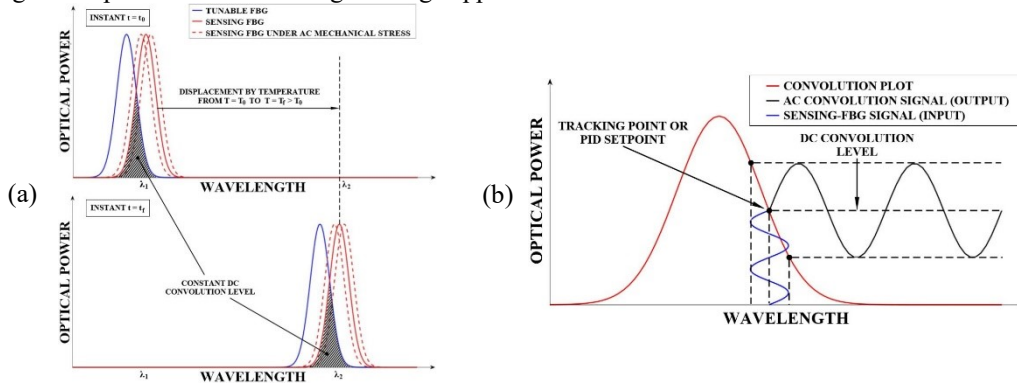


Fig. 1. (a) Graphical representation of the FBGs spectra convolution independent of temperature variations on the sensor; (b) convolution plot obtained from the FBGs spectra, the tracking point and typical input and output signals of a sensor.

If, at the instant  $t_f$ , the center wavelength of the sensing-FBG spectrum moves due to a change on temperature, the closed-loop control keeps the filter-FBG, which is installed over the TEC, tracking the sensing-FBG over low frequency, temperature-induced shifts. It is performed by a firmware-based routine that reads continuously the DC level of the optical signal acquired by the photodetector and feeds it back to a proportional-integral-derivative (PID) controller. The setpoint is chosen to be the one that keeps the filter-FBG overlapped over the sensing-FBG at an optimal point of operation, which is the point of the convolution plot (see Fig. 1(b)) that allows for the best linearity in the output signal (black line). The blue line relates to the high-voltage signal read by the sensing-FBG.

### 3.3. Experimental Setup - FBGs and TEC Element

In this project, two similar FBGs (Technica SA) were used, which specifications are:  $(1530 \pm 0.5)$  nm center wavelength, 2-mm length and reflectivity higher than 50 % of the input power. The thermoelectric actuator in this work is a  $(15 \times 15 \times 4.3)$ -mm TEC (Adaptive Thermal Management Ltd., model ET-031-10-20). It supports a 2.5 A, 3.8 V, with power capacity up to 5.8 W in a maximum 75°C temperature shift.

### 3.4. Overview of the Optical and Electronic Setup

The experimental setup in Fig. 2(a) was assembled in laboratory. The sensing-FBG was bonded to the piezoelectric actuator (PZT-4,  $d_{33} = 300$  pm/V, Sparkler Piezoceramics Pvt Ltd) employed as a high-voltage sensor. To enhance the wavelength range of the filter-FBG and, hence, the interrogation system temperature compensation capability, it was bonded to an aluminium plate, which was placed in thermal contact with the TEC. Fig. 2(b) shows both FBGs bonded to their respective substrates using an industrial cyanoacrilate adhesive (Loctite 401).

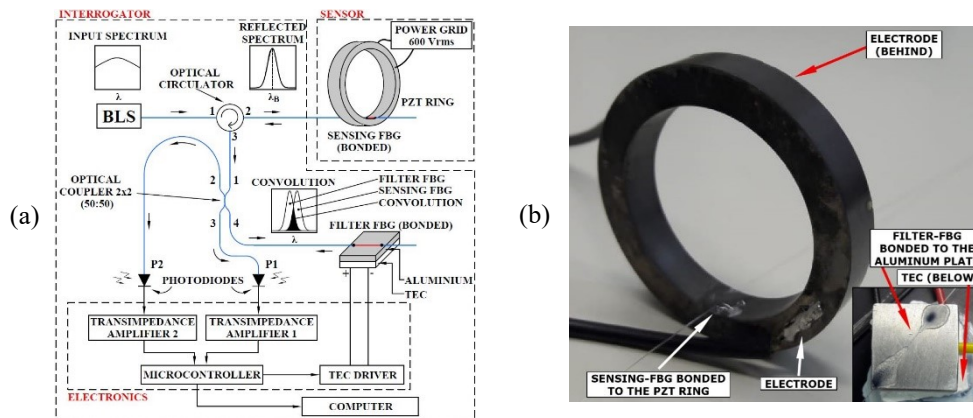


Fig. 2. (a) Optical and electronic setup of the proposed interrogation system; (b) sensing-FBG bonded to the inner diameter of a ring-shaped PZT ceramics. Inset: filter-FBG bonded to an aluminium substrate.

### 3.5. Principle of Operation

A subroutine in firmware determines the optimal point of operation of the system (the point in which the output signal presents the least distortion). After that, the PID controller keeps the filter-FBG tracking the sensing-FBG over slow, temperature-induced wavelength shifts, maintaining the average of the convolution signal fixed. The filter-FBG, bonded to the aluminium plate, has its sensitivity to temperature about three times of the bare FBG. This is also an advantage of the proposed system over the one in [2] because it allows a larger range of temperature compensation.

As shown in Fig. 2(a), part of the optical power reflected by the sensing-FBG is guided through port 3 of the optical coupler and it is continuously monitored by photodiode P1 to compensate for optical power fluctuations of the BLS. The compensation is performed by a normalization between the digital values read from photodiodes.

## 4. Results and Discussion

### 4.1. Implementation and Tests of the Main Control Routine

The controller parameters are set in firmware, then a first run is performed after the system is turned on. The TEC is driven through a pulse-width-modulated (PWM) driver implemented with a full H-bridge, whose analog input is also provided by the microcontroller. Fig. 3 shows a time-record plot of the main control routine starting when the electronic system is turned on.

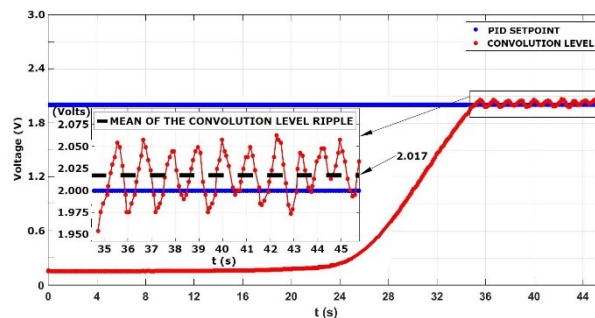


Fig. 3. Graph showing the controlled variable reaching the PID setpoint proving the proper work of the controller.

It is possible to see that the convolution power (red curve) is near zero at the beginning, because the FBGs spectra are only slightly overlapped. As the filter-FBG is heated, its spectrum overlaps the spectrum of the sensing-FBG, causing the convolution power to rise to the optimal point of operation (blue line). It is also seen in Fig. 3 that, within 30 s, the control routine keeps the filter-FBG tracking the sensing-FBG over temperature-induced wavelength shifts.

At the steady-state, the convolution level ripples around the PID setpoint due to the noise and inherent characteristics of the components. In the inset graph of Fig. 3, the referred ripple can be seen, as well as the control maintaining the convolution DC level within  $\sim 100$  mV, that means approximately  $5 \times 10^{-3}$  pm.

### 4.2. Temperature-Compensated Voltage Measurements

The experiments performed in laboratory consisted of immersing the sensor in a bowl with insulating oil heated up to 50°C and then, tests were conducted with AC voltage at 600 Vrms. They were performed with the sensor cooling down to room temperature, around 30°C. Fig. 4 shows convolution level data points acquired during the temperature variation of the sensor, which means that the filter FBG was kept tracking the sensing FBG through the temperature range shown. It can also be seen in Fig. 4 that the maximum deviation of the experimental data points is 30 mV, which denotes the high stability achieved by the control implemented.

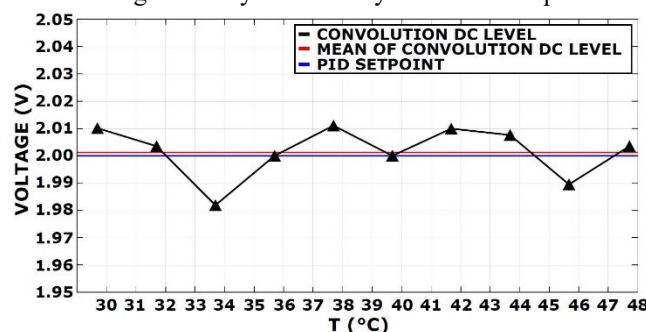


Fig. 4. Temperature compensation performed by the developed interrogation system.

The interrogation system also acquires the AC optical signal. Fig. 5(a) show one cycle of the input high-voltage signal applied to the sensor and Fig. 5(b) its fast Fourier transform (FFT). For a comparison between the input and output signals and the characterization of the interrogation system, Figs. 5(c) and 5(d) show three one-cycle acquisitions of the output signal and their FFTs, respectively. They were acquired with the sensor prototype in three different temperatures, 33.7°C, 43.7°C, and 47.7°C. A comparison between the FFT levels of Figs. 5(b) and 5(d) shows that their spectral compositions are well correlated. This result is of great importance because it means that the developed interrogation system is capable of AC measurements independent of temperature variations, without the need for a temperature sensor.

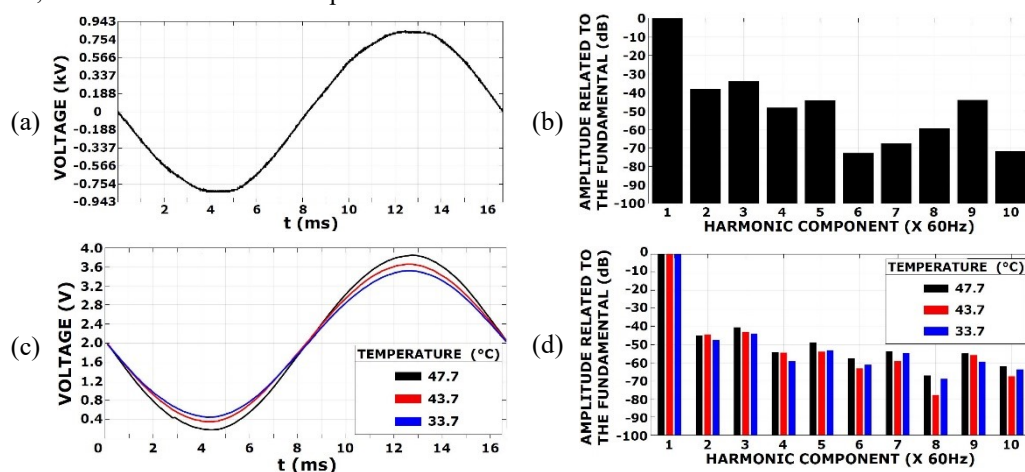


Fig. 5. (a) The power grid AC voltage signal and (b) its FFT. (c) Output signals of the interrogation system in different temperatures and measured at the sensing point and (d) their FFTs.

## 5. Conclusions

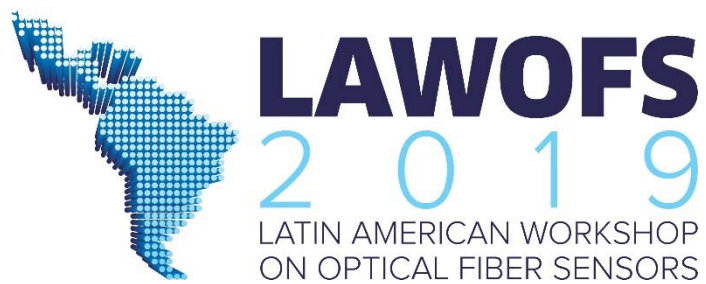
A closed-loop optoelectronic interrogation system for FBG sensors was built and tested in laboratory. A high-voltage sensor prototype was employed under a temperature range of 20 °C. The temperature compensation performed provides a very accurate tuning for the filter-FBG, since an active system does so. Experimental results have shown that the closed-loop control maintains the filter-FBG tracking the sensing FBG within a  $\Delta\lambda$  of  $5 \times 10^{-3}$  pm. This is an important result, since the stability of the tracking point is directly related to the level of distortion at the output signal. Other methods (passive ones) to compensate thermal variations do not offer a precise tuning.

One of the advantages of the proposed system is that it does not require a temperature sensor at the sensing point, as done by Ribeiro *et al.* [4]. Instead, the system relies on the measurement of the optical convolution signal between the reflection spectra of two FBGs to control it. Furthermore, the proposed system is easily expandable for monitoring an array of sensing-FBGs.

## 6. References

- [1] G. Fusiek, J. Nelson, P. Niewczas, J. Havunen, E. P. Suomalainen, and J. Hallstrom, "Optical voltage sensor for MV networks", in Proceedings of IEEE Sensors, Vol. 2017-december, pp. 1-3, (2017).
- [2] A. Dante, R. M. Bacurau, A. W. Spengler, E. C. Ferreira and J. A. S. Dias, "A temperature-independent interrogation technique for FBG sensors using monolithic multilayer piezoelectric actuators", IEEE Trans. on Instr. and Measurement, Vol. 65, n. 11, pp. 2476-2484, (2016).
- [3] F. V. B. Nazaré and M. M. Werneck, "Compact optomagnetic Bragg-grating-based current sensor for transmission lines", IEEE Sensors Journal, Vol. 15, n. 1, pp. 100-109, (2015).
- [4] B. A. Ribeiro, M. M. Werneck, F. B. V. Nazaré and M. N. Gonçalves, "A Bragg grating tunable filter based on temperature control system to demodulate a voltage sensor", 24th International Conference on Optical Fiber Sensors, Vol. 9634, pp. 963444-1 – 963444-4, (2015).
- [5] G. Fusiek, P. Orr, and P. Niewczas, "Temperature-independent high-speed distributed voltage measurement using intensimetric FBG interrogation", IEEE International Instrumentation and Measurement Technology Conference, Vol. 1, n. 2015, pp. 1430–1433, (2015).
- [6] A. O. Cremonesi, E. C. Ferreira, A. J. B. Filho, and J. A. S. Dias, "A fiber bragg grating RMS current transducer based on the magnetostriction effect using a terfenol-D toroidal-shaped modulator", IEEE Sensors Journal, Vol. 13, n. 2, pp. 683-690, (2013).
- [7] F. W. D. Pfrimer, M. Koyama, A. Dante, E. C. Ferreira and J. A. S. Dias, "A closed-loop interrogation technique for multi-point temperature measurement using fiber Bragg gratings", Journal of Lightwave Technology, Vol. 32, n. 5, pp. 971-977, (2014).
- [8] R. C. S. B. Allil, and M. M. Werneck, "Optical high-voltage sensor based on fiber Bragg grating and PZT piezoelectric ceramics", IEEE Transactions on Instrumentation and Measurement, Vol. 60, n. 6, pp. 2118-2125, (2011).

**Page left in blank due to paper no-show at the workshop.**



# Humidity monitoring in acidic sewer environments using Fibre Bragg Grating-based sensors

Matthias Fabian<sup>1</sup>, Bruno Rente<sup>1</sup>, Heribert Bustamante<sup>2</sup>, Louisa Vorreiter<sup>2</sup>, Chen Ye<sup>1</sup>, Miodrag Vidakovic<sup>1</sup>, Tong Sun<sup>1</sup> and Kenneth T.V. Grattan<sup>1</sup>

<sup>1</sup> School of Mathematics, Computer Science and Engineering, City, University of London, 10 Northampton Square, London EC1V 0HB, UK

<sup>2</sup> Sydney Water, PO Box 399, Parramatta, NSW 2124, Australia  
matthias.fabian.1@city.ac.uk

**Abstract:** Innovative fibre Bragg grating-based sensors have been designed and implemented to monitor reliably the relative humidity and temperature in the challenging harsh, corrosive environment of a working sewer. The robustness and long-term performance of the sensor system has been demonstrated through an extensive 2-month field test, showing excellent performance with no major signs of deterioration.

## 1. Introduction

The corrosion of the aging concrete-based sewage infrastructure in modern cities poses a huge financial burden on urban societies in terms of infrastructure maintenance, rehabilitation and repair. While there are a multitude of factors leading to the corrosion of concrete sewer pipes, the oxidation of hydrogen sulfide (H<sub>2</sub>S, hydrosulfuric acid) is playing a key role in the process of initiating corrosion [1]. Once initiated, the rate of corrosion is then accelerated by high humidity levels [2]. A third factor is the temperature inside the sewer which influences the emission rate of H<sub>2</sub>S from the liquid to the gas phase [3].

It is therefore desirable to monitor the key parameters that contribute to degradation in such acidic sewer environments, often stretching for hundreds of miles. However, most conventional sensors do not withstand such conditions over the extended periods of time needed for effective long-term monitoring required by industry, especially when exposed to permanently high humidity (>95%rh) and the acid environment.

Due to their robustness, light weight, chemical inertness and potential for multiplexing, optical fibre sensors offer a viable solution to this critical monitoring problem. In this paper, the results of an extensive 2-month test trial of an FBG-based combined humidity and temperature sensor system, exposed to a real sewer environment, are reported and discussed.

## 2. Sensor design and instrumentation

The working principle of FBGs as the basis of sensor systems has been widely reported, e.g. in the work of Rao [4], and will therefore not be repeated here. In order to create the sensors used in this study, a pair of FBGs of 5 mm in length were inscribed into germanium-doped photosensitive fibre (Fiber Core SM1500(4.2/125)) using the phase mask technique [4]. The arrangement used is shown in Fig. 1. Following grating inscription, one of the FBGs (FBG2 in Fig. 1) was dip-coated with a total of 20 layers of a hygroscopic material, individually applied, in this case using polyimide as the active element in the sensor (PI, HD Microsystems PI-2525), resulting in an overall coating thickness of approximately 22 µm. The dip-coating process is described in detail in [5] for long period gratings but applies in the same way to the coating of FBGs. The hygroscopic material reacts to the humid environment (and thus changes in the relative humidity) by expanding or contracting, thus exerting strain on the coated section of fibre, i.e., changing the characteristic wavelength of FBG2. To facilitate the bonding of the PI to the bare fibre, the latter was first coated with one layer of 3-APTS (3-Aminopropyltriethoxysilane). As FBG2 responds to both humidity and temperature changes, FBG1 was left bare to allow it to be used for temperature compensation, as explained below.

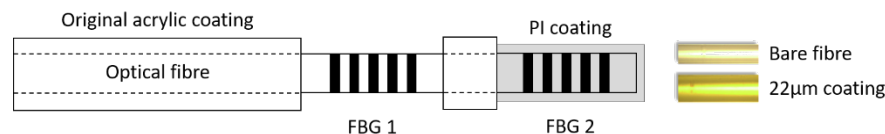


Fig. 1. Schematic of a fibre with two FBGs as used in this study. FBG1 is bare (uncoated) whereas FBG2 is coated with a hygroscopic material

Both FBGs in Fig. 1 are strain-relieved (and thus not responsive to any changes in their characteristic wavelengths due to external strains), i.e., FBG2 is designed to be responsive to changes in temperature (T) and humidity (RH) whereas FBG1 is responsive only to temperature changes. Therefore, the temperature-induced changes in FBG2 can be compensated through a knowledge of the wavelength changes to FBG1 and both parameters can be expressed by the following equations:

$$T = \frac{1}{c_{T1}}(\lambda_1 - \lambda_{1(0)}) \quad (1)$$

$$RH = \frac{1}{c_{RH2}}(\lambda_2 - \lambda_{2(0)} - c_{T2} \cdot T) \quad (2)$$

where  $\lambda_i$  are the measured Bragg wavelengths (nm) of FBG1 and FBG2,  $\lambda_{i(0)}$  their Bragg wavelengths at 0°C,  $c_{Ti}$  their temperature coefficients or sensitivities (nm/°C), and  $c_{RH_i}$  their moisture sensitivities (nm/%RH). In Matrix form, the impact of changes in temperature and humidity on the FBG peak wavelengths can be described as:

$$\Lambda = C \cdot X \quad (3)$$

With

$$\Lambda = \begin{bmatrix} \Delta\lambda_1 \\ \Delta\lambda_2 \end{bmatrix} \quad C = \begin{bmatrix} c_{T1} & c_{RH1} \\ c_{T2} & c_{RH2} \end{bmatrix} \quad X = \begin{bmatrix} \Delta T \\ \Delta RH \end{bmatrix} \quad (4)$$

Where  $c_{RH1}$  equals zero as FBG1 does not respond to changes in relative humidity.

Apart from the two Bragg wavelengths,  $\lambda_i$ , measured, all other parameters have been obtained through the calibration of the sensors in a controlled temperature/humidity environment where these parameters can be carefully controlled.

The coated fibre lies at the core of the moisture-sensitive instrument which has been developed and was carefully packaged with the fibres carefully placed inside a perforated PEEK (polyether ether ketone) tube. This has an outer diameter of 8 mm (Fig. 2). PEEK offers excellent mechanical and chemical resistance, characteristics that are retained to high temperatures and which makes this material highly suitable for its intended use in a sewer environment. The sensor package consists of both an inner and outer tube with a PTFE (polytetrafluoroethylene) layer in-between to prevent solids from entering the tube and thus potentially damaging the key sensor element.

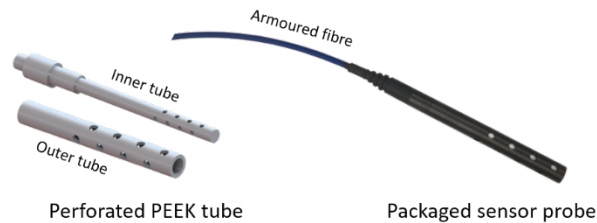


Fig. 2. Two-component perforated PEEK outer tube and smaller diameter inner tube (left) and (right) the packaged sensor probe with an armoured fibre.

The packaged sensor was then carefully calibrated in an environmental chamber (Binder KBF115) as shown in Fig. 3. The peak wavelengths of both FBGs were recorded in a calibration over a temperature range of 25-45°C (the maximum temperature excursion expected in the sewer environment where the sensors would be used), in steps of 5°C, as well as over a humidity range of 35-75%rh, in steps of 10%rh. The wavelength readings were then fitted in order to obtain the calibration coefficients and reference peak wavelengths used in equations (1) and (2).

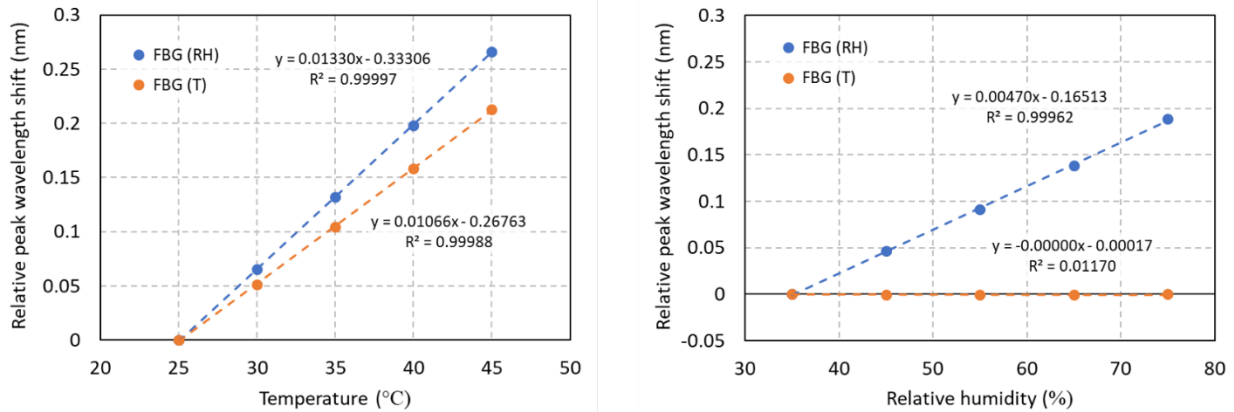


Fig. 3. Sensor calibration carried out in the Binder KBF115 environmental chamber. The temperature (left) and humidity (right) responses of both the FBGs used in the sensor probe are shown.

It is clear from Fig. 3 that, as designed, both FBGs are sensitive to temperature whereas only the coated FBG is responsive to changes in RH and will act as the humidity sensor. It is also clear from Fig. 3 that the responses of both sensors to T and RH are strongly linear (with  $R^2$  values > 0.999).

The sensor performance, obtained through the monitoring of the wavelength characteristic of the FBGs used was interrogated using a ‘Micron Optics si155’ unit. Due to the intended testing location, which is remote from access to main electricity, battery-operation was required necessitating a shut-down of the unit between measurements to conserve energy and extend the useful measurement lifetime. This was achieved using a Raspberry Pi 3 (model B) module which at the same time provided 4G connectivity to allow remote data transfer. The Pi module itself was disconnected from power between measurements using a low-power extension board (Sleepy-Pi 2). The whole hardware setup (Figure 4) was then mounted in a suitable enclosure, type IP65 (ingress protection 65, dust tight and protected against water projected from a nozzle), to protect the system during the field tests.

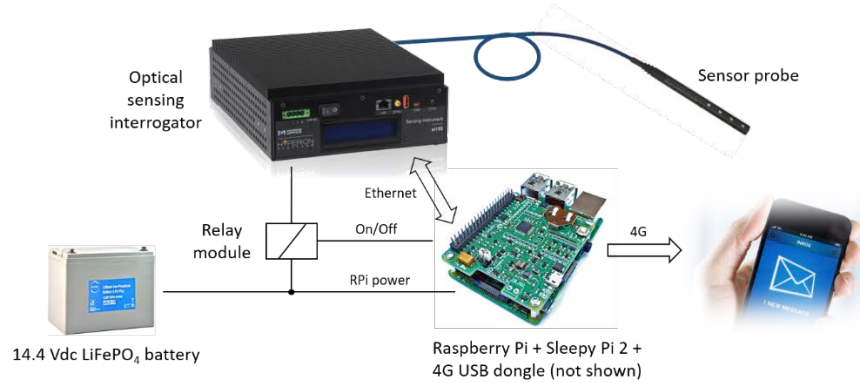


Figure 4. Hardware setup for sensor interrogation and data transfer.

### 3. Experimental results and discussion

Field trials were carried out in Manly, Australia (approximately 15 km north of Sydney) at a sewer access facility operated by Sydney Water. The lead fibre of the developed sensor probe was protected by a drain pipe before being lowered into a sewer access hole (Figure 5) which was then covered. The sensor output was monitored fully over the full duration of the tests, reporting data at 20-minute intervals. The results of the data collection exercise undertaken over the two-month test period (December 2018 – February 2019) are shown in Figure 66, with data collected plotted against the above-ground weather conditions [6].



Figure 5. Photograph of the sensor probe (left) and (right) the sensor being lowered into the sewer via the sewer access hole.

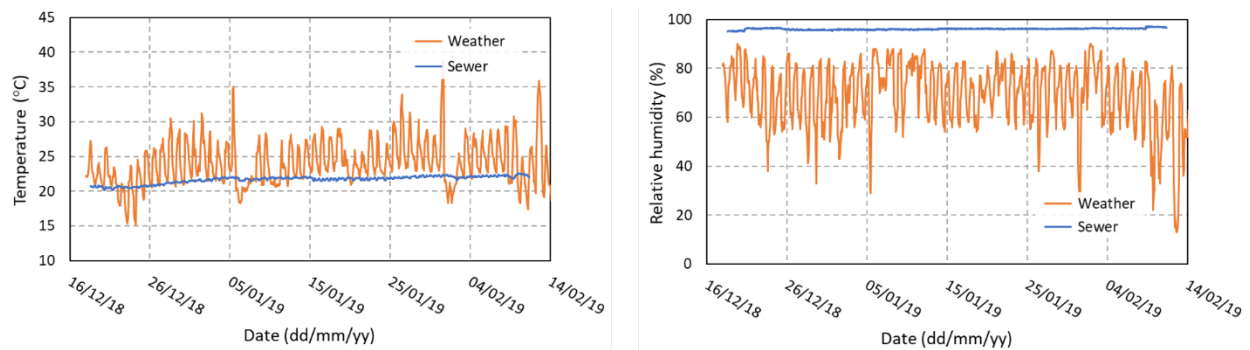


Figure 6. Data obtained from the sensor system installed in the sewer monitored over a 2-month period. Left – temperature data monitored in the sewer using the sensor (with for comparison external temperature data). Right – relative humidity data monitored in the sewer (with for comparison external humidity data)

It can be seen from the data reported in Figure 66 that the sewer temperature is relatively stable with commonly less than half a degree variation between day and night, despite much larger temperature variations above ground. The sewer humidity at 95-97%rh is constantly well above the ambient air humidity and, again, with only minor fluctuations seen between day and night. Most importantly, the sensor performance does not show any sign of deterioration within the two-month period over which data were reported. These data, in conjunction with those of other parameters in the sewer, provide engineers and scientists with vital information on the sewer corrosion process (which is beyond the scope of this report), allowing engineers to develop appropriate maintenance and prevention strategies to ensure continuity of performance for customers.

#### 4. Conclusion

The FBG-based temperature and humidity sensor system developed has been demonstrated to offer robustness and continuous performance when operated in the acidic sewer environment of a working sewer, one where conventional sensors fail after use for relatively short periods of time. Reliable data were obtained for two months from a battery-powered system operating remotely. An extended dataset on the tests carried out will be published in due course.

Future work will include trialing an extended distributed monitoring approach using multiple sensor probes along extended sections of sewage infrastructure. In addition, an FBG-based  $H_2S$  sensor system is being considered for potential integration into the sensor probe, allowing a more comprehensive sewer monitoring approach.

#### 5. References

- [1] A.P. Joseph, J. Keller, H. Bustamante, and P.L. Bond, "Surface neutralization and  $H_2S$  oxidation at early stages of sewer corrosion: Influence of temperature, relative humidity and  $H_2S$  concentration," *Water Research* **46**, 4235-4245 (2012).
- [2] G. Jiang, J. Keller, and P.L. Bond, "Determining the long-term effects of  $H_2S$ , relative humidity and air temperature on concrete sewer corrosion," *Water Research* **65**, 157-169 (2014).
- [3] C. Yongsiri, J. Vollertsen, and T. Hvitvet-Jacobsen, "Effect of temperature on air-water transfer of hydrogen sulfide," *Journal of Environmental Engineering* **130**(1), 104-109 (2004)
- [4] Y.-J. Rao, "In-fibre Bragg grating sensors," *Measurement Science & Technology* **8**(4), 355-375 (1997).

- [5] L. Alwis, T. Sun, and K.T.V. Grattan, "Design and performance evaluation of polyvinyl alcohol/polyimide coated optical fibre grating-based humidity sensors," *Review of Scientific Instruments* **84**, 025002 (2013).
- [6] [https://rp5.ru/Weather\\_archive\\_in\\_Sydney,\\_Australia](https://rp5.ru/Weather_archive_in_Sydney,_Australia)

# Strain Measurements for a Magnetostrictive Material Using Fiber Bragg Gratings

Oscar Sosa Puerto, C. Camilo Cano and Margarita Varón Durán

High Frequency Electronics and Telecommunications Research Group – CMUN. Universidad Nacional de Colombia – Sede Bogotá.  
{oasosap, cccanov, gmvarond}@unal.edu.co

**Abstract:** Magnetostrictive materials change their crystal network structure properties due to an external magnetic field action. These changes also affect a macroscopic property such as their physical dimension. Optical fiber Bragg gratings could be used to monitor any elongation in a piece of a magnetostrictive material, mainly thanks to of their complete electromagnetic immunity. In this paper, we present the design and complete characterization of the system that uses a Helmholtz coil to produce a controlled magnetic field that is applied to a sample of the magnetostrictive material. Current results include a characterization of both strain and temperature sensitivity of the FBGs to be used.

## 1. Introduction

A magnetostrictive material is a smart or adaptative structure that changes its properties when an external magnetic field is applied [1,2]. Magnetostriction is usually an inherent effect on magnetic transition materials like iron and nickel. Magnetic transitions are accompanied by structural changes in the material, such as its crystal network structure or spatial distribution [3]. It is possible to identify a magnetic phase transition through the variation of the crystal network parameters with neutron diffraction or x-ray diffraction. In both cases, to obtain the network parameters high refining and processing of data are required. The use of fiber optic sensors has shown to be effective in the evaluation of magnetostrictive materials [4], offering information of macroscopic changes in the dimensions of materials, whether in block, film or powder.

To measure the change in the dimension of the magnetostrictive material, optical fiber Bragg grating sensors (FBGs) emerge as a good alternative as they offer three main advantages: electromagnetic immunity; linearity with variables such as strain and temperature; and long-distance measurement with no other media than the one used to feed the sensor [6,7]. In this paper, we present advances of an ongoing study to detect a magnetic transition by a macroscopic measurement (microns) in a magnetostrictive material when exposed to an external magnetic field. We made two FBGs customized sensors to measure both strain and temperature on a magnetostrictive material submitted to a magnetic field produced with a Helmholtz coil.

## 2. Fiber Bragg Gratings sensors principles

A FBG sensor operates as a wavelength filter, which is built performing a periodic perturbation of the effective refractive index in the core of an optical fiber [5]. A broad-spectrum light source is used to feed the optical fiber that contains the FBG sensor. When this wave arrives to the FBG sensor, almost all of the incident light is transmitted, excluding one specific wavelength that satisfies the Bragg condition  $\lambda_B$  defined in Equation (1):

$$\lambda_B = 2\eta_{eff}\Lambda \quad (1)$$

where  $\eta_{eff}$  is the effective refractive index, and  $\Lambda$  is the periodic space between each grating. When the FBG sensor is exposed to strain ( $\Delta l$ ) or temperature changes ( $\Delta T$ ),  $\Lambda$  is affected inducing a shift in the reflected wavelength [5]. This shift induced in the Bragg wavelength ( $\Delta\lambda_B$ ) is proportional to the external change, and it can be quantified with Equation (2), as follows:

$$\Delta\lambda_B = 2 \left( \eta_{eff} \frac{d\Lambda}{dT} + \Lambda \frac{d\eta_{eff}}{dT} \right) \Delta T + 2 \left( \eta_{eff} \frac{d\Lambda}{dl} + \Lambda \frac{d\eta_{eff}}{dl} \right) \Delta l \quad (2)$$

It is possible to calculate a value for both coefficients that accompany the temperature and strain changes in Equation (2). These coefficients are also known as temperature and strain sensitivity and their typical values are around  $12 \text{ pm}\cdot^\circ\text{C}^{-1}$  and  $1.2 \text{ pm}\cdot\mu\text{e}^{-1}$ , respectively. More accurate values could be obtained through a sensor calibration.

### 3. Experimental setup

The complete experimental setup for the magnetostrictive material is depicted in Figure 1. The main objective of the characterization process is to obtain a magnetic field vs. an induced strain curve for the material sample. In order to get this curve, two bare FBG sensors placed in a magnetostrictive material sample are used to monitor its strain and temperature changes. The reflected wavelengths of the FBGs are acquired using a FBG sensors interrogator (Micron Optics sm125), and processed to obtain the corresponding values of strain shifts. Then, a Helmholtz coil is used to generate a time-variant magnetic field. The material sample is placed in between the plates of the Helmholtz coil. To monitor the effective magnetic field produced, a teslameter (FW Bell 8010) with a magnetic field probe is deployed in the same place. This equipment is connected via Ethernet to a computer that collects all the data and process the results.

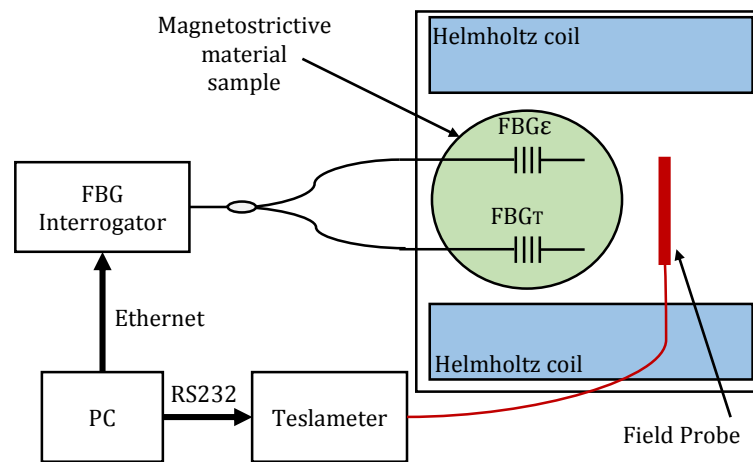


Figure 1. Experimental setup used to characterize the magnetostrictive material sample.

One of the main challenges of the measurement was the deployment of the FBG sensor between the plates of the Helmholtz coil, mainly because of the small gap between them. Figure 2 shows a frontal view of this device. In order to place the material sample inside the coil, a 3D printed holder was designed and implemented. As shown in Figure 2, the sensors were fabricated using low bend loss fiber, due to the small curvature radius of the fiber at the bottom. Another challenge was the size of the material sample, which is a cylinder of manganese ferrite ( $\text{MnFe}_2\text{O}_4$ ) with a diameter of 3.5 mm, hereby, 3 mm long FBG sensors were fabricated and fixed to the sample.

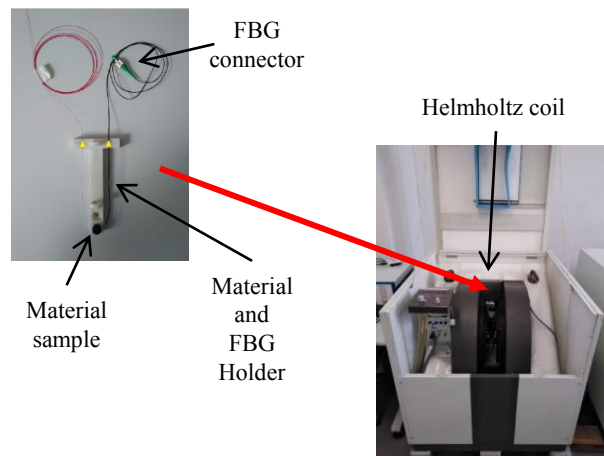


Figure 2. Helmholtz coil used for the experimental setup with the material sample and FBG sensor.

#### 4. Current results.

Due to requirements of the complete experimental setup, FBG sensors of temperature and strain were characterized. The first one is a polyamide-coated FBG temperature sensor with a Bragg wavelength of 1550 nm. It has a minimum bend radius of 1.5 mm and a length of 3 mm. The sensor was placed inside a temperature oven, whose temperature varied between 30 °C and 90 °C. Temperature measurement was performed in a 3 minutes time interval, leaving 90 data points in each one to be averaged. Figure 3 shows the wavelength as a function of temperature for the FBG sensor, which indicates a sensitivity of approximately 8.40 pm·°C<sup>-1</sup>. Results showed that the FBG sensor has a linear response at least in the range that it was characterized.

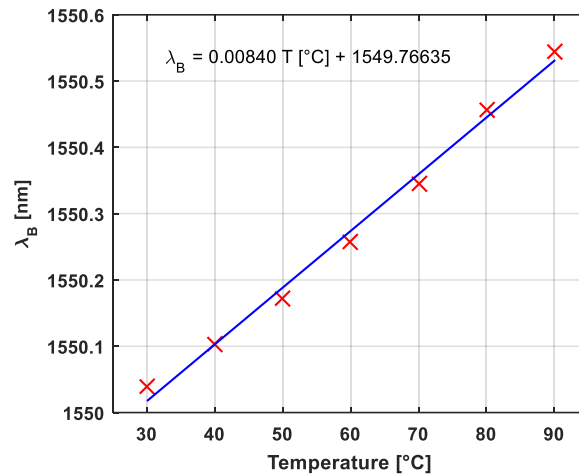


Figure 3. Polyamide-coated FBG sensor characterized as a function of temperature.

The second FBG sensor is a polyamide-coated FBG strain sensor with Bragg wavelength of 1535 nm, 3mm length and a minimum bend radius of 1.5 mm. During the characterization experiment, the FBG sensor was fixed to a mechanical structure that induces strain shifts using a micrometer head (Thorlabs 150-801ME) with steps of 10 μm. During the experiment, strain shifts between 0 με and 3500 με were performed. Each measurement of strain is done in a 3 minutes time interval, averaging 90 data points for each one. Figure 4 depicts the Bragg wavelength as a function of strain for the FBG sensor, which indicates a sensitivity of 1.203 pm·με<sup>-1</sup>. Despite the fact that measurements were not done with a uniform step, results well demonstrate the linearity in strain response of the polyamide FBG sensor in a wide range.

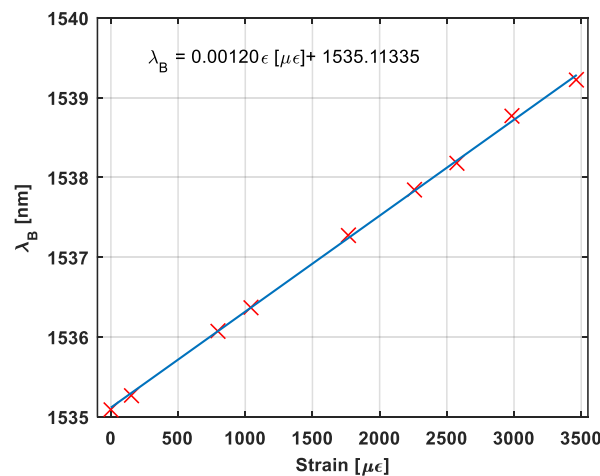


Figure 4. Polyamide coated FBG sensor characterized as a function of strain.

## 5. Conclusions

In this paper we presented the temperature and strain characterization of two FBG sensors. This is part of an ongoing work made to detect a magnetic transition in a magnetostrictive material. These sensors were constructed in a customized way to fulfill this specific application. On the one hand, the FBG temperature sensor has a sensitivity of  $8.40 \text{ pm}\cdot\text{C}^{-1}$ . On the other hand, the strain FBG sensor gets a sensitivity of  $1.20 \text{ pm}\cdot\mu\text{e}^{-1}$ . The characteristics of both FBG sensors are demonstrated in a wide temperature and strain range, which makes them suitable to use in the sample magnetostrictive material sample to obtain a magnetic field vs. an induced strain curve.

## 6. References

- [1] Dapino, Marcelo J., On magnetostrictive materials and their use in adaptive structures, *Structural Engineering and Mechanics*, Vol. 17, No. 3-4, 2004
- [2] O. Lopez, A.Carnicero, *Materiales inteligentes I/II. Introducción a los materiales del siglo XXI*. Madrid: Universidad Pontificia de Comillas, 2003, pp.16-20.
- [3] Harutoshi Ogai, Bishakh Bhattacharya, *Pipe Inspection Robots for Structural Health and Condition Monitoring*, Springer, 2017, pp 137.
- [4] G. Lanza, A. Cusano, G. Breglio, M. Giordano, A. Gaddi and S. Buontempo, "Effect of the anisotropic magnetostriction on Terfenol-D based fiber bragg grating magnetic sensors," *Sensors*, 2011 IEEE, Limerick, 2011, pp. 456-459.
- [5] M. Varón, O. Sosa, F. E. Barón, C. C. Cano, and G. Álvarez-Botero, *Optical Sensing Using Fiber Bragg Gratings: Fundamentals and Applications*, *IEEE Instrumentation & Measurement Magazine*, Vol. 20, No 2, pp 33-38, April 2017.
- [6] D. Chen, W. Liu, M. Jiang, and S. He, High-Resolution Strain/Temperature Sensing System Based on a High-Finesse Fiber Cavity and Time-Domain Wavelength Demodulation, *Journal of Lightwave Technology*, Vol: 27, No 13, 2009
- [7] A. Ferreira da Silva, A. Gonçalves, L. A. de Almeida, F. Moita, P. Mateus, and J. Higinio, A Smart Skin PVC Foil Based on FBG Sensors for Monitoring Strain and Temperature, *IEEE Transactions on Industrial Electronics*, Vol. 58, No. 7, pp. 2728 - 2735 Jul. 2011

# Macrobending SMS Fiber-Optic Arc Sensor Using Fixed Curvature Radius

Jesse Werner Costa<sup>a</sup>, Marcos Antônio Ruggieri Franco<sup>b</sup> and Maria Thereza Rocco Giraldi<sup>c</sup>

<sup>a</sup> Centro Federal de Educação Tecnológica Celso Suckow da Fonseca – CEFET-RJ, Rio de Janeiro-RJ, Brazil. (jcesse@gmail.com)

<sup>b</sup> Instituto de Estudos Avançados – IEAv, São José dos Campos-SP, Brazil (marcos.a.r.franco@gmail.com).

<sup>c</sup> Instituto Militar de Engenharia – IME, Rio de Janeiro-RJ, Brazil (mtmrocco@gmail.com).

**Abstract:** A simple and low-cost concept of fiber-optic arc sensor based on single mode-multimode-single mode (SMS) structure is reported. The output power intensity of SMS bend sensors may increase or decrease with the rise of curvature, depending on Multimodal Interference (MMI) conditions. In order to avoid slope inversions due to wide range bend applications, it is possible to choose a fixed curvature radius and let MMI effects happen due to arc variation, as demonstrated with experimental tests. Absolute output power peak sensitivity of 2.65 dB/cm is reported.

## 1. Introduction

Several bend sensors have been proposed based on: misalignment between the light transmitter and receiver [1,2], Michelson interferometer [3], fiber bending loss induced by flow stream [4], cantilever structures [5], Fabry-Perot cavity [6], and a variety of Fiber Bragg Gratings devices [7,8]. Besides that singlemode-multimode-singlemode (SMS) devices have been investigated as bend sensor and flow measurement where the sensor element is dragged by a flow stream.

This work proposes a simple and low-cost optical fiber SMS arc sensor in which the bending effect can be caused by any applied force or flow rate acting over the fiber sensor. Such device can be used as flow rate meter, anemometer, stall detector in airplane aerodynamic surfaces and also as a general bending sensor. MMI self-image condition is used to allow higher output power evaluation, since nearly the input light power is replicated at this point. Among many advantages of the proposed fiber sensor we can point out its electromagnetic immunity, resistance to corrosion and, as it virtually doesn't create obstruction to flow, there is no pressure loss.

In section 2 the basic principles of the SMS sensor are presented. In section 3 the MMI bend effects on the output power slope inversions are discussed. Experimental measurements were implemented to confirm that behavior. The arc sensing mechanism is described in section 4 along with the experimental setup. In section 5 experimental results are discussed including sensitivity report. In section 6 the conclusions are exposed due to the utilization of the proposed sensor as an arc sensor.

## 2. Basic Principles

SMS is typically an optical configuration obtained by splicing a multimode fiber (MMF) piece between two single mode (SMF) fibers. The electromagnetic field from the SMF segment is coupled to several modes into the MMF section and the multimode interferometry happens due to constructive and destructive interferences along the fiber. At the end of the MMF segment the light is coupled to the last SMF segment where its intensity depends on the amplitudes and relative phases of the several modes at the exit end of the MMF. Fig. 1 depicts the SMS structure. The experimental SMF segments are standard Corning SMF-28 and MMF is a no-core fiber with 125  $\mu\text{m}$  diameter, which is basically a cylinder of silica.

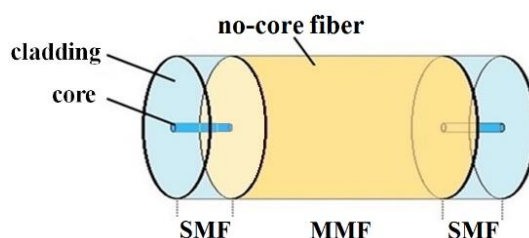


Fig. 1. SMS general structure.

A periodic disposition found along the direction of propagation where field concentration occurs due to constructive interference among the guided modes leads to the self-imaging effect where the light field at the input of the MMF section is nearly reproduced at a defined propagation distance for a determined wavelength in both amplitude and phase. The first self-image distance from the MMF light input is given by [9,10],

$$Z_{self-imaging} = \frac{4n_{core}d^2}{\lambda}, \quad (1)$$

where  $n_{core}$  is the refractive index of the MMF fiber,  $d$  is its diameter and  $\lambda$  is the wavelength of the light source.

### 3. Bending effect on the output power profile

The way SMS bend sensors output power behave as a function of the curvature radius ( $R_c$ ) is directly associated to the power distribution in the MMF excited modes and how they interfere when bending is applied. Total power at the SMS output depends on the constructive and destructive interferences in amplitude and phase caused by each mode and the total effect is the sum of the contributions. At first impression it may seem that the total output power will lower with the rise of curvature, or reduction of the curvature radius, due to loss attenuation. This is not entirely true. The output power intensity as a function of the curvature radius has alternate slopes since the contributions of each mode to the constructive and destructive interferences along the propagation varies with the bending radius, which changes the transverse energy distribution in a manner that in some ranges the output power decreases when the bending radius decreases and in others it has the opposite behavior. Another contribution to this compartment is the field deformation caused by curvature. The fields in low order modes may be changed by curvature and so the losses, as depicted in [11], since it shifts away from the axis in the direction opposite to the center of curvature and narrows as it shifts. The losses of modes that are deformed by curvature actually decrease if the narrowing effect happens. Wide fields are more affected by curvature loss than narrow field distributions.

Each mode has its specific response to curvature, since each one has its own coupled power, amplitude and phase contributions, with its effective refractive index. The lower order modes are more paraxial at the self-image region and, therefore, less sensitive to high curvature radius, which is the opposite of the higher order modes which are more external [12]. It is not expected that amplitude and phase will match the same way among several propagating modes as the curvature is increased. Therefore, the sum of the contributions is not linear neither continuously increases with curvature radius.

Experimental tests were made to confirm this alternating slope behavior. Fig. 2(a) shows the experimental setup built to measure the transmitted light power through a SMS sensor as a function of the bending radius. The bending effect was obtained using a micro positioner with resolution of 10  $\mu\text{m}$ . The sensor was placed at half distance between the two posts and the curvature, which is the inverse of the curvature radius, is given by [13],

$$C = \frac{1}{R_c} \cong \frac{4}{L_0} (L_0^2 - (L_0 - \Delta L)^2)^{\frac{1}{2}}, \quad (2)$$

where  $L_0$  is the initial distance and  $\Delta L$  is the distance variation.

The experimental results of the bending sensor are shown in Fig. 2(b) where the output power profile is obtained for a wide range of bending radius. The light source was a wide band light source (Thorlabs Fiber Coupled SLD) and the interrogator is a commercial OSA (Optical Spectrum Analyzer). The MMF segment uses the self-image condition stated in Eq. (1) and has a length of 55.98 mm ( $\lambda = 1611.5$  nm).

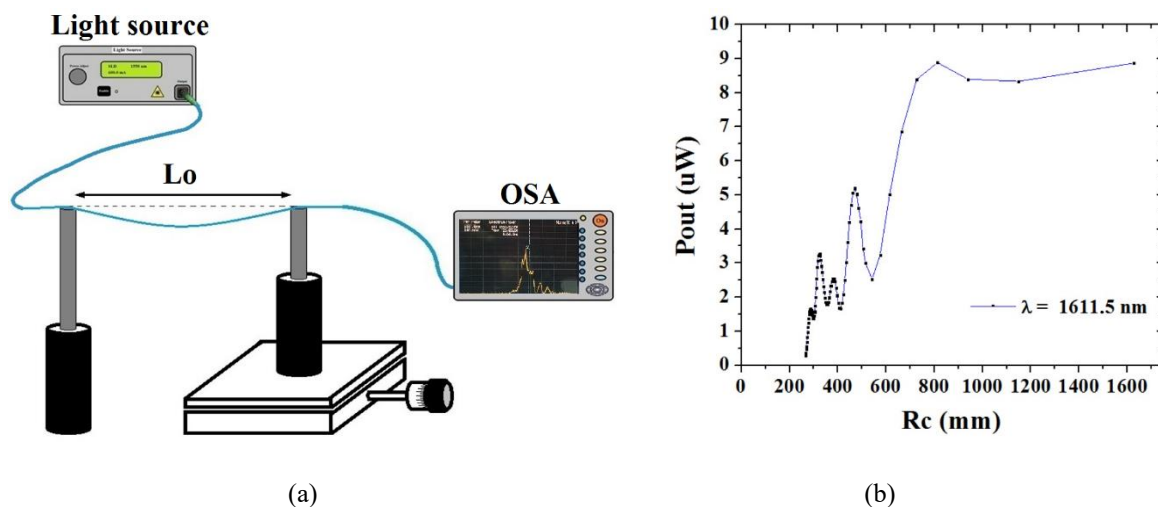


Fig. 2. (a) Experimental setup to measure bending effect on the SMS sensor and (b) experimental results.

### 4. Flow sensing principle and experimental setup

A schematic diagram of the experimental setup is shown in Fig. 3(a). The SMS arc sensor experiment uses the same fibers and equipment of the bending experiment shown at Fig. 2(a). The light emitted from the wideband source is guided into the sensor and transmitted to the OSA. The micropositioner is used to push the tip of the MMF segment in steps of 0.5 mm, forcing the sensor to bend along the boundary of the circular support with constant curvature radius of 670 mm. Fig. 3(b) shows the resulting spectra variation due to the arc described by the sensor as a function of the tip shifting steps. The corresponding arc lengths are listed at the right side of the figure.

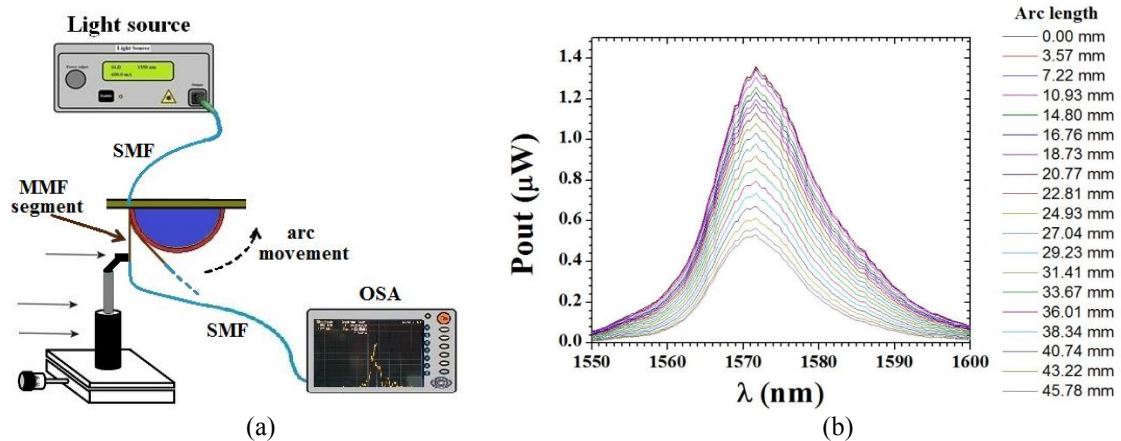


Fig. 3. (a) SMS fiber optic sensor using a  $R_c = 670$  mm circular support and (b) experimental results.

### 5. Experimental Results and Discussions

The bending experiment shown in Fig. 2 demonstrates that the output power as a function of the curvature radius has slope inversions. It is possible to avoid that behavior in applications where a wide range of curvature radius is imposed by the experiment nature, using a circular support with a fixed curvature radius and let MMI effects happen due to arc variation, as demonstrated with the experiment illustrated in Fig. 3. Little changes in the experiment with fabricated arc sensor, as inaccurate cleavage position of MMF section, led to a spectral peak at wavelength  $\lambda = 1571.7$  nm, meaning that the MMF segment has length of 57.41 mm, as established using Eq. (1) with the refraction index updated by the well-known Sellmeier equation [14]. Fig. 4(a) shows the transmitted power intensity as a function of the arc length at the peak wavelength. The red solid line is a polynomial fitting of order 2. Fig. 4(b) shows the sensitivity of the sensor to arc variation.

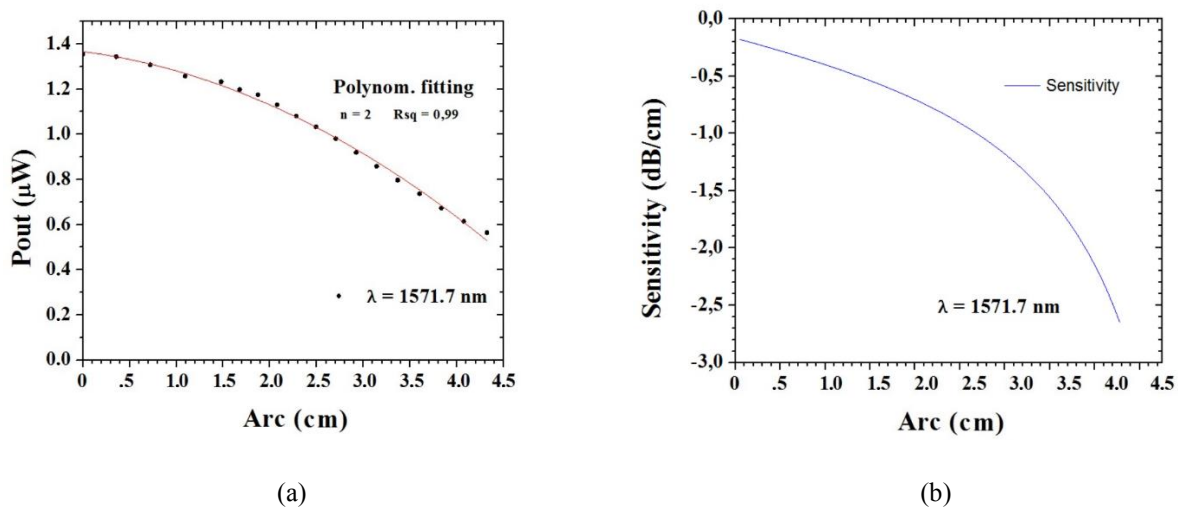


Fig. 4. (a) Output power intensity for the spectral peak at  $\lambda = 1571.7$  nm as a function of the arc length with a polynomial fitting of order 2 as the solid line and (b) Sensitivity for the experimented sensor.

The spectral peak is the wavelength where the higher number of constructive interferences happens, which corresponds to the self-image distance. Therefore, at this wavelength the sensor is more sensitive to bend

variations, as can be stated from Fig. 3(b). As the peak wavelength has no significant spectral displacement, the sensor interrogation is based on power amplitude. For the spectral peak, the sensitivity has an absolute maximum value of 2.65 dB/cm and, in the experimented range of arc variation, the average sensitivity is 0.95 dB/cm.

## 6. Conclusions

A simple and low-cost concept of a transmission optical fiber arc sensor using SMS structure implementing multimode interference has been described and investigated. The output power slope inversions of the bend sensor with the curvature radius has been experimentally demonstrated. It is possible to avoid that behavior in applications where a wide range of curvature radius is imposed by the experiment nature, using a circular support with a determined curvature radius. The bending effect on the arc variation of the sensor along the circular boundary of the support changes the MMI patterns and, therefore, the output light spectra. Experimental data demonstrate that there is a clear relation between the sensor light output power and arc variation produced by the bending agent. This type of sensor can be used in a wide variety of applications. Inside a pipe, the sensor is naturally used as velocity and flow rate sensor. In free space it can be used as an anemometer or other important applications, such as stall detector for aerodynamic surfaces and displacement sensor for moving system as mechanic ramps, for instance. A reflective simple and low-cost of optical fiber arc sensor device using SMS-MMI structure is reported in a subsequent text to be submitted. Experimental results attest the relation between the sensor light output power and arc variation produced by the bending forces. The MMF segment with half self-image length, due to the reflection effect, has its end coated with gold film. This structure is more suitable for practical sensor devices in applications like flow sensor when placed inside a pipe.

## 7. References

- [1] L. Battista, S. Sciuto and A. Scorza, "Preliminary evaluation of a fiber-optic sensor for flow measurements in pulmonary ventilators," IEEE International Symposium on Medical Measurements and Applications, Bari, 29-34 (2011).
- [2] E. Schena, P. Saccomandi, and S. Silvestri, "A high sensitivity fiber optic macro-bend based gas flow rate transducer for low flow rates: Theory, working principle, and static calibration," Rev. Sci. Instrum. 84, 024301-1-024301-7 (2013).
- [3] L. Yuan, J. Yang, and Z. Liu, "A Compact Fiber-Optic Flow Velocity Sensor Based on a Twin-Core Fiber Michelson Interferometer," IEEE Sens. J 7, 114-1117 (2008).
- [4] R. Hu and X. Huang, "A Simple Fiber-Optic Flowmeter Based on Bending Loss," IEEE Sens. J 12, 952 – 1955 (2009).
- [5] A. Vijayan, V. Thakare, R. Karekar, and R. Aiyer, "Optical fiber-based macrobend free air flow sensor using a hinge joint: A preliminary report," Microw. Opt. Technol. Lett. 10, 2543-2546 (2008).
- [6] G. Liu, Q. Sheng, G. Piassetta, W. Hou, and M. Han, "A fiber-optic water flow sensor based on laser-heated silicon Fabry-Perot cavity," Proc. of SPIE 9852 (2016).
- [7] Y. Zhao, K. Chen, and J. Yang, "Novel target type flowmeter based on a differential fiber Bragg grating sensor," Meas. 38, 230-235 (2005).
- [8] S. Thekkethill, R. Thomas, H. Neumann<sup>1</sup>, and R. Ramalingam, "Experimental investigation on mass flow rate measurements using fibre Bragg grating sensors," IOP Conf. Ser.: Mater. Sci. Eng. 171, 012136 (8pp) (2017).
- [9] L. Soldano and E. Pennings, "Optical Multi-Mode Interference Devices Based on Self-Imaging: Principles and Applications," J. Light. Technol. 13, 615 - 627 (1995).
- [10] W. Mohammed, A. Mehta, and E. Johnson, "Wavelength Tunable Fiber Lens Based on Multimode Interference," J. Light. Technol. 22, 469 - 477 (2004).
- [11] D. Marcuse, "Field deformation and loss caused by curvature of optical fibers," J. Opt. Soc. Am. 66, 311-320 (1976).
- [12] Y. Gong, T. Zhao, Y. Rao, and Y. Wu, "All-Fiber Curvature Sensor Based on Multimode Interference," IEEE Photonics Technol. Lett. 23, 679 - 681 (2011).
- [13] C. S. Fernandes, M. T. M. R. Giraldo, M. J. Souza, J. C. W. A. Costa, C. Gouveia, P. Jorge, and M. A. R. Franco, "Curvature and vibration sensing based on Core Diameter Mismatch Structures," IEEE Trans. Instrum. Meas. 65, 2120-2128 (2016).
- [14] I. H. Malitson, "Interspecimen comparison of the refractive index of fused silica", J. Soc. of America 55, 1205-1209, (1965).

# External Refractive Index Sensitivity Enhancement of a Long Period Grating by Graphene Oxide Overlay

Kasun Dissanayake\*<sup>1</sup>, Souvik Ghosh<sup>1</sup>, Leonardo Binetti<sup>2</sup>, Bruno Rente<sup>1</sup>, Lourdes Alwis<sup>2</sup>, and Tong Sun<sup>1</sup> and Kenneth Grattan<sup>1</sup>

<sup>1</sup>City, University of London, Northampton Square, London EC1V 0HB, United Kingdom

<sup>2</sup>Edinburgh Napier University, Merchiston Campus, Edinburgh EH10 5DT, United Kingdom

\*Kasun.Dissanayake@city.ac.uk

**Abstract:** In this paper, an external refractive index sensor is presented based on a graphene oxide coated long period grating and based on creating a stable graphene oxide coating on the fibre surface using a drop casting technique. The wavelength shift sensitivity was enhanced by 43% compared to the response of a bare long period grating when used to monitor external refractive index.

## 1. Introduction

Fibre optic sensors are preferred over electrical sensors due to their small size, immunity to electromagnetic interference, multiplexing capability, ability to be deployed in very hazardous environments and bio-compatibility [1]. For these reasons, optical fibre sensors are continuing to gain attention among researchers in the last decade.

Fibre Bragg Grating (FBG)-based sensors, tapered fibre sensors, tilted and chirped Fibre Bragg Grating sensors, interferometric-based sensors, and long period grating (LPG) based sensors are examples of the most common types of optical fibre sensors [2]. Among these, when it comes to external refractive index (RI) sensing, LPG-based sensors show a significant advantage over other types of optical fibre sensors due to their simplicity, low production cost and an enhanced light-matter interaction at the fibre cladding/surrounding jacket interface.

Graphene oxide (GO) is a nanomaterial that has been researched extensively since the discovery of graphene itself in 2004 [3]. Due to its unique two dimensional nature, along with the oxygen containing group at the end of the single layer graphene sheets, GO shows unique properties allowing excellent sensor fabrication, such as the tunability of the conductivity, high surface-to-volume ratio, ability to be dispersed in most of organic and inorganic compounds, ability to be functionalized with various nanomaterials and structures and tuneable optical properties [4].

In this work, GO has been coated on a Long Period Grating (LPG) to fabricate an enhanced optical fibre-based external RI sensor. To calibrate the device, NaCl solutions of different concentrations were prepared and the RI values of these solutions were measured in room temperature with an Abbe refractometer at the wavelength of 500 nm. The external RI response of the fabricated GO-coated LPG sensor was recorded over a lower RIU range of 1.33 to 1.38. Such a RI range is of high importance when it comes to biosensors, as the RI of most of the common bio-fluids lies in that range.

## 2. Theoretical Background

In an optical fiber, the effective RI associated with the cladding modes is based on two factors, the RI of the core, cladding, and the RI of the surrounding medium. Therefore, when the RI of the surrounding medium changes, (in this case that of the GO overlay), it results in a shift of the resonance wavelength. The wavelength of a resonance loss band  $\lambda_{res}$  is governed [5] by equation (1) where,

$$\lambda_{res} = (n_{core}^{eff} - n_{cladd.m}^{eff})\Lambda_{LPG} \quad (1)$$

$n_{core}^{eff}$  is the effective RI associated with the fundamental core mode and  $n_{cladd.m}^{eff}$  is the effective RI for the  $m^{\text{th}}$  order cladding mode.  $\Lambda_{LPG}$  represents the grating period of the LPG. The variations of the wavelength peaks of the resonance loss bands of a LPG can be explained by this phenomenon.

### 3. Sensor Fabrication

The LPGs used in this work were fabricated by exposing a Fibrecore (PS1250/1500) B/Ge co-doped photosensitive fibre to the light from a 248 nm KrF excimer laser through a metal amplitude mask of pitch 250  $\mu\text{m}$ . The laser pulse energy was set to 10 mJ, with a pulse repetition rate at 100 Hz. 3 cm of the photosensitive fibre length was exposed to the UV light for 4 minutes and 30 seconds to complete the LPG inscription process. Following that, to stabilize the sensor performance, the LPGs were annealed at 100° C for three hours.

GO used in this research was synthesised by using an improved version of the Hummer’s methods as discussed in prior work [6]. Using this method involved 0.5 g of this prepared GO flakes being dispersed in 10 ml of deionized (DI) water by using an ultrasonic bath for 2 hours. The GO aqueous dispersion prepared in this way was then centrifuged at 3000 rpm, for 15 minutes, and the supernatant was used to coat the optical fibre surface.

After cleaning with 99% pure isopropyl alcohol (IPA), the LPG was first placed on a metal groove. Then ~200  $\mu\text{l}$  of the prepared GO supernatant was poured onto this groove and the LPG was left at 70° C for 1 hour to coat the fibre surface with GO using a drop casting technique. This method was repeated twice to achieve an efficient and stable GO-coating on the fibre surface.

Fig. 1(a) depicts the transmission spectrum of the LP<sub>08</sub> mode of this GO coated LPG sensor, before and after GO deposition, these being shown by the black and red lines, respectively. A SEM image of the fibre surface after the GO deposition had been carried out, is shown in Fig. 1(b). These results indicate that an efficient and sufficiently uniform GO overlay was achieved by using relatively simple and easy to reproduce coating technique. The red highlighted section in fig. 1(b) also shows an evidence of the cubic shaped NaCl crystals deposited on the fibre surface after carrying out the experiment. The thickness of the GO layer was measured from the image to be ~115 nm.

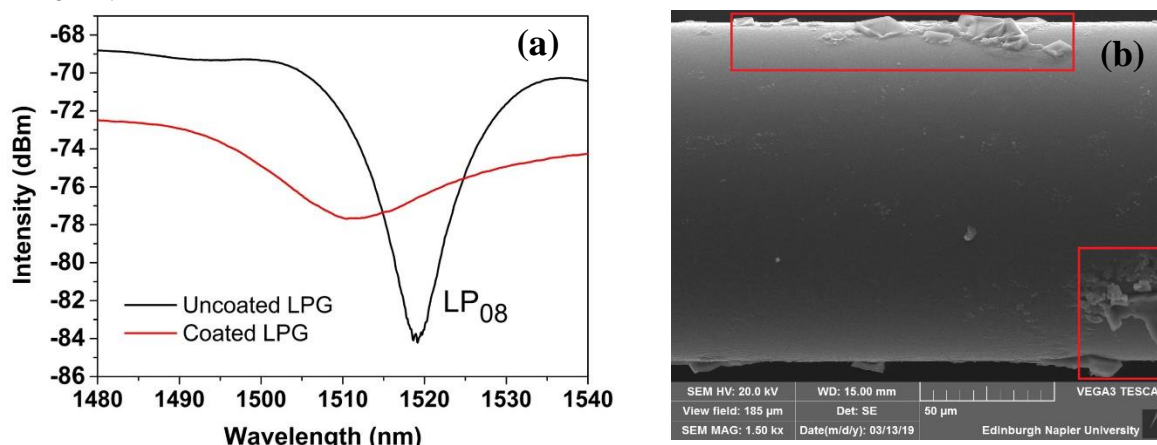


Fig. 1 (a). Transmission spectrum of the LPG (b) SEM image of the GO-coated LPG.

#### 3.1. Experimental Setup

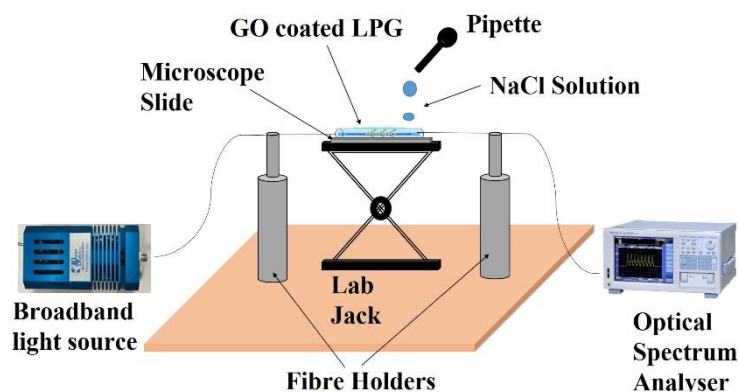


Fig. 2. Schematic of the experimental setup used to measure external RI response

To record the external RI response of the GO coated LPG sensor, one end of the probe was connected to a broadband halogen light source and the other end to an optical spectrum analyser, as shown in Fig. 2. Then the sensor probe was carefully placed on two fibre holders and a pipette was used to drop NaCl solutions of different concentrations (and thus of different refractive indices) onto the microscope slide. The slide was then pushed up using the lab jack so that the GO coated LPG section was covered with the NaCl solution. At this point, the transmission spectrum of the LP<sub>08</sub> mode was recorded, this being repeated for each of the different refractive indices of the NaCl solutions used. All the experiments were conducted at room temperature (22° C).

#### 4. Results and Discussion

The resonance loss band, which corresponds to the highest order cladding mode, in this case the LP<sub>08</sub> (lowest attenuation point at 1511 nm), was chosen to be interrogated, as opposed to the other loss bands of the GO-coated LPG, due to its improved sensitivity to the external RI. The recorded transmission spectra of this LP<sub>08</sub> resonance loss band of the GO-coated LPG probe plotted against different NaCl refractive indices are presented in Fig. 3(a). With the increasing external RI values used, a blue shift of the resonance wavelength and a decrement of the intensity were observed.

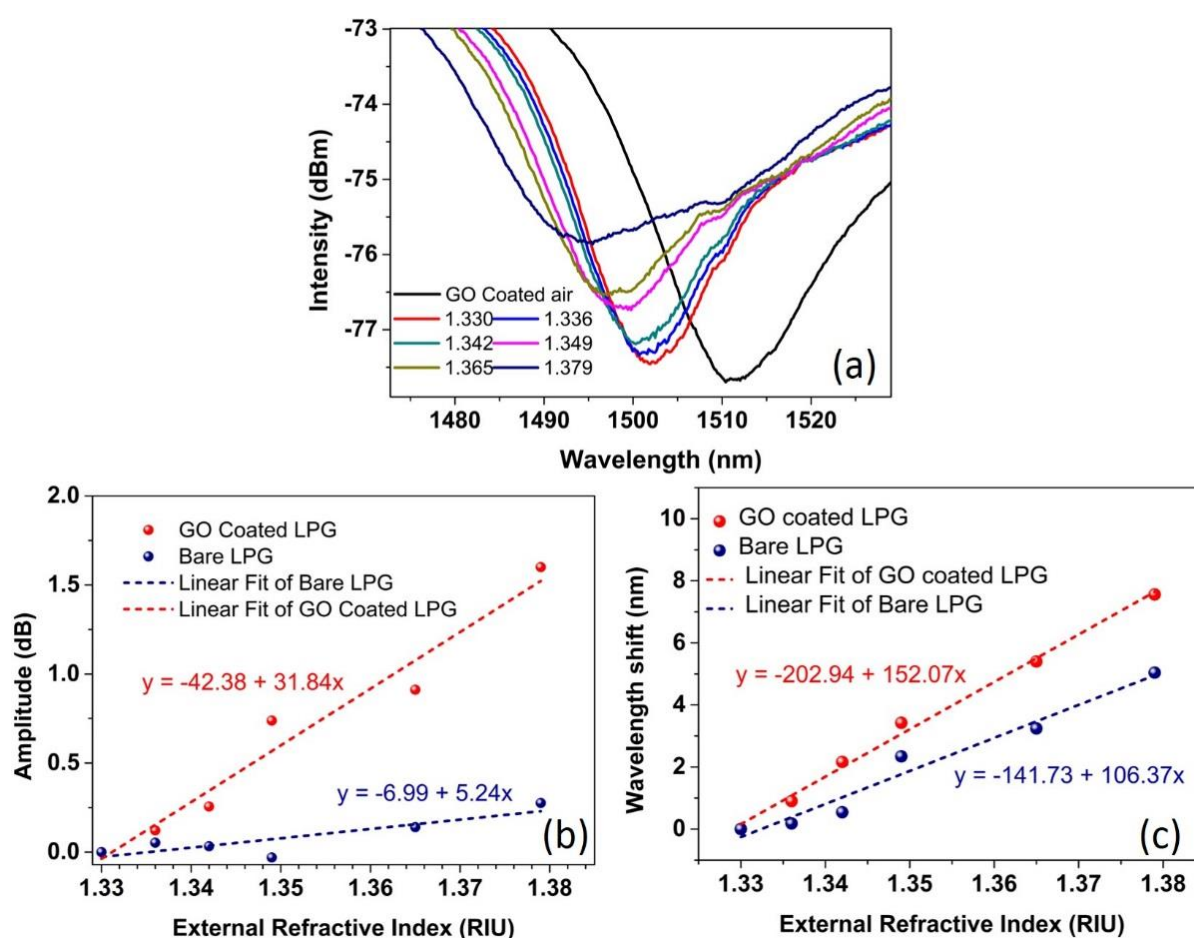


Fig. 3 (a) Transmission spectra of GO coated LPG against different RI solutions of NaCl solutions, (b) amplitude shift vs external RI (c) wavelength of the resonance band vs external RI

Fig. 3(b) shows the wavelength shift of the GO-coated LPG with increasing external refractive index solution on the coating. The LPG sensors was not cleaned after each refractive index change. Therefore, a cumulative effect of the external refractive index change can be seen in our LPG response. To investigate further this response, it has been compared with the external RI response of an uncoated (bare) LPG to provide a comparison. A good linear response of the wavelength shift against the increasing external RI was recorded in the range of 1.33 – 1.38 RIU, with a linear correlation coefficient of 0.9929. This leads to a sensitivity of 152.1 nm/RIU compared to the

106.4 nm/RIU sensitivity of a bare LPG, which indicates an improvement in the sensitivity of 43%. The observed wavelength shift can be explained in two ways. Firstly, the GO layer changes its optical properties, such as refractive index when it is in contact with the NaCl solution. This leads to a change in effective RI seen by the cladding modes, which eventually leads to a shift in the resonance wavelength. Secondly, as stated in the work of Zeheng *et al* [7], the d-spacing between two GO nano-layers changes in the presence of NaCl, which results in a change of thickness of the GO layer deposited on the LPG fibre surface. This phenomenon can also account for the observed resonance wavelength shift.

Fig. 3(c) illustrates the intensity change of the output of the GO-coated LPG sensor probe with increasing external RI, compared to the response seen from a bare LPG. A linear response of the intensity change against the increasing external RI was observed in the range of 1.33 - 1.38 RIU, with a linear correlation coefficient of 0.9502. This leads to a sensitivity of 31.84 dB/RIU compared to the 5.24 dB/RIU sensitivity of the bare LPG, which shows an improvement in the sensitivity of 507.6%. The RI change induced by the GO-based thin layer affects the coupling coefficient of the core and cladding modes and this results in the change of intensity of the resonance loss bands which is seen in [5]. This shows the operation of the sensor device.

## 5. Conclusion

A GO-coated LPG based external RI sensor has been presented as a promising way to develop a sensor scheme for both physical and bio-fluids by exploiting an important optical property of the GO-layer which changes its RI based on the surrounding medium. The GO-layer was deposited on the fibre surface successfully by using a drop casting technique. A very satisfactory linear response of the wavelength shift was recorded in the external RI range from 1.33 to 1.38 RIU, which led to a 43% improvement of the sensitivity, compared to the response of a bare LPG. Further, a much higher sensitivity was achieved for the intensity change against external RI, taking into account the interrogation efficiency and pointing to the interrogating wavelength shift being the way forward in the fabrication of GO-coated LPG based biosensors. In the future, work can be developed on the GO coating overlay which potentially could be functionalized with bioreceptors for a specific biosensing applications, building on the foundation in this paper of coated grating sensors.

## 6. References

- [1] Byoung-ho Lee, "Review of the present status of optical fiber sensors," *Optical Fiber Technology* **9**, 57-79 (2003).
- [2] Ming-jie Yin, Bobo Gu, Quan-Fu An, Chengbin Yang, Yong Liang Guan, Ken-Tye Yong, "Recent development of fiber-optic chemical sensors and biosensors: Mechanisms, materials, micro/nano-fabrications and applications", *Coordination Chemistry Reviews* **376**, 348-392 (2018).
- [3] K.S. Novoselov, A. K. Geim et. al., "Electric Field Effect in Atomically Thin Carbon Films," *Science*, 666-669 (2004).
- [4] Deepali Sharma, Suvardhan Kanchi, Myalowenkosi I. Sabela, K. Bisetty, "Insight into the biosensing of graphene oxide: Present and future prospects", *Arabian Journal of Chemistry* **9**, 238-261 (2016).
- [5] W. J. Stephen and P. T. Ralph, "Optical fibre long-period grating sensors: characteristics and application," *Measurement Science and Technology* **14**(5), (2003).
- [6] Kasun Prabuddha Wasantha Dissanayake, Weiping Wu, Hien Nguyen, Tong Sun, and Kenneth T. V. Grattan, "Graphene-Oxide-Coated Long-Period Grating-Based Fiber Optic Sensor for Relative Humidity and External Refractive Index," *J. Lightwave Technol.* **36**, 1145-1151 (2018)
- [7] Zheng, Sunxiang and Tu, Qingsong and Urban, Jeffrey J. and Li, Shaofan and Mi, Baoxia, "Swelling of Graphene Oxide Membranes in Aqueous Solution: Characterization of Interlayer Spacing and Insight into Water Transport Mechanisms", *ACS Nano* **11**, 6440-6450 (2017).

# Development of a Solid Substrate for Surface Enhanced Raman Spectroscopy

**Felipe Hornung, Marcia Muller and José Luís Fabris**

*Federal University of Technology-Paraná, 3165 Av. Sete de Setembro, Curitiba, Brazil, 80230-901  
felipehornung@alunos.utfpr.edu.br, mmuller@utfpr.edu.br, fabris@utfpr.edu.br*

**Abstract:** In this work, a solid substrate for Surface Enhanced Raman Spectroscopy was developed and characterized. The interaction of silver nanoparticles with the probe molecule rhodamine 6G was compared for both liquid and solid substrates. Parameters of the solid substrate were optimized for use with an optical fiber Raman spectrometer.

## 1. Introduction

Surface Enhanced Raman Spectroscopy (SERS) is a powerful technique that extends the applications of traditional Raman spectroscopy, normally impaired by a poor signal-to-noise ratio. The enhancement is observed when an analyte is adsorbed on or is close to a specially designed metal surface. This kind of spectroscopy has shown prospective applications in the fields of biochemistry, forensics, food and beverage safety, environmental control and medical diagnosis [1]. Under appropriate circumstances, enhancements of 14 magnitude orders can be reached, making possible the identification of organic compounds in sub-micromolar concentrations or even single molecules [2].

The development of active SERS substrates with nanoparticles of noble metals is a key step for the detection and characterization of substances at the molecular level [3]. Nanostructures deposited on solid substrates present increased enhancement factors when compared with colloidal substrates due to the facility of the former in producing the so-called hot spots, well-defined regions where the electromagnetic fields are maximized. However, there are technological challenges for producing reproducible and uniform solid SERS substrates with large number of such hot spots [4].

In this work, a solid substrate for SERS was developed using silver nanoparticles produced by laser ablation in liquid as enhancement medium. As probe molecule, rhodamine 6G was chosen owing to its high efficiency for Raman scattering [5].

## 2. Materials and Methods

Silver nanoparticles (AgNPs) were produced by laser ablation of a silver plate in liquid solution. The light of a Nd:YAG (New Wave, Tempest 20, 532 nm, 3-5 ns pulse width) was focused by a 15 cm focal length lens onto a silver plate (Sigma Aldrich®, 99,9% CAS: 6440-22) submersed in 10 mL of a 0.1 mM dihydrate sodium citrate solution (Biotec®, 99%) in a glass beaker. Ablation was carried out at 17 mJ laser pulse energy, 10 Hz pulse rate along 20 minutes at a room temperature of approximately 22 °C. A polytetrafluoroethylene (PTFE) membrane filter (22 µm pore diameter) presenting one rough and one smooth side was used as base for the solid substrate for SERS. Samples for SERS measurements in liquid substrate (R6G-AgNPs) were prepared using 1.95 mL of the AgNPs colloid and 50 µL of rhodamine 6G (R6G, Sigma Aldrich®, solution @ 10<sup>-3</sup> mM concentration). For the solid substrate, drops (7 µL) of the R6G-AgNPs colloid were transferred to the PTFE membrane and allowed to dry.

UV-Vis extinction/absorption spectra of samples were measured with an optical fiber spectrometer (Ocean Optics, HR4000, 6.6 nm resolution) and a tungsten halogen lamp (Ocean Optics, LS-01), connected by optical fibers to a cuvette holder (Ocean Optics, CUV-ALL-UV). Raman spectra were measured by an optical fiber spectrometer (StellarNet, HR-TEC-X2, 200 - 3900 cm<sup>-1</sup>, 4 cm<sup>-1</sup> resolution) excited by a 638 nm, 50 mW spectrum stabilized single-mode semiconductor laser (StellarNet, Lab-LS-638), plus an optical fiber Raman probe (StellarNet, Raman-Probe-638). For liquid samples it was used a vial & probe holder (StellarNet, RPH4) and for solid samples an Olympus CX31 microscope (4x, 10x and 40x objectives).

The produced solid substrates were tested by individually analyzing the hole of the following parameters: roughness versus smoothness of PTFE membrane side; microscope objective lens magnification (4x, 10x, 40x); PTFE drying time and colloid pH. Changes in the pH of AgNPs colloids were accomplished by adding minute amounts of H<sub>2</sub>SO<sub>4</sub> or NaOH. When not otherwise specified, colloids present pH = 7. SERS intensities for liquid and solid substrates were compared in the experiments.

### 3. Results and Discussion

The interaction between the AgNPs and the analyte was verified by the UV-Vis spectra of the liquid samples. Figure 1 shows UV-Vis spectra of AgNPs, R6G and the interaction between them. The interaction gives rise to a band around 600 nm that increases at the expense of both the AgNPs plasmon band at 397 nm and the R6G band at 527 nm.

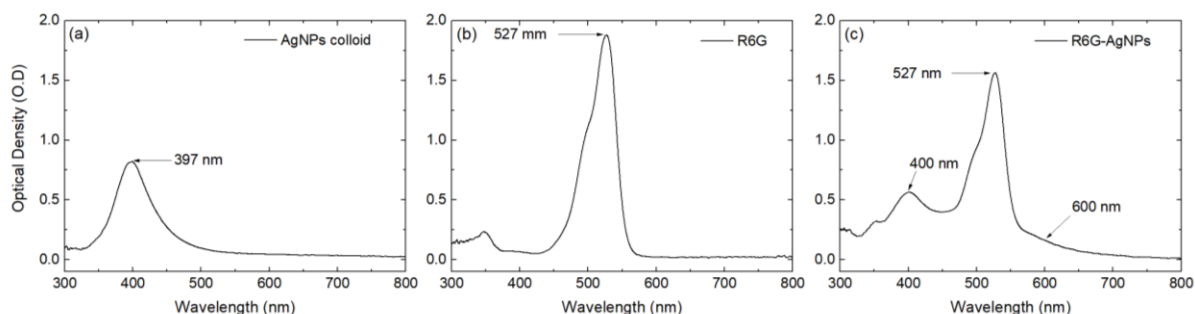


Fig. 1. UV-Vis spectra of: (a) the plasmon band of the AgNPs colloid, (b) the optical absorption spectrum of R6G in water and (c) the resulting interaction between AgNPs and R6G at pH = 7.

Figure 2 presents the SERS spectra of R6G in liquid (pH = 7) and solid substrates (smooth side) dried for 3 hours at room temperature. In order to compare the SERS intensity for liquid and solid substrates, an intensification of 15x was obtained for the solid substrate by employing the relative intensities of the typical R6G normal Raman band around  $1510\text{ cm}^{-1}$  (SERS at  $1517\text{ cm}^{-1}$  and  $1514\text{ cm}^{-1}$  in AgNP liquid and solid substrates, respectively).

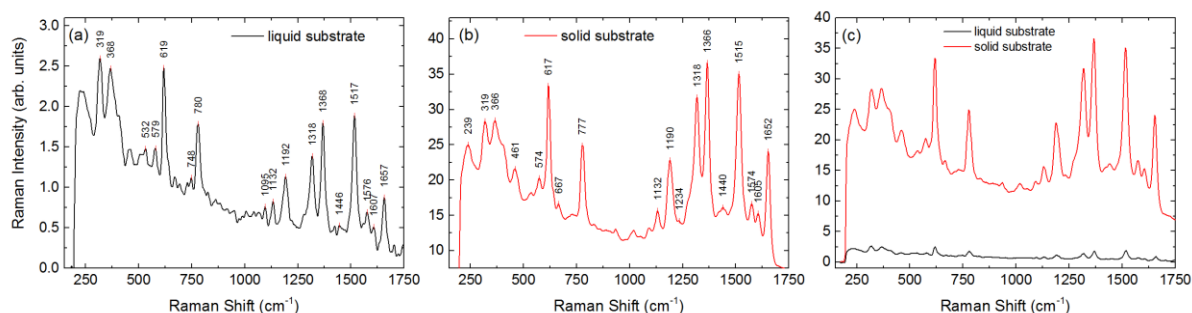


Fig. 2. SERS spectra of R6G collected with integration time of 3000 ms and with the 10x objective: (a) for the liquid substrate, (b) for the solid substrate and (c) a comparison between them.

Figure 3(a) shows the comparative performances of the solid substrates for SERS of R6G-AgNPs on PTFE concerning to the topological characteristic of the PTFE membrane. By using again the typical R6G normal Raman band around  $1510\text{ cm}^{-1}$ , an intensification of 2.8x was experienced on the rough side comparatively to the smooth side. In Figure 3(b) is shown a comparison of the normal Raman bands characteristic of the PTFE itself. The same bands are present on both sides of the membrane, although the intensity is lower in the rough side. As such scattering is superimposed to the R6G bands as noise, there is an extra advantage in using the smooth side of the PTFE membrane. Figures 3(c) and 3(d) present the aspect of smooth and rough sides of PTFE membrane, seen under the microscope objective with magnification of 10x. The fibers that constitute the PTFE are more exposed on the rough side than on the smooth side, what accounts for the more intense normal Raman bands on the rough side.

Figure 4 shows the influence of the objective lens magnification in the SERS spectrum of R6G-AgNPs at  $1510\text{ cm}^{-1}$ . An intensification of 7.4x is obtained for 10x objective comparatively to the 4x. For the 40x objective the signal is mainly dominated by fluorescence (the higher bandwidth signal superimposed to the Raman bands), what makes difficult to quantify the SERS intensity.

Figure 5 shows the influence of the solid substrate drying time in the SERS signal. The black line corresponds to the R6G-AgNPs on PTFE dried along 3 hours at room temperature ( $22\text{ }^{\circ}\text{C}$ ), whereas the red line is for a drying time of 15 minutes under the light from a 70 W incandescent lamp ( $60\text{ }^{\circ}\text{C}$ ). An intensification of 2.4x is obtained for the lower drying time at  $1510\text{ cm}^{-1}$ . The decrease in the SERS signal for longer drying times can be caused by an oxidative process of the AgNPs when in contact with the air, decreasing the interaction between the nanoparticles and the R6G.

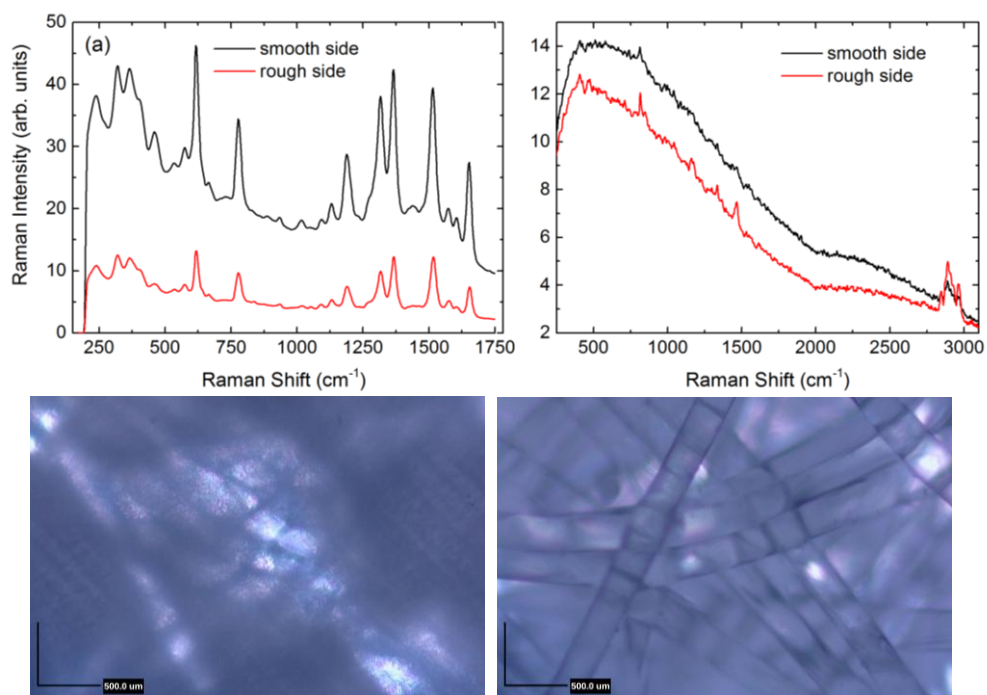


Fig. 3: (a) SERS spectra of R6G-AgNPs on PTFE (5000 ms integration time, 10x objective), (b) Normal Raman spectra from PTFE, smooth and rough sides (20000 ms integration time, 10x objective), (c) PTFE smooth side, (d) PTFE rough side.

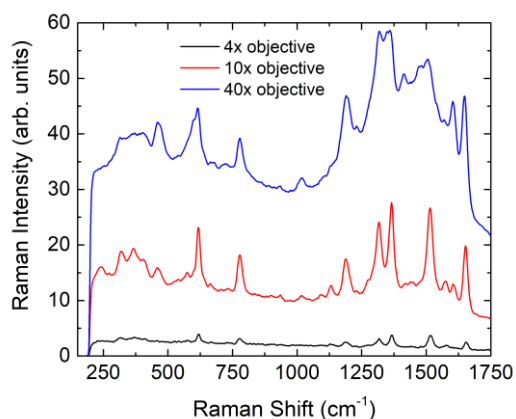


Fig. 4. SERS spectra of R6G-AgNPs for three microscope objectives (3000 ms integration time).

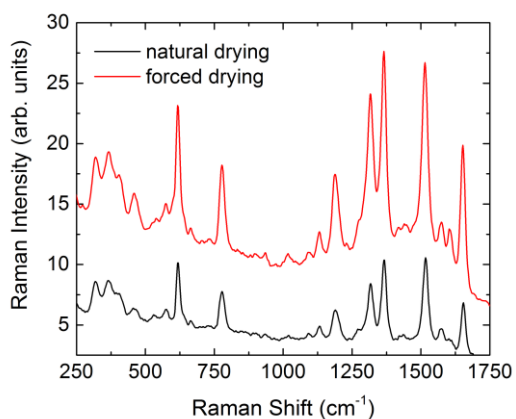


Fig. 5. SERS spectra of R6G-AgNPs for different drying times (3000 ms integration time, 10x objective).

In Figure 6 is presented the effect of the AgNPs colloid pH in the interaction R6G-nanoparticles. The most intense interaction, characterized by the arising of a UV-Vis band at 600 nm, is attained for a pH = 5, Figure 6(a). The intensification at  $1500\text{ cm}^{-1}$  (ratio of intensities solid/liquid substrates) is calculated as 2.6x (pH = 3), 6.0x (pH = 5) and 13.7x (pH = 7). As expected from the behavior depicted in Figure 6(a), the SERS signal for both substrates is more intense at pH = 5, although the comparative intensification is higher for pH = 7. The increase in the SERS signal for pH = 5 is attributed to the decrease in the plasmon band at 400 nm, followed by an important increase in the interaction band at 600 nm. On the other hand, the decrease in the SERS signal for pH = 3 is associated to a reduction in the plasmon band without a corresponding increase in the interaction band. Such effect can be caused by an excessive oxidation of AgNPs at lower pH values, reducing the number of AgNPs available for the interaction with the R6G molecules.

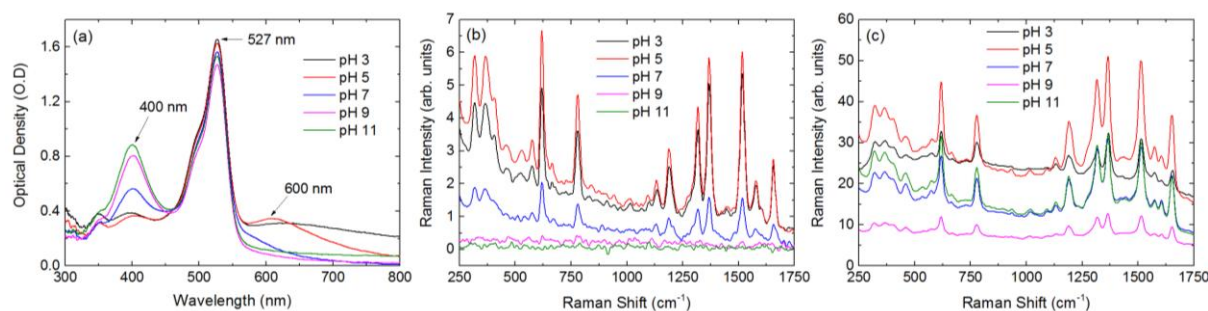


Fig. 6. (a) UV-Vis extinction spectra for R6G-AgNPs at different pH, (b) SERS for liquid substrate at different pH (3000 ms integration time, 10x objective), (c) SERS for solid substrate at different pH (3000 ms integration time, 10x objective).

#### 4. Conclusion

This work discusses the characteristics of a PTFE solid substrate developed for SERS. Under the experimental conditions of the work, the solid substrate revealed a better performance for SERS when compared with the liquid substrate. It was determined a set of parameters that allows obtaining the higher SERS signals, comparatively to the AgNPs liquid substrate. The parameters that optimize the SERS spectrum of the solid substrate are: smooth side of the PTFE membrane, 10x objective of the optical fiber Raman microscope, forced drying of the substrate at  $60\text{ }^{\circ}\text{C}$  for 15 minutes and pH = 5 of AgNPs colloid.

Although the technique developed in this work uses R6G as probe molecule, the results can be extended for a variety of other analytes. As example, the technique can be adapted for detection of pesticides in water and used as an auxiliary technique to determine the potability standards. The use of optical fiber to integrate all the components requires minimum alignment for the sensor, what in turn makes it adequate for field measurements.

An advantage of the developed technique when compared to other similar studies in the literature [6] resides in the fact that no lubricant additives are used, reducing the appearance of interfering lines in the Raman spectrum. In addition, as the AgNPs are produced by laser ablation in a top-down technique, the presence of chemical components is reduced when compared to the bottom-up techniques, further contributing to achieve simpler spectra.

#### Acknowledgments

The authors acknowledge the financial support received from Coordenação de Aperfeiçoamento de Pessoal de Nível Superior - Brasil (CAPES) - Finance Code 001, CNPq, FINEP and Fundação Araucária.

#### References

- [1] T. O. Deschaines and D. Wieboldt, "Practical Applications of Surface-Enhanced Raman Scattering (SERS)," in *Thermo Fisher Scientific*, Technical note 51874 (Madison, WI, USA, 2010).
- [2] T. B. Nguyen, T. K. T. Vu, Q. D. Nguyen, T. D. Nguyen, T. A. Nguyen and T. H. Trinh, "Preparation of metal nanoparticles for surface enhanced Raman scattering by laser ablation method," *Advances in Natural Science: Nanoscience and Nanotechnology* **3**, 025016 (2012).
- [3] P. G. Martínez-Torres, M. M. Martínez-García, P. E. Cardoso-Ávila and J. L. Pichardo-Molina, "Facile Nanostructured Substrate Preparation Using Gold Nanocuboids for SERS", *Nanomaterials and Nanotechnology*, 5-12 (2015).

[4] H. Liu, L. Zhang, X. Lang, Y. Yamaguchi, H. Iwasaki, Y. Inouye, Q. Xue, M. Chen, "Single molecule detection from a large-scale SERS-active Au<sub>79</sub>Ag<sub>21</sub> substrate," *Scientific Reports* **1**, 112 (2011).

[5] K. Kneipp, Y. Wang, R. R. Dasari and M. S. Feld, "Approach to single-molecule detection using Surface-Enhanced Resonance Raman-Scattering (SERS) - A study using rhodamine 6G on colloidal silver," *Applied Spectroscopy* **49**, 780-784 (1995).

[6] P. A. Mosier-Boss, "Review of SERS Substrates for Chemical Sensing", *Nanomaterials*, **7**, 142 (2017).

# Optical Sensor to Monitor the Fermentation Process of Beers Based on Etched Fibre Bragg Gratings

Oliveira, Vicente A.<sup>1</sup>; Silva, Vinicius N. H.<sup>1\*</sup>; Kuhne, Jean<sup>2</sup>; Peixoto, Fernando C.<sup>3</sup>; Sphaier, Leandro A.<sup>4</sup>; Barbero, Andrés Pablo L.<sup>1</sup>

<sup>1</sup>Universidade Federal Fluminense and Centro de Educação Tecnológica Celso Suckow da Fonseca, Postgraduate Program in Instrumentation and Applied Optics, Rua Passo da Pátria 156, bloco D, sala 307, Niterói, RJ, 24210-240, Brazil

<sup>2</sup>Universidade Tecnológica do Paraná, Postgraduate Program in Electrical Engineering and Industrial Computing,

<sup>3</sup>Universidade Federal Fluminense, Postgraduate Program in Chemical Engineering.

<sup>4</sup>Universidade Federal Fluminense, Postgraduate Program in Mechanical Engineering.

\*Corresponding Author: Silva, Vinicius N. H., viniciusnhs@id.uff.br

**Abstract:** In this paper it is presented preliminary results in the development of a sensor to monitor the fermentation process of beers in real time based on Etched Fibre Bragg Gratings (EFBG). The experiments show that these sensors are extremely responsive to the density variations, which makes them useful for the monitoring beer fermentation.

## 1. Introduction

Beer is a beverage obtained from the alcoholic fermentation of wort made mainly of malt, water and yeast. Besides the different types of ingredients that can be used, the brewing process has an important role in the production of a specific beer style. This process includes mashing, lautering, boiling, fermenting and conditioning. Thus, in order to have reproducibility of the final product, the breweries should control temperature and specific gravity during each step [1].

The most critical step in the brewing process is the fermentation by which yeast converts fermentable sugars to alcohol and carbon dioxide gas. Fermentation is sensitive to temperature, pH, and wort composition and these variables interfere in the biochemical processes carried out by yeasts modifying the sensorial profile (esters, high molecular weight alcohols, sulfur compounds and other) of the final product. At this stage, there are also risks of contamination if the inoculum does not have enough yeast [2].

During the fermentation, while the yeast transforms the fermentable sugars into alcohol the specific gravity of the wort decreases until there are no more sugars to be transformed. At that point, the beer should be matured for weeks depending of the beer style. In the brewing industry, the control of the specific gravity is done using handheld hydrometers or refractometers that an operator has to collect a sample in regular intervals. It is a manual procedure that increases the possibility batch contamination. Another factor that needs to be monitored is the temperature of the wort, since the fermentation an exothermic process and the tanks need to be cooled in order to maintain the proper temperature [2].

Optical sensors rise as an interesting alternative to chemical and bio-chemical applications due to some unique characteristics high sensitive and fast response. In recent years, fibre Bragg grating sensors have been widely used in many sensing applications including temperature, strain and pressure measurements [3]. An FBG based refractometer is an attractive RI sensor due to the advantages cited above. An FBG based refractometer was first reported by Asseh et al. in 1998 using an etched FBG as refractive index (RI) sensor [4] and recently have been used to realize a concentration sensor [5]. This paper reports the spectral (response) characteristics of the FBG sensor to density concentrations which can use in a measurement of beer fermentation.

## 2. Etched Fibre Bragg Gratings

The Bragg resonance wavelength condition can be expressed as [6]:

$$\lambda_B = 2n_{eff}\Lambda \quad (1)$$

where  $n_{eff}$  is the effective refractive index of the fiber,  $\Lambda$  is the grating pitch, and  $\lambda_B$  is the reflected Bragg wavelength (Fig. 1). In FBG sensors, the effective refractive index of the fundamental mode is practically independent of the refractive index of the medium surrounding by the cladding [7]. However, if the cladding diameter is reduced (Fig. 1),  $n_{eff}$  shows a non-linear dependence on the external medium as well as the Bragg wavelength [8]. The cladding reduction enhances the evanescent wave, which interacts with the external refractive index changing the  $n_{eff}$  inducing a shift of  $\lambda_B$ .

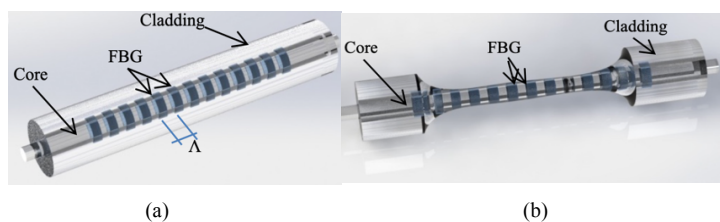


Fig. 1. Fiber Bragg grating: (a) standard and (b) etched.

### 3. The Fermentation Etched Fibre Bragg Gratings Sensor

To produce the EFBG sensor first the FGB was written in an optical fibre and after it was etched. The FBG were inscribed on Fibracem single mode fibre (SM 9/125). Then, the grating was recorded using phase-mask technique with a pulsed ArF excimer laser (Xantos XS, Coherent, 193 nm) operating at 250 Hz with 4 mJ over 4 minutes and an IBSEN phase mask (1552.13 and 1541.5 nm, unchirped). The grating spectra were monitored during the fabrication process by an optical spectrum analyzer (OSA - Yokogawa, AQ6375, ± 5 pm of wavelength stability) connected to an optical circulator and an amplified spontaneous emission (ASE). After the fibre was fixed in a rod, Fig. 3, of polyvinyl chloride (PVC) with an acrylic resin, which does not react with the acid, and it was etched by submerging it in a hydrofluoric acid (HF) solution. The fibre becomes extremely fragile after the etching due to the diameter around 7 μm (Fig. 5).

As it can be seen in Fig. 2, the rod has two “windows”, one for the EFBG and the other window to have a FBG to sensor the temperature. Notice that the latter was not used in this work and experiments are still in progress. The idea is to measure temperature and specific gravity using just one fibre [10, 11].



Fig. 2 The fibre with two sensors FBG fixed in the rod before chemical etching.

The EFBG was etched in 40% hydrofluoric acid (HF) solution and in Fig. 4 it can be seen a schematic diagram of the experimental setup to prepare the sensor. The spectrum of the ASE reflected by FBG was measured by the OSA while the FBG was etching. Then, the etching was stopped when the wavelength of FBG was shifted 5 nm, it means that the EFPG reaches the maximum sensibility according to theoretical and experimental results [12]. The etching process is neutralized by immersing the fibre in an aqueous solution of sodium hydroxide (NaOH, 2 M). After that, the fibres were washed with distilled water and dried in air.

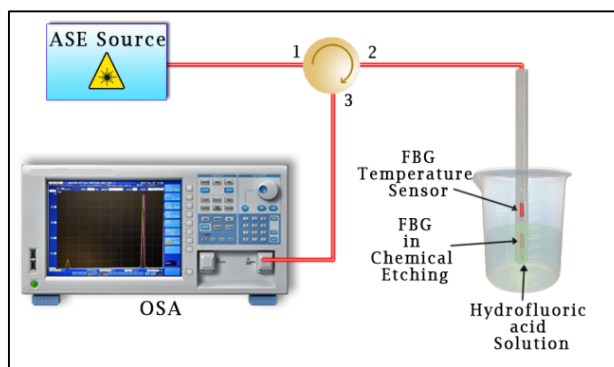


Fig. 3. Schematic diagram of the setup for sensor preparation.

In Fig. 4 it is shown the SEM picture of the FBG after the etching process and in Fig. 5 it is possible to see the integrity of the EFBG sensor when the fibre is lightened by a visible ASE.

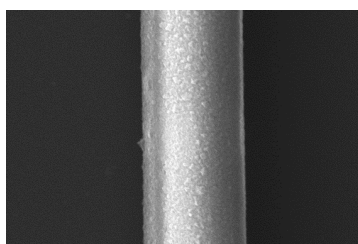


Fig. 4. The fibre after the etching process.



Fig. 5. The EFBG sensor lightened by the ASE.

#### 4. Experimental Results and Discussions

In order to the characterize spectral response of the EFBG as a specific gravity sensor, solutions of different concentrations were prepared, as it can be seen in Tab. 1. The solutions were prepared mixing sugar (sucrose) in dechlorinated water. Solutions from 0 to 20 Brix range were made to mimic the common original gravities of commercial beers. Thus, the sensor was immersed in a beaker containing the solution listed in Tab. 1, one at a time. The light beam from broadband source (ASE) was injected into the fiber and the reflected spectrum from EFBG for different concentrations of solution was observed with an optical spectrum analyzer (OSA). Changes in Bragg wavelength are noted at different concentrations Fig 6.

Table 1. Sample solutions of different density.

Solution	Brix (°Bx)	Density (g/L)	RI
1	20	1.083	1.3638
2	17.8	1.069	1.3600
3	16.6	1.064	1.3579
4	14.2	1.055	1.3539
5	12.5	1.040	1.3494
6	8.6	1.034	1.3447
7	7.1	1.028	1.3420
8	4.6	1.018	1.3378
9	1.9	1.008	1.3339
10	0	1	1.3330

The sensor sensitivity as a function of concentration in terms of wavelength shift has been analysed. In Fig. 6 it is shown the measured wavelength shift for the different solutions. It is important to note that two identical EFBG was prepared and analysed. Fig. 7 shows that wavelength shift increases with the increase of the original gravity and the result of two sensors are similar.

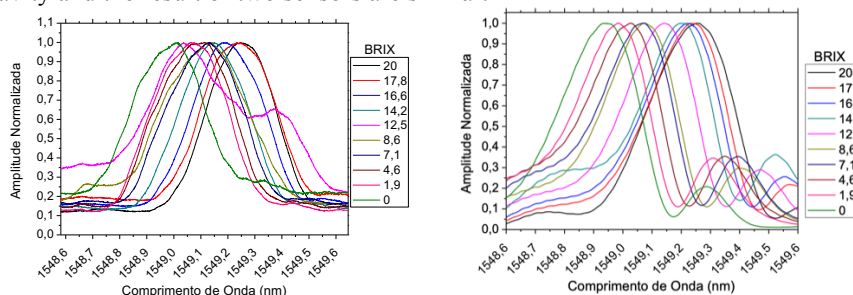


Fig. 6. Spectral response FBG to various density values.

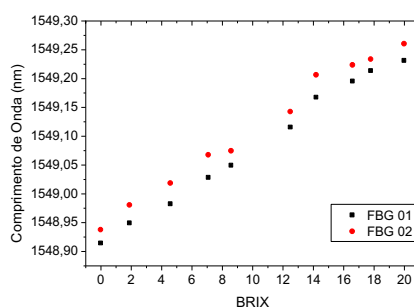


Fig 7. Measured wavelength in function of density for the two sensors EFBG.

## 5. Conclusions

It was proposed a refractometer sensor using technique involving chemical etching. The results show that sensor respond with high sensitivity to small density variations. It can be seen that there is a good linear relationship between the sugar concentration and the shifted wavelength showing that the sensor could be used for measure the fermentation process beers. The advantages are: aseptis and real-time monitoring.

## Acknowledgements

We would like to thank the Universidade Tecnológica Federal do Paraná and Coordenação de Aperfeiçoamento de Pessoal de Nível Superior - Brasil (CAPES) - Finance Code 001, Conselho Nacional de Desenvolvimento Científico e Tecnológico (CNPq – Universal 421019/2016-6) and Fundação Carlos Chagas Filho de Amparo à Pesquisa do Estado do Rio de Janeiro.

## References

- [1] H. V. AMORIM, *Fermentação alcoólica*, São Paulo: Ciência e tecnologia, 2005.
- [2] C. WHITE e J. Y. ZAINASHEFF, *The Practical Guide to Beer Fermentation*. Boulder, Colorado,: Brewers Publications, 2010.
- [3] Kersey, Brian, Culshaw e Alan, "Fiber-Optic Sensing: A Historical Perspective," *Fiber-Optic Sensing: A Historical Perspective*, vol. 26, n° n° 9, pp. 1064 - 1078, 2008.
- [4] A. Asseh, S. Sandgren, H. Ahlfeldt, B. Sahlgren e R. Stubbe, "Fiber Optical Bragg Grating Refractometer," *Fiber and Integrated Optics*, vol. 17, pp. 51-62, 1998.
- [5] C. Xianfeng, Z. Kaiping, Z. Lin e B. Ian, "Simultaneous measurement of temperature and external refractive index by use of a hybrid grating in D fiber with enhanced sensitivity by HF etching," *Applied Optics*, vol. 44, pp. 178-172, 2005.
- [6] K. O. Hill e G. Meltz, "Fiber Bragg Grating Technology," *JOURNAL OF LIGHTWAVE TECHNOLOGY*, vol. 15, n° 8, pp. 1263-1273, August 1997.
- [7] R. Kashyap, *Fiber Bragg Gratings*, San Diego, California: Elsevier Inc., 2010.
- [8] I. Agostino, C. Andrea, C. Stefania e C. a. M. G. Antonello, "Thinned Fiber Bragg Gratings as Refractive Index Sensors," *IEEE SENSORS JOURNAL*, vol. 5, n° N° 6, p. 1288, December 2005.
- [9] o. F. Dieg, W. Rosângela, F. K. Jean, G. M. Andréia, C. C. d. S. Jean e C. K. Ricardo, "Multimode fiber refractive index sensor based on wavelength modes separation," *LAWOFS - SBMO*, 2016.
- [10] A. Iadicicco, S. Campopiano, A. Cutolo, M. Giordano e A. Cusano, "Self temperature referenced refractive index sensor by non-uniform thinned fiber Bragg gratings," *Science Direct*, vol. B, n° 120, pp. 231-237, 2006.
- [11] D. Fernandes, R. C. Barreto, A. G. Macedo, J. C. C. Silva e R. C. Kamikawachi, "A Simple Equation to Describe Cross-Sensitivity Between Temperature and Refractive Index in Fiber Bragg Gratings Refractometers," *IEEE SENSORS JOURNAL*, vol. 18, n° 3, pp. 1104-1110, 2018.
- [12] G. Tsigaridas, D. Polyzos, A. Ioannou, M. Fakis e P. Persephonisa, "Theoretical and experimental study of refractive index sensors based on etched fiber Bragg gratings," *ScienceDirect*, vol. A, n° 209, pp. 9-15, 2014.

# Optical Fiber Bragg Grating Sensors for Temperature Measurements in the Hyperthermia Treatment.

Nicolas Ospina Mendivelso<sup>1</sup>, Juan Coronel-Rico<sup>1,2</sup>, Hector Fabian Guarnizo<sup>2</sup>, C. Camilo Cano<sup>1</sup> and Margarita Varón Durán<sup>1</sup>.

<sup>1</sup> High Frequency Electronics and Telecommunications Research Group. Universidad Nacional de Colombia.

<sup>2</sup> Universidad El Bosque.

Corresponding Author: nospinam@unal.edu.co

## Abstract

Hyperthermia is a treatment that consists in raising the temperature of the whole body or a part of it above the normal range (usually between 35 °C and 45 °C) for a defined period of time using microwave radiation, as an adjuvant for the treatment of tumors. However, the use of conventional sensors (thermocouples, thermistors, RTD) present interference issues linked to the scattering of microwave energy that can affect surrounding tissues of the body, among other problems. The goal of these proposal is to give a proof of concept of the feasibility of using an optical fiber-based system for temperature measurement taking advantage of the transparency of optical fiber materials when facing microwave energy. This means no undesired reflections or scattering inside the body. In this stage of the work, a gelatin phantom was built in order to measure the temperature reached when it is irradiated using a 2.45 GHz and 800 W microwave source. From these results a linear relation can be inferred between the temperature reached and the irradiation time, thus a proof of concept of real time measurement for hyperthermia applications is obtained.

## 1. Introduction

Hyperthermia is a treatment that consists in raising the temperature of the whole body or a part of it above the normal range (usually between 35 °C and 45 °C) for a defined period of time as an adjuvant for the treatment of tumors. This is a low-toxicity complementary treatment that is usually combined with chemotherapy and radiotherapy. The accuracy of the heating dose applied to the tumor is a key factor to enhance the success rate of the treatment [1] [2].

The use of conventional sensors (thermocouples, thermistors, RTD) present problems since hyperthermia is performed by means of microwaves. This leads to interference issues linked to the scattering of the microwave energy that can affect surrounding tissues of the body. Additionally, the voltages and currents induced by the electromagnetic waves on the metal elements of the sensors and the self-heating phenomena, produce erroneous readings in the measurements. Optical fiber based sensors are used for this type of applications because they are known as non-perturbators of the electromagnetic field [3].

The objective of this work is to develop a real-time thermometry system which can be used for hyperthermia treatments. In this text we present the first step that consists in validating the possibility of building a gelatin phantom due to its capability to imitate soft tissues, where it is possible to embed fiber optic sensors (Fiber Bragg Grating - FBG) in order to measure the temperature reached within it. This testbench is built to determine a preliminary relation between the applied microwave energy, the exposure time and the increase in the measured temperature at the phantom.

## 2. Fiber Bragg Grating (FBG) fundamentals

FBGs are known also as wavelength modulated sensors that use changes in the wavelength to detect changes in a parameter of interest. For example, in the measurement of strain, temperature, pressure, and dynamic magnetic field [4] [5] [6] [7]. Their structure works as a highly wavelength-selective reflection filter, where the spectrum of light whose wavelengths do not satisfy the Bragg condition pass through the grating essentially unaffected. However, when the light arrives at the at the Bragg resonant wavelength  $\lambda_B$ , the signal is back-reflected (Figure 1).

This wavelength  $\lambda_B$  depends on the period of the index perturbations  $\Lambda$  in the grating and the refractive index of the guided mode  $n_{eff}$ , which is an inherent property of the fiber (Equation 1) [4] [5] [6] [7].

$$\lambda_B = 2n_{eff}\Lambda \quad (1)$$

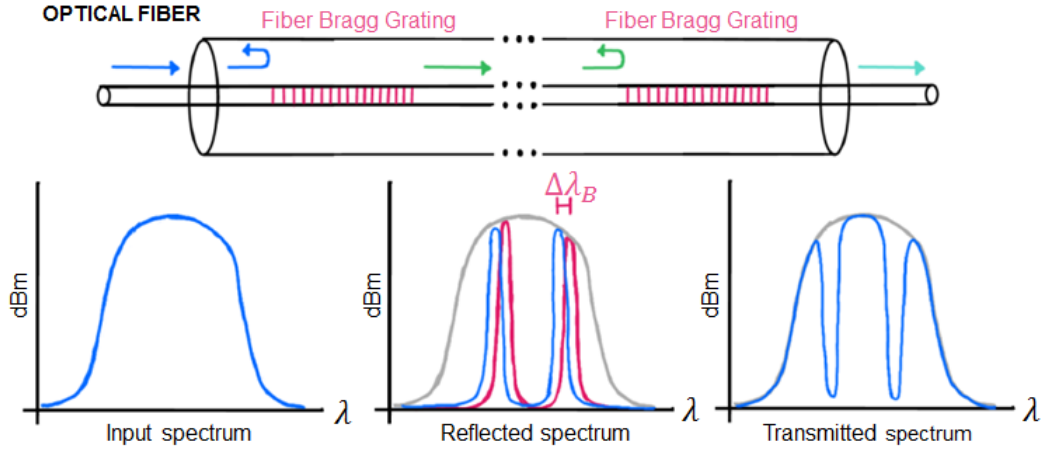


Fig. 1. Schematic diagram of structure and spectral response of fiber Bragg grating.

The sensing ability of an FBG derives from the sensitivity of both the refractive index and the grating period to externally applied mechanical or thermal perturbations. For instance, the strain on the fiber affects the response of the FBG through the expansion and compression of gratings period  $\Lambda$ . Additionally the photo-elastic coefficient of the fiber  $\rho_a$  relates the modification in the refractive index with strain-induced modifications and can affect the behavior of the sensor. The temperature sensitivity of an FBG is related to the thermo-optic coefficient  $\alpha$  i.e. change in the refractive index with response to temperature, and the thermal expansion coefficient of the fiber  $\zeta$  (Equation 2) [4] [6] [7].

$$\Delta\lambda_B = \lambda_B [(1 - \rho_a)\Delta\xi + (\alpha + \zeta)\Delta T] \quad (2)$$

In Equation 2,  $\Delta\lambda_B$  refers to changes in the magnitude of the Bragg resonant wavelength,  $\Delta\xi$  and  $\Delta T$  refer to the changes in magnitude of the strain and temperature, respectively. The previous equation can be further simplified to obtain the responsivity of the FBG, considering that the value of  $\lambda_B$  in the sensor is  $1550 \text{ nm}$ . In consequence, Equations 3 and 4 were obtained.

$$\frac{\Delta\lambda_B}{\Delta\xi} = (0.78 \times 10^{-6} \mu\xi^{-1})\lambda_B = 1.21 \frac{pm}{\mu\xi} \quad (3)$$

$$\frac{\Delta\lambda_B}{\Delta T} = (6.678 \times 10^{-6} \text{ } ^\circ\text{C}^{-1})\lambda_B = 10.35 \frac{pm}{^\circ\text{C}} \quad (4)$$

To validate the theory presented so far, a Universal Oven UM Memmert is used to characterize the response  $\Delta\lambda_B$  of the fiber to several temperature steps  $\Delta T$  (Equation 5).

$$\frac{\Delta\lambda_B}{\Delta T} = 8.7 \frac{pm}{^\circ\text{C}} \quad (5)$$

### 3. Experimental setup

For the tests, a magnetron and a pyramidal horn were used to irradiate a phantom due to its moderate directivity. This antenna has a power handling of  $800 \text{ W}$  and was used with an operating frequency of  $2.45 \text{ GHz}$  (Figure 2). In addition, realistic body models are needed to measure the temperature and simulate the penetration of microwave energy in the tissue, in consequence oil-in-gelatin dispersions are used due to its ability to mimic different tissues by selection of an appropriate concentration of oil, those materials possess long-term stability, they are suited for ultrawideband (UWB) applications over the frequency range of  $500 \text{ MHz}$  to  $20 \text{ GHz}$ . Furthermore they can be employed in heterogeneous configurations without change in geometry or dielectric properties due to diffusion across the interface which is useful due to the composition of the breast that requires low-water-content tissues (breast fat), intermediate-water-content tissues (skin) and high-water-content tissues (glandular tissues and cancerous tumors) [8] [9].

The goal is to build a structure as close as possible to a human breast with multiple fiber optic sensors within, to see the temperature gradient product of radiation inside the phantom. In this first approach, there is a fiber optic

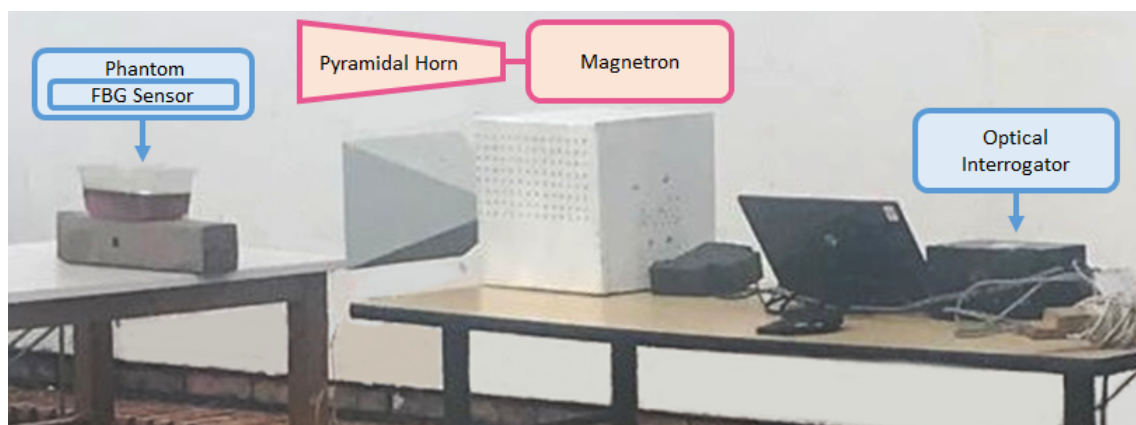


Fig. 2. Setup for performing the  $\Delta\lambda_B$  measurements used for temperature calculations of  $\Delta T$ .

sensor embedded in the center of the phantom. It is expected to improve the construction process to ensure the integrity of the fiber when inserting or extracting it from the phantom (Figure 3).

#### 4. Results and discussion

Table 1 summarizes the changes in  $\Delta\lambda_B$  and the theoretical temperature associated  $\Delta T$  with different measurements made at different distances and exposure times. In addition, the raw measurements and the linear approach of changes in  $\Delta\lambda_B$  respect to time can be seen in Figure 4. It can be observed that the anomalous values of the sensor readings are due to external stresses induced in the fiber by the wind. It is necessary to make the measurements for longer periods of times on a controlled space to avoid perturbations in the fiber due to external stresses.

The slope that associates the temperature change with the elapsed time is inversely proportional to the distance between the magnetron and the phantom. However, it is necessary to perform more tests at different distances to validate the proposal, obtain the tendency curve and locate the distances where it would be more suitable to expose the phantom.

For this result, the fiber presents a linear behavior between the time elapsed and the change in the temperature. However, it is necessary to make tests in longer periods of time in order to observe if the behavior is maintained.

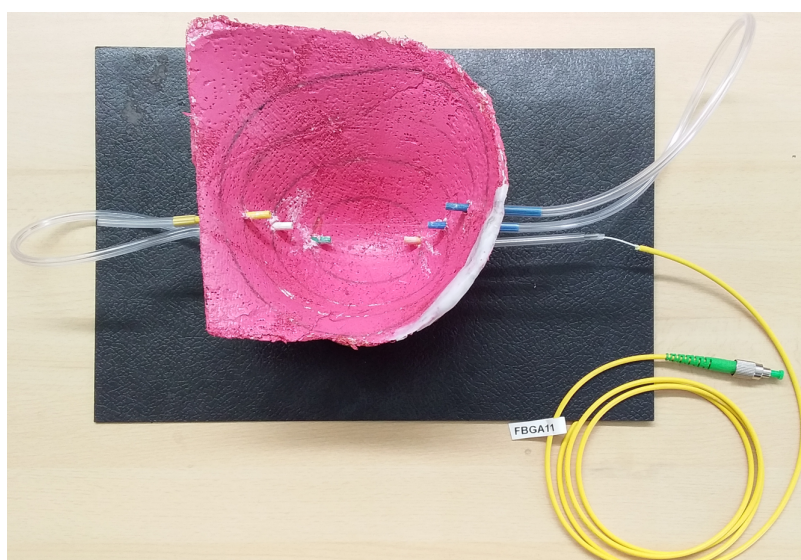


Fig. 3. Mold with embedded fiber for phantom construction.

Table 1. Changes in Bragg resonant wavelength  $\Delta\lambda_B$  and associated theoretical temperature  $\Delta T$  for measurements at different distances with different times of exposition.

Test (#)	Distance (m)	Exposure time (min)	$\Delta\lambda_B$ (pm)	$\Delta T$ (°C)
1	1.00	2	3.16	0.36
2	0.64	3	8.87	1.02
3	0.64	6	20.67	2.38

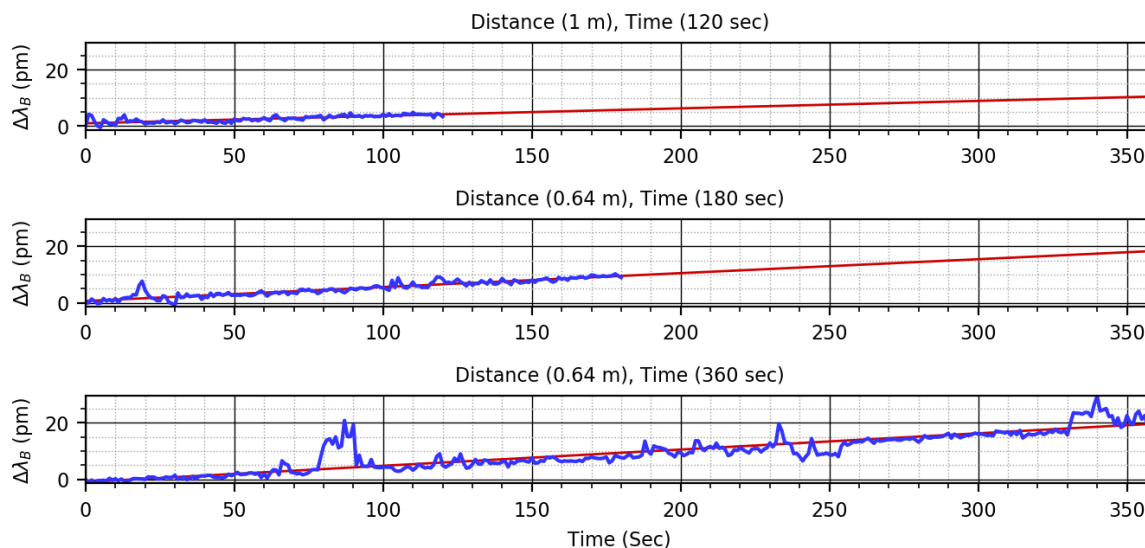


Fig. 4. Changes in  $\Delta\lambda_B$  for different distances and different times of exposition

## 5. Conclusions

The implementation of a testbench to verify the effects of the microwave energy radiation with real time temperature monitoring evidences the feasibility to use optical fiber temperature measurement for hyperthermia treatment. Optical fiber sensors are immune to high power microwave radiation, this makes the FBGs sensors suitable for in-body applications.

Despite the clear response of the optical fiber sensor facing temperature changes, more research is necessary to enhance the microwave energy dosage and application through a high directivity antenna. Furthermore, it should be considered to test the phantom and sensors under a wider microwave frequency range in order to find the most efficient response and assure the best radiation/heating response.

Once the optical fiber sensor performance for hyperthermia applications is probed to be feasible, it is recommended to test the setup using ex-vivo animal tissues to compare the sensor performance to that one inside the phantom.

## References

- [1] G. van Rhoon, M. Paulides, T. Drizdal, and M. Franckena, "Hyperthermia and the need to monitor temperature," in *2015 International Conference on Electromagnetics in Advanced Applications (ICEAA)*. IEEE, 2015, pp. 1181–1185.
- [2] M. Mallory, E. Gogineni, G. C. Jones, L. Greer, and C. B. Simone II, "Therapeutic hyperthermia: The old, the new, and the upcoming," *Critical reviews in oncology/hematology*, vol. 97, pp. 56–64, 2016.
- [3] J. Chong, L. Leija, C. Pennisi, and W. Fonseca, "Optical fiber based thermometry system for a hyperthermia laboratory," in *2001 Conference Proceedings of the 23rd Annual International Conference of the IEEE Engineering in Medicine and Biology Society*, vol. 3. IEEE, 2001, pp. 3036–3039.
- [4] Y.-J. Rao, "In-fibre bragg grating sensors," *Measurement science and technology*, vol. 8, no. 4, p. 355, 1997.
- [5] D. A. Krohn, T. MacDougall, and A. Mendez, "In-fiber grating optic sensors," in *Fiber optic sensors: fundamentals and applications*. Spie Press Bellingham, WA, 2014, ch. 4, pp. 110–154.
- [6] S. Yin and T. Francis, "Wavelength-modulated sensors," in *Fiber optic sensors*. CRC press, 2002, ch. 5, pp. 63–77.

- [7] G. Wehrle, P. Nohama, H. J. Kalinowski, P. I. Torres, and L. C. G. Valente, "A fibre optic bragg grating strain sensor for monitoring ventilatory movements," *Measurement Science and Technology*, vol. 12, no. 7, p. 805, 2001.
- [8] M. Ostadrahimi, R. Reopelle, S. Noghianian, S. Pistorius, A. Vahedi, and F. Safari, "A heterogeneous breast phantom for microwave breast imaging," in *2009 Annual International Conference of the IEEE Engineering in Medicine and Biology Society*. IEEE, 2009, pp. 2727–2730.
- [9] M. Lazebnik, E. L. Madsen, G. R. Frank, and S. C. Hagness, "Tissue-mimicking phantom materials for narrowband and ultrawideband microwave applications," *Physics in Medicine & Biology*, vol. 50, no. 18, p. 4245, 2005.

# Fiber Bragg grating coated with diphenylalanine nanotubes for methanol vapor detection

**Raquel de Paiva Corotti, Bruno Barros Cunha, Rafael Carvalho Barreto, André Luiz Coelho  
Conceição and Ricardo Canute Kamikawachi**

*Federal University of Technology - Paraná, Av. Sete de Setembro, 3165, Curitiba-PR*

*Postal Code 80.230-901 -Brazil*

*Author e-mail address: canute@utfpr.edu.br*

**Abstract:** In this work, etched fiber Bragg gratings (EFBG) coated with diphenylalanine nanotubes (DNT) are studied for methanol vapor detection. The DNT morphology is characterized by Scanning Electron Microscopy and the temperature transition is determined by Small-Angle X-Ray Scattering technique. After the phase transition, a significant increase in wavelength shift can be observed.

## 1. Introduction

Fiber Bragg gratings are a very well established technology for temperature and strain monitoring. Some advantages that have drawn the attention of the researchers to this device are electrical passivity, electromagnetic immunity, reduced dimensions and high multiplexing capability.

In the last few years, the development of new materials has allowed great scientific and technological advances, especially those applied in sensing solutions. Recently, a large number of works has reported fiber gratings functionalized with nanostructured materials for biosensing [1-5] and chemical detection [6-9]. Nanotubes are a class of nanostructures that have been studied as an active layer for sensing purposes. It has been shown that the DNT presents great potential in the development of chemical and biochemical sensors, in which the water present in the nanotube channels play a key role.

The methanol is an important raw material in the chemical industry, being used in the production of formaldehyde, methyl tert-butyl ether (MTBE), as pure fuel, or in mixture with gasoline for light vehicles. However, methanol is hazardous to human health, especially to the nervous system. The toxicity and volatility of methanol have motivated several researchers to develop sensors capable of detecting methanol vapor [10-13], and in recent years, optical fiber sensors have also been reported [14-16]. Okuda et al., proposed an optical fiber sensor modified with a nanoporous thin film coating for organic solvent vapors detection [14]. Liu et al. reported high sensitivity sensors for volatile organic compounds (VOCs) based on a tapered small core single mode fiber and a microfiber coupler [15]. Hromadka et al. proposed a long period grating sensor coated with ZIF-8 to detect VOCs with high sensitivity [16].

In this work, DNT was tested as an active element in gas sensors based on EFBG for methanol vapor detection. The DNT was deposited on an EFBG by drop casting. The DNT morphology was characterized by Scanning Electron Microscopy (SEM), and the phase transition temperature was determined by Small Angle X-Ray Scattering (SAXS) technique. The sensor's response of the orthorhombic and hexagonal phases were compared.

## 2. Materials and Methods

### 2.1. Chemicals

The dipeptide L,L-diphenylalanine (FF), 1,1,1,3,3,3-hexafluoro-2-propanol (HFIP) and methanol were purchased from Sigma-Aldrich. All chemicals were used without any further purification and the solutions prepared using ultrapure water from a Milli-Q system.

## 2.2. Sensor fabrication and peptide synthesis

The FBG was inscribed in a single mode fiber (Draka, G.652) using the phase-mask technique. ArF excimer laser (Xantos XS, Coherent, 193 nm 250 Hz and 2.5 mJ per pulse energy) was used for the grating inscription. The etching was performed using an aqueous hydrofluoric acid solution (HF 40%), followed by a neutralization procedure using an aqueous sodium hydroxide solution (NaOH 2 mol/L). The rate of corrosion was monitored in situ by the shift of the wavelength peak of the reflected signal. Chemical etching is an isothermal process that initially causes a redshift in wavelength until the evanescent field penetrates with the external medium. From this point the wavelength present a blue shift, and a wavelength shift of 5 nm from the initial wavelength corresponds to a final fiber diameter of 8  $\mu\text{m}$ .

The DNT at concentrations of 100 mg/mL were produced by dissolving the lyophilized peptide in HFIP and self-assembled in water vapor.

The DNT structure was characterized by SEM (EVO MA 15, Carl Zeiss Microscopy) and the temperature transition between hexagonal and orthorhombic phases was determined by SAXS measurements, using a Bruker Nanostar system equipped with Genix3D microfocus source, Fox3D focusing mirrors and scatterless slits, all provided by Xenocs company at the Institute of Physics at University of São Paulo.

The EFBG was covered by drop casting procedure with 320 mmol/L of L,L-diphenylalanine in HFIP solutions, after the first battery of measurements of methanol vapor, the coated EFBG was heated at 190  $^{\circ}\text{C}$  for 14 minutes to change to the orthorhombic phase. The average DNT layer thickness was 10  $\mu\text{m}$ .

## 2.3. Sensor Characterization

The sensor's response to methanol vapor was obtained using a 3 L vessel with 50  $\mu\text{L}$  of methanol injected with a micropipette. The sensor was alternately exposed to ambient laboratory air for 5 minutes, and then to the vessel vapor for 15 minutes. This cycle of measurements was repeated three times. The wavelength response was monitored with a Micron Optics SM-125 optical interrogator (2 Hz scan rate, 1 pm wavelength accuracy). The experiments were carried out in the laboratory with the controlled temperature maintained at  $(22 \pm 1)$   $^{\circ}\text{C}$ .

## 3. Results and discussions

The results of the Small Angle X-Ray Scattering measurements are shown in Fig. 1. We observe a peak at  $q = 1.68$   $\text{nm}^{-1}$  until 135  $^{\circ}\text{C}$ . At 190  $^{\circ}\text{C}$ , there is a shift in the peak to 2.07  $\text{nm}^{-1}$ , which indicates the transition from hexagonal to orthorhombic phase.

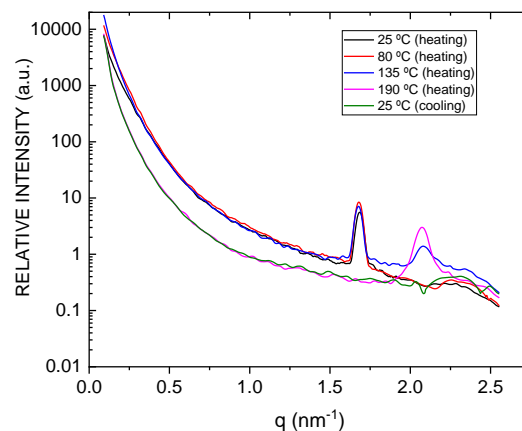


Fig. 1. Shift in the peak of the Small Angle X-Ray Scattering from  $q = 1.68$   $\text{nm}^{-1}$  to  $2.07$   $\text{nm}^{-1}$  indicating the transition between hexagonal and orthorhombic phases.

The SEM image of DNT before the phase transition shows a nanotube forest morphology characteristic of hexagonal phase (Fig. 2A). The orthorhombic phase obtained after the transition at 190 °C, in which was observed a rodlike morphology (Fig. 2B).

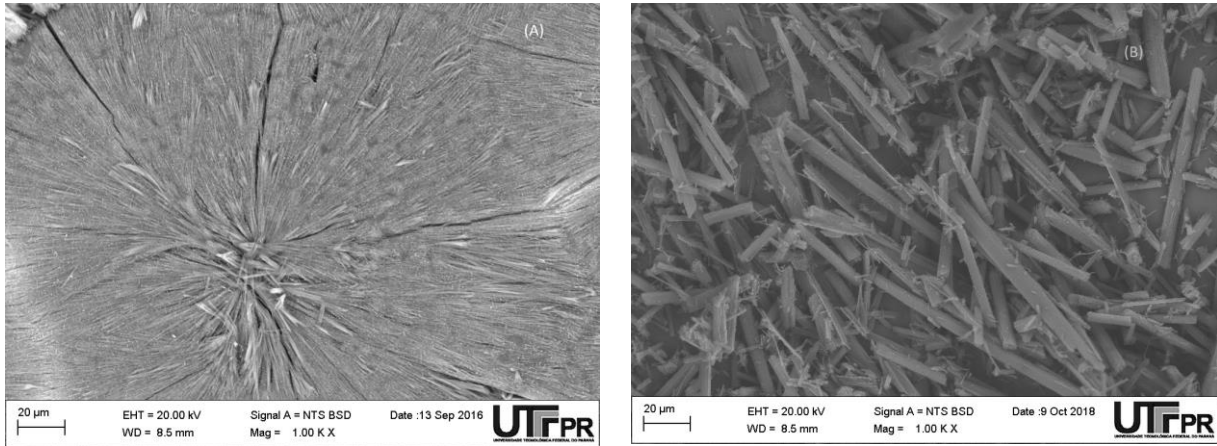


Fig. 2. Morphology of DNT for (A) hexagonal phase and (B) orthorhombic obtained by SEM.

Fig. 3 shows the wavelength response of the DNT coated etched FBG as a function of the time for three cycles of exposure to air and methanol vapor under saturation conditions, for hexagonal and orthorhombic phases. After the transition, when exposed to air, the wavelength shifted from 1549.18 nm to 1549.79 nm.

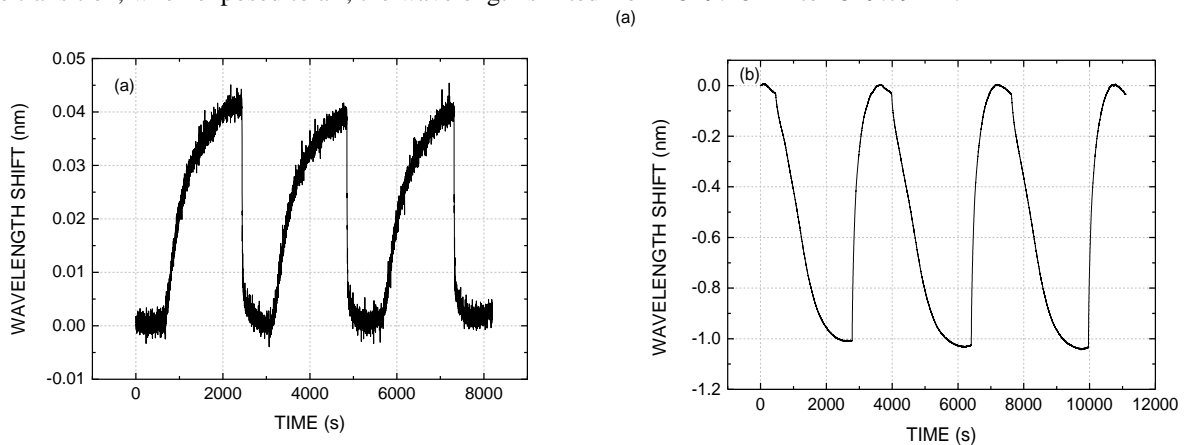


Fig. 3. Bragg wavelength shift as a function of the time for three cycles of exposure to air and methanol vapor under saturation conditions for (a) hexagonal and (b) orthorhombic phases.

The wavelength response was red-shifted in the hexagonal phase, while in the orthorhombic, it is blue-shifted. In the orthorhombic phase, the observed wavelength shift response was 1.0 nm, which is 25 times greater than the wavelength shift response of the hexagonal phase. Due to the phase transition from the hexagonal to orthorhombic, the characteristic time response increased from 540 seconds to 976 seconds, and the characteristic time recovery increased from 50 seconds to 183 seconds. One hypothesis for the increase in the sensitivity is the change in the nanotubes morphology, that can be seen in Fig 2. In the orthorhombic phase, the structure presents gaps which can result in a greater diffusion of the vapor molecules. After the phase transition, the wavelength response in air

presents a red shift of 0.7 nm. This result indicates that the DNT may present a higher refraction index when it is in the orthorhombic phase compared to the hexagonal phase, which contributes to the increase in the sensitivity.

#### 4. Conclusions

In this work, we investigated the response to methanol vapor of EFBG coated with DNT. The response of the hexagonal and orthorhombic phases was compared. After the phase transition from hexagonal to orthorhombic, the wavelength shift response increased 25 times and changed from red to blue shift. One hypothesis for this sensitivity increase is the change in the nanotubes morphology, which allows a higher diffusion. Also, after the phase transition the wavelength response in air presented a redshift of 0.7 nm, which indicates that the DNT may present a higher refraction index in the orthorhombic phase when compared to the hexagonal phase. These results point out the possible application of EFBG functionalized with DNT for methanol vapor detection.

#### Acknowledgments

This work was supported by the Brazilian Agencies CNPq 443134/2014-6, CAPES Finance Code 001, SETI, FINEP, and Fundação Araucária.

#### References

- [1] E. Brzozowska, M. Mietana, M. Koba, S. Grska, K. Pawlik, A. Gamian, W. J. Bock, "Recognition of bacterial lipopolysaccharide using bacteriophage-adhesin-coated long-period gratings," *Biosensors and Bioelectronics* **67**, 93-99 (2015).
- [2] S. Sridevi, K. Vasu, S. Asokan, A. Sood, "Sensitive detection of c-reactive protein using optical fiber bragg gratings," *Biosensors and Bioelectronics* **65**, 251-256 (2015).
- [3] R. Garg, S. M. Tripathi, K. Thyagarajan, W. J. Bock, "Long period fiber grating based temperature-compensated high performance sensor for bio-chemical sensing applications," *Sensors and Actuators B: Chemical* **176**, 1121-1127 (2013).
- [4] S. S, K. Vasu, N. Jayaraman, S. Asokan, A. Sood, "Optical bio-sensing devices based on etched fiber bragg gratings coated with carbon nanotubes and graphene oxide along with a specific dendrimer," *Sensors and Actuators B: Chemical* **195**, 150-155 (2014).
- [5] S. M. Tripathi, W. J. Bock, P. Mikulic, R. Chinnappan, A. Ng, M. Tolba, M. Zourob, "Long period grating based biosensor for the detection of escherichia coli bacteria," *Biosensors and Bioelectronics* **35**, 308-314 (2012).
- [6] J. Cheng, W. Zhu, Z. Huang, P. Hu, "Experimental and simulation study on thermal gas flowmeter based on fiber bragg grating coated with silver film," *Sensors and Actuators A: Physical* **228**, 23-27 (2015).
- [7] B. Shivananju, G. Prashanth, S. Asokan, M. M. Varma, "Reversible and irreversible ph induced conformational changes in self-assembled weak polyelectrolyte multilayers probed using etched fiber bragg grating sensors," *Sensors and Actuators B: Chemical* **201**, 37-45 (2014).
- [8] S. Korposh, S.W. Lee, S. W. James, R. P. Tatam, "Refractive index sensitivity of fibre-optic long period gratings coated with SiO<sub>2</sub> nanoparticle mesoporous thin films," *Measurement Science and Technology* **22**, 075208 (2011).
- [9] A. Cusano, P. Pilla, L. Contessa, A. Iadicicco, S. Campopiano, A. Cutolo, M. Giordano, G. Guerra, "High-sensitivity optical chemosensor based on coated long-period gratings for sub-ppm chemical detection in water," *Applied Physics Letters* **87**, 234105 (2005).
- [10] D. Das, P. Choudhury, L. J. Borthakur, I. R. Kamrupi, U. Gogoi, S. K. Dolui, "Methanol vapor sensor based on poly(styrene-cobutylacrylate)/polypyrrole-eg coreshell nanocomposites," *Sensors and Actuators B: Chemical* **199**, 320-329 (2014).
- [11] C.F. Fong, C.L. Dai, C.C. Wu, "Fabrication and characterization of a micro methanol sensor using the cmos-mems technique," *Sensors* **15**, 27047-27059 (2015).
- [12] B. Kieser, F. Dieterle, G. Gauglitz, "Discrimination of methanol and ethanol vapors by the use of a single optical sensor with a microporous sensitive layer," *Analytical Chemistry* **74**, 4781-4787 (2002).
- [13] T. Someya, J. Small, P. Kim, C. Nuckolls, J. T. Yardley, "Alcohol vapor sensors based on single-walled carbon nanotube field effect transistors," *Nano Letters* **3**, 877-881 (2003).
- [14] H. Okuda, T. Wang, S.W. Lee, "Selective methanol gas detection using a u-bent optical fiber modified with a silica nanoparticle multilayer," in *Electronics and Communications in Japan* Vol. 100 pp. 43-49.

[15] D. Liu, R. Kumar, F. Wei, W. Han, A. K. Mallik, J. Yuan, S. Wan, X. He, Z. Kang, F. Li, C. Yu, G. Farrell, Y. Semenova, Q. Wu, "High sensitivity optical fiber sensors for simultaneous measurement of methanol and ethanol," *Sensors and Actuators B: Chemical* **271**, 1-8 (2018).

[16] J. Hromadka, B. Tokay, R. Correia, S. P. Morgan, S. Korposh, "Highly sensitive volatile organic compounds vapour measurements using a long period grating optical fibre sensor coated with metal organic framework zif-8," *Sensors and Actuators B: Chemical* **260**, 685-692 (2018).

# Interrogation of Long-Period Grating Temperature Sensor Using Fiber Bragg Gratings and Artificial Neural Network

Marco Aurélio Jucá<sup>1,2</sup>, Alexandre Bessa dos Santos<sup>1</sup>

<sup>1</sup>Universidade Federal de Juiz de Fora, Juiz de Fora, MG, Brazil

<sup>2</sup>Centro Federal de Educação Tecnológica Celso Suckow da Fonseca, Petrópolis, RJ, Brazil  
marco.juca@engenharia.ufff.br

**Abstract:** Considering the increasingly wide application of optical fiber sensors, this paper aims to present an alternative form of interrogation without the use of an optical spectrum analyzer or any other high-cost devices. The sensor studied here is a long-period grating being used to measure temperature. The interrogator is composed of optical filters and photodetectors whose responses are processed by a suitably trained artificial neural network. Results show that this technique enables effective interrogation of a range limited only by the optical bandwidth of the light source.

## 1. Introduction

In recent years, optical fiber sensors have been established as an effective means of performing sensing operations due to a number of advantages over common electronic sensors. The main advantages include their immunity to electromagnetic interference, light weight, small size, chemical inertia, and the possibility of multiplexing sensors and of performing remote sensing [1].

In this paper, we chose to study a long-period grating (LPG) temperature sensor. An LPG is an optical device that couples light from the fundamental core mode into co-propagating cladding modes, whose attenuation is considerably higher due to large scattering losses at the cladding-air interface and bends in the fiber [2]. In order to enable the light coupling, the effective refractive indices of the modes must satisfy the phase-matching condition, given by [3]:

$$\beta_1 - \beta_2 = \Delta\beta = 2\pi/\Lambda, \quad (1)$$

where  $\Lambda$  is the period of the LPG,  $\beta_1$  and  $\beta_2$  are the propagation constants of the modes being coupled and  $\Delta\beta$  is the differential propagation constant. This condition can be achieved by several cladding modes, resulting in attenuation bands centered at discrete resonant wavelengths,  $\lambda_{\text{res}}^m$ , which can be represented as [4]:

$$\lambda_{\text{res}}^m = (n_{\text{eff,co}}^{01} - n_{\text{eff,cl}}^m) \Lambda, \quad (2)$$

where  $n_{\text{eff,co}}^{01}$  is the effective refractive index of the fundamental core mode,  $n_{\text{eff,cl}}^m$  is the effective refractive index of the  $m$ -th cladding mode. The resonant wavelength  $\lambda_{\text{res}}^m$  is a function of both effective refractive indices and the grating period, which in turn vary with external variables such as temperature, strain, refractive index and bending [5]. This sensitivity of the resonant wavelengths to environmental parameters allows the use of LPGs in sensing applications, by tracking the resonant wavelength of one or more cladding mode orders in the transmission spectrum of the LPG.

In a laboratory, the response of the sensor is obtained through an optical spectrum analyzer (OSA), which is a large, high-cost device. In field applications, alternative interrogation techniques are preferred, frequently involving optical filtering of the sensor output. Alternative methods for interrogating LPG sensors are discussed in [6] and [7], where the authors use fiber Bragg gratings (FBG) as optical filters. The main advantage of using alternative methods of interrogation is cost reduction, along with portability and automation made easier.

The interrogation methods using optical filtering require some processing. In recent years, artificial intelligence techniques have been successfully applied in processing sensor data for interrogation purposes, especially using artificial neural networks (ANN) [8-11]. In a previous work, [12], we have proposed an interrogation system for an FBG sensor, which we extend in this work to apply to the interrogation of an LPG sensor.

## 2. Methodology

### 2.1. Sensor and Interrogator Setup

The working principle of this interrogation system can be explained as follows. Light is emitted by the light source, a superluminescent diode (SLD), and propagates through an LPG sensor. The LPG inserts attenuation bands centered in resonant wavelengths which depend upon the temperature of the surrounding medium. The interrogation system must process the information received from the sensor and return the estimated value of the temperature. In order to do that, the sensor output is filtered by FBGs centered in suitable wavelengths so as to allow the identification of the sensor response. The output of each filter is collected by a photodetector whose value is digitalized and sent to the ANN for processing. The ANN is responsible for identifying the sensor temperature from the photodetector outputs and returning the estimated temperature value in degrees Celsius. This process is illustrated in Fig. 1, where a set of three filters was used. Depending on the dynamic range of interest for interrogation, more filters may be necessary, as will be shown in Section 3.

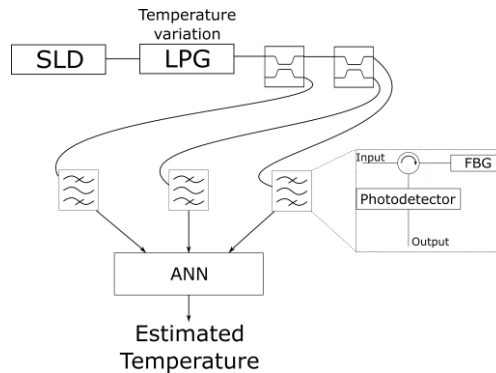


Fig. 1. Sensor and interrogator setup.

### 2.2. Interrogation

The set of filters seen in Fig. 1 separates the signal coming from the sensor in sub-bands. Each photodetector produces an electric current proportional to the optical power contained in the respective sub-band. This value, for each photodetector, is an input to the ANN, which will process the data and return an estimate of the temperature measured by the sensor. Thus, the ANN will have as many inputs as there are filters and one output. The ANN in question is a multilayer perceptron (MLP) and was trained using the resilient backpropagation learning algorithm. One hidden layer was used to process the input values and different numbers of neurons were tested for this layer. The activation function in the hidden layer is a hyperbolic tangent and in the output layer it is linear. The ANN inputs are normalized before processing and the output is denormalized to yield the estimated temperature.

## 3. Tests and Results

The objective of the tests was to interrogate the largest possible dynamic range for the sensor in question. We used an LPG written on a standard single-mode fiber with core radius of 4.15  $\mu\text{m}$  and cladding radius of 62.5  $\mu\text{m}$ , core refractive index of 1.449 and cladding refractive index of 1.444. The period of the LPG was 522.9  $\mu\text{m}$ . We observed the attenuation band corresponding to the  $LP_{05}$  mode, which has a resonant wavelength around 1550 nm at 25  $^{\circ}\text{C}$ , under the aforementioned circumstances. The light source was an SLD with an optical bandwidth of 100 nm centered around 1550 nm. Considering the LPG in question has a temperature sensitivity of 6.3 nm/ $^{\circ}\text{C}$ , the theoretical dynamic range is approximately from 17 to 33  $^{\circ}\text{C}$ , which could be larger with a more broadband source.

For the tests, we created two independent sets of data: one for training the ANN and one for testing its performance. There is no overlap between both sets of data. The parameter used to measure the performance of the ANN was the mean squared error (MSE) calculated on the testing dataset after the ANN was trained using the training dataset.

We conducted three tests with different numbers of filters in the setup: three, five and seven. With three filters, the spacing between their central wavelengths must be high in order to cover the theoretical dynamic range, which hinders the accuracy of the interrogator. The filters were designed for the following wavelengths: 1505 nm, 1500 nm and 1595 nm. Table 1 shows the results of the tests with several sizes of the hidden layer, considering the MSE as a performance parameter. A lower value of MSE means the system is more accurate. The results for three filters show that the best configuration for the hidden layer is using 3 neurons.

In order to increase accuracy, we must decrease the spectral spacing between the filters. To do so while covering the same range, we must also increase the number of filters. Thus, we tested the system with five filters, designed for the following wavelengths: 1500 nm, 1525 nm, 1550 nm, 1575 nm and 1600 nm. The results of this test can also be seen in Table 1. It may be noted that the accuracy of the system is indeed better than the previous test. For this configuration, it was found that the ANN performs best if the hidden layer has 13 neurons.

The last test conducted was an attempt to increase accuracy by reducing even more the spectral spacing between the filters. This test considered seven filters with the following resonant wavelengths: 1505 nm, 1520 nm, 1535 nm, 1550 nm, 1565 nm, 1580 nm and 1595 nm. The hidden layer configuration that showed the best performance in this case was that which used 6 neurons, as can be seen in Table 1. Figure 2 shows the performance of this filter configuration using an ANN whose hidden layer has 6 neurons. The horizontal axis indicates the actual temperature whereas the vertical axis indicates the system output. The solid black line represents an ideal sensor/interrogator system which would return the temperature with zero error. The red dots represent the output of this system. It is noteworthy that, in this configuration, the worst case estimation error was found to be 1.8% of the real measured value.

Table 1. Mean squared error for the trained ANNs for different sizes of the hidden layer.

Number of neurons in the hidden layer		1	2	3	4	5	6	7	8	9	10	11	12	13	14	15
MSE [(°C) <sup>2</sup> ]	Three filters	4.0	3.8	<b>3.0</b>	3.4	4.2	4.0	7.8	3.8	3.8	4.4	5.7	4.2	4.6	4.9	4.3
	Five filters	3.4	2.7	4.8	3.0	2.9	3.4	1.5	3.6	2.6	2.8	4.6	6.5	<b>1.3</b>	2.1	5.2
	Seven filters	2.9	1.9	1.6	1.4	0.9	<b>0.7</b>	2.8	0.8	1.3	4.4	3.6	4.5	7.6	2.3	6.0

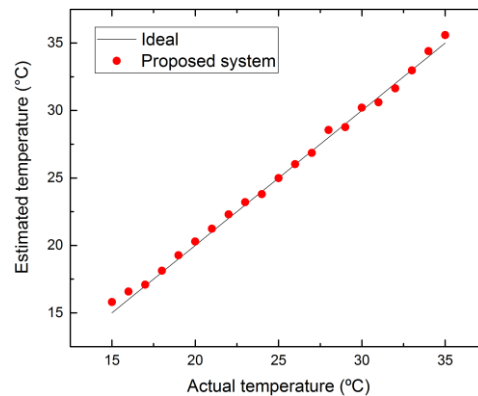


Fig. 2. Temperature estimation of the interrogation system consisting of seven filters using a 6-neuron hidden layer.

Figure 3 shows the normalized ANN input values as a function of the temperature for the three tests. In Fig. 3(a), there are two noticeable regions of ambiguity, around 22 °C and 28 °C. This is due to the large spectral spacing between the interrogator filters in the three-filter configuration. The regions of ambiguity are decreased in the five-filter configuration, as can be seen in Fig. 3(b), and are practically inexistent in the seven-filter configuration, as shown in Fig. 3(c). The elimination of ambiguity means a great advantage for the performance of the ANN and justifies the results in Table 1.

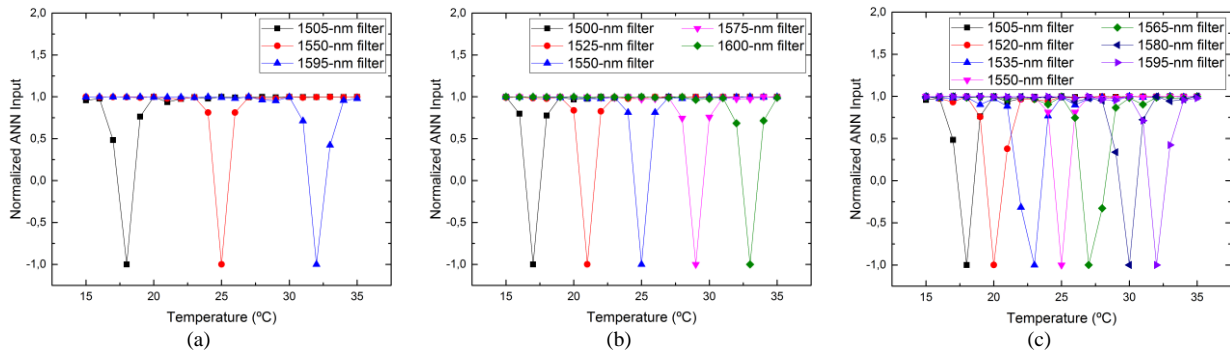


Fig. 3. Normalized ANN input values for the systems with (a) three filters, (b) five filters and (c) seven filters.

#### 4. Conclusion

In this work, our objective was to present an interrogation setup capable of effectively interrogating the whole dynamic range of an LPG temperature sensor excited by an SLD light source. We showed that, using the system presented here, it is possible to adjust the range and the accuracy of the interrogation by setting the number of filters and the spectral spacing between them. We note that the equipment used to build the system is composed of basic fiber optics equipment, such as couplers, FBGs and photodetectors. This allows for a cost-effective system that can be replicated at any optics laboratory. We tested the system using three, five and seven filters to separate the sensor signal in sub-bands using several sizes of the hidden layer of the ANN, from 1 to 15 neurons in the hidden layer, and found that the best accuracy occurs when we use the seven-filter system using a hidden layer composed of 6 neurons. This technique is especially useful in the field, where the use of an OSA is not viable, or in laboratories where an OSA is not available.

#### 5. References

- [1] Ginu Rajan (Ed.), *Optical Fiber Sensors: Advanced Techniques and Applications*, CRC Press, 2015.
- [2] Qin Chen et al., "Investigation of tuning characteristics of electrically tunable long-period gratings with a precise four-Layer model," *Journal of Lightwave Technology* **24**, 2954-2962 (2006).
- [3] Vikram Bhatia; Ashish M. Vengsarkar, "Optical fiber long-period grating sensors," *Optics Letters* **21**, 692-694 (1996).
- [4] P. Biswas et al., "Sensitivity Enhancement of Turn-Around-Point Long Period Gratings By Tuning Initial Coupling Condition," *IEEE Sensors Journal* **15**, 1240-1245 (2015).
- [5] Stephen W. James; Ralph P. Tatam, "Optical fibre long-period grating sensors: characteristics and application," in *Measurement Science and Technology* **14**, R49-R61 (2003).
- [6] T. V. N. Coelho et al., "A numerical and experimental study of the remote long-period grating fiber sensor with Raman Amplification," in *2015 SBMO/IEEE MTT-S International Microwave and Optoelectronics Conference (IMOC 2015)*, Porto de Galinhas, 2015.
- [7] D. Viegas et al., "Long-Period Grating Fiber Sensor With In Situ Optical Source for Remote Sensing," *IEEE Photonics Technology Letters* **22**, 1533-1535 (2010).
- [8] E. Lewis et al., "Principal component analysis and artificial neural network based approach to analysing optical fibre sensors signals," *Sensors and Actuators A: Physical* **136**, p. 23-38 (2007).
- [9] M. Jiang et al., "CFRP damage identification system by using FBG sensor and RBF neural network," in *2015 IEEE 10th Conference on Industrial Electronics and Applications (ICIEA)*, p. 1487-1490, Auckland, 2015.
- [10] L. Negri et al., "FBG refractometry and electrical impedance analysis in fuel samples characterization," in *2011 SBMO/IEEE MTT-S International Microwave and Optoelectronics Conference (IMOC 2011)*, p. 867-871, Natal, 2011.
- [11] G. C. Kahandawa, J. Epaarachchi, K. T. Lau and J. Canning, "Estimation of strain of distorted FBG sensor spectra using a fixed FBG filter circuit and an artificial neural network," in *2013 IEEE Eighth International Conference on Intelligent Sensors, Sensor Networks and Information Processing*, p. 89-94, Melbourne, 2013.
- [12] Marco Aurélio Jucá and Alexandre Bessa dos Santos, "Fiber Bragg grating interrogation using FBG filters and artificial neural network," in *2017 SBMO/IEEE MTT-S International Microwave and Optoelectronics Conference (IMOC 2017)*, Águas de Lindoia, 2017.

# Adaptive Data Compression Method for Distributed Temperature Sensors

**Luís C. B. Silva<sup>\*</sup>, Jorge L. A. Samatelo, Marcelo E. V. Segatto and Maria J. Pontes**

*Telecommunications Laboratory (LabTel), Electrical Engineering Department, Federal University of Espírito Santo, Vitória-Espírito Santo 29075-910, Brazil.*

*<sup>\*</sup>E-mail: bluisicero@yahoo.com*

**Abstract:** This paper presents a new method of adaptive data compression for DTS systems that preserve the curve profile, spatial resolution and temperature accuracy of the sensor. The approach allows compressing the data at a compression ratio of 2.65x, saving 62.3% of the hard disk memory, and reducing the processing time of the generated data.

## 1. Introduction

Distributed Temperature Sensors (DTS) have been widely used in the borehole monitoring (geothermal, oil and gas), transmission lines and power generation, fire detection in tunnels, process plant, cryogenic measurements, leak detection in pipelines, cement and dykes, environment and climate studies, liquid-level measurement and other applications [1]. Such sensors measure the temperature in a distributed form along a fiber optic cable considering a given spatial resolution. Its principle of working consists of generates the spontaneous Raman scattering signal into the core of the fiber, which has a strong dependence on the temperature. By performing the processing of this signal, it is possible to raise the temperature profile along the entire length of the fiber [2].

Commercial DTS can, for example, provide temperature measurements with 0.05 °C resolution, 1 m spatial resolution in a range up to 35 km in multiple channels. The system can be also configured to produce both single-ended and double-ended measurements, with a minimum measurement time of 1 s [3,4]. Based on these specifications, the equipment generates a large amount of data to be processed and stored. The size of the file generated throughout the DTS acquisition process can be determined by the following expression:

$$M = n_s \times t_t \times n_b \times n_{ch} . \quad (1)$$

$n_s$  is the number of independently sensed points,  $t_t$  is the number of traces collected during a day,  $n_b$  the number of bytes per sample and  $n_{ch}$  the number of channels. For example, the AP Sensing DTS model generates a file of approximately 0.4 TByte/day [3], while the ULTIMA™ DTS model can generate a file of nearly 1 TByte/day [4]. The size of these files is a problem in terms of processing in some applications, such as those which by regulation, require the generated data to be stored for a long period of time, or situations which demand rapid data processing, i.e. real time.

Alternatives to solve limitations such as processing time, storage space and power saving can be found in the literature. For example, in [5] a hybrid data compression scheme for power reduction in wireless sensors for Internet-of-Things (IoT) was proposed. In this study, the method is applied to electrocardiogram signals, in which the data is first compressed using a lossy compression technique with a high compression ratio (CR). The residual error between the original data and the decompressed data is preserved using entropy coding, enabling a lossless restoration of the original data when required. To perform lossy compression Fan Algorithm is used. This operates by drawing the longest possible straight line between the starting sample and the ending sample.

While Ke et al. [6] proposed a compression algorithm composed of three steps including pre-compression, lossy compression and lossless compression for weather radar. Based on the users' requirement and in redundant information, the algorithm mentioned in [6] can achieve a compression ratio of 18x (eighteen times), even under complicated weather conditions in which data cannot be discarded.

In previous work we have proposed a method that performs an extraction of characteristics of the temperature profile generated by the DTS before the data processing [7]. Such an approach significantly reduces the datafile size to be further processed. However, the temperature curve profile is lost during the feature extraction. In applications such as leak detection and flow assurance in pipelines, the full profile of the temperature curve is not essential since the interest is in the detection of hot spots along the monitored region.

However, in the detection of fires in tunnels, the knowledge of the complete profile of the temperature curve is fundamental to indicate not only the location of the fire but also the direction of the flames [1].

This work proposes for the first time, to the best of the author's knowledge, a method of data compression to be applied directly under the temperature profile generated by the DTS equipment so that its format is not altered, besides preserving both the spatial resolution and the temperature accuracy of the sensor. This paper is organized as follows. In Section 2, the proposed compression model is detailed. Next, the evaluation of the compressed signal is discussed in Section 3. And the conclusions are given in Section 4.

## 2. Adaptive Compression Model for DTS

The proposed compression method consists of determining the minimum number of points needed to represent the temperature profile generated by the DTS without losing spatial resolution and temperature accuracy and preserving the original curve format. For this, the derivative of the temperature at each position  $z_i$  of the fiber is calculated. At specific points where the derivative module takes values below a threshold  $\varepsilon$ , the signal is suppressed. Mathematically:

$$\left| \frac{dT_i}{dz_i} \right| < \varepsilon \Rightarrow T_i = \emptyset. \quad (2)$$

The compression process begins with the signal with all points and continues discarding points that satisfy equation 2 according to the update of threshold  $\varepsilon$  until the stopping criterion is reached. The stopping criterion will be given when  $\varepsilon$  assumes a value in which the conditions  $\delta z_{cp} = \delta z_{og}$  and  $T_{abs} = std(\Delta T_i) \leq 0.06$  become true. The updating of the threshold  $\varepsilon$  is accomplished by decreasing 0.005% of its initial value to each interaction.  $\delta z_{cp}$  and  $\delta z_{og}$  are the spatial resolutions of the compressed and original signal, respectively.  $T_{abs}$  is the absolute accuracy (uncertainty) taken as the standard deviation (denoted by  $std$ ) of the difference  $\Delta T_i$  between the temperature values of the original signal  $T_{og}$  and the temperature values of the compressed signal  $T_{cp}$  over measurements  $i$ . We also require that the compressed signal preserve the maximum and minimum values of the original signal. These two conditions complete the requirements during the compression process. Since  $\delta z$  is related to the measure of the heated region in the fiber, to preserve its value during the compression process, we calculate the value of the full width at half maximum (FWHM) of  $T(z)$  along the fiber, so that  $\delta z = z_1 - z_2$ , as shown in Fig. 1:

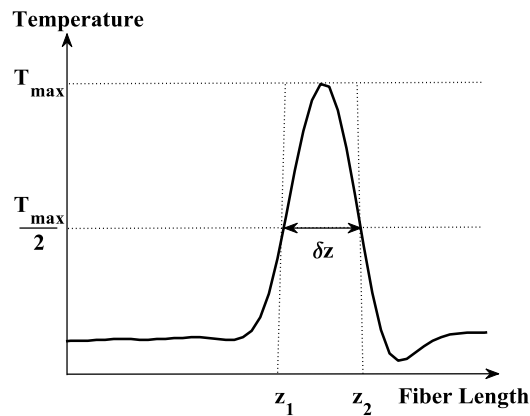


Fig. 1. Definition of the spatial resolution by FWHM.

Similarly, this same procedure applies to profiles with negative temperature variations. In this way, the result obtained at the end of this process is a compressed signal composed of dense regions in points, corresponding those with the highest degree of information; and regions with fewer points, which are not relevant information to be preserved.

### 3. Performance Evaluation

To evaluate the performance of the algorithm described in Section 2, we used real data from a commercial DTS, model AP Sensing N4385B composed of temperature profiles obtained by reading the equipment of hot spots along the fiber. More details about the data used can be found in [7]. The criteria to evaluate the performance of the proposed algorithm were the Root Mean Square Error (RMSE) and the Compression Ratio (CR = original data size/compressed data size). Figure 2 shows the temperature profile of the DTS before and after the compression. It is observed that for a CR = 2.66x the shape of the temperature profile is maintained, fact that is justified by the RMSE of 0.053. In Fig.3 we plot the signals before and after the compression together, which allows us to observe how close the compressed signal is to the original.

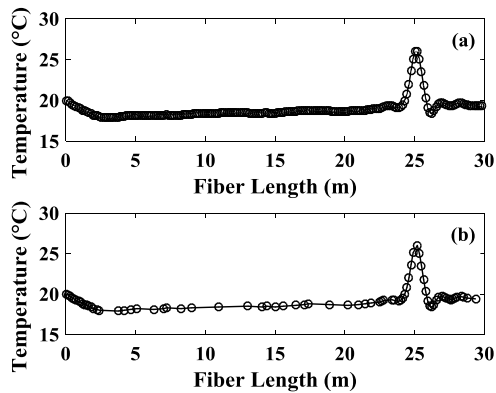


Fig. 2. In (a) Original signal and (b) compressed signal.  $\epsilon = 0.6$ .

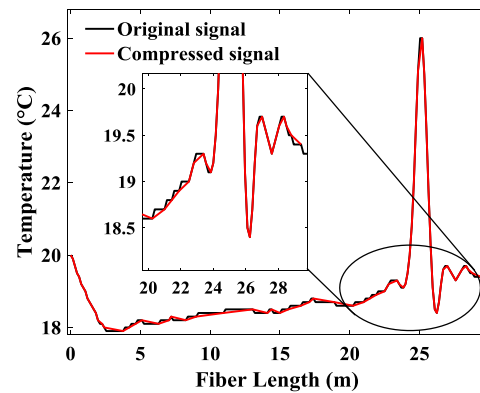


Fig. 3. Temperature profile of compressed versus original signal.

Figure 4 shows the derivative of the temperature (from the curve of Fig. 2a) as a function of the position in the fiber. In this curve, it is observed that in the regions of the fiber whose derivative module is close to zero there is no relevant information i.e. temperature is practically constant (see, for example, Fig. 4 and Fig. 2a), it means that the signal at these points is discarded. However, in regions whose derivative has a larger module, the signal is preserved integrally.

If there was no update of the value of  $\epsilon$ , it would be impossible to determine the minimum number of points to be kept in order to preserve the shape of the curve and to satisfy the four requirements that the compressed signal must meet. Because in this situation, the value of  $\epsilon$  could be poorly determined, and consequently a change in the value of  $\epsilon = 0.1$  in relation to its best value already introduces an error in position determination of the hot spot shown in Fig. 2 of 4.7 cm and an error of the 0.5 °C in reading the temperature in that region. In Fig.5, it is observed that with each update of  $\epsilon$ , the CR value tends to be reduced until there is a minimum number of points to accurately represent the DTS signal. When this occurs the maximum CR is obtained.

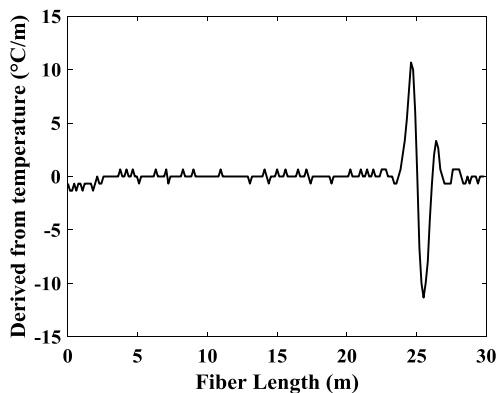


Fig. 4. Derivative from the temperature profile.

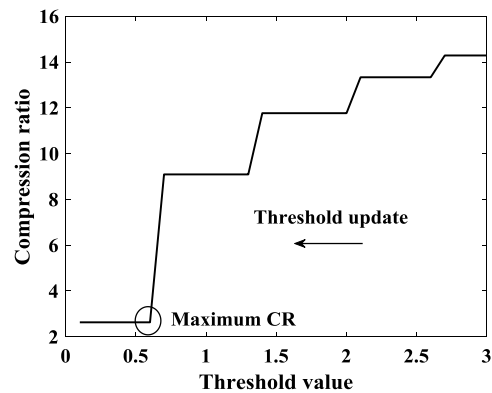


Fig. 5. Updating the value of  $\epsilon$ .

So far we have analyzed the proposed algorithm for a low noise (well behaved) temperature profile. Now we will take the worst case, corresponding to a rather noisy signal and a greater range of the sensor. Although in such a situation the temperature alternates rapidly over the fiber, a CR of 1.68x and RMSE of 0.065 as shown in Fig.6 was obtained. It is noteworthy that even for the CR and RMSE values found for the worst case, the shape of the curve is completely conserved, as well as spatial resolution and temperature accuracy. Making possible a correct reading of the temperature, especially in the region where there is a hot spot.

Moreover, regardless of the noise level in the sensor signal, a higher CR is obtained in regions where the temperature value is more stable. This is justified by the fact that the threshold value  $\epsilon$  is below the noise level. Consequently, the worst case will be the one in which the signal represents abrupt variations in the temperature in a small region in the fiber (hot spots of narrow width) that was the situation of the temperature profiles evaluated in this study.

Finally, Fig.7 shows the CR and RMSE respectively of 44 compressed temperature profiles that were generated by the DTS equipment. Figure 7 shows the repeatability of the algorithm when applied to different temperature profiles. In addition, by dynamically compressing the signal along the fiber, regions with low CR have lower RMSE, preserving almost completely the region of interest in the fiber, corresponding to a hot spot.

In Fig. 7a the CR value is given for each compressed temperature profile and in Fig. 7b its respective RMSE.

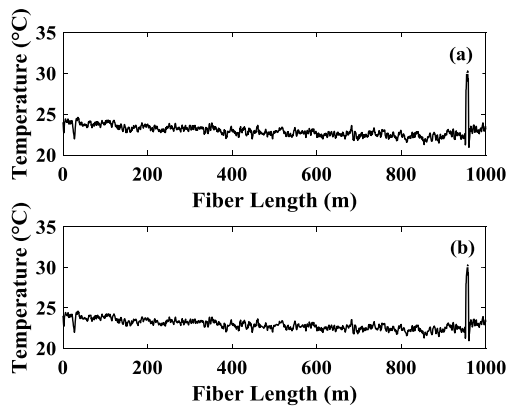


Fig. 6. In (a) Original signal and (b) compressed signal.  $\epsilon = 0.15$ .

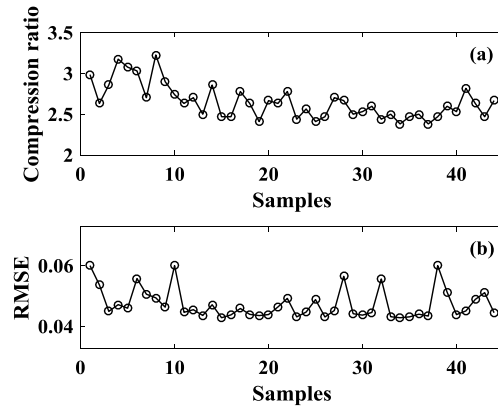


Fig. 7. General performance analysis of the data compression algorithm.

#### 4. Conclusions

This work presents for the first time an adaptive loss data compression method for temperature profiles generated by Distributed Temperature Sensors. The proposed compression model consists of removing regions of the signal whose temperature value is practically constant while preserving others otherwise. The algorithm allows determining the minimum number of points required to represent the sensor signal without loss of spatial resolution or temperature resolution, thus preserving its original format.

The threshold update is one of the innovations that our algorithm exhibits in terms of data compression. Since it generates the compression rate to be adaptive/variable according to the degree of information contained in the data and the requirements that these after compressed need to present.

A total of 45 different temperature profiles were compressed so that an average compression ratio of 2.65x and an average RMSE of 0.046 were achieved. These results show the robustness of the method that can be applied to any commercial equipment to improve the processing time and to reduce the amount of hard disk space by more than half when there is a need for data storage. For example, as mentioned earlier, a 0.4 TByte/day (value calculated by equation 1) file obtained by AP Sensing DTS model is reduced to 0.15 TByte/day by applying the proposed compression method. Future works include exploring lossless data compression algorithms in order to configure a second step to the proposed algorithm, saving more memory or even power in applications that require wireless transmission of data.

#### References

[1] A. Hartog, An Introduction to Distributed Optical Fibre Sensors. Series in Fiber Optic Sensors. CRC Press: Boca Raton, FL, USA, 2017.

- [2] A. Ukil, H. Braendle, and P. Krippner. Distributed Temperature Sensing: Review of Technology and Applications. *Sensors Journal*, vol. 12, no. 5, pp. 885–892, 2012.
- [3] AP-Sensing®. DTS-Distributed Temperature Sensing. Online. Available: <https://www.apsensing.com/technology/distributed-temperature-sensing-dts/>.(visited on 05/06/2019).
- [4] Silixa®. ULTIMA™ DTS-distributed temperature sensor. Online. Available: <https://silixa.com/products/ultima-dts/>.(visited on 01/28/2019).
- [5] C. J. Deepu, C.-H. Heng, and Y. Lian. A Hybrid Data Compression Scheme for Power Reduction in Wireless Sensors for IoT. *IEEE Transactions on Biomedical Circuits and Systems*, vol. 11, no. 2, pp. 245–254, 2017.
- [6] K. Ma, C. Li, and H. Li. A new hybrid data compression algorithm for weather radar. in *11th International Symposium on Antennas, Propagation and EM Theory (ISAPE)*, 2016, pp. 886–889.
- [7] L. C. B. Silva, J. L. A. Samatelo, M. E. V. Segatto, J. P. Bazzo, J. C. C. Silva, C. Martelli, and M. J. Pontes. Narx neural network model for strong resolution improvement in distributed temperature sensor. *Applied Optics*, vol. 57, no. 21, pp. 1–6, 2018.

# Study on the best reflection spectra of FBGs for dynamic sensing

Talitha Trovão<sup>1</sup>, Alex Dante<sup>1</sup>, Juan David Lopez<sup>2</sup>, Cesar Cosenza Carvalho<sup>1</sup>, Regina Celia da Silva Barros Allil<sup>1</sup>, and Marcelo M. Werneck<sup>1,2</sup>

<sup>1</sup>Photonics and Instrumentation Laboratory, Electric Engineering Program, Federal University of Rio de Janeiro (UFRJ), RJ 21941-594, Brazil

<sup>2</sup>Photonics and Instrumentation Laboratory, Nanotechnology Engineering Program, Federal University of Rio de Janeiro, RJ 21941-594, Brazil

**Abstract:** This paper presents a study of FBG reflection spectrum for application in dynamic measurements, such as AC current and voltage. In this work, we show the best reflection spectra of two FBGs employed in a twin-grating interrogation technique that guarantees the best linearity levels possible in the response of the dynamic measurement sensor. © 2019 The Author(s) OCIS codes: 060.3735, 060.2370.

## 1. Introduction

Since its discovery by K. O. Hill et al. in 1978 [1], fiber Bragg gratings (FBG) have been applied as optical sensors to the measurement of several physical variables thanks to their intrinsic sensitivity to mechanical strain and temperature. Some advantages of FBG sensors are immunity to electromagnetic interference, high electrical isolation, no cable-induced noise, and small size. The possibility of multiplexing several sensors in a single optical cable, and the capability of monitoring sensors over long distances are also key features of FBGs, which make them suitable sensors for oil & gas, chemical, aerospace, biomedical, and energy industries [2][3].

Given that the sensitivity of FBGs to strain and temperature is encoded in a characteristic narrowband reflected spectrum of the incident light, the interrogation of these sensors is usually accomplished by either determining the spectral position of the reflected peak in the light frequency domain (first approach), or measuring the intensity of the reflected light modulated by a spectral filter (second approach). Most of the interrogation techniques employing the first approach rely on optical spectral decomposition using fast-scanning tunable laser technology to recover the full spectrum reflected by the sensing FBG [2][4]. These techniques are frequently employed in optical spectrum analyzers (OSAs) as well as in commercial interrogators specifically designed for FBG sensors. These instruments allow for accurate measurements related to FBG sensors, though they are usually very expensive and have limitations when dynamic measurements are needed. For instance, measurements of fast dynamic physical variables with FBG sensors, such as vibration or AC (50–60 Hz) voltage and current, cannot be performed using an OSA. Instead, this task should be performed with high-speed-scanning interrogators that rely on special algorithms to recover the reflected spectra from the FBG sensors in order to track their spectral peak position [5][6]. However, these instruments are still not capable to decouple the cross-sensitivity to strain and temperature intrinsic to FBG sensors. These limitations can be avoided by employing the second approach, in which FBG interrogators are based on the measurement of the optical power reflected by the FBG. These interrogators are usually composed by a photodetector and some passive spectral filter that modulate the reflected optical power of the FBG. This approach is also preferred to achieve cost-effective sensing solutions.

One particular interrogation technique that employs the second approach is the so-called “twin-grating technique”, in which the optical power reflected by a sensing FBG is modulated by a second FBG acting as an edge filter, both FBGs having close Bragg wavelengths ( $\lambda_{\text{Bragg}}$ ). This technique presents some advantages, such as high resolution, especially for FBG sensors applied to AC measurements [7]. However, one limitation of this technique is that the nonlinearities present in the filter FBG spectrum contribute to measurement errors in the output signal of the interrogation system.

In this work, we performed a study of several reflection spectra of FBGs on a LabVIEW™ simulation tool aiming at to identify the best type of FBG spectrum that guarantee the lowest distortion level in the output of a twin-grating interrogation system. We have also manufactured FBG sensors in laboratory in order to perform this study.

## 2. Theoretical Background

### 2.1 Fiber Bragg Grating

An FBG consists of a periodic modulation of the effective refractive index of the fiber core generated by radiation with an appropriate ultraviolet light pattern. When a light beam of a given spectral width propagates through the fiber and reaches the FBG, a very narrow spectral band (centered at the Bragg wavelength,  $\lambda_{\text{Bragg}}$ ) is reflected, while the

other components pass through it without modification. The variation produced in the fiber refractive index, the modulation period and the length of the grating are determining factors for the transmission and reflection properties of each sensor. Mathematically, the  $\lambda_{Bragg}$  is given by Eq. 1 [4]:

$$\lambda_{Bragg} = 2n_{eff}\Lambda \quad (1)$$

Where  $n_{eff}$  is the effective refractive index of the fiber core and  $\Lambda$  is the periodicity of the refractive index change.

Since the creation of the first FBGs, researchers have noticed that their spectra, even during inscription, were sensitive to variations in temperature and strain. In fact, there is a direct relation between  $n$  and the periodicity of the change of refractive index  $\Lambda$  with the variations of temperature and strain, according to Eq. 2:

$$\Delta\lambda/\lambda_{Bragg} = (1 - \rho_e)\varepsilon + (\alpha + \eta)\Delta T \quad (2)$$

Where  $\rho_e$  is the photo-elastic coefficient of the fiber,  $\alpha$  is the coefficient of thermal expansion and  $\eta$  is the thermo-optical coefficient.

## 2.2 Twin-Grating Interrogation Technique for AC Signals

Fig. 1(a) shows a schematic setup diagram of the twin-grating interrogation technique. In this technique, light from a broadband light source (BLS) is guided to a sensing FBG, whose reflection spectrum reaches a filter FBG through an optical circulator. Since both FBGs are optical bandpass filters, the reflected light from the filter FBG is the convolution between both spectra, which is guided to an acquisition system. Any change in the optical power of convolution denotes a relative shift of the Bragg wavelengths of the FBGs. If the sensing FBG is under dynamic strain signals, such as in vibration or AC voltage and current applications, the filter FBG usually tracks the sensing FBG over wavelength shifts in order to compensate for optical power changes due exclusively to temperature [7][8][9][10]. Thus, the optical power signal received by the acquisition system in Fig. 1(a) contains both AC and DC components. The AC signal is directly affected by the nonlinearities present in the transfer function of edge filter implemented by the filter FBG.

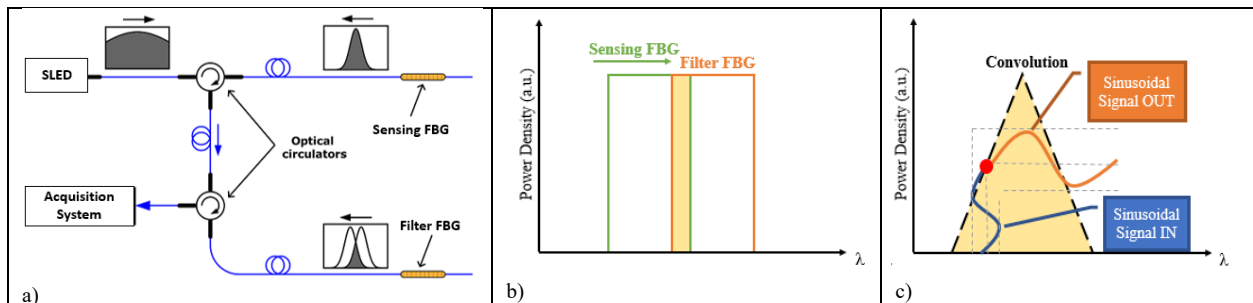


Fig. 1. (a) Schematic diagram of a classic twin-grating interrogation technique experimental setup; (b) Theoretical case of convolution between ideal FBGs; (c) Representation of convolution shape between two ideal FBGs and how does it influence an input sinusoidal signal (Adapted from [7]).

Fig. 1(b) shows a condition/situation in which two hypothetical rectangular-shaped, wavelength-matched FBGs convolute in the frequency domain in a twin-grating interrogation system. In that situation, the sensing FBG is under AC wavelength shift and the filter FBG is fixed on/at a given wavelength. Fig. 1(c) shows schematically the full convolution spectrum originated by the twin FBGs spectra. It can also be seen in Fig 1(c) that, in that hypothetical condition, the interrogation system outputs a perfectly linear signal relative to the input, with sensitivity given by the slope of the convolution function at the operation point (red dot). In real world, however, FBGs do not have such rectangular-shape reflection spectra, and an actual twin-grating interrogation system is in fact a nonlinear system. Thus, the output signal seen in Fig. 1(c) using actual/real FBGs would contain nonlinearities inherent to the spectrum of the filter FBG.

### 3. Experiments

#### 3.1 FBG Fabrication

The experimental setup used to manufacture the FBG sensors is shown schematically in Fig. 2 and consists of a Nd:YAG pulsed laser with two frequency modulators  $2\omega$  and  $4\omega$  (1), a phase mask for 1535 nm (2), a germanium-doped fiber coil (3), an optical circulator, a broadband light source (ASE) (5) and an optical spectrum analyzer (OSA) (6) with a computer software to read the spectrum (7). After the inscription of the FBG in the fiber optic core, we used an Optical Sensing Interrogator (OSI) to extract its reflection spectrum.

For a statistical study, we have manufactured a group of ten FBGs under the same conditions (temperature, UV energy, longitudinal stretch, time of exposition). Each pair of FBGs chosen for the simulation study in this work is statistically different.

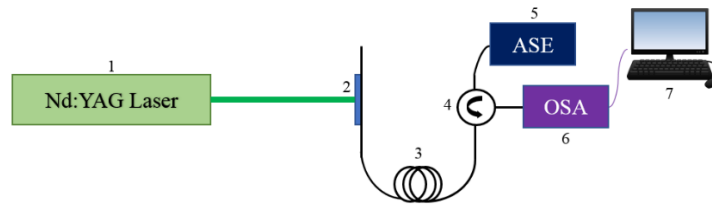


Fig. 2. Experimental setup for FBG fabrication in laboratory.

#### 3.2 Emulation of a Twin-Grating Interrogation System Using LabVIEW

For the analysis of the output response of a twin-grating interrogation system using several pairs of FBGs manufactured in laboratory, we developed a simulation tool in LabVIEW, which control panel is shown in Fig. 3. In the developed software, the discrete-signal spectra of two wavelength-matched FBGs acquired previously in the OSI are read and mathematically convoluted. A subroutine is responsible for emulate a sinusoidal wavelength shift in one of the FBGs (sensing FBG), which simulates a sinusoidal strain signal applied to the sensing FBG, keeping the other (filter FBG) static. The result of this simulation is an AC signal that has AC and DC levels, as expected (“convolution signal output” graph in the control panel of Fig. 3) with acquisition rate of 60Hz. The Fast Fourier Transform of this signal is shown in FFT graph.

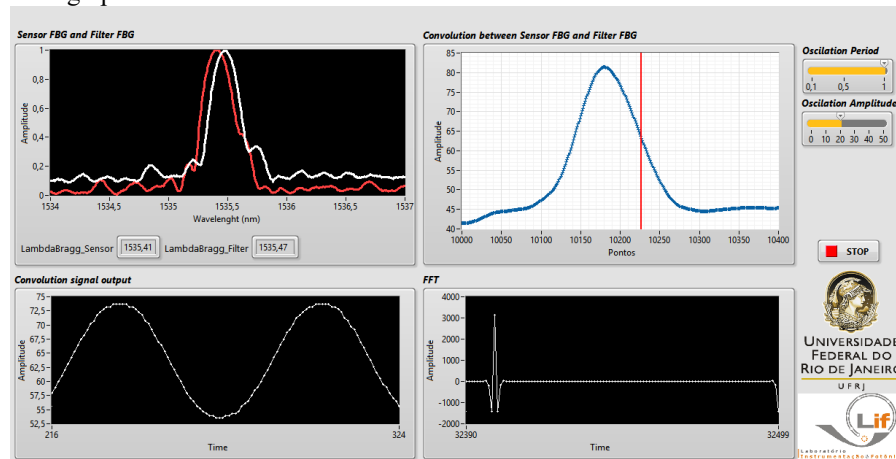


Fig. 3. LabVIEW interface developed.

The developed software allows the user to change the frequency and amplitude of oscillation of the sensing FBG, as well as its spectral position relative to the filter FBG. It is worth to mention that the relative spectral position between both FBG peaks determines the operation point of the interrogation system, which is represented by the vertical red line in the convolution plot of Fig. 3. The red line indicates the point on the convolution plot at which the input sinusoidal signal will be modulated. Thus, the linearity of the output signal will depend on the linearity of the region centered at the red line in the convolution plot. These are important features of the developed software, since the distortion level in the output signal is directly related to these key parameters.

## 4. Results and Discussion

Fig. 4 shows a comparison between the results from the LabVIEW simulation tool for two pairs of twin FBGs manufactured in our laboratory. The pairs are distinguished by the UV energy used in fabrication. Fig. 4 shows: (a) the reflection spectra, (b) the convolution plot, (c) the output AC signal, and (d) discrete Fourier transform (DFT) for the first pair of twin FBGs. The same analysis can be seen in Figs. 4(e)-(h) for the second pair of twin FBGs. Both output signals were acquired using the same parameters in the LabVIEW simulation tool.

It is clear from the qualitative analysis presented in Fig. 4 that the reflection spectra of the first pair of FBGs is the best choice for an FBG sensor applied to AC measurement, since it presented the lowest harmonic distortion, as shown in Fig. 4 (d) and (h). It can also be seen in the results that the best reflection spectra are those with highest side lobe suppression ratio (SLSR), which is one of the main parameters in the fabrication process of FBGs sensors.

The results shown in Fig. 4 allow us to conclude that the output response that presented the lowest distortion is also related to the pair of FBGs that have the highest cross-correlation coefficient (greater than 0,9), which means that the repeatability of the spectra of the FBGs produced in our laboratory is of utmost importance to a twin-grating interrogation system.

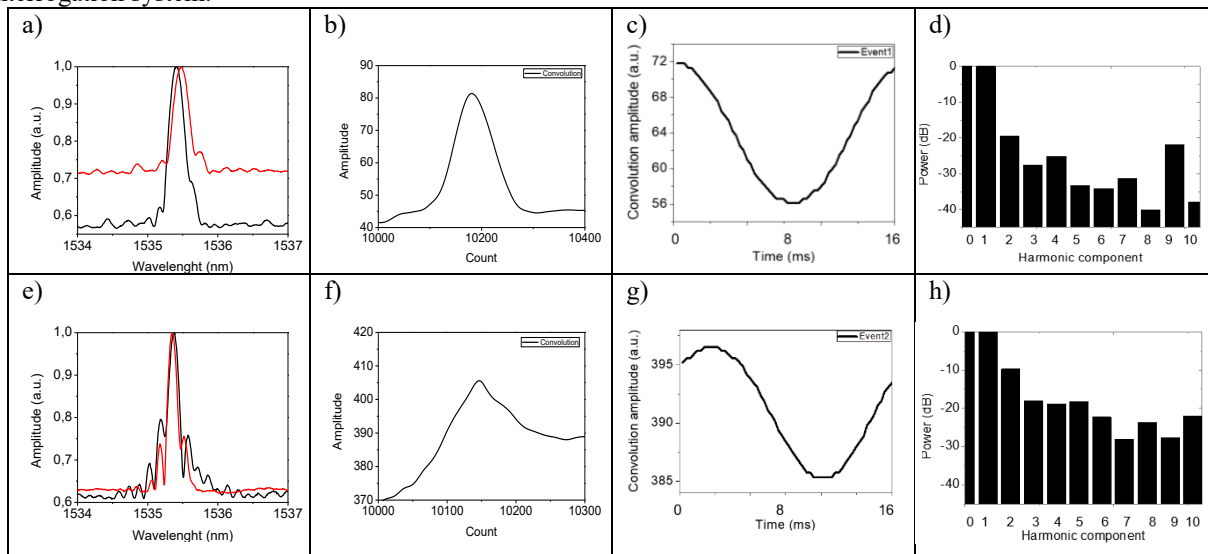


Fig. 4. Reflection spectra of manufactured FBGs, with response under sinusoidal input signal, and spectral responses in function of best tracking point.

The results obtained in this work are helping our research group to optimize critical parameters of the fabrication process of FBGs in laboratory, especially for application in twin-grating interrogation systems. Further experiments are being performed with an actual high-voltage sensor based on FBG that is being interrogated by a twin-grating optoelectronic system.

Future work will include a systematic optimization of our laboratory FBG fabrication process taking into account other parameters, such as exposition time of the optical fiber to UV radiation, energy of UV beam, with the implementation of apodization techniques.

## 5. References

- [1] K. O. Hill, Y. Fujii, D. C. Johnson, and B. S. Kawasaki, "Photosensitivity in optical fiber waveguides: Application to reflection filter fabrication," *Appl. Phys. Lett.*, vol. 32, no. 10, pp. 647–649, 1978.
- [2] C. E. Campanella, A. Cuccovillo, C. Campanella, A. Yurt, and V. M. N. Passaro, "Fibre Bragg Grating based strain sensors: Review of technology and applications," *Sensors (Switzerland)*, vol. 18, no. 9, 2018.
- [3] M. M. Werneck, R. C. Allil, and F. V. B. de Nazaré, *Fiber Bragg Gratings: Theory, Fabrication, and Applications*, 1st ed., no. March. Bellingham, WA: SPIE PRESS, 2017.
- [4] R. Kashyap, *Fiber Bragg Gratings*, 2nd ed. Burlington, MA: Academic Press, 2010.
- [5] J. Cui, Y. Hu, K. Feng, J. Li, and J. Tan, "FBG interrogation method with high resolution and response speed based on a reflective-matched FBG scheme," *Sensors (Switzerland)*, vol. 15, no. 7, pp. 16516–16535, 2015.

- [6] C. A. R. Díaz, C. Leitão, C. A. Marques, M. F. Domingues, N. Alberto, M. J. Pontes, A. Frizera, M. R. N. Ribeiro, P. S. B. André, and P. F. C. Antunes, "Low-cost interrogation technique for dynamic measurements with FBG-based devices," *Sensors (Switzerland)*, vol. 17, no. 10, pp. 1–10, 2017.
- [7] A. Dante, R. M. Bacurau, A. W. Spengler, E. C. Ferreira, and J. A. S. Dias, "A Temperature-Independent Interrogation Technique for FBG Sensors Using Monolithic Multilayer Piezoelectric Actuators," *IEEE Trans. Instrum. Meas.*, vol. 65, no. 11, pp. 2476–2484, 2016.
- [8] B. De Assumpção Ribeiro, M. M. Werneck, and J. L. Da Silva-Neto, "Novel optimization algorithm to demodulate a PZT-FBG sensor in AC high voltage measurements," *IEEE Sens. J.*, vol. 13, no. 4, pp. 1259–1264, 2013.
- [9] G. Fusiek and P. Niewczas, "Laboratory investigation of an intensimetric dual FBG-based hybrid voltage sensor," in *24th International Conference on Optical Fibre Sensors*, 2015, vol. 9634, pp. H1–H4.
- [10] L. A. Garção, F. V. B. De Nazaré, R. C. Allil, R. Mok, P. Silveira, A. Dante, C. Carvalho, M. Keley, and M. M. Werneck, "Temperature compensation method for FBG-based current sensors for transmission lines," *I2MTC 2018 - 2018 IEEE Int. Instrum. Meas. Technol. Conf. Discov. New Horizons Instrum. Meas. Proc.*, pp. 1–6, 2018.

# LPG Spectrum Estimation Using Neural Networks and Temperature Modulated FBG

Felipe Oliveira Barino, Alexandre Bessa dos Santos

Departamento de Engenharia Elétrica, Universidade Federal de Juiz de Fora.  
 Rua José Lourenço Kelmer, s/n, São Pedro, 36036-900, Juiz de Fora, Minas Gerais, Brazil.  
 felipe.barino@engenharia.ufff.br, alexandre.bessa@engenharia.ufff.br

**Abstract:** This work proposes a novel approach to Long Period Fiber Grating (LPFG) interrogation involving power measurements to estimate the transmission spectra. The aim of this work is to develop a cheap alternative to the Optical Spectrum Analyzer. To accomplish this task a temperature modulated Fiber Bragg Gratings array was used. Accuracy close to half input spectrum resolution was obtained.

## 1. Introduction

Advances in instrumentation field have helped develop optical sensors technology due to optical components offer increase at a good cost benefit and a vast option of suppliers [1]. The so called Bragg Gratings (FBGs) and Long Period Fiber Gratings (LPFGs) are two important structures in optical sensing. Both are in fiber devices based on periodic modulation of fiber's refractive index.

The LPFGs are easier to build structures in comparison to FBGs, once its modulation period is considerably bigger. This devices can be treated as sensor once they are notch filters whose central wavelength, denoted by  $\lambda_{res}^m$ , varies accordingly to the environment, such as effective refractive index of the core  $n_{eff,co}$ , cladding  $n_{eff,cl}$  and grating period  $\Lambda$  [2,3]. The relationship between those parameters is:

$$\lambda_{res}^m = (n_{eff,co} - n_{eff,cl}^m)\Lambda \tag{1}$$

This way one is able to correlate the actual measurement to LPFG's transmission spectra. This process is called interrogation and there is a great amount of techniques reported in literature, some require big and expensive equipment. One approach is to apply a broadband light source to the optical sensor and trace the spectrum variation using an Optical Spectrum Analyzer (OSA), another technique uses Tunable-lasers [4,5]. A cheap and compact solution is to use band-pass filters and photodetectors and track power variation [6-8].

Here we propose a mixed technique, in which, based on power measurements provided by an FBG array, LPFG's transmission spectra is estimated. To accomplish this task 5 temperature modulated FBGs and 5 photo-detectors are used to send their readings to a computer.

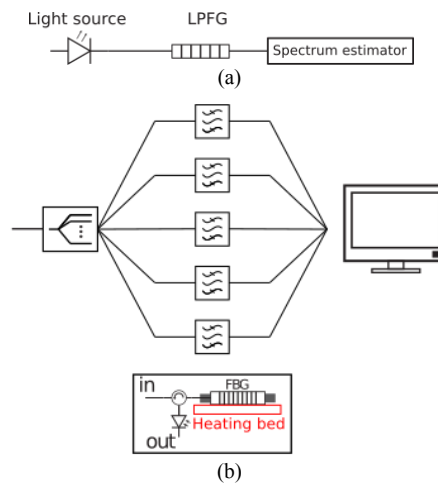


Fig. 1. (a) Experimental setup. (b) Spectrum estimator scheme.

## 2. Methods

The experimental setup proposed in this work consists of a broadband light source, the LPFG sensor and the spectrum estimator, as illustrated in Fig. 1a. The spectrum estimator itself is shown in Fig. 1b and it's made by a set of five filters and a PC. Each filter block has a FBG, a controlled heating bed to perform the temperature modulation, an optical circulator and a photodetector.

Simulation of the proposed interrogation method was made to validate the quality of spectrum estimation, all of those five FBGs were simulated on OptiGrating at the central wavelengths: 1500nm, 1520nm, 1535nm, 1550nm and 1570nm. Each FBG were characterized by varying temperature in grating from 15°C to 125°C. A linear regression between temperature variation (where reference temperature considered was  $T_{ref} = 25^\circ\text{C}$ ) and central wavelength displacement on each FBG was performed to obtain the gratings sensitivities. Those regression plots can be seen in Fig. 2.

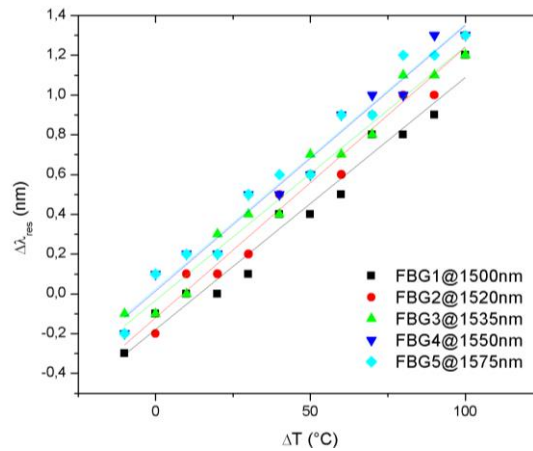


Fig. 2. Linear regression between temperature variation and central wavelength displacement on each FBG.

Optical power at measured by the photodetector is calculated by numerical integration on the reflected spectrum of FBG. Let  $R(\lambda)$  be the FBG refraction spectrum (after filtering the LPFG's spectrum) and  $\Delta\lambda_{OSA}$  the OSA resolution:

$$P_{photodetector} \approx \frac{1}{\Delta\lambda_{OSA}} \int R(\lambda) d\lambda \quad (2)$$

This calculation is performed for each filter that composes the array 11 times, since the FBG array is modulated with temperatures from 25°C to 100°C in eleven evenly spaced rounds. Therefore, a total of 55 power measurements are made, and those values are used as input to a Neural Network. The output of this network is the LPFG transmission spectra, and the reference data used to train and test the estimator is given by 24 transmission spectra of four different LPFGs, obtained previously by an OSA Anritsu MS9740A.

Those reference data were filtered using mean-average filter to smooth the curve and to simplify the neural network architecture all of the 24 filtered spectra were down-sampled to 133 points at the same wavelength, so that the spectrum can be treated as a vector. Those 133 points corresponds to 1500nm to 1580nm evenly spaced samples, therefore, resulting resolution is 600pm. Finally, the dataset were split into groups: train (70%), test (15%) and validation (15%).

The Artificial Neural Network (ANN) used in this work has a single hidden layer and sigmoid activation function. An ANN is a computation model inspired by animal's nervous system. This model is made by a set of units called artificial neurons, connected between each other, and it is capable of mapping input-output based on a set of examples learned at training phase [9].

An artificial neuron makes a linear combination of its input ( $x_i$ ) by weights tuned during training ( $w_i$ ), summed with a given bias ( $b$ ) and passes this value to an activation function ( $\Phi$ ), as illustrated in Fig. 3a. Those neurons are

layered in a net structure, the first layer is called input layer, the last output layer and all layers between those are called hidden layers, Fig. 3b shows a three input network with two hidden layers (four neurons each) and single

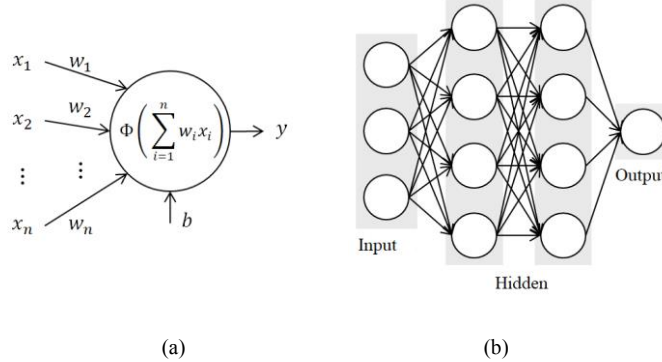


Fig. 3. (a) Artificial neuron. (b) 3x4x4x1 neural network (bias were omitted).

output.

To train the network used in this work, Bayesian Regularization Backpropagation algorithm was used. This method was chosen because regularization algorithms aims not only to minimize the neural network error, but also the weights, so that the network is smoother and has a better generalization [10], being great for small datasets.

### 3. Results

In order to find the best hidden layer size, several ANNs were developed, trained and the resulting data analyzed. Ten tests were made for each topology, to minimize random initial weights impact. Those ANNs had from 4 to 32 neurons in its hidden layer. To determine the most efficient hidden layer size, comparison based on Mean Squared Error (MSE) and Coefficient of Determination ( $R^2$ ) on both train and test dataset was made.

The chosen number of neurons is the least one that has acceptable error at train and test stage, to avoid overfitting. In order to improve the ANN generalization, similar performance in both train and test are desirable. Fig. 4 shows the results obtained from this model selection study, note that for a hidden layer size greater than 16 neurons there is no significant improvement in MSE and  $R^2$  from the test set data, indicating that there is no improvement in model's generalization for bigger hidden layers. Therefore the 55x16x133 topology was adopted to perform the spectrum regression.

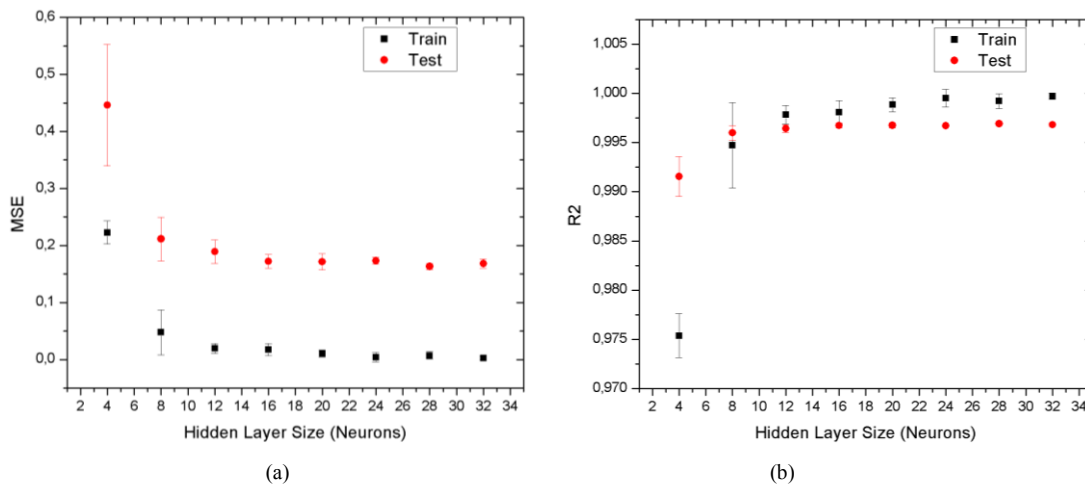


Fig. 4. (a) Relationship between Hidden Layer Size and MSE. (b) Relationship between Hidden Layer Size and  $R^2$ .

The resulting MSE for the final Neural Network chosen is 0.0194 at the train set, close to the mean of tests for 16 neurons on hidden layer obtained at the model selection (0.0174). During training, weights optimization is made to reduce the error (MSE), this error gives an idea of how well the predicted spectrum curve represents the actual LPFG's transmission spectra, since outputs are given by optical power at a fixed set of wavelengths, so MSE

has units of dBm<sup>2</sup>. But to evaluate the spectrum approximation, resonant wavelength displacement ( $\delta\lambda_{res}$ ) was also taken into account. Once MSE evaluates the whole spectrum approximation,  $\delta\lambda_{res}$  evaluates the measure error, since it changes with environment properties variation. Table 1 shows both errors on each subset of the actual dataset.

Table 1. Spectrum estimation errors.

	MSE (dBm <sup>2</sup> )	$\delta\lambda_{res}$ (nm)
Train	0.0194	0.1889
Test	0.8609	0.9114
Validation	1.0444	0.4557

Note that obtained mean resonant wavelength error in train and validation subsets are smaller than input spectrum resolution, while test resonant wavelength is smaller than twice this value. And especially, the whole dataset errors: MSE and  $\delta\lambda_{res}$  are, respectively, 0.3305dB and 354.4pm, being that resonant wavelength error close to half the target spectrum resolution.

#### 4. Conclusion

Although a practical implementation of the proposed method is required to measure the time needed to perform the FBG modulation and its stability, this work shows that one can estimate a long period fiber grating transmission spectra using only five temperature modulated FBGs. This method decrease overall cost in interrogation methods that need whole spectrum evaluation. Future studies on other FBG modulation techniques and the use of fixed FBGs can lead to more practical applications of the proposed interrogation system.

The proposed method also gives the opportunity to not only trace resonant wavelength displacement, but other spectrum based variables like attenuation and rejection band, for example. And accuracy can be improved by increasing reference spectrum resolution and training examples.

#### Acknowledgements

This work was supported by FAPEMIG, CNPq, PROPP-UFJF, Inerge-UFJF, CAPES and CPFL Energia.

#### References

- [1] J. L. Santos and F. Farahi, *Handbook of optical sensors*, 1st ed. (CRC Press, 2014).
- [2] T. Erdogan, "Fiber grating spectra," *Journal of Lightwave Technology*, vol. 15, no. 8, pp. 1277–1294, 1997.
- [3] X. Shu, L. Zhang, and I. Bennion, "Sensitivity characteristics of long period fiber gratings," *Journal of Lightwave Technology*, vol. 20, no. 2, pp. 255–266, 2002.
- [4] B. C. Lee, E.-J. Jung, C.-S. Kim, and M. Y. Jeon, "Dynamic and static strain fiber Bragg grating sensor interrogation with a 1.3  $\mu\text{m}$  fourier domain mode-locked wavelength-swept laser," *Measurement Science and Technology*, vol. 21, no. 9, p. 094008, 2010.
- [5] J. Park, Y. S. Kwon, M. O. Ko, and M. Y. Jeon, "Dynamic fiber bragg grating strain sensor interrogation based on resonance fourier domain mode-locked fiber laser," in *Avionics and Vehicle Fiber-Optics and Photonics Conference (AVFOP)*, 2016 IEEE. IEEE, 2016, pp. 291–292.
- [6] H. Patrick, G. Williams, A. Kersey, J. Pedrazzani, and A. Vengsarkar, "Hybrid fiber Bragg grating/long period fiber grating sensor for strain/temperature discrimination," *IEEE Photonics Technology Letters*, vol. 8, no. 9, pp. 1223–1225, 1996.
- [7] G. Kahandawa, J. Epaarachchi, H. Wang, D. Followell, and P. Birt, "Use of fixed wavelength Fibre-Bragg Grating (FBG) filters to capture time domain data from the distorted spectrum of an embedded fbg sensor to estimate strain with an artificial neural network," *Sensors and Actuators A: Physical*, vol. 194, pp. 1–7, 2013.
- [8] M. A. Jucá and A. B. dos Santos, "Fiber Bragg grating interrogation using fbg filters and artificial neural network," in *Microwave and Optoelectronics Conference (IMOC), 2017 SBMO/IEEE MTT-S International*. IEEE, 2017, pp. 1–4.
- [9] F. Murtagh, "Multilayer perceptrons for classification and regression," *Neurocomputing*, vol. 2, no. 5-6, pp. 183–197, 1991.
- [10] F. D. Foresee and M. T. Hagan, "Gauss-Newton approximation to Bayesian learning," in *Neural networks, 1997., international conference on*, vol. 3. IEEE, 1997, pp. 1930–1935.

# A Simple Optoelectronic Load Cell

**Camila Carvalho de Moura<sup>1</sup>, Lorena Pereira de Carlos Jeranoski<sup>1</sup>,  
Pedro Michalowski Santos Lima<sup>1</sup>, Fernando Cardoso Castaldo<sup>1</sup>,  
Valmir de Oliveira<sup>1</sup>, Hypolito José Kalinowski<sup>2</sup>**

*Federal University of Technology – Paraná<sup>1</sup>, Rua Sete de Setembro 3165, Rebouças, Paraná - Brazil  
Universidade Federal Fluminense<sup>2</sup>, Niterói, Rio de Janeiro - Brazil  
camilacmwill@gmail.com, ljeranoski@gmail.com, valmir.utfpr@gmail.com, hjkalinowski@id.uff.br*

**Abstract:** In this work, an optical load cell was developed based on the intensity light variation get as a distance function between a light emitting diode (LED) and a FC-PC multimode optical fiber connector. The load cell is composed by a spring return and mass displacement system. The optical system consists of a LED in the infrared band whose emission is directed to a FC-PC multimode optical cord (MMF 62.5/125), at another end of the optical cord the power was applied to a phototransistor. The resulting current in the phototransistor was amplified in a two-stage transimpedance circuit using general purpose operational amplifier. The voltage response was correlated to the value of the load applied to the system. Four tests were carried out, in which they exchanged the springs for return and loads intensities. Through the tests, the transducer's calibration curves were done. The optical load cell shown in this work was developed for the cost reduction purpose and the reasonableness simple solution.

## 1. Introduction

Load cells are transducers with a great importance in industrial, commercial and laboratory applications. The operation principle is based in the applied force conversion into an electrical potential difference, in general, the load cells can be classified according to the output signal generated and the signal detection mode: metal strain gauge cells [1–3], mechanical cells [4], fiber optic cells [5], and semiconductor cells [6]. One of the conventional load cells applications is the quantification of breakage caused by cylindrical rocks impact [7]. The optical load cells technology, when compared with conventional load cells, have some advantages, such as electromagnetic interference immunity and, potentially, a simpler detection system. An using example of an optical load cell consists of measuring deformation on biological soft tissues, where the deformation is captured with an optical microscope [8]. Another load cells application is based in Bragg grating sensors, which can monitor temperature and strain, to prevent ice accumulation on transmission lines [9]. The optical load cells based in Bragg gratings have a relatively high-cost production and high-cost measurement instrumentation [10]. In this work is propose, develop and calibrate an optical load cell based on light intensity changes, avoiding the use of Bragg gratings.

## 2. Methodology

The opto-mechanical load cell system proposed and characterized is formed by a movable beam sliding in two circular section rods, whose course is limited by compression springs involving the rods. On the movable beam, the load is applied with calibrated masses. In the loading process, the mass is applied in movable beam center through a negligible mass nylon thread. The weight force as opposed to springs resistance and causes displacement in movable beam, as shown in Fig. 1. The constructed optical load cell working principle is based on distance variation between a light emitting diode (LED) on a fixed base, height adjustable with FC-PC multimode fiber optic connector, 62.5/125 $\mu\text{m}$ , to movable beam fastened. Light is coupled and guided on optical fiber, and at other end to a phototransistor applied, which will present variation in its current conduction, in proportion to incident optical power. The power coupled to optical fiber undergoes variation directly proportional to the load applied on load cell movable beam, due to distance reduction between the LED and the fiber optic input. The light intensity applied to phototransistor and converted into electric current variation is subsequently amplified by the transimpedance, providing proportional output voltage. The distance between LED and fiber optic input can be adjusted to determine an average voltage level at transimpedance amplifier output, as well maximum movable beam elastic displacement. Springs with different elasticity coefficients are changed depending from applied load range.

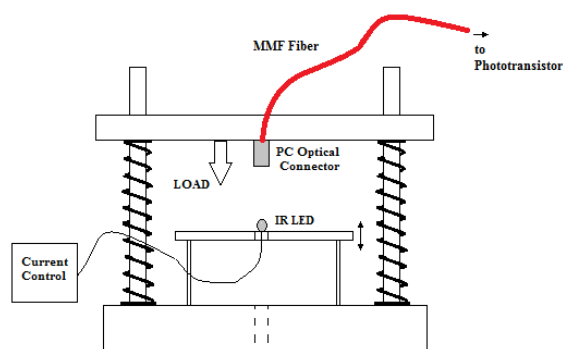


Fig.1. schematic opto-mechanical load-cell

The transducer mechanical part was made, which is formed by aluminum base (24 x 80 x 98 mm), two stainless steel rods with 8 mm diameter and 90 mm length, on which the compression springs were assembled. The same rods support and guide the movable beam displacement, through two holes with brass bushings, which laid down on the springs. At the transducer base there is a hole through which a nylon thread is attached to the moving beam, whereas, at the other end are applied different loads for transducer calibration tests using standard loads. The loads are from 100 g to 10 kg against gravity. Three compression springs pairs with different elastic coefficients are used. The load cell was assembled using aluminum/stainless steel/ brass parts and was to the optoelectronic system connected, as shown Fig. 2:

1. Optical connector FC-PC, fiber MMF 62.5/125
2. Stainless steel metal rod for movable beam support and guidance
3. Limit lock for movable stainless-steel beam
4. Movable beam with optical connector support and for loading
5. Stainless steel spring
6. Stainless steel phototransistor support
7. Loading Pendulum
8. Pendulum passage hole
9. Aluminum system base
10. LED
11. Metal base for LED fixing with height adjustment

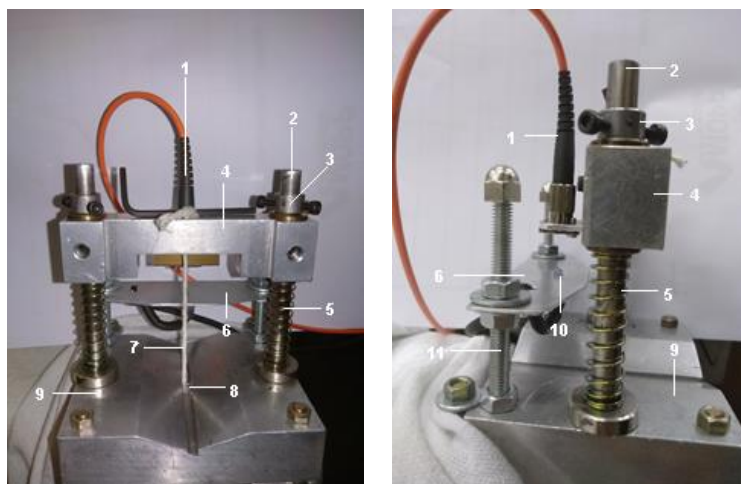


Fig.2. Load cell (A). front view; (B) side view

The optoelectronic circuit is proposed, designed, assembled and characterized. Such circuit is composed of an IR LED as light source, model TIL 32, with wavelength centered at 940 nm (Fig. 3, block 2). As photodetector an IR band phototransistor TIL78 is used (Fig. 3, block 3). A two-stage transimpedance amplifier circuit is developed, with the amplifying purpose of photocurrent detected by the phototransistor (Fig. 3, block 4). The general-purpose operational amplifier integrated circuit chosen is TL084. Preliminarily the LED was aligned with the phototransistor, keeping distance of 30 mm, then the emission power is varied, as well as the amplifier gain, defining LED current values and amplifier output voltage range. Still on the transducer base, the LED was assembled in a system that allows height adjustment. Lastly,

an optical FC-PC connector, which captures the LED light and guide via the multimodal fiber (MMF 62.5/125 μm), to the movable beam was attached, in line with the LED, to the phototransistor on the electronic board. The LED at constant current is biased in the range between 5 and 15 mA, using a DC voltage source (model TDS1001B) (Fig. 3, block 1). The temperature during all tests is maintained at 22 °C. The opto-mechanical load cell system maintains vertical alignment between the LED and the FC-PC connector, varying the distance between them, which is inversely proportional to the applied load. At the transimpedance amplifier output is obtained a DC response which is to the photo detected power proportional, which is measured with a digital oscilloscope, Tektronix (model DDS 1001B) (Fig. 3, block 5). Fig. 1. shows the sensor block diagram.

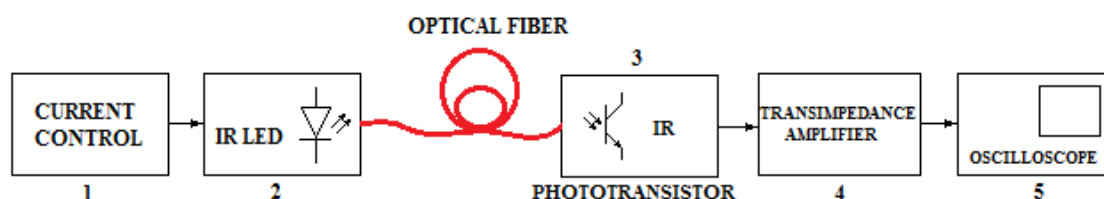


Fig. 3. Electronic system block diagram.

Three springs are used to characterize the load cell, named A, B and C. The first spring used was A, with elastic coefficient 754,97 N/m. The second used spring was B with elastic coefficient 1208,09 N/m. The third used spring was C with elastic coefficient 6569,2 N/m. Four tests were performed to mechanical system characterize. Due to the spring's different properties, the distance between the LED and the phototransistor had to be adjusted in a range between 15 mm and 35 mm, to avoid electric signal saturation. In the first test, the spring A was used with loads between 2.5 kg and 6 kg, with 500 g increments. Each loading is repeated 15 times to obtain an average, with load relief, 15 seconds stabilization time and load replacement. In the second test, the spring B is used with loads between 500 g and 3 kg, with the same increment. Each loading was 10 times repeated to obtain an average, with load relief, 15 seconds stabilization time and load replacement. In the third test, the spring A is used with load between 1 kg and 10 kg, again using the same increment. Each load test is 5 times repeated to obtain an average, with load relief, 15 seconds stabilization time and load replacement. In the fourth test, the spring is used with loads between 0.3 kg and 0.9 kg, with 100 g pitch. Each load is 5 times repeated to obtain an average, with load relief, 15 seconds stabilization time and load replacement.

### 3. Results

The obtained function for the second and third tests, using a least squares exponential fitting is shown in equation 1:

$$y = y_0 + A_1 * e^{\left(\frac{x-x_0}{t_1}\right)} \tag{1}$$

where  $A_1$  is constant,  $y_0$  is the initial system voltage,  $x_0$  is the initial system load and  $t_1$  growth rate. In Table 1 are shown the coefficient values for the second and third tests.

Table 1. Coefficient values for the second and third tests

Coefficient	Second test	Third test
$y_0$	0.4616	0.9110
$x_0$	243.2884	1.8042
$A_1$	1.7001	0.4078
$t_1$	466.6899	3.5304

The fitting function for the first and fourth tests presents a polynomial dependence, as shown in equation 2:

$$y = a * x^2 + b * x + c \tag{2}$$

where a, b e c are constants, x is the load variable and y is voltage value. In Table 2 are shown the coefficient values for the first and fourth tests.

Table 2: Coefficient values for the first and fourth tests

Coefficient	First test	Fourth test
a	0.1845	0.0000
b	-0.2306	-0.0030
c	2.1836	2.4981

Due to the fact that uncertainties are small compared to averages, they would not appear if they were inserted in the graphs. The Fig. 3. shows the obtained graphs for the four tests, respectively, comparing the applied load and output voltage.

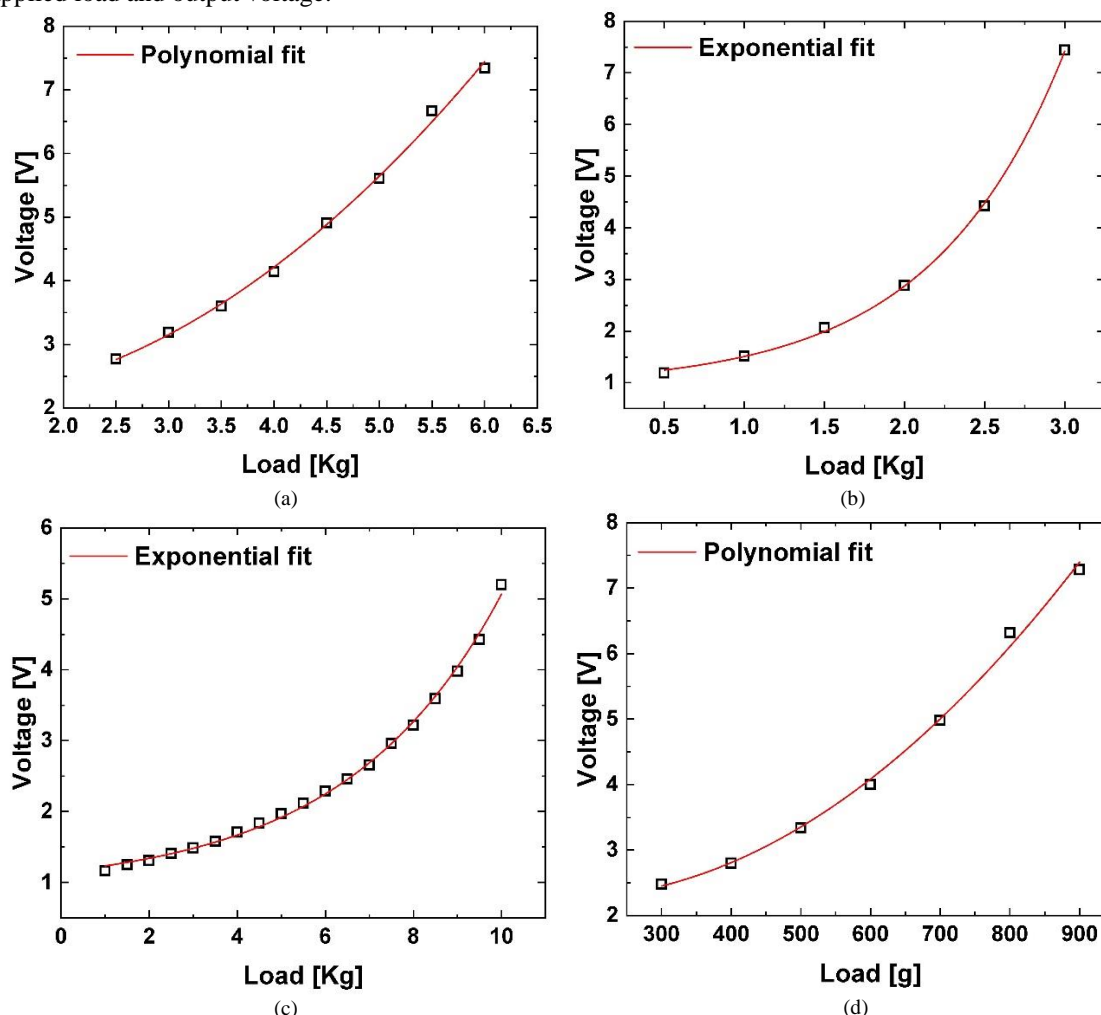


Fig. 3. (a) First, (b) Second, (c) Third and (d) Fourth tests

The Table 3 shows the average voltage values obtained through tests for the springs A, B and C.

Table 3. Average voltage results and standard deviation for different applied loads in each spring

Load(kg)	First test Spring A Voltage (V)	Second test Spring B Voltage (V)	Third test Spring A Voltage (V)	Fourth test Spring C Voltage (V)
0.3				2.48 ± 0
0.4				2.80 ± 0
0.5		1.19 ± 0		3.34 ± 0.04
0.6				4.00 ± 0.06
0.7				4.98 ± 0.04
0.8				6.32 ± 0
0.9				7.28 ± 0
1		1.52 ± 0.01	1.17 ± 0	
1.5		2.07 ± 0.01	1.25 ± 0	
2		2.88 ± 0.03	1.31 ± 0	
2.5	2.77 ± 0.07	4.42 ± 0.03	1.41 ± 0.01	
3	3.19 ± 0.07	7.44 ± 0	1.49 ± 0.01	

3.5	$3.6 \pm 0.06$	$1.58 \pm 0$
4	$4.14 \pm 0.08$	$1.71 \pm 0.01$
4.5	$4.91 \pm 0.09$	$1.84 \pm 0.01$
5	$5.61 \pm 0.07$	$1.97 \pm 0.01$
5.5	$6.67 \pm 0.11$	$2.12 \pm 0.01$
6	$7.34 \pm 0.14$	$2.29 \pm 0.02$
6.5		$2.46 \pm 0$
7		$2.66 \pm 0.01$
7.5		$2.96 \pm 0$
8		$3.22 \pm 0.02$
8.5		$3.59 \pm 0.01$
9		$3.98 \pm 0.03$
9.5		$4.43 \pm 0.06$
10		$5.2 \pm 0$

The spring A resolution was  $4,08 \mu\text{V} / \text{g}$ , spring B  $1,84 \mu\text{V} / \text{g}$  and spring C  $9,33 \mu\text{V} / \text{g}$ .

#### 4. Conclusion

The described optical load cell used low cost materials and easily accessible in the market, it also presents a direct response in terms of the electrical potential, avoiding the use of specific, high-end test & measurement equipments as, e.g., occurs with fiber Bragg grating sensors. Comparing with electro-electronic load cells, the proposed configuration has the sensing head independent of the data acquisition system, requiring only a single battery for powering the LED. It can also be used to monitor remote positions, as the optical signal, whose intensity changes with the applied load, is along the multimode optical fiber guided, which presents immunity to electromagnetic interference. The used spring can be calibrated for several mass ranges, allowing a large operational dynamic range. The mechanical assembly is quite robust, allowing its use in several demanding applications. The calibration curves are either exponential or polynomial, both of which can be easily embedded in an appropriate firmware.

#### 5. Bibliography

- [1] A. Karaus, H. Paul, "Load cells with small nominal load based on strain gauges using thin-film techniques," *Measurement*, 10 (1992) 133–139.
- [2] C.K. Demetropoulos, C.R. Morgan, D.K. Sengupta, H.N. Herkowitz, "Development of a 4-axis load cell used for lumbar interbody load measurements," *Medical Engineering and Physics*, 31 (2009) 846–851.
- [3] Measurements Group, Inc., Technical Staff, "Strain Gage Based Transducers: Their Design and Construction," *Measurements Group*, 1988.
- [4] F.J.M. Farley, J.K. Vij, A. Kocot, U.M.S. Murthy, M. Burgess, "Mechanical loadcell based on cavity-controlled microwave-oscillators," *IEEE Transactions on Microwave Theory and Techniques*, 39 (1991) 1611–1616.
- [5] K. Nakamura, T. Matsumura, S. Ueha, "A load cell using a fiber Bragg grating with inherent mechanical temperature compensation," *Structural and Control Health Monitoring*, 12 (2005) 345–355.
- [6] R.A.F. Zwijze, R.J. Wiegerink, G.J.M. Krijnen, T.S.J. Lammerink, M. Elwenspoek, "Low-cost piezoresistive silicon load cell independent of force distribution," *Journal of Micromechanics and Microengineering*, 10 (2000) 200–203.
- [7] Bonfils, B., "Quantifying of impact breakage of cylindrical rock particles on an impact load cell," in *International Journal of Mineral Processing*, 161 (2017) 1–6.
- [8] Faturechi, R.; Hashemi, A.; Abolfathi, N., "A tensile machine with a novel optical load cell for soft biological tissues application," *J Med Eng Technol*, 2014; 38(8): 411–415
- [9] Ma, G; Li, C.; Jiang, J.; Luo, Y.; Cheng, Y., "A novel optical load cell used in icing monitoring on overhead transmission lines," in *Cold Regions Science and Technology* 71 (2012) 67–72.
- [10] Campanella C.E., Cuccovillo A., Campanella C., Yurt A., Passaro V.M.N. Fibre Bragg Grating Based Strain Sensors: Review of Technology and Applications. *Sensors*. 2018;18:3115. doi: 10.3390/s18093115.

# Study of Core Diameter Mismatch Based Optical Fiber Sensors for Salinity and Temperature

**Tanushree Selokar**

*Centro Federal de Educação Tecnológica Celso Suckow da Fonseca, Photonics Lab, Electrical Engineering Department, Avenida Maracanã, 229, Rio de Janeiro, Brazil, 20271-110  
tanushree.selokar6@gmail.com*

**Maria Thereza M. Rocco Giraldi**

*Instituto Militar de Engenharia, Photonics Lab, Electrical Engineering Department, Praça General Tibúrcio, 80, Rio de Janeiro, Brazil, 22290-270, mtmrocco@ime.br*

**Abstract:** In this paper it is presented core diameter mismatch structured devices that use multimode interference technique as optical fiber sensors. Singlemode-Multimode-Singlemode (SMS) and Singlemode-Multimode-Singlemode-Multimode-Singlemode (SMSMS) configurations are used for measurement of refractive index (RI) and temperature. The best sensitivity achieved for RI measurements is obtained with the SMS sensor: 273.63 nm/RIU. For temperature sensing, the best sensitivity attained is accomplished using the SMSMS sensor: 312.75 pm/°C.

**Keywords:** Core Diameter mismatch, Multimode interference technique, Reimaging.

## 1. Introduction

Optical fiber sensor (OFS) technology has been a major user of the technology associated with the optoelectronic and fiber optic communications industries. Many of the components associated with these industries were often used for fiber optic sensor applications [1-3]. OFS works by modulating one or more properties of the propagating light wave, including intensity, phase, polarization, and frequency, in response to the environmental parameter being measured. OFS has been studied intensively based on physical phenomena such as wavelength dependent absorption, photoluminescence and phase detection [3]. Compared with traditional sensors using electrical or magnetic principles, optical fiber sensors have a number of advantages, including low signal loss (attenuation), immunity to electromagnetic noise and chemical material erosion, small size and lightweight, possibility of multiplexing, feasibility of distributed and remote sensing, electrical passivity [1-5]. Measurement of salinity by using optical fiber technology has attracted lots of attentions in recent years due to the well known advantages of fiber optic sensors such high sensitivity, immunity to electromagnetic interference, low cost and weight.

Multimode Interference (MMI) effect has recently attracted significant interest for a range of applications. A consequence of constructive MMI is the so called self imaging effect where a spatially periodic electromagnetic field can reproduce itself periodically along the propagation direction [6]. Meng *et al.* [7] produced a laser based salinity sensor on SMS fiber based on no-core multimode fiber section with 125  $\mu\text{m}$  diameter. Enhanced measurement accuracy is achieved by inserting the sensor head into the cavity of an erbium-doped fiber ring laser, because the laser's linewidth is much narrower than that of the transmission peak. Salinity sensitivity of 19.4 pm/% in the range of 3.86% to 21.62% of NaCl was achieved. Aguilar-Soto *et al.* [8] used the self-imaging effect of an SMS fiber structure, based on a no-core MMF with 125  $\mu\text{m}$  in diameter, to measure temperature; a typical sensitivity of approximately 13 pm/°C in the temperature range from 25°C to 375°C was achieved. Silva *et al.* [9] used MMI effect in an SMS structure, based on three MMFs with different diameters namely, 55, 78, and 125  $\mu\text{m}$ . The sensitivity to external RI variations increased as the MMF diameter was decreased; the maximum sensitivity of 2800 nm/RIU for 55  $\mu\text{m}$  MMF was attained.

## 2. Theoretical Analysis

### 2.1. Core Diameter Mismatch Structures

Singlemode-Multimode-Singlemode (SMS) fiber structures offer all-fiber solutions for optical sensing with the advantages of easy of packaging and connection to optical fiber system [10]. The reflection occurring at the interface between the single-mode fiber and multimode fiber (MMF) due to the mismatch of the refractive index is found to be very small and can be neglected in practice [10]. The basic structure of this device is the SMS as shown in figure 1(a). The device consists of a short section of multimode fiber of 5.8cm length to ensure reimaging, which works as the sensing element, inserted between two singlemode (SMF) fibers.

The MMF section in the SMS acts as a core-cladding coupling mechanism due to the large core diameter mismatch (CDM) [11]. The SMS configuration concept is based on the fact that when the light field from the first SMF enters the MMF section, it excites several higher order modes, generating a periodic interference pattern along the MMF section. The MMF couples part of the light traveling along the core of the first SMF to the cladding of the second SMF, and this coupling induces a loss of power in the transmitted signal traveling along the core.

Another kind of CDM arrangement which is very similar to the SMS structure is the SMSMS structure in which two multimode fibers are spliced between three singlemode fibers. The basic structure of the SMSMS device is shown in figure 1(b). The middle SMF of length 2 cm is placed between the two MMF's. To ensure reimaging the length of the MMF's are chosen to be 5.8 cm. The reimaging is used because it enables to obtain the narrowest spectral bandwidth and minimum insertion losses [7]. When light propagates from MMF to SMF, part of the light will leak from the core of MMF to the cladding layer of SMF due to the different cores diameter between SMF and MMF. After they propagate to the second MMF, they re-couple to the core mode. Since the cladding modes in the SMF are guided by the cladding boundary, the middle SMF section is much more sensitive to the surrounding medium [12].

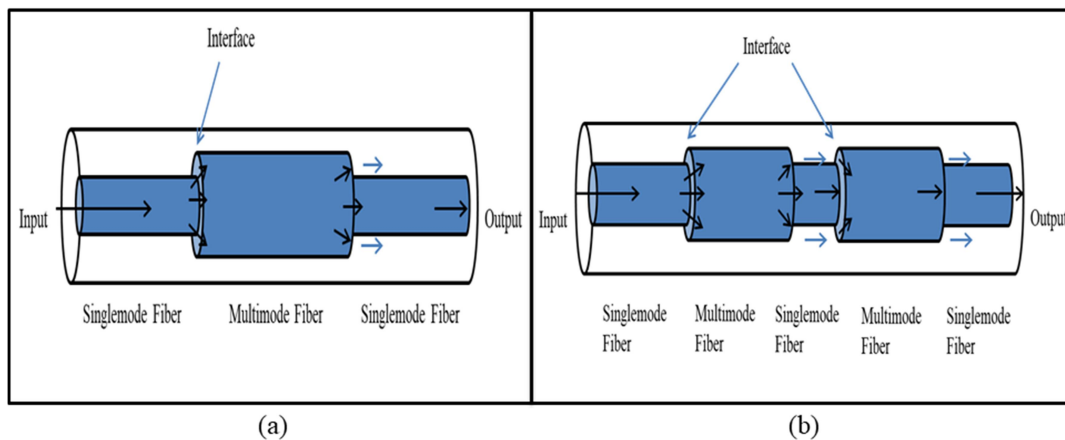


Fig.1. (a) Singlemode- Multimode-Singlemode structure (SMS), (b) Singlemode- Multimode-Singlemode-Multimode-Singlemode structure (SMSMS).

The principle of the reimaging concept can be used in CDM structures and can be stated as follows: reimaging is a property of multimode waveguides by which an input field profile is reproduced in single or multiple images at periodic intervals along the propagation direction of the guide [6]. The reimaging distance occurs where the input source is replicated in both amplitude and phase. Reimaging for step index fiber appears at the distance  $L_i$  [13]:

$$L_i = 16n_{core}a^2p/(4m + 1)\lambda \quad (1)$$

Where  $n_{core}$  is the refractive index of the core,  $a$  is the radius of the fiber core,  $p$  is an integer,  $m$  is the excited mode,  $\lambda$  is the wavelength. Assuming that  $p = 1$  and  $m = 0$ , the field distribution at the input of the MMF is reproduced at:

$$L_i = 16n_{core}a^2/\lambda \quad (2)$$

### 3. Experimental Setup

The experiments were conducted for refractive index (RI) and temperature (T) measurements with SMS and SMSMS structures. A no core multimode fiber of length 5.8 cm is used as the MMF and a Corning SMF-28 as the SMF. The experimental setups are shown in figure 2(a) for RI and (b) for temperature. The light from the broadband source (BBS) is transmitted through the sensor until the optical spectrum analyzer (OSA). The refractive index solutions are prepared by mixing NaCl and water. RI of the solutions is directly proportional to salinity [7]. The SMS and SMSMS sensors are tested for the refractive index ranging from the 1.338 to 1.376, which are the values of salinity in water. For temperature measurements, the SMS and SMSMS sensor are tested for the range between 23.5°C to 63.2°C. The sensors are placed alternately in the beaker with the refractive index solution and the experiment is conducted. For repeatability of the sensors every experiment is repeated three times. Sensitivities were obtained for all measurements and the best values only were used.

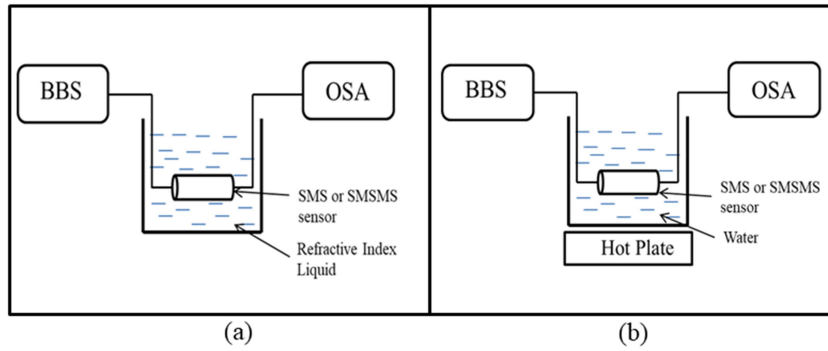


Fig. 2. Experimental setup for measuring (a) refractive index and (b) temperature.

### 4. Results and Discussion

#### 4.1. Refractive Index Measurement

Figure 3 shows the variation in the spectrum with different refractive indexes for (a) SMS and (b) SMSMS sensors. The sensitivities obtained for the sensors are shown in figure 4. The sensitivity attained for the SMS at dip 1 is 273.63 nm/RIU with  $R^2$  equals to 0.944. The sensitivity achieved for the SMSMS sensor at dip 1 is 148.85 nm/RIU with  $R^2$  equals to 0.988.

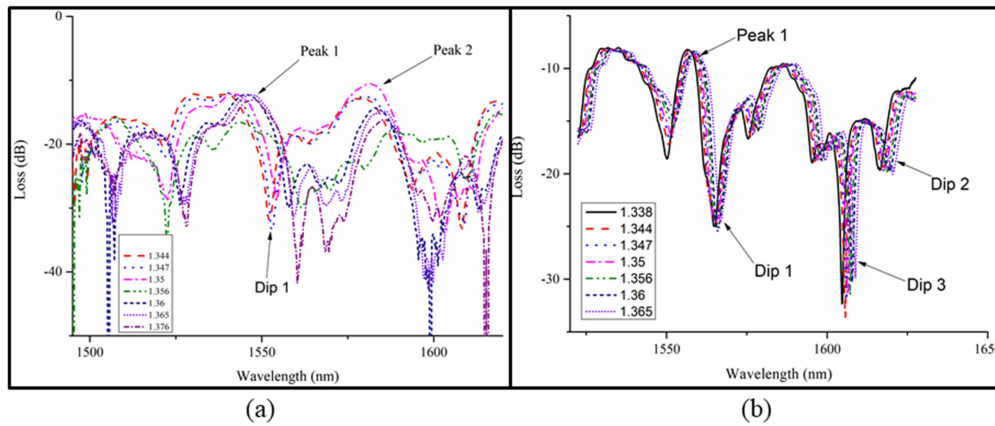


Fig. 3. Sensors spectrum variation for different Refractive Indexes (a) SMS sensor (b) SMSMS sensor.

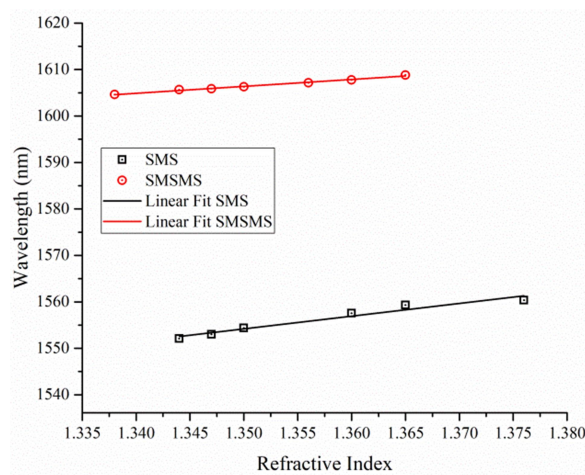


Fig. 4. Sensitivities for the SMS and SMSMS sensors for refractive index measurement.

### 4.2. Temperature Measurement

Figure 5 shows the variation in the spectrum with the change in the temperature for the (a) SMS sensor and (b) SMSMS sensor. The sensitivities attained for the sensors are shown in figure 6. The sensitivity obtained for the SMS sensor at dip 1 is 155.82 pm/°C with  $R^2$  equals to 0.98. The sensitivity acquired for the SMSMS sensor at dip 1 is 312.75 pm/°C with  $R^2$  equals to 0.975.

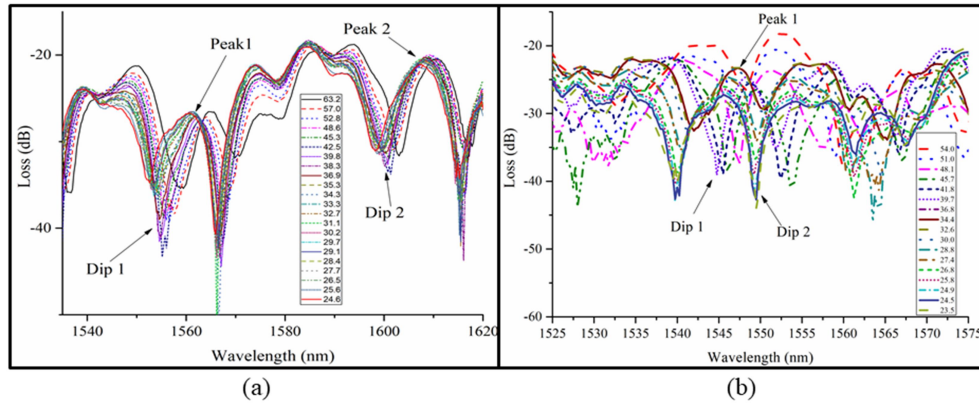


Fig. 5. Variation in the spectrum due to changes in temperature for the (a) SMS and (b) SMSMS sensors.

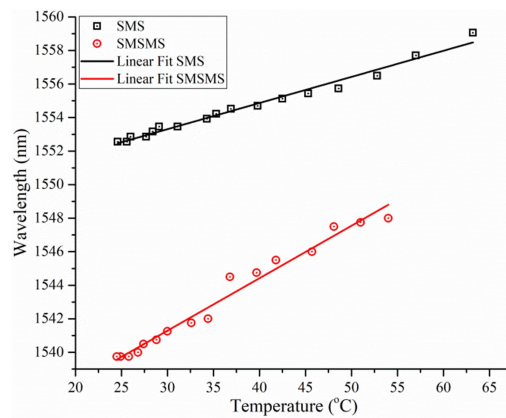


Fig. 6. Sensitivities for the SMS and SMSMS temperature sensors.

## 5. Conclusion

In this work, optical fiber refractive index sensors and temperature sensors based on multimode interference effect are developed as an initial characterization analysis of these sensors. Refractive index and temperature change in the liquid can be measured from the wavelength shift in the sensors transmission peaks and valleys. The main contribution to the temperature sensitivity is due to the liquid temperature variation. The SMSMS sensor is more sensitive to temperature whereas the SMS sensor is more sensitive to refractive index. In a future work the simultaneous measurement of salinity and temperature will be proposed.

## 6. Reference

- [1] K. Fidanboyly, and H. S. Efendioglu, "Fiber optic sensors and their applications", in *Proceeding of International Advanced Technologies Symposium*, (Turkey, 2009), pp. 01-06.
- [2] M. S. Shaikh and M. A. Patil, "Analysis, designing and working principal of optical fiber (OF) biosensors", *International Journal of Engineering and Science V 1*, 52-57 (2012).
- [3] B. Gholamzadeh, and H. Nabovati, "Fiber optic sensor", *International Journal of Electronics and Communication Engineering V 2*, 1107-1117 (2008).
- [4] Dakin, and B. Culshaw, *Optical fiber sensors-Principles and components* (Artech House, 1988), Chap. 1.
- [5] F. T. S. Yu, P. B Ruffin, S Yin, *Fiber optic sensor* (CRC Press, Boca Raton, 2008), Chap 1.

- [6] L. B. Soldano, and E. C. M. Pennings, "Optical multi-mode interference devices based on selfimaging: principles and applications", *Journal of Lightwave Technology* V **13**, 615-627 (1995).
- [7] Q. Meng, X. Dong, K. Ni, Y. Li, B. Xu, and Z. Chen, "Optical fiber salinity sensor based on multimode interference effect", *Journal of IEEE Sensors* V **14**, 1813-1816 (2014).
- [8] J. G. Aguilar-Soto, J. E. Antonio-Lopez, J.J. Sanchez-Mondragon, and D.A . May-Arroja, "Fiber optic temperature sensor based on multimode interference effects", *Journal of Physics* V **274**, 012011 (2011).
- [9] S. Silva, E. G. P. Pachon, M. A. R. Franco, J. G. Hayashi, F. X. Malcata, O. Frazao, P. Jorge, and C. M. B. Cordeiro, "Ultrahigh – sensitivity temperature fiber sensor based on multimode interference ", *Journal of Applied Optics* V **51**, 3236-3242 (2012).
- [10] Q. Wang, G. Farrell, and W. Yan, "Investigation on single-mode–multimode–single-mode fiber structure", *Journal of Lightwave Technology* V **26**, 512-519 (2008).
- [11] J. Villatoro, and D Monzón-Hernández, "Low-cost optical fiber refractive-index sensor based on core diameter mismatch", *Journal of Lightwave Technology* V **24**, 1409-1412 (2006).
- [12] Z. Tong, J. Su, Y. Cao, and W. Zhang, "Simultaneous measurement based on composite interference structure", *IEEE Photonics Technology Letters* V **26**, 1310-1313 (2014).
- [13] A. H. Morshed, "Self-imaging in single mode-multimode-single mode optical fiber sensors", in *Proceeding of IEEE*, (Saudi Arabia , 2011), Vol. 10, pp. 1-5.

# Multi-parameter Non-Invasive Monitoring of Lithium-Ion Batteries Using Fibre Bragg Gratings

**Bruno Rente\*, Matthias Fabian, Tong Sun and Kenneth T V Grattan**

*City, University of London, Northampton Square, London EC1V 0HB, United Kingdom*

*Bruno.Rente@city.ac.uk*

**Abstract:** The integration of Fibre Bragg Gratings (FBG) into the body of Lithium-Ion battery cells, for measuring both their strain and temperature to achieve better overall condition monitoring is reported. Sufficient data have thus been gathered to develop an appropriate model for the prediction and thus the prevention of battery failure.

## 1. Introduction

Lithium-Ion batteries are well known as a key technology of modern energy storage systems, with major applications both in electric vehicles and a significant range of portable devices used by us all day-to-day. This type of battery has been shown to be the most effective to meet the energy requirements of these devices, allowing as they do both high peak power and high capacity [1].

Despite all these advantages seen in Lithium-Ion batteries over other energy storage technologies, there are still clear limitations in their use, which mainly are related to the safety and the optimization of the battery life-span and capacity. For this reason, a number of studies involving better modelling of key Lithium-Ion battery parameters, to allow a better understanding of the dynamics of their chemistry in order to maximize their performance, while not compromising the safety of their operation, have been carried out.

The methods usually used to measure the battery state-of-charge (SOC) and state-of-health (SOH) are based on voltage and current measurements, using such data to create models that simulate as closely as possible the actual state of the batteries [1]. However, these methods have limitations and must be used together to enhance the reliability of the results and improve the real-life operation of Lithium-Ion battery systems for many operational uses. Fibre optic sensors have proven very valuable for obtaining useful data, to allow better battery characterization and create other electrical measurements. On that rationale, Fibre Bragg Gratings (FBG) take advantage of their immunity to electromagnetic interference and their being good insulators, with the additional advantage of being easily multiplexed as compared to their electrical competitors, such as thermocouples or strain gauges. For these reasons, FBG technology has been widely applied to the measurement of both temperature [2] and strain [3] in Lithium-Ion batteries, as a knowledge of these parameters is essential for the better understanding of the lithiation/delithiation processes and their influence on the battery SOC and SOH.

Although the integration of FBGs inside the battery cell has proven feasible, the thrust of this work has been to measure the strain and temperature outside the battery package where the data are easier to obtain and yet can be equally effective, in that way to enhance the applicability of this kind of measurement in industry. It is well known that battery performance could be affected by the integration of fibres inside the battery cell [4]. A similar approach has already been proven useful to enhance the performance over that available from conventional sensors for thermal characterization [5]. Thus, the focus of this work has been to extend this to multi-parameter measurement, as a knowledge of strain plays a key role in understanding the dynamic of the process [3] and battery performance and safety.

As a result, this work has aimed to apply the advantages of FBG technology to measure the strain and temperature conditions in Lithium-Ion batteries, to serve as a proof-of-concept of a non-invasive optical fibre-based method to create a self-sensing smart-battery capable of optimized operation to meet the high performance in measurement, demanded by the next generations of electrification systems.

## 2. Experimental Methods

The FBGs used in this work were manufactured using the phase mask method and inscribed in photosensitive fibres supplied by Fibercore (PS1250/1500), using ultraviolet light from a high power KrF excimer laser. Further, in order to create an effective comparison with well-established methods, a Coulomb-counting set-up was created using a NI DAQ USB-6211 and a 0.1  $\Omega$  resistor, set up in parallel with the fibre sensors and thus to allow a

measurement of the current and the voltage of the cell. All cycles were performed at constant current and constant voltage (CCCV) charge and constant current (CC) discharge. Fig. 1 shows an illustration of the set-up used.

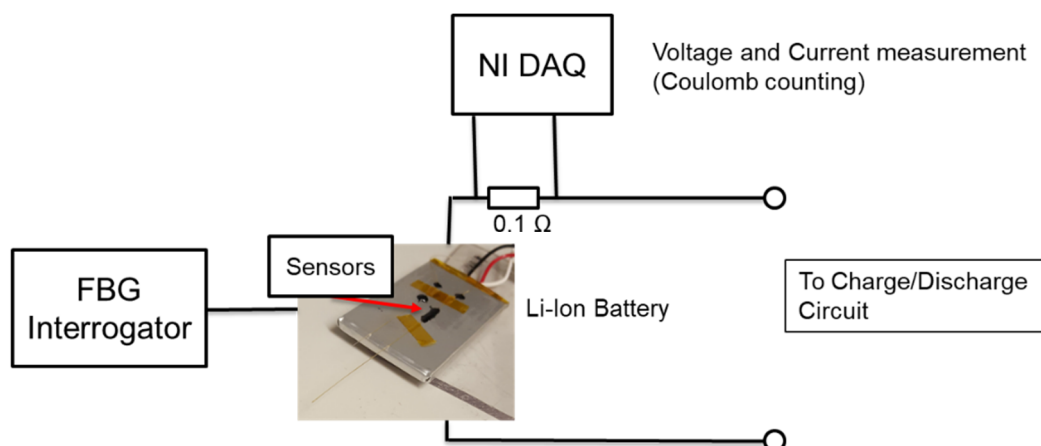


Fig. 1. Schematic of the electrical assembly, the fibre optic monitoring system and the Coulomb counting circuit.

The batteries were monitored by using both the Coulomb counting circuit and the optical fibre sensors, measurements being made for each cycle, using current rates of 0.5C, 1C and 2C, at room temperature. In addition, a further temperature sensor was used for monitoring the room temperature. Two different models of Li-Ion batteries were evaluated: a Lithium-Polymer type from Varta (with capacity 1100 mAh) and a more widely used type, a Duracell DR9664 (with capacity 700 mAh), such as is used in digital cameras.

The main differences between them is in their chemistry, capacity and packaging, where the Varta battery is a pouch cell and the Duracell has a rigid metal package. Two FBGs were used in the monitoring system: the first to measure strain (where the fibre was glued to the battery surface), and the second to monitor temperature, this one being left unglued to avoid any strain cross-sensitivity. The interrogator used to monitor the FBG characteristic response was a Micron Optics device, type SM 130.

### 3. Results

Several tests were carried out where the batteries were monitored and the data on temperature and strain were logged and then plotted to allow a comparison of the effects of current rates and battery types. Fig. 2 shows the graphs plotted of temperature and strain changes during the cycling of the batteries using 0.5C (Fig. 2a and Fig. 2d), 1C (Fig. 2b) and 2C (Fig. 2c). Data from Fig. 2a, 2b and 2c were results from tests done with the Lithium-Polymer battery, while data shown in Fig. 2d were obtained from the Duracell type. All the graphs shown were obtained after cycling the battery 10 times, with the same current rate used in the cycling recorded.

It is clear from the graphs shown in Fig. 2 that the current rate with which the battery is charged and discharged will affect the strain and temperature recorded. The graphs obtained maintain the same shape when the same current rate is applied (data not shown), which indicates these data are representative of the battery itself – thus this approach could be used to characterize these batteries. This shows a very important aspect on the optimization of the battery that is to determine whether the current applied could then damage the battery and whether it would be possible to identify any changes arising due to damage to the cells from the profiles shown in the figures.

Comparing the graphs seen in Fig. 2d, with those in Fig. 2a, 2b and 2c, it can be seen that the chemistry of the battery will also influence the shape of the graphs, indicative of the fact that the battery can be characterized through a closer analysis of their temperature and strain behaviour, under charging and discharging. In the case of the battery data which are shown in Fig. 2d, the behaviour seems simpler and indeed more linear, as the strain increases on charging and decreases on discharging – the same pattern as observed in the work of Bae et al [3]. These results are indicative that the chemistry of this battery is simpler than that of the Lithium-polymer batteries which have also been tested.

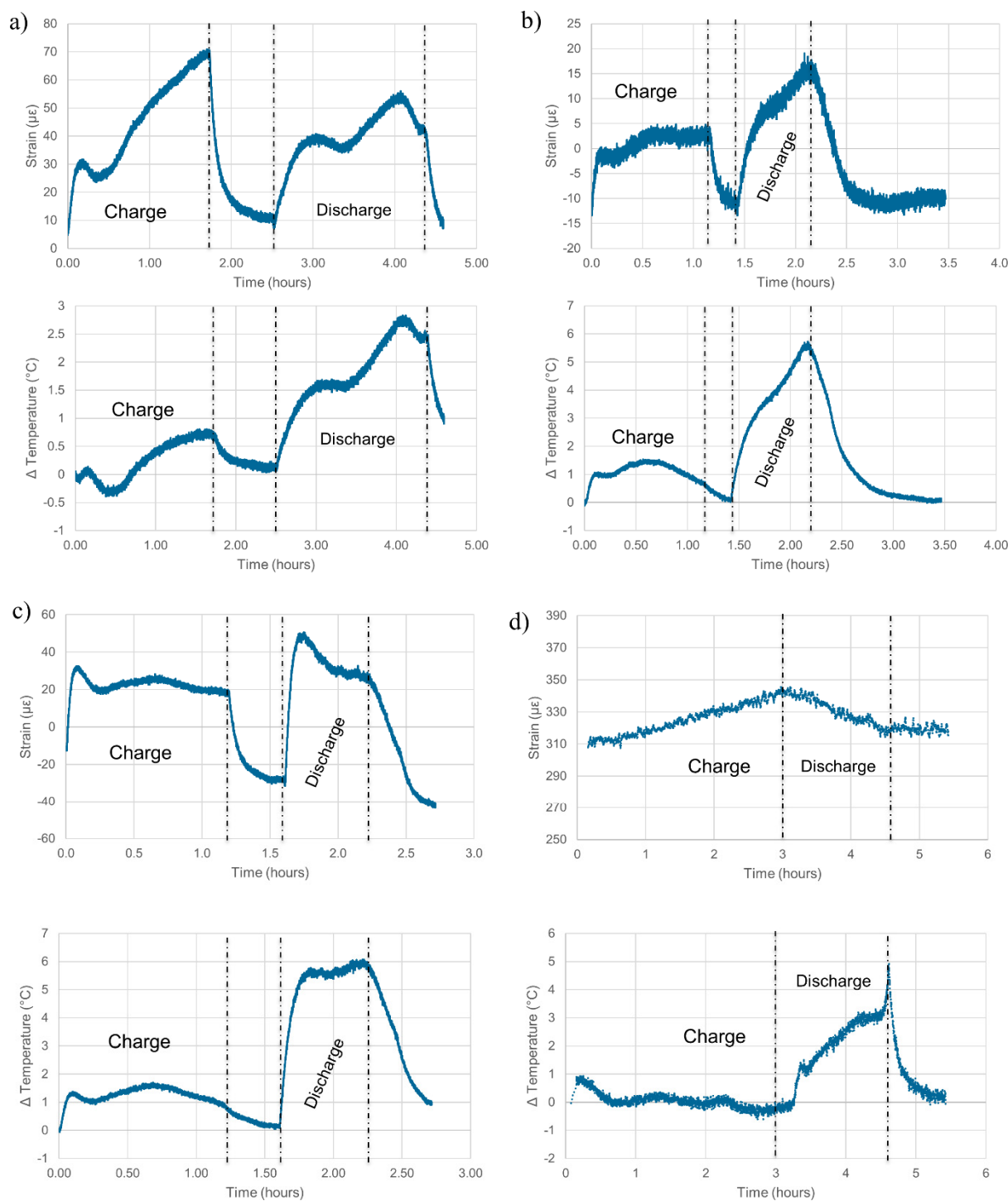


Fig. 2. Representative graphs of strain and temperature measurements for the Lithium-Polymer pouch cell (a, b and c) and for Duracell (d) during a cycle of CCCV charging and CC discharging with current rates of 0.5C (a and d), 1C (b) and 2C (c).

Comparing the graphs seen in Fig. 2d, with those in Fig. 2a, 2b and 2c, it can be seen that the chemistry of the battery will also influence the shape of the graphs, indicative of the fact that the battery can be characterized through a closer analysis of their temperature and strain behaviour, under charging and discharging. In the case of the battery data which are shown in Fig. 2d, the behaviour seems simpler and indeed more linear, as the strain increases on charging and decreases on discharging – the same pattern as observed in the work of Bae et al [3]. These results are indicative that the chemistry of this battery is simpler than that of the Lithium-polymer batteries which have also been tested.

To investigate further the applicability of this measurement approach for the future estimation of both SOC and SOH, strain data were compared to the battery capacity over a known period of time. Fig. 3 shows these

parameters which were monitored during one charging/discharging cycle of the batteries. The graphs begin at zero capacity, which is fully discharged, to approximately -1 Ah, indicating a fully charged Lithium-Polymer batteries.

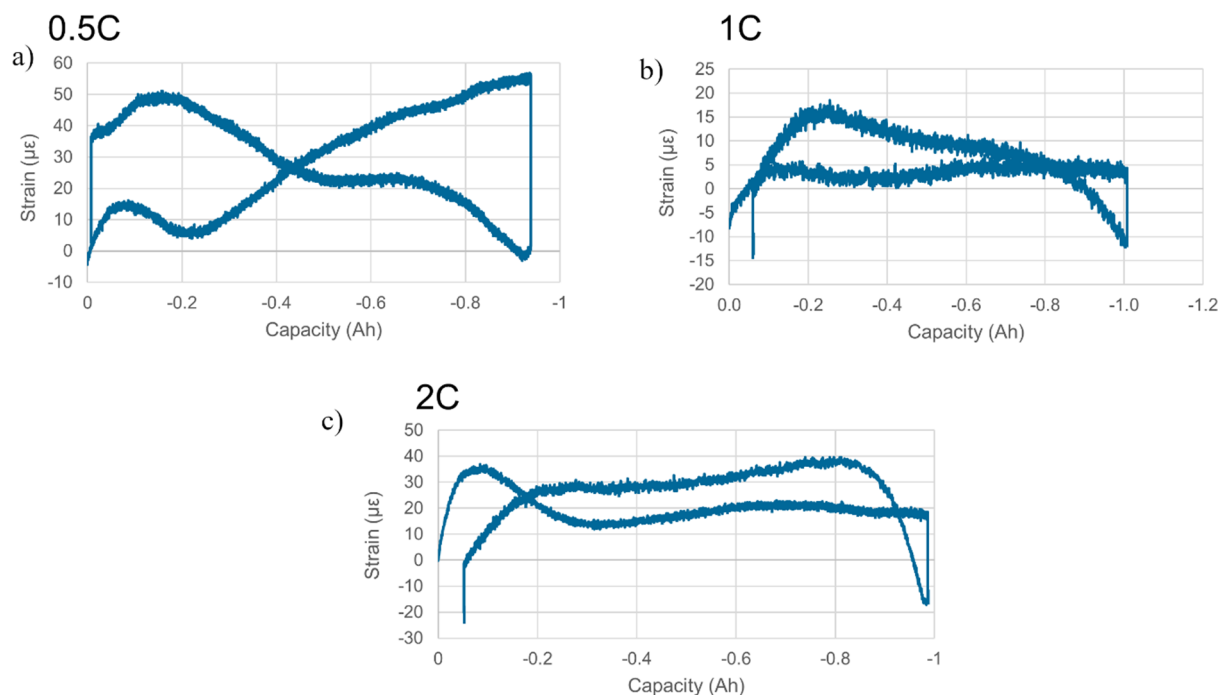


Fig. 3. Graphs showing the strain and the capacity during a full cycle of charging/discharging of the batteries at 0.5C (a), 1C (b) and 2C (c).

In Fig. 3, as with Fig. 2, again the shapes of the graphs are consistent when comparing the data obtained from the cycling at the same current rate, but they differ when the current rate is changed. As expected, data for the cycling at 1C shows a lesser level of strain compared to other rates and cycling at higher rates will cause the battery to lose capacity over multiple cycles. Therefore, monitoring of this kind of relationship is crucial to the optimization of the battery health, in addition to the strain data obtained over time.

#### 4. Conclusion

Data obtained from cycling of the batteries discussed suggests that there is a very characteristic dynamic that can be perceived through the strain and temperature measurements made. They also relate directly to the capacity of the batteries, in a way that can be used as an input for an effective modelling of the battery characteristics and the actual SOC and SOH. Future work planned aims to use these kinds of data to create a classification algorithm that may be able to quantify the SOC and SOH and thus ultimately optimize the battery to create a maximum life span and battery performance.

#### 5. References

- [1] J.Zhang, and J. Lee, "A review on prognostics and health monitoring of Li-ion battery," *Journal of Power Sources* **15**, 6007-6014 (2011).
- [2] S. Novais, M. Nascimento, I. Grande, M. F. Domingues, P. Antunes, N. Alberto, C. Leitao, R. Oliveira, S. Koch, G. T. Kim, S. Passerini, and J. Pinto, "Internal and External Temperature Monitoring of a Li-Ion Battery with Fiber Bragg Grating Sensors," *Sensors* **16**, 1394-1403 (2016).
- [3] C. J. Bae, A. Manandhar, P. Kiesel, and A. Raghavan, "Monitoring the Strain Evolution of Lithium-Ion Battery Electrodes using an Optical Fiber Bragg Grating Sensor," *Energy Technology*, **4**, 851-855 (2016).
- [4] J. Fleming, T. Amietszajew, E. McTurk, D. Greenwood, and R. Bhagat, "Development and evaluation of in-situ instrumentation for cylindrical Li-ion cells using fibre optic sensors," *HardwareX*, **3**, 100-109 (2018).
- [5] M. Nascimento, M. S. Ferreira, and J. L. Pinto, "Real time thermal monitoring of lithium batteries with fiber sensors and thermocouples: A comparative study," *Measurement*, **111**, 260-263 (2017).

# Fabrication of a Flexible Tactile Sensing System with Macro-Bend Optical Fiber Sensors

**Diogo Lugarini, Vinicius de Carvalho, Marcos Aleksandro Kamizi, José Luís Fabris, Marcia Muller**

*Federal University of Technology-Paraná, 3165 Av. Sete de Setembro, Curitiba, Brazil, 80230-901; diogolugarini@gmail.com, vcarvalho2812@gmail.com, marcoskamizi@gmail.com, fabris@utfpr.edu.br, mmuller@utfpr.edu.br*

**Abstract:** Fabrication steps of a sensing system composed of four optical fiber macro-bend sensors embedded in silicone sheet are described. Sensing ability was tested by individually applying loads from 0.0 kg to 3.0 kg on the sheet surface. Preliminary results show the system ability of detecting loads applied in areas not coinciding with the sensors positions.

## 1. Introduction

Optical fiber and its based technologies have been extensively exploited in the last decades promoting advances and innovations in different areas. Industries, mainly those related with optoelectronics and optical communications, have experienced a remarkable growing by reducing fabrication costs and providing new technologies also used to leverage other areas as optical fiber sensing [1]. Optical fiber inherent characteristics as reduced weight and size, electromagnetic immunity, high sensitivity and high temperature resistance enable its application for sensing parameters as electrical and magnetic fields, temperature, pressure, vibration, deformation, humidity, among others [2]. As a consequence of the optical fibers great versatility, more complex applications have emerged requiring simultaneous monitoring of single or multiple parameters. As a result of the efforts spent to fulfill the special sensing needs, a great variety of multiplexing and distributed optical fiber systems have been proposed [3]. A multiplexed sensing system allows collecting information from each sensor of a sensing array enabling the mapping of the measurand over a large area, with a simpler setup when compared with a non-multiplexed system.

Among the optical fiber sensors, those based on macro-curvatures which are intensity-modulated sensors play an important role due to the simple and low-cost characteristics of fabrication as well as interrogation schemes. Intensity losses, resulting from coupling between guided and radiation modes that occur when the fiber bending changes, are the basis of the macro-bend sensors operation. However, since losses in optical fibers are also wavelength dependent, complex models have been developed to take in account the combined effect of both parameters [4-6]. Nevertheless, simplified models consider losses having exponential dependence with the curvature radius and wavelength as  $\exp(-R)$  and  $\exp(+\lambda)$ , respectively [7]. Another phenomenon that allows the application of this type of sensor is the interference between whispering gallery modes and the core mode, which results in fringes in the transmission spectrum of the fiber [8,9]. Such class of devices was applied, e.g., for voltage and temperature sensing as well as part of a refractometer [10-12].

In a previous work, it was proposed a method for multiplexing a set of in-series optical fiber macro-bend sensors [13]. The method was tested in the detection of the location and magnitude of loads applied directly on the sensors. In this work, a set of macro-bend sensor elements was embedded in silicone elastomer forming an array of four in-series sensors. Preliminary tests were carried out in order to determine the system ability in detecting loads applied in areas that are not coinciding with the sensors locations.

## 2. Methodology

The sensing array is composed of four in-series macro-curvature sensors embedded in a silicone elastomer sheet (Dow Corning, BX3-8001). This elastomer was used in previous works for encapsulation of FBG based sensors, where the sensitivity and hysteresis characteristics of the silicone were studied [14,15]. First, the four sensor elements were individually fabricated using monomode optical fiber (SSMF, G-652, Draktel), producing four slightly different sensors. Each element is an optical fiber loop with diameter of 5.0 mm encapsulated in silicone elastomer (Dow Corning, BX3-8001) resulting in a small cylinder, Figure 1. Then, the four elements were adequately arranged in a square mold, with the lateral surface of the cylinders kept in contact with the mold. After than, the mold is filled with silicone elastomer in order to completely embed the elements forming a square sheet with smooth and flat surface and dimensions of  $(100.00 \pm 0.05)$  mm x  $(100.00 \pm 0.05)$  mm x  $(8.00 \pm 0.05)$  mm, Figure 2(a). Sensing is based on the intensity changes of the optical signal transmitted by the set of sensors when loads are applied on the sheet surface. Five different regions of sensing indicated in Figure 2(b) were tested by detecting the transmitted signal when loads of 0.5 kg, 1.0 kg, 1.5 kg, 2.0 kg, 2.5 kg or 3.0 kg

were positioned on one of the sensing regions. The transmitted spectra were recorded 10 s after the loads application. Each test, carried out at a controlled temperature of  $(22.0 \pm 0.5) ^\circ\text{C}$ , was repeated 10 times in time intervals of 20 s.

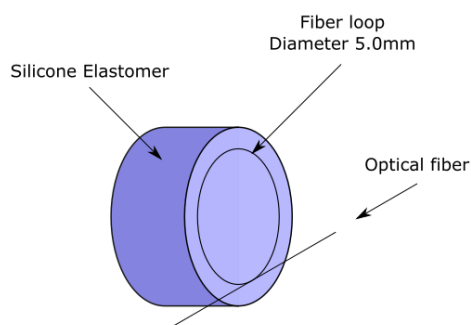


Fig. 1 - Diagram of an individual cylindrical sensor element. The fiber is encapsulated with a 5 mm diameter loop in silicone elastomer.

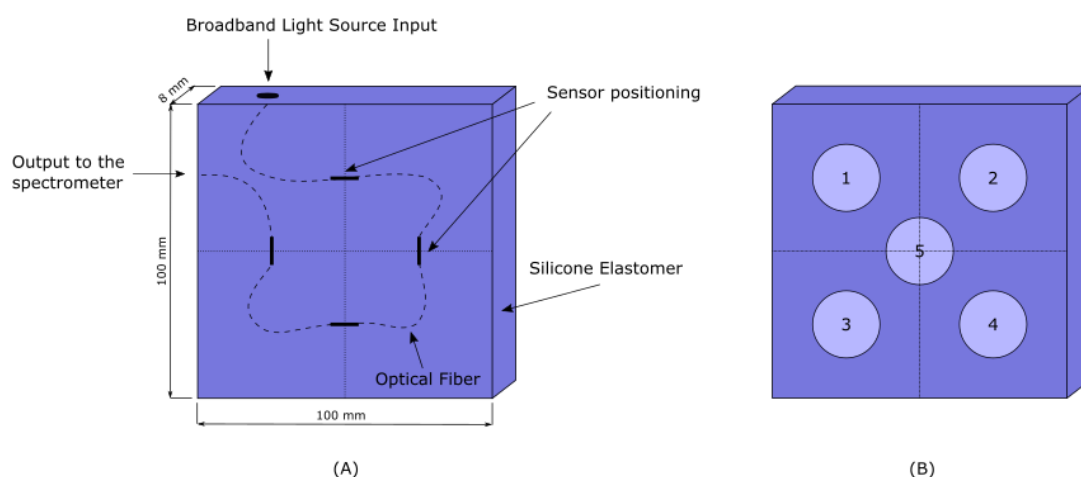


Fig. 2 - Square sensing array: (a) Sensors positioning: the four individual in-series sensors are encapsulated together and symmetrically in a mold filled with the same silicone elastomer, forming a flexible tactile system. (b) The five sensing areas used to probe the sensing scheme.

Light of a broadband visible source (LS-1 Tungsten halogen lamp, Ocean Optics, 360 a 2000 nm) transmitted by the sensing array is collected by a spectrometer (HR4000, Ocean Optics) and its spectrum is recorded in the range from 400 to 800 nm. Each spectrum is averaged 10 times with an acquisition time of 70 ms. The interrogation scheme is shown in Figure 3.

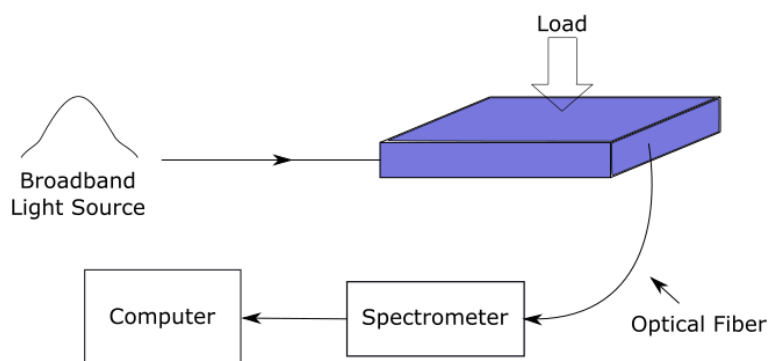


Fig. 3 – Interrogation scheme used to characterize the tactile sensing system.

### 3. Results and Discussion

In order to evaluate the macro-bend sensor ability of detecting loads, an individual macro-bend sensor element was submitted to loads from 0 kg to 3.0 kg applied directly on the lateral surface of the silicone cylinder. The obtained results are shown in Figure 4, which reveals a complex behavior for the sensor. Each applied load produces a distinct transmission spectrum, nevertheless with a different non-linear response at any specific wavelength. The observed spectral changes are associated with both, bending losses and light coupling between whispering gallery modes and core mode.

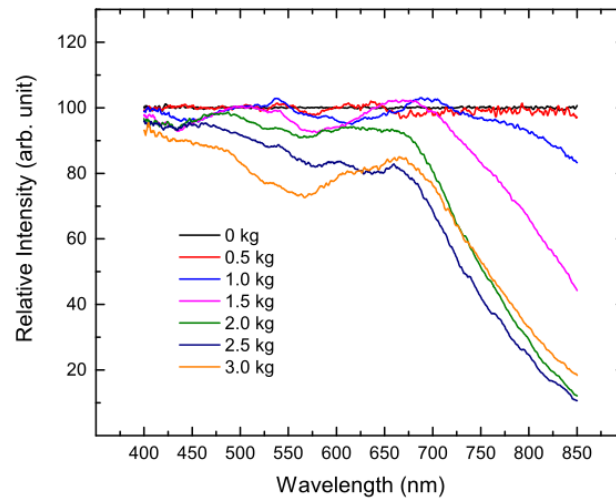


Fig. 4 - Transmission spectra obtained for different loads applied directly to an individual macro-bend sensor.

Figure 5 shows the sensing array response to different loads applied individually on the 5 regions indicated in Figure 2. For all the tested loads and sensing regions, changes are observed in the transmission spectrum of the sensing array at the visible spectral region. From a general point of view, as the applied load increases more perceptible spectral changes are generated. Transmission spectra are distinct when the sensing array is submitted to a specific load on different regions. This behavior points out to the possibility of extracting the spatial information coded in the signal, related to the load application position. Besides, different loads acting in the same position changes the array transmission, making possible to access the magnitude of load from the spectrum.

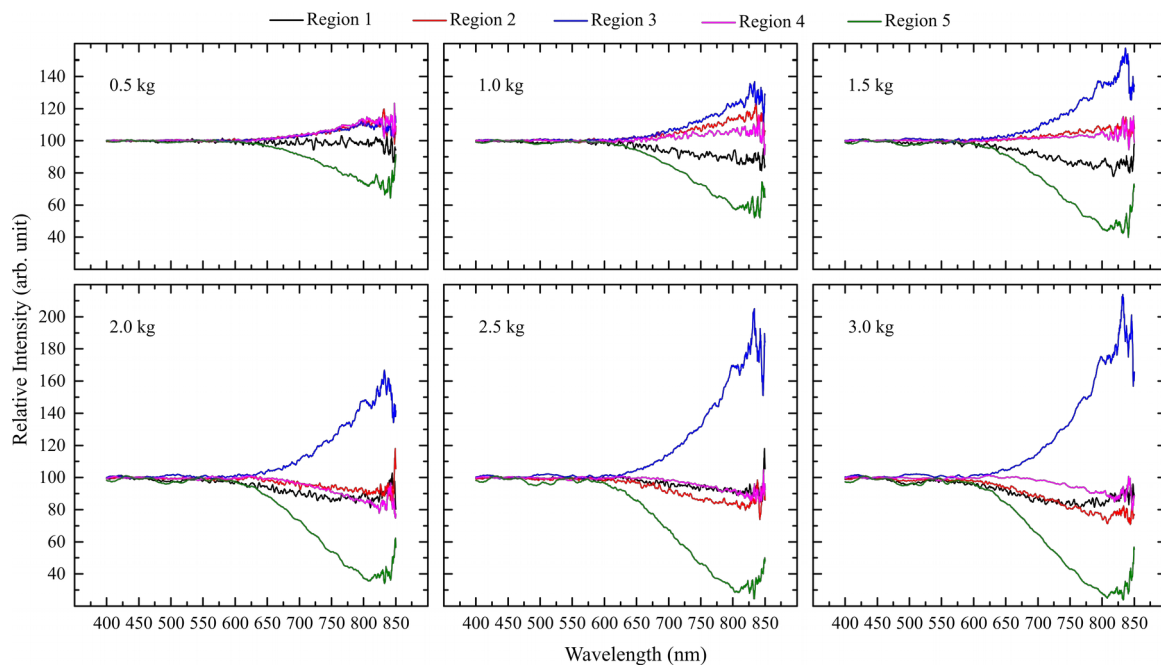


Fig. 5 - Transmission spectra obtained for different loads applied individually on 5 different regions of the sensing array.

Positive or negative intensity changes can be produced depending on both, the load and the position of the sensor elements with respect to the sensing region. Regardless the magnitude of the load, for the tested sensing array, the central sensing region (named region 5) results in more significant losses. For this configuration, the detected intensity losses are probably due to deformations induced in the four sensing elements. On the other hand, the most significant positive changes of intensity are produced with load application on sensing region 3. Despite being pairs of regions symmetric and diagonally opposite, regions 1 and 4 as well as 2 and 3 provide distinct transmission spectra when subject to a same load. Because the four sensors are slightly different, it is possible to create regions that have different sensitivities when subjected to the test loads. Therefore, despite the symmetry between regions and sensor distribution, it is expected that symmetrically spaced regions present different sensitivities, which justifies, for example, the high sensitivity of the region 3 when compared with the 1, 2 and 4 regions.

The complexity of the spectral changes generated in the transmission spectrum when a load is applied to the sensing array is associated with bending losses occurring in the sensing elements as well as light coupling from whispering gallery modes. The combined response of the four sensors depends on the manner in which the array of sensors is affected by the applied load and carries information about the wavelength dependent intensity losses.

#### 4. Conclusions

A flexible sensing system based on an array of macro-bend sensors containing a reduced number of sensors regarding the number of sensing regions was fabricated. The preliminary tests carried out with the sensing system indicate that the information present in the array transmission spectra at the visible spectral range may be used for the determination of the magnitude and/or location of loads applied to the system. For this purpose, additional tests involving not only the simultaneous application of two or more loads but also the increase in the number of sensing areas are still necessary. Additionally, a detailed examination of the results should lead to the choice of an adequate method for the data analysis.

Other sensing approaches can be used to evaluate the multiplexing capability of optical sensors, such as the optical time domain reflectometry (OTDR) or fiber Bragg gratings (FBGs). Compared with OTDR, the main advantage of the system proposed in this work is its spatial resolution. The most common OTDR systems have a spatial resolution of about 1 m, whereas the system demonstrated here have an average distance of 4 cm. On the other hand, FBGs normally require the use of more expensive infrared interrogation equipment when compared with the visible spectrometer used in the present work.

#### Acknowledgments

The authors acknowledge the financial support received from Coordenação de Aperfeiçoamento de Pessoal de Nível Superior – Brasil (CAPES) – Finance Code 001, CNPq, FINEP and Fundação Araucária.

#### References

- [1] E. Udd, "An overview of fiber-optic sensors," *Review of Scientific Instruments* **66** (8), 4015-30 (1995).
- [2] B. Gholamzadeh, H. Nabovati, "Fiber Optic sensors," *World Academy of Science, International Scholarly and Scientific Research & Innovation* **2** (6), 1107-17 (2008).
- [3] P. Dakin, "Multiplexed and distributed optical fibre sensor systems," *Phys. E: Sci. Instrum.* **20** (8), 954-67 (1987).
- [4] H. F. Taylor, "Bending Effects in Optical Fibers," *Journal of Lightwave Technology*. **LT-2** (5), 617-28 (1984).
- [5] D. Marcuse, "Curvature loss formula for optical fibers," *Journal of the Optical Society of America* **66** (3), 216-220 (1976).
- [6] J. Sakai, "Simplified bending loss formula for single-mode optical fibers," *Applied Optics* **18** (7), 951-52 (1979).
- [7] S. L. Tsao and W. M. Cheng, "Simplified formula of bending loss for optical fiber sensors," *Fiber and Integrated Optics* **21** (5), 333-44 (2002).
- [8] S. H. Nam and S. Yin, "High-temperature sensing using whispering gallery mode resonance in bent optical fibers," *IEEE Photonics Technology Letters*. **17** (11), 2391-93 (2005).
- [9] A. J. Harris and P. F. Castle, "Bend Loss Measurements on High Numerical Wavelength and Bend Radius," *Journal of Lightwave Technology* **LT-4** (1), 34-40 (1986).
- [10] P. Wang, Y. Semenova, Q. Wu, G. Farrel, "A fiber-optic voltage sensor based on macrobending structure," *Opt. and Laser Technol.* **43** (5), 922-4 (2011).
- [11] P. Wang, G. Rajan, Y. Semenova, G. Farrel, "Temperature dependence of a macrobending edge filter based on high-bend loss fiber," *Opt. Lett.* **33** (21), 2470-2 (2008).

- [12] P. Wang, Y. Semenova, Q. Wu, G. Farrel, Y. Ti, J. Zheng, "Macrobending single-mode fiber-based refractometer," *Appl. Opt.* **48** (31), 6044- 49 (2009).
- [13] M. A. Kamizi, M. A. Pedroso, J. L. Fabris, M; Muller, "Smartphone technology applied in an approach for multiplexing of fibre optic intensity-modulated macro-bend based sensors," *6<sup>th</sup> International Conference on Optical Fiber Sensors -OFS26, TuE82*, (2018).
- [14] M. A. Kamizi, M. A. Pedroso, J. L. Fabris, and M. Muller, "Fabrication and characterization of fiber Bragg grating based sensors for force measurements," in *2017 SBMO/IEEE MTT-S International Microwave and Optoelectronics Conference (IMOC)*, (2017).
- [15] M. A. Pedroso, L. H. Negri, M. A. Kamizi, J. L. Fabris, and M. Muller, "Tactile Sensor Array with Fiber Bragg Gratings in Quasi-Distributed Sensing," *Journal of Sensors*, **2018**, 1-8 (2018).

# Experimental and Simulated Curvature Analysis in a Structure Based on Core Diameter Mismatch

Felipe Masashi Takeda<sup>1</sup>; Victor Henrique Rodrigues Cardoso<sup>1</sup>; Cindy Stella Fernandes<sup>2</sup>; João Weyl Costa<sup>1</sup>; Maria Thereza Miranda Rocco Giraldi<sup>3</sup>.

*Laboratory of Applied Electromagnetism - Federal University of Pará - Belém - Brazil<sup>1</sup>*

*Laboratory of Applied Electromagnetism - Federal University of the south and southeast of Pará - Marabá - Brazil<sup>2</sup>*

*Laboratory of Photonic - Military Engineering Institute - Rio de Janeiro - Brazil<sup>3</sup>*

*e-mail: felipemasashitake@gmail.com*

**Abstract:** In this paper a study of multimodal interferences in optical fiber curvature sensor is presented. The sensor consists of a Mach-Zehnder interferometer based on Core Diameter Mismatch technique. The analysis provided a numerical model of adjustment by the diameter in the multimode section with the purpose of acquiring better linear results.

## 1. Introduction

Recent advances and cost reductions in optical devices have stimulated the interest in Optical Fiber Sensors (OFS) applied to measure physical and mechanical parameters. Countless researches have exposed the great advantages of OFS such as low cost, compatibility, electromagnetic interference immunity, applicability and their versatility such as sensors of temperature, vibration, magnetic field, curvature, among others compared to conventional ones [1-4]. The wide versatility of optical sensors permits the measurement of curvature with great applicability as fluid flow sensor [5] and monitoring of Structural Health Monitoring (SHM) [6]. In these cases the real-time measurement sensor is crucial for the quantification of structural data in order to provide the reliability of the results [7]. Considering this fact, optimization methods become extremely important for the purpose of acquiring higher accuracy in instantaneous feedback measurement.

In this work the study of modal optical power propagating in Singlemode-Multimode-Singlemode-Multimode-Singlemode (SMSMS) structure with curvature enables a way to ensure adjustment in the linearity of the OFS based on core diameter mismatch technique. Section 2 shows the operation principle of the sensor. Section 3 presents the modeling of the sensor with practical results and the theoretical analysis. In section 4 it is presented the results and the reasons of the adjustment in the core diameter of the OFS based when curvature is applied.

## 2. Sensor Structure and Principle of Operation

The proposed sensor is a Mach-Zehnder interferometer and its configuration is showed in Fig. 1. The sensor is formed by fused splicing process of a Single Mode Fiber (SMF) section between two Multi Mode Fibers (MMF) sections and each MMF is spliced to an incoming and output SMF. The fused process is provided by the FSM-60S splicing machine from Fujikura Ltd. The MMFs sections act as light couplers and re-couplers due to the core diameter mismatch, and the SMF section in the middle acts as the sensor element due to the modes that propagate in its cladding [7]. The fibers used in this work have the following diameters of core/cladding: SMF is standard SMF-28 from Corning, Inc. and MMF 105/125  $\mu\text{m}$ .

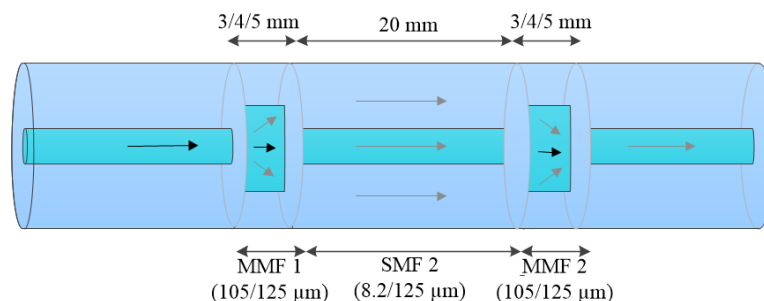


Fig. 1. Schematic diagram of the SMSMS structure.

The light of the Broadband source (BBS) is injected into the input SMF to MMF1. The BBS used is the SLD1005S THORLABS model. Part of the light scatters in the MMF region. When the light is coupled from MMF1 to SMF2 low order cladding modes are excited [7]. The cladding modes will be re-coupled to the fundamental mode of the output SMF through the MMF2, in this union point the modes interfere with each other due to the phase difference between them [7].

### 3. Experimental Setup and Simulation

Fig. 2 shows the experimental setup, which bend measurements were performed by fixing the SMSMS sensor straightly on two blocks. One of them was mounted on a micropositioner stage for bending the fiber. The measurement was performed using an Optical Spectrum Analyzer (OSA) and BBS operating with a bandwidth of 100nm and a central wavelength at 1550nm. When the light from the BBS is injected into the straight fiber, the OSA is used to interrogate the sensor when the bent is applied. The range of curvature is calculated using Eq.1 [8].

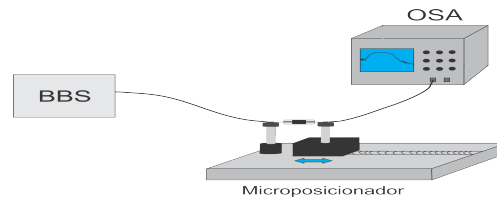


Fig. 2. Experimental Setup.

$$C = \frac{1}{R} = \frac{2h}{h^2 + (d/2)^2} \quad (1)$$

where  $d = L_0 - \Delta L$ ,  $L_0$  is the initial distance between the two micro-positioners,  $\Delta L$  is the distance variation and  $h$  is the bend deepness. The MMFs sections, due to the large CDM, act as light couplers and re-couplers, and the SMF section in the middle acts as the sensor element due to the modes that propagate in its cladding. Initially, three lengths of MMFs sections were analyzed: 3mm, 4mm and 5mm. As one can observe in Fig. 3(a), for the curvature range from  $2.8\mu\text{m}^{-1}$  to  $5.5\mu\text{m}^{-1}$ , the length that performs an acceptable linear behavior is 4mm, while those of 3mm and 5mm present positive and negative trends inclination depending on the curvature range. This phenomenon is explained by the influence of the field deformation consisting in a possibility to use a range of curvature in multimode optical fiber structures that provide the decrease in the radiation losses of low order modes and increase the losses in high order modes [9]. Thus, the length of 4 mm was chosen for the analysis of the sensor.

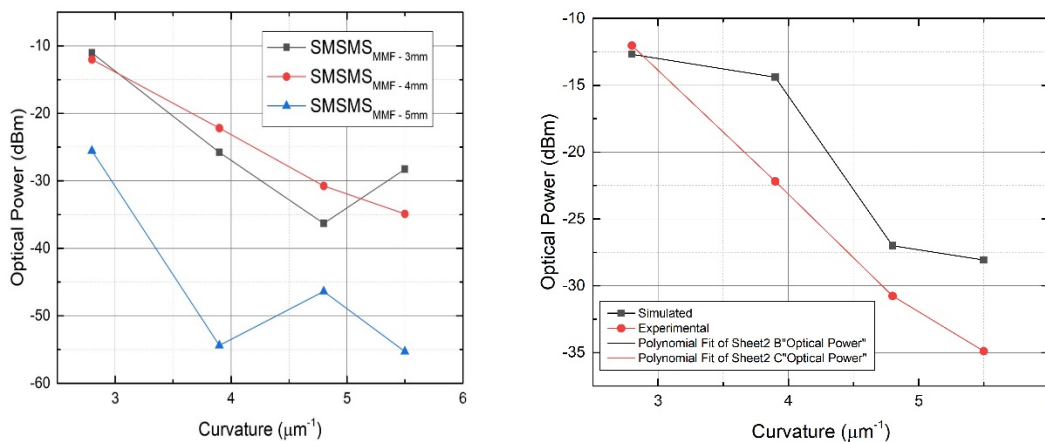


Fig. 3. (a) Experimental Results for 3mm,4mm and 5mm of MMF section length. (b) Experimental and Simulated curves are compared to SMSMS curvature sensor with 4mm MMF length.

Fig. 3(b) compares the experimental and simulation results for the sensor which comprises the MMFs with 4 mm. The simulations were performed using the Beam Propagation Method (BPM), through the BeamPROP® program from Rsoft company in conjunction with the conformal mapping technique [10] which consists of a coordinate transformation in which a curved fiber is represented in a straight line, as described by Eq.2:

$$n_{eq}(x, y) = n(x, y) \left( 1 + \frac{x}{R_{eff}} \right) \quad (2)$$

where  $n_{eq}(x, y)$  is the equivalent refractive index,  $n(x, y)$  is the refractive index of the straight fiber,  $R_{eff}$  is the equivalent bend radius and  $x$  is the perpendicular axis in which the curvature occurs. A 3D-BPM model was used with an implicit finite-difference approach. It is necessary to consider that analyzing the input numerically approximations are fundamental to acquire better results like boundary conditions and grid. The maximum and minimum value of the mesh grid was  $1\mu\text{m}$  and  $0.01\mu\text{m}$  respectively and the value of the wavelength used was  $1550\text{nm}$  to get closer to the experiment. Transparent boundary conditions were numerically included to avoid reflection of computational mesh limits. We used only 4 sampling points due to the high fragility of the sensor within the range of macro curvature. The information collected was sampled as the sensor was curved and then sampled again stretching the sensor to realize that in this array of curvature the sensor was in the elastic region of deformation [11]. Fig. 3(b) shows that the simulated result has a non-linear behavior with a loss tendency like the experiment result.

#### 4. Results and Discussion

It has been numerically and experimentally verified that variations in the structure specifications cause changes in the sensor output results. Fig. 4 shows the energy per length of the SMSMS fiber structures with diameter of the MMFs of  $50\mu\text{m}$ ,  $62\mu\text{m}$  and  $105\mu\text{m}$  in curvature action. The results obtained numerically show that the structures for  $50\mu\text{m}$  and  $62\mu\text{m}$  to this range of curvature ( $2.8\mu\text{m}^{-1}$  to  $5.5\mu\text{m}^{-1}$ ) do not have a desirable behavior. One of the factors is the presence of energy peaks by constructive modal interferences in the MMF1 marked by red. These peaks vary the amplitude as a function of the curvature by the same reason of the field deformation. This effect provides difficulties to acquire more linearity in the results in Fig. 4(a) and Fig. 4(b). In contrast, the structure with MMF diameter of  $105\mu\text{m}$ , Fig. 4(c), presents more stable energy propagation through the fiber length.

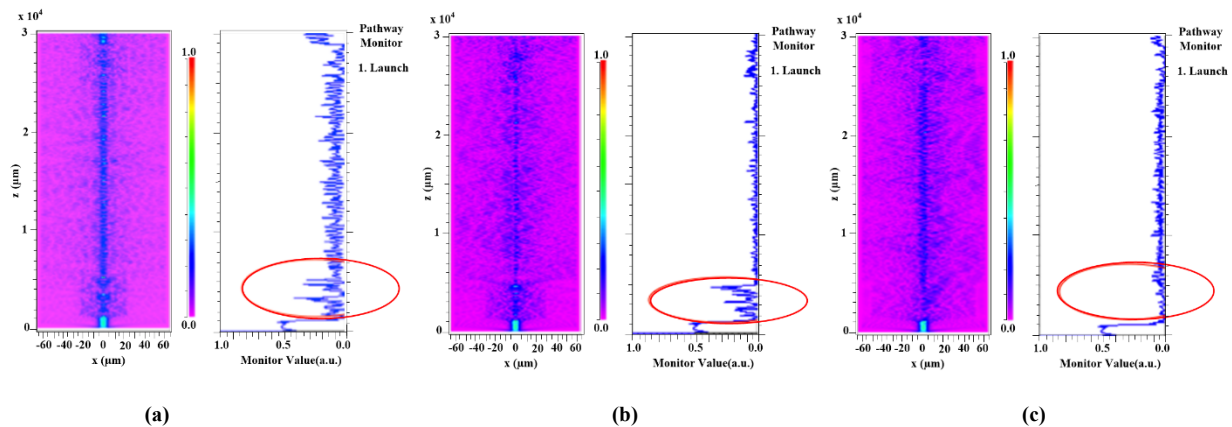


Fig. 4. Energy per length of the SMSMS fiber structure:  $50\mu\text{m}$ (a)  $62\mu\text{m}$ (b) and  $105\mu\text{m}$ (c)

Considering a SMSMS curvature sensor with  $105\mu\text{m}$  of core diameter and length of  $4\text{mm}$  as the best option within the range of analyzed parameters we can consider the internal modal power division in curvature action like one of the cases to study with the finality to acquire a better performance in the sensor. It is possible to change the number of modes excited in the input of a multimode sensor varying the width of the multimode section thereby creating a new energy distribution in modes. The numerical simulation was performed to enhance the SMSMS curvature sensor (Fig. 3(b)). In this case, varying the multimode section diameter, one can provide different propagation energies of the modes as a function of the curvature and find one with good performance to base the study of this paper.

Fig. 5 presents the results of two simulated structures with the MMF core diameter sections of  $94.5\mu\text{m}$  (90 percent of  $105\mu\text{m}$ ) and  $93.45\mu\text{m}$  (89 percent of  $105\mu\text{m}$ ). The values of the determination coefficient ( $R^2$ ) are 0.96009 and 0.99831 respectively. The  $R^2$  in Fig. 3(b) is 0.88709. So, it is possible to see that adjusting some parameters of the sensor enables considerably more linearity in the result whereas the value of  $R^2$  higher than 0.99 presents good performance.

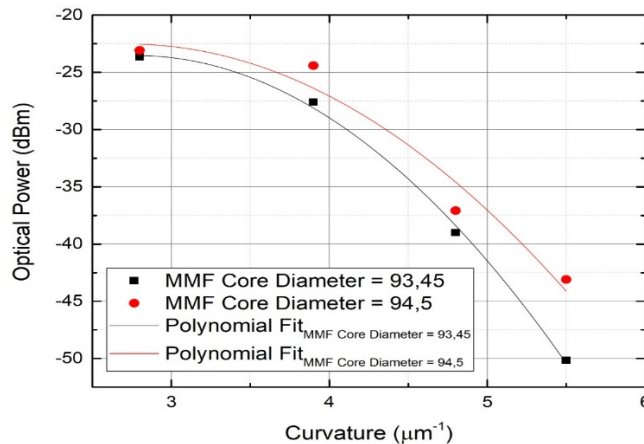


Fig. 5. Optical Power as a function of Curvature variation in SMSMS sensor with  $94.5\mu\text{m}$  and  $93.45\mu\text{m}$  of MMF core diameter.

## 5. Conclusion

In this work we presented numerical and experiment study that provided an adjustment by core diameter based on the Beam Propagation Method that is able to acquire better performance to SMSMS curvature sensor. This goal was based in studies of multimode interferences that occurs in this kind of sensor and achieved simulated results with the determination coefficient from 0.88709 to 0.99831. This analysis has a great potential for future studies to obtain a method that consists in creating a better performance in optical fiber sensors and bring to this kind of sensor more applicability to analysis that is necessary a real time feedback response.

## 6. Acknowledgment

This work was supported by the Federal University of Para (UFPA), Department of Electrical Engineering of UFPA, National Council of Scientific and Technological Development (CNPq) and Coordination of Improvement of Higher-Level Personnel (CAPES), the Military Engineering Institute (IME) and the Institute of Advanced Studies (IEAV).

## 7. References

- [1] Susana Silva, O Frazo I, J Viegas, L A Ferreira, F M Arajo, F Xavier Malcata and J L Santos (2011). "Temperature and strain-independent curvature sensor based on a singlemode/multimode fiber optic structure". (Measurement Science and Technology, Volume 22, Number 8, 2011).
- [2] Qiang Wu a,b,n, Minwei Yang a, Jinhui Yuan b, Hau Ping Chan c, Youqiao Maa, Yuliya Semenova a, Pengfei Wang a, Chongxiu Yu b, Gerald Farrell. "The use of a bend singlemode–multimode–singlemode (SMS) fibre structure for vibration sensing". (Optics & Laser Technology, 2014).
- [3] Yaofei Chen, Qun Han, Tiegeng Liu, Xinwei Lan and Hai Xiao. "Optical Fiber magnetic field sensor based on single-mode-multimode-single-mode structure and magnetic fluid". (October 15, 2013. Vol. 38, No. 20, Optics Letters).
- [4] Yinping Miao, Jixuan Wu, Wei Lin, Binbin Song, Hao Zhang, Kailiang Zhang, Bo Liu and Jianquan Yao. "Magnetic Field Tunability of Square Tapered No-Core Fibers Based on Magnetic Fluid". (Journal of Lightwave Technology, Vol. 32, No. 23, December 1, 2014).
- [5] V.H. R. Cardoso, J. C. W. A. Costa, C. S. Fernandes, L. K. D. Braga, M. O. Silva and M. T. M. R. Giraldo. "Sensor Óptico de Vazão Baseado em Técnica de Descasamento de Diâmetro de Núcleo". (18º SBMO – Simpósio Brasileiro de Micro-onda e Optoeletrônica, Santa Rita do Sapucaí. MOMAG 2018, 2018).
- [6] Hong-Nan Li, Dong-Shend Li and Gang-Bing Song. "Recent applications of Fiber optic sensors to health monitoring in civil engineering". (Engineering Structures, Elsevier, 2004).
- [7] Fernandes, C. S. "Desenvolvimento de sensores baseados em fibra óptica para monitoramento estrutural". 2016. Tese (Doutorado em Programa de Pós-Graduação em Engenharia Elétrica) – Universidade Federal do Pará.

- [8] Cindy S. Fernandes, Maria Thereza M. Rocco Giraldo, Marco J. de Sousa, João C. W. A. Costa, Carlos Gouveia, Pedro Jorge, and Marcos A. R. Franco. "Curvature and Vibration Sensing Based on Core Diameter Mismatch Structures". (IEEE Transactions on Instrumentation and Measurement, Vol. 65, No. 9, September 2016).
- [9] Dietrich Marcuse. "Field deformation and loss caused by curvature of optical fibers". (J. Opt. Soc. Am., Vol. 66, No. 4, April 1976).
- [10] Ross T. Schermer and James H. Cole. "Improved Bend Loss Formula Verified for Optical Fiber by Simulation and Experiment." (IEEE Journal of Quantum Electronics, Vol. 43, No. 10, October 2007).
- [11] Antunes, Paulo & Domingues, Fatima & Granada, Marco & André, Paulo. (2012). "Mechanical Properties of Optical Fibers". 10.5772/26515.

# Fabrication of Arc-Induced Long Period Fiber Grating with Opposite Point-by-point Modulation

F. S. Delgado, Deivid Campos, T. V. N. Coelho and A. Bessa dos Santos

Federal University of Juiz de Fora, Electrical Engineering Department, Juiz de Fora - MG, Brazil, 36036-330  
felipe.souza@engenharia.ufjf.br

**Abstract:** We demonstrate the fabrication of an arc-induced long period fiber grating (LPFG) with opposite point-by-point modulation. The produced LPFG exhibited low polarization dependent loss (PDL) and a linear torsion sensitivity up to 0.197 nm/(rad/m), which is higher than that of the traditional arc-induced LPFGs.

## 1. Introduction

Long Period Fiber Gratings (LPFGs) are optical devices, which have been widely used in optical fiber communication [1,2] and sensing systems [3,4]. Over the years, different methods for fabricating LPFGs have been demonstrated. For instance, LPFGs were fabricated based upon ultraviolet (UV) laser irradiation [5], mechanical deformation [6], electric arc induced perturbations [7] and CO<sub>2</sub> exposure method [8]. Among them, the arc discharge method has particularly drawn wide attention due to its straight, flexible and economical step-by-step procedure [9]. In this method, the grating is produced by exposing periodically the longitudinal axis of the optical fiber to electric arc discharges, which are generated by a fusion splicer machine. During the inscription procedure, the fiber is kept under constant longitudinal tension, which thins and elongates the fiber section heated by the arc discharge [10]. Moreover, the electric arc discharge has a temperature gradient, which causes asymmetry of perturbation in the optical fiber and therefore, induces transverse and longitudinal perturbations in each arc-induced section and depends on the fabrication conditions [11,12]. Furthermore, the formation of the LPFGs are mainly attributed to the modulation in the geometry along the optical fiber due to fiber localized tapering and changes in the refractive index of the silica [13-15].

In this paper, we report a new fabrication technique of arc-induced LPFGs. Distinguishing from the traditional arc discharge technique for inscribing LPFGs, the proposed method is based on axial rotation of the optical fiber at each electric arc discharge so that the induced asymmetric perturbation rotates by an axial angle of 180° along the axial direction of the fiber. Therefore, inducing the opposite asymmetric modulations along the cross section of the fiber. Moreover, we present an investigation of the torsion sensitivity of the produced LPFG and its spectral characterization of polarization dependent loss (PDL). By using the proposed electric arc technique, the results show that it is possible to fabricate a grating sensor with a low PDL less than 1 dB, whose torsion sensitivity is higher than that of the conventional arc-induced LPFGs.

## 2. LPFG fabrication

The representation of the experimental setup for fabricating the LPFG rotated by an axial angle of  $\theta = 180^\circ$  at each electric arc discharge is shown in figure 1. We developed an automatic computer-assisted fabrication process to control the inscription process of the grating and improve the alignment of the fiber position and electrodes. It consists of a commercial fusion splicer (Jilong KL-300T) integrated with two motorized rotation and translation stages (RTS), a mass of 12 g weight to apply a constant tensile force of approximately 0.12 N to the fiber before it is fixed in the RTS, a high precision pulley, and a personal computer (PC). Furthermore, the inscription system has two high precision rotation and translation stages (RTS). Each one comprises a translation motor to displace the fiber in +z direction and a rotation motor to perform the rotation of the fiber by an axial angle of  $\theta = 180^\circ$ . It is important to note that both RTS 1 and RTS 2, which can be observed in figure 1, are synchronized and controlled by a personal computer. Therefore, the translation motors move the optical fiber in the same direction (+z) at the same time, whereas the rotation motors rotate the fiber by the same axial angle. Moreover, we used two flags attached to both ends of the fiber to visualize the rotation of the optical fiber at each arc discharge throughout the fabrication process. The grating sensor was inscribed in a Corning SMF-28 with arc power of 90 bits (manufacturer unit), exposure time of 500 ms, and grating period of  $\Lambda = 530 \mu\text{m}$ . The transmission spectrum of the LPFG was monitored using an Optical Spectrum Analyzer (OSA) from Anritsu (MS9740A) with a wavelength resolution of 30 pm and its built-in broadband light source (BBS). The proposed fabrication procedure consists of two main steps. The first step consists of applying the first electric arc discharge, moving the fiber according to the desired grating modulation period towards +z direction, which translates the fiber to the next arc discharge longitudinal position, and rotating the fiber by an axial angle of  $\theta = 180^\circ$ . The second one performs the next arc discharge, inverse rotates the optical fiber, which implies in an axial rotation of  $\theta = 180^\circ$  in the opposite direction (- $\theta$ ), and translates the fiber in +z direction for the next electric arc discharge position. Then, these steps are repeated many times until a desired transmission spectrum is achieved.

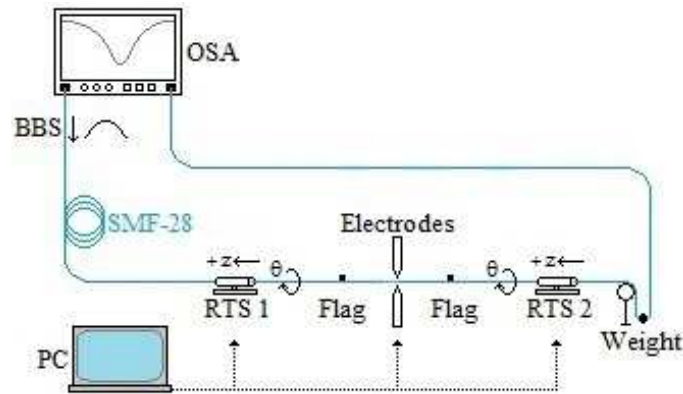


Fig. 1. Schematic representation of the fabrication setup of LPFGs with rotation of the fiber by an axial angle of  $\theta = 180^\circ$ .

Figure 2 shows the experimental microphotograph of produced grating, which emphasizes a section of the LPFG with the location of two consecutive arc zones and therefore, representing an approximation of the modulation period of the grating. In addition, we can observe the geometric modulation of the optical fiber, which is visualized as a reduction of the fiber diameter of approximately  $14.1 \mu\text{m}$ . Figure 3(a) shows the transmission spectrum of the LPFG produced with grating modulation period of  $\Lambda = 530 \mu\text{m}$ , grating length of  $20\Lambda = 10.6 \text{ mm}$  and axial rotation angle of  $180^\circ$ . Besides, we can observe two attenuation dips located at resonant wavelengths of  $1505.37 \text{ nm}$  and  $1565.75 \text{ nm}$ . In order to identify the cladding modes of the resonant wavelengths observed in figure 3(a), we have simulated the phase-matching curves for the produced LPFG using *OptiGrating v. 4.2* software by *Optiwave*, which can be observed in figure 3(b).

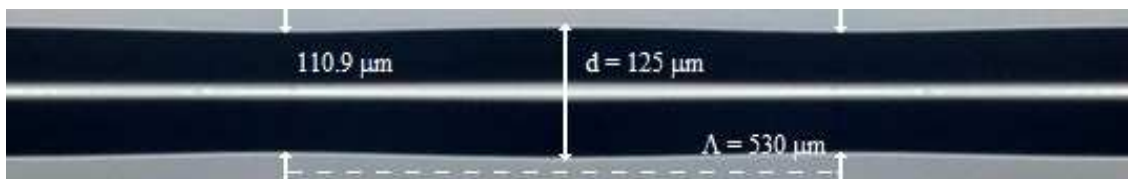


Fig. 2. Microphotograph of the LPFG produced with opposite point-by-point modulation.

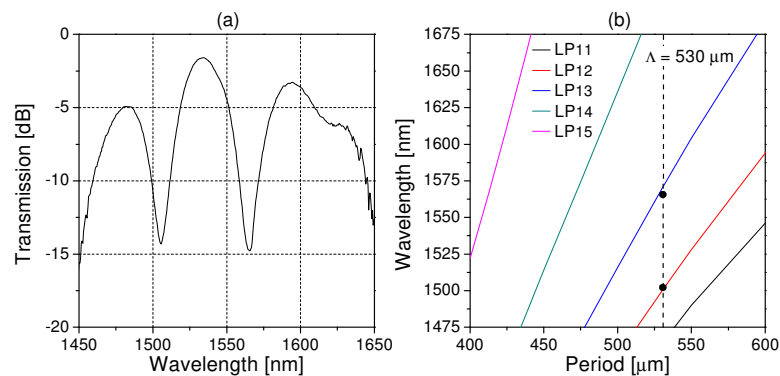


Fig. 3. (a) Transmission spectrum of the produced LPFG with  $\Lambda = 530 \mu\text{m}$  and fiber axial rotation angle of  $\theta = 180^\circ$  at each arc discharge. (b) Simulation of the phase-matching curves (solid lines) and experimental values (black dots).

### 3. Results

In order to analyze the torsion sensitivity of the LPFG produced with opposite point-by-point modulation, we investigated the spectral response of the different attenuation dips observed in figure 3(a), which have been identified as the  $LP_{12}$  and  $LP_{13}$  cladding modes. Torsion tests were performed using the same setup used for fabrication by fixing the optical fiber with the LPFG in the middle between two rotation and translations stages (RTS-1 and RTS-2), with  $14 \text{ cm}$  separation length ( $L_0$ ) between them. Furthermore, it is important to mention that one end of the fiber was fixed to the RTS-1, which provided controlled mechanical torsion to the grating, whereas the other one was fixed to the RTS-2, which was stationary. During the tests, the torsion rate  $\tau$  was measured by the applied angle  $\alpha$  and the twist length  $L_0$ , such that  $\tau = \alpha/L_0$ , and the torsion angles ( $\alpha$ ) varied in the range from  $0^\circ$  to  $360^\circ$  in steps of  $60^\circ$ , which equals to a torsion rate in the range  $0\text{--}44.88 \text{ rad/m}$ .

Figure 4 shows the experimental results for the LPFG exposed to the effects of torsion and its inset graphs show the spectral evolutions of resonance dips of the LP<sub>12</sub> and LP<sub>13</sub> cladding modes. In the inset graphs of figure 4, we can observe that the transmission of the attenuation bands decrease as the torsion rate increases. We can also observe that the resonant wavelength of both cladding modes shift continuously in the direction of shorter wavelengths of the spectrum as the mechanical torsion increases. At the torsion rate of 44.88 rad/m, the attenuation band of the LP<sub>12</sub> cladding mode shifted from 1505.35 nm to 1499.31 nm, with a spectral variation shift of -6.04 nm, whereas the resonance dip of the LP<sub>13</sub> mode, which was initially at 1565.75 nm, tuned to 1557.30 nm, therefore, experiencing a total wavelength shift of -8.45 nm. Moreover, it was found that the response of both cladding modes varied monotonically and linearly and by experimental data fitting with a linear regression approach, the LP<sub>12</sub> cladding mode showed a sensitivity of -0.13369 nm/(rad/m) with high degree of torsion linearity, confirmed by the R<sup>2</sup> coefficient of 0.999 derived from the fitting process. On the other hand, the experimental data fitting of the LP<sub>13</sub> mode resulted in an enhanced sensitivity of 0.19702 nm/(rad/m) with a R<sup>2</sup> coefficient value of 0.998 over the torsion sensing range, as observed in figure 4. It is important to mention that the torsion sensitivity of the LPFG with opposite point-by-point modulation is higher than that of a traditional arc-induced LPFG. For instance, a torsion sensitivity of 0.0245 nm/(rad/m) was reported in [16].

We also report the polarization characteristics of the arc-induced LPFG with opposite point-by-point modulation. As shown in figure 5, for the produced grating a maximum PDL value is up to 0.87 dB, which is relatively lower than the typical values of LPFGs fabricated by the traditional arc discharge technique [17,18].

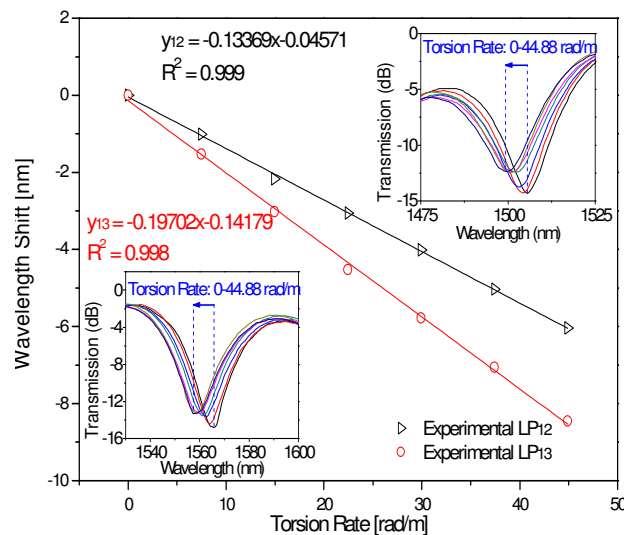


Fig. 4. Experimental data fit of the measured resonant wavelength shift of the LP<sub>12</sub> and LP<sub>13</sub> cladding modes as a function of torsion rate.

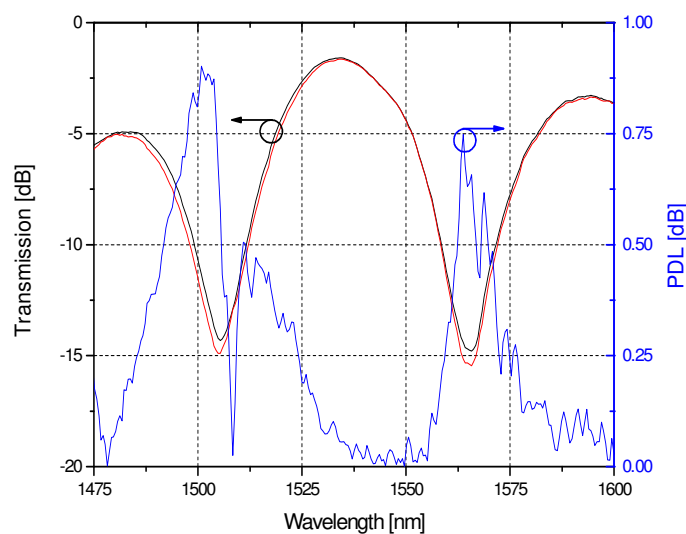


Fig. 5. Transmission spectrum of LPFG for minimum (red) and maximum (black) transmission, and PDL (blue) measurement.

#### 4. Conclusion

We have presented the opposite point-by-point modulation fabrication technique to realize arc-induced LPFGs. By using this technique, it is possible to produce LPFGs with higher torsion sensitivity than the conventional arc-induced LPFGs and decrease the intrinsic polarization dependent loss, which is one of the weakness of these gratings.

#### 5. Acknowledgements

The work was supported by funding from Coordenação de Aperfeiçoamento de Pessoal de Nível Superior (CAPES), CNPq, INERGE, FAPEMIG and CPFL Energia.

#### 6. References

- [1] J. Wei, M.-Y. Chen, Q. Xiang, R. Huang, "Design of a mode-field converter based on a two-core optical fiber with a long-period fiber grating," *Opt. Eng.* 55(6) 066110 (14 June 2016).
- [2] A. Hasegawa-Urushibara, T. Mori, T. Sakamoto, M. Wada, T. Yamamoto, K. Nakajima, "Experimental verification of mode-dependent loss reduction by mode coupling using long-period grating," 2017 Optical Fiber Communications Conference and Exhibition (OFC), Los Angeles, CA, 2017, pp. 1-3.
- [3] J. Hromadka, S. Korposh, M. C. Partridge, S. James, F. Davis, D. Crump, S.-W. Lee, R. P. Tatam, "Multi-parameter measurements using optical fibre long period gratings for indoor air quality monitoring," *Proc. SPIE 10323*, 25th International Conference on Optical Fiber Sensors, 103233J (23 April 2017).
- [4] J. Luo, C. Zhao, J. Li, M. He, "Study on temperature sensitivity of topological insulators based on long-period fiber grating," *Opt. Eng.* 56(6) 067106 (12 June 2017).
- [5] M. Smietana, W. J. Bock, P. Mikulic, "Comparative study of long-period gratings written in a boron co-doped fiber by an electric arc and UV irradiation." 2010 *Meas. Sci. Technol.* 21 025309.
- [6] M. Smietana, W. J. Bock, P. Mikulic, J. Chen, "Increasing sensitivity of arc-induced long-period gratings-pushing the fabrication technique toward its limits," 2011 *Meas. Sci. Technol.* 22 015201.
- [7] T. Almeida, R. Oliveira, P. André, A. Rocha, M. Facão, R. Nogueira, "Automated technique to inscribe reproducible long-period gratings using a CO2 laser splicer," *Opt. Lett.* 42, 1994-1997 (2017).
- [8] A. S. Nair, V. P. S. Kumar, and H. Joe, "Twist sensitivity of cladding-mode resonances and its cross-sensitivity to strain and temperature in a mechanically induced long-period fiber grating," *Fiber Integr. Opt.* 2014;33:347-359.
- [9] F. Esposito, R. Ranjan, S. Campopiano, A. Iadicicco, "Experimental Study of the Refractive Index Sensitivity in Arc-induced Long Period Gratings," in *IEEE Photonics Journal*, vol. 9, no. 1, pp. 1-10, Feb. 2017.
- [10] O. V. Ivanov, G. Rego, "Origin of coupling to antisymmetric modes in arc-induced long-period fiber gratings," *Opt. Express* 15, 13936-13941 (2007).
- [11] A. Martinez-Rios, I. Torres-Gomez, D. Monzon-Hernandez, G. Salceda-Delgado, V.-M. Duran-Ramirez, G. Anzueto-Sanchez, "Random period arc-induced long-period fiber gratings," *Opt. Laser Technol.* 2012;44:1176-1179.
- [12] P. Wang, M. H. Jenkins, T. K. Gaylord, "Arc-discharge effects on residual stress and refractive index in single-mode optical fibers," *Appl. Opt.* 55, 2451-2456 (2016).
- [13] R. Ranjan, F. Esposito, S. Campopiano, A. Iadicicco, "Fabrication of arc-induced long-period gratings in different silica fibers," *Proc. SPIE 10231*, Optical Sensors 2017, 102312N (16 May 2017).
- [14] G. Rego, "Arc-Induced Long Period Fiber Gratings," *Journal of Sensors*, vol. 2016, Article ID 3598634, 14 pages, 2016.
- [15] K. Mullaney, S. E. Staines, S. W. James and R. P. Tatam, "Optimised process for fabricating tapered long period gratings," 2017 25th Optical Fiber Sensors Conference (OFS), Jeju, 2017, pp. 1-4.
- [16] P. Caldas, G. Rego, O. V. Ivanov, and J. L. Santos, "Characterization of the response of a dual resonance of an arc-induced long-period grating to various physical parameters," *Appl. Opt.*, vol. 49, no. 16, pp. 2994-2999, Jun. 2010.
- [17] G. M. Rego, J. L. Santos, and H. M. Salgado, "Polarization dependent loss of arc-induced long period fibre gratings," *Optics Communications*, vol. 262, no. 2, pp. 152-156, Jun 15, 2006.
- [18] G. Yin, J. Tang, C. Liao, and Y. Wang, "Automatic arc discharge technology for inscribing long period fiber gratings," *Appl. Opt.* 55, 3873-3878 (2016).

# Optical Current Sensor Based on Magnetostrictive Composites

Juan David Lopez<sup>1</sup>, Alex Dante<sup>2</sup>, Talitha Trovão<sup>2</sup>, Roberto Wu Mok<sup>2</sup>, Cesar Cosenza Carvalho<sup>2</sup>, Regina Celia da Silva Barros Allil<sup>2</sup>, Fabricio Borghi<sup>3</sup> and Marcelo Martins Werneck<sup>1,2</sup>

<sup>1</sup>Photonics and Instrumentation Laboratory, Nanotechnology Engineering Program

<sup>2</sup>Photonics and Instrumentation Laboratory, Electric Engineering Program

<sup>3</sup>Magnetic Nanomaterials Laboratory, Physics Institute

Federal University of Rio de Janeiro (UFRJ), RJ 21941-594, Brazil

<sup>1</sup>lopezjuan@lif.coppe.ufrj.br

**Abstract:** This paper presents a novel compact fiber-optic current sensor (FOCS) based on magnetostrictive composites that employ only 1 gram of Terfenol-D. Finite element method (FEM) simulations supported the design and construction of two versions of FOCS, which were capable to measure on a.c. current from 200 to 800 A<sub>rms</sub> in laboratory.

## 1. Introduction

Terfenol-D (TD) is an alloy of type Tb<sub>x</sub>Dy<sub>1-x</sub>Fe<sub>2</sub>, which is well-known for its giant magnetostrictive properties. These properties make TD a useful material for magnetic field sensing, which is an application that has been explored [1]. In recent years, fiber Bragg grating (FBG) sensors have been used in association with magnetostrictive materials for the development of magnetic field sensors, stress sensors, and current sensors [1-5]. Coupling TD with an FBG results in a compact current sensor that inherits intrinsic properties of optical fibers, such as immunity to electromagnetic interference (EMI), malleability, high electrical isolation, and the possibility of multiplexing several sensors in one single optical cable.

Fiber optic current sensors (FOCS) based on TD coupled with an FBG have been proposed as the core of optical instrument transformers to monitor transmission and distribution lines in replacement for heavy and large conventional current transformers (CT). In 2013, Cremonesi *et al.* proposed a FOCS with an FBG bonded to a 144-grams solid toroidal core of TD for measurement of a.c. current in the range of 200–900 A<sub>rms</sub> [4]. Since TD presents positive magnetostriction, an external a.c. magnetic field causes it to expand over positive and negative cycles of the sinusoidal field applied, which causes the output signal to be rectified. Using this effect along with external pressure applied to the TD core in order to obtain a quadratic function response, the authors simplified the direct measurement of the rms value of the applied current. In 2015, Nazaré and Werneck reported the development of an FOCS employing an FBG bonded to a 74-gram solid bar of TD [5]. In order to recover the full cycle of the current signal applied, the authors employed a d.c. magnetic biasing to the proposed sensor core by incorporating a series of permanent magnets to the magnetic circuit, which was also composed by the TD bar and Fe-Si plates. In comparison with the FBG-based FOCS proposed by Cremonesi *et al.* [4], the use of magnetic biasing allows for a detailed analysis of the current signal applied, such as harmonic distortion.

However, since TD is a brittle and expensive alloy, the use of a large, solid block of TD for the development of FBG-based FOCS should be avoided. Moreover, the operation of solid TD above a few kilohertz is significantly limited by the presence of eddy-current losses [6,7]. Thus, magnetostrictive composites of TD powder and epoxy resin, instead of using solid TD bars, have been proposed in many applications [8-11]. In 2010, Quintero *et al.* proposed a d.c. and a.c. magnetic field sensing head based on a TD composite, which was manufactured using TD particles in different sizes mixed with epoxy resin with an embedded sensing FBG [8]. In 2012, Liu *et al.* proved that magnetostrictive composites have a wide range of extrinsic magneto-optical signal frequency up to at least 60 kHz for magnetic field measurement [9]. In 2018, Elhajjar *et al.* performed a series of experiments aiming at to reduce cost, size and nonlinearities presented by solid TD [10]. The authors investigated the effects of different sizes of TD-powder composites mixed with several kinds of resins. The authors reported that composites with particles sizing range of 200–300 μm present the higher magnetostriction using a reduced mass of TD. Also, in 2018, Bieler and Werneck reported a magnetic field sensor composed by magnetostrictive TD composite with an embedded FBG applied to detect faults in industrial electric motors [11].

In this work, we present a compact FOCS based on FBG and magnetostrictive composites using TD with oriented magnetic domains for monitoring of a.c. current in transmission lines. Two versions of the proposed FOCS were manufactured and characterized in laboratory with currents from 200–800 A<sub>rms</sub>.

## 2. Proposed Sensor and Experimental Setup

Finite element method (FEM) simulations were performed as a qualitative guidance to the design of the proposed FBG-based FOCS. For the simulations was employed COMSOL Multiphysics version 5.1 with the DC and AC modules. Figs. 1(a) and 1(b) show the simulation results for the magnetic flux density induced by a d.c. current of 500 A into a TD composite ( $\mu_r = 10$ ) coupled to a pair of permanent magnets for Model 1 and Model 2, respectively. Both versions differ in geometry and in the mass of TD employed (2 grams of TD in Model 1 vs. 1 gram of TD in Model 2). As can be seen in Fig. 1(b), Model 2 presents an open-loop configuration that allows an easy installation of the proposed FOCS on the high-voltage cables for current monitoring. Fig. 1 (c) shows the proposed Model 1 and Model 2 assembled with an FBG sensor ( $\lambda_B = 1535.150$  nm) embedded within the magnetostrictive composite. A 3D-printed holder was used to accommodate all parts of the prototype in a robust assembly.

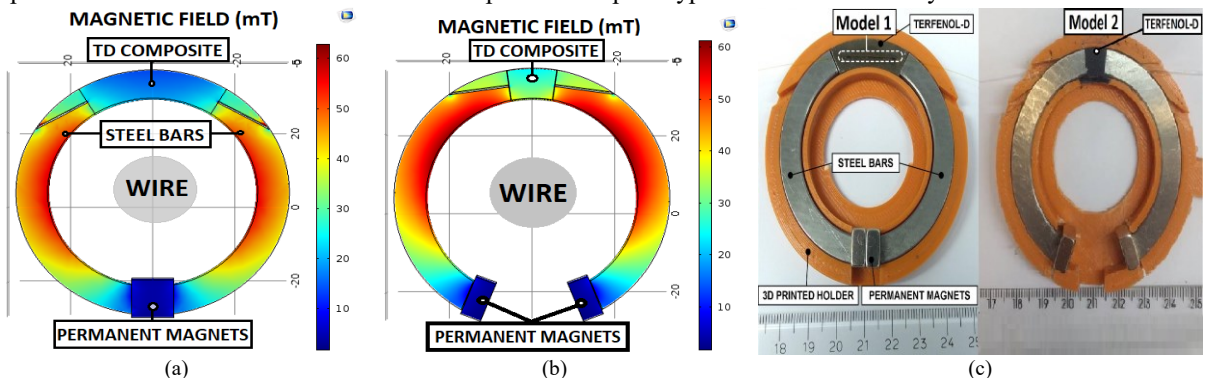


Fig. 1. (a) Model 1, FEM simulation of a d.c. magnetic field in a toroidal core of TD; (b) Model 2, simulation with reduced TD; (c) The proposed FOCS.

Steel bars (99.5% Fe,  $\mu_r = 500$ ) were employed in the proposed FOCS in order to shorten its magnetic circuit, which allowed not only a reduction in the mass of TD used, but also an increase in the magnetic flux density. In order to perform laboratory tests with the proposed FOCS, the setup shown in Fig. 2 was assembled. A current transformer (CT) was employed to induce a.c. current signals of up to 800 A<sub>rms</sub> to the proposed FOCS. A homogeneous mixture of resin (X-120<sup>TM</sup> adhesive, HBM) with TD powder with grain sizes of 200–300  $\mu\text{m}$  was employed to prepare the magnetostrictive composites. During the curing process, a stepper motor was employed to rotate the prototype in order to guarantee a uniform homogeneity of the composites, during 8 hours. Two magnets having a magnetic field of 160 mT were also employed in the curing process in order to orient the magnetic domains of the composites. X-ray diffraction (XRD) was applied with an X-ray tube of  $\text{CuK}\alpha$  (MiniFlex, Rigaku) to study the structural composition of the TD powder prior to preparation of the composites.

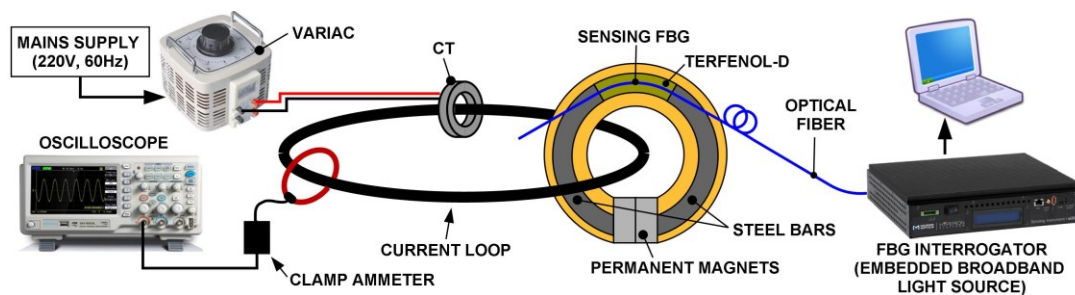


Fig. 2. Schematic diagram of the experimental setup.

## 3. Results and Discussion

The results of the characterization of TD powder by XRD are shown in Fig. 3(a). In this characterization, we found a pattern similar to that described by Meng *et al.* [12], in which the peak corresponding to crystallographic plane  $\langle 111 \rangle$  is directly associate with the magnetostrictive property of TD. In addition, the magnetic domains of the composite were oriented during the curing process, since there is an increases in the intensity of the peak corresponding to the magnetostrictive property, which is proved in the Meng *et al.*[12]. The acquisition of the output signals from the proposed FOCS prototypes was performed by an si155 FBG Interrogator (Micron Optics, Inc.) with

a resolution of  $\pm 10$  pm and maximum frequency response of 1kHz. The input signals were acquired by a clamp meter i2000FLEX (Fluke Co.) connected to a digital oscilloscope. Fig. 3(b) shows the full waveforms of the output signals acquired from the FBG interrogator generated by current signals applied in the range of 400–800 Arms. It can also be seen in Fig. 3(b) that the output signals contain distortions due to the wavelength tracking algorithm employed by the FBG interrogator and its resolution. In order to eliminate the observed noise and reconstruct the sinusoidal signal, a sinusoidal fitting was performed using the actual data, shown in fig. 3(c).

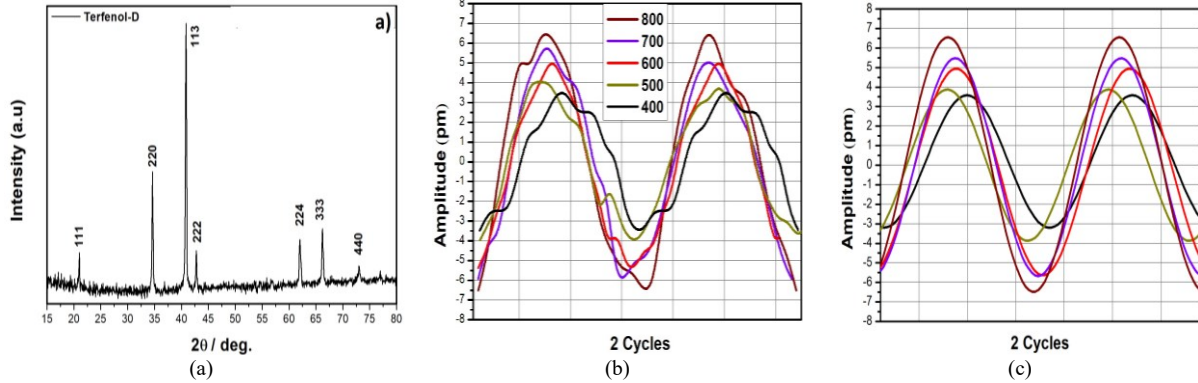


Fig. 3. (a) Results of XRD; (b) Output signals acquired with FBG interrogator from FOCS Model 1; (c) Sinusoidal fitting of the output signals.

Model 1 showed a low sensitivity to current measurement since the amplitude of the output signal was 6.5 pm for a maximum applied current of 800 Arms. According to the results in Figs. 1(a) and (b), FEM simulation showed that the magnetic field in the magnetostrictive composite of Model 1 is approximately 15 mT. In contrast, the magnetic field observed in the magnetostrictive composite of Model 2 was 30 mT, which led us to expect an increase in the sensitivity for Model 2. Although the open-loop design of Model 2 should have weakened the magnetic flux density through the TD composite in comparison to Model 1, the reduced size of the composite block in Model 2 contributed to an increase in the overall magnetic flux density at that point.

Fig. 4(a) shows the results of laboratory tests for Model 2. There was a nine-fold increase in the amplitude of the response, as compared to that of Model 1. Fig. 4(b) shows that the developed FOCS presented a sensitivity of 0.065 pm/A<sub>rms</sub> for Model 2. In addition, the nonlinear behavior is due to the characteristic magnetostriction of the TD. However, the nonlinearity levels due to the characteristic magnetostriction of TD can be decreased by applying external pressure to the TD, as reported by Cremonezi *et al.* [4]. Moreover, it also can be seen in Fig. 4(b) that Model 1 was not capable to measure current levels lower than 400 Arms. The amplitude of the response of Model 2 is comparable to the result presented by Nazaré and Werneck [5], which employed 74 grams of TD. In contrast, Model 2 proposed in this work employed only 1 gram of TD. Thus, Fig. 4(c) shows that an increase in the sensitivity of the proposed FBG-based FOCS was achieved by modifying the geometry of the magnetostrictive composite while reducing the amount of TD used. In addition, it is important to note that a higher resolution in the output of the sensor can be achieved using other interrogation techniques, such as the "twin-grating" technique [13].

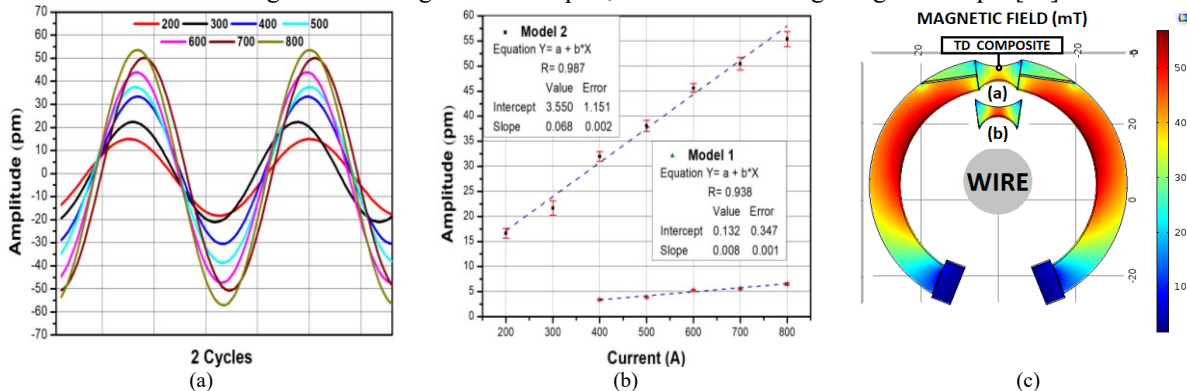


Fig. 4. (a) Model 2, Fit sinusoidal output signals; (b) Linearity characterization of the proposed FOCS; (c) Proposed sensor for future work.

#### 4. Conclusions

The preliminary results achieved in this work allow us to conclude that the proposed sensor was successfully implemented with a mass reduction of TD employed by more than 93% in comparison to the FBG-based FOCS proposed in previous works [4,5].

Therefore, we conclude that the proposed FOCS using magnetostrictive composite can be employed as the sensing head of an optical current transformer for monitoring of high-voltage transmission and distribution lines. Furthermore, the proposed FOCS designs simulated, built and characterized in this work allowed for a reduction in size and cost compared to current sensors proposed in previous works. Moreover, the use of magnetostrictive composites facilitates the manufacture of sensors in several geometry patterns, such as that of the FEM simulation presented in Fig. 4(c), which shows a hyperboloid-shaped composite that maximizes the magnetostriction at the point where the FBG is to be located. Future work will include field tests and temperature characterization of the FBG-based FOCS with the geometries presented in this work.

#### 5. References

- [1] Darrel K. Kleinke and H. Mehmet Uras, "A magnetostictive force sensor," *Rev. Sci. Instrum.* 65 1699-710, (1994).
- [2] Kin S. Chiang, Ramesh Kancheti and Vipul Rastogi, "Temperature-compensated Fiber-Bragg- grating-based magnetostrictive sensor for dc and ac currents," *Opt. Eng.* 42, 1906-1909, (2003).
- [3] Debashis Satpathi, Jason J. Moore and Mary G. Ennis, "Desing of a Terfenol-D based fiber-optics current transducer," *IEEE Sensor Journal*, 5, 1057-1065, (2005).
- [4] Alcides O. Cremonesi, Elnatan C. Ferreira, Alcino J. B. Filho and Jose. A. S. Dias, "A Fiber Bragg Grating RMS Current Transducer Based on the Magnetostriction Effect Using a Terfenol-D Toroidal-Shaped Modulator," *IEEE Sensor Journal*, Vol. 13, N. 2, (2013).
- [5] Fabio V. B. Nazaré and Marcelo M. Werneck, "Compact Optomagnetic Bragg-Grating-Based Current Sensor for Transmission Lines," *IEEE Sensor Journal*, Vol. 15, N. 1, (2015).
- [6] Stephen C. Butler, "A 2.5 kHz magnetostrictive Tonpilz sonar transducer design," *Proc. SPIE* 4699, 510–521 (2002).
- [7] Geoffrey P. McKnight, "[1 1 2] oriented Terfenol-D composites, PhD." *Thesis*, University of California, Los Angeles, (2002).
- [8] Sully M. M. Quintero, Arthur M. B. Braga, Hans I. Weber, Antonio C. Bruno, and Jefferson F. D. F. Araújo, "A Magnetostrictive Composite-Fiber Bragg Grating Sensor," *Sensors*, Vol. 10, N. 9, 8119-8128 (2010).
- [9] Heliang Liu, Siu W. Or and Hwa Y. Tam, "Magnetostrictive composite–fiber Bragg grating (MC–FBG) magnetic field sensor," *Sensors and Actuators A*, 173, 122-126 (2012).
- [10] Rani Elhajjar Chiu-Tai Law and Alessandro Pegoretti, "Magnetostrictive polymer composites: Recent advances in materials, structures and properties," *Progress in materials science*, 97, 204-229 (2018).
- [11] Geraldo Bieler and Marcelo M. Werneck, "A magnetostrictive-fiber Bragg grating sensor for induction motor health monitoring," *Measurement*, Vol. 122, Pages 117-127 (2018).
- [12] Hao Meng, Tianli Zhang, Chengbao Jiang, and Huibin Xu, "Grain-<111>-oriented anisotropy in the bonded giant magnetostrictive material," *Applied Physics Letters* 96, 102501 (2010).
- [13] Alex Dante, Rodrigo M. Bacurau, Anderson W. Spengler, Elnatan C. Ferreira, and José A. S. Dias, "A Temperature-Independent Interrogation Technique for FBG Sensors Using Monolithic Multilayer Piezoelectric Actuators," *IEEE Transactions on instrumentation and measurement*, Vol. 65, N. 11, (2016).

# Analysis of magnetic field sensor based on intermodal interference using tapered square no-core fiber

Wilson Francelino de Morais Júnior<sup>1,2</sup>; Maria Thereza Miranda Rocco Giraldi<sup>2</sup>.

1. Instituto Militar de Engenharia – Rio de Janeiro/RJ – Brazil

2. Instituto de Tecnologia em Fármacos/Fiocruz – Rio de Janeiro/RJ – Brazil

wilson.junior@far.fiocruz.br; mtmrocco@ime.eb.br

**Summary:** This paper presents the computational implementation of a magnetic field sensor model, based on the principle of intermodal interference using a taper with square section in an optical fiber. Simulations were performed varying its constructive dimensions in order to analyze the influence of them in the sensor performance.

## 1. Introduction

Sensors based on intermodal interference have been applied in several areas and used for measuring various quantities, such as temperature, relative humidity, refraction index, etc [1-3]. No-core fibers have been used as an alternative to multimode fiber, for ease of manufacturing and lower cost [4]. Some different cross-sectional formats, such as square ones, were also employed for the measurement of different parameters [3,5]. In addition, the evanescent field of a no-core fiber can be better harnessed by introducing a taper, which may result in a improvement of the sensitivity of the device.

Magnetic field detection has attracted research interests in various areas of industry and physics. Several Magnetic Fluids (MF) have been studied in recent years [6,7]. Magnetic field sensors combining optical fibers and MF have presented distinct advantages, such as high sensitivity, linear response, and compact size. This paper presents a computational analysis of a magnetic field sensor model using a tapered square no-core fiber (TSNCF) [8] based on the concept of intermodal interference.

## 2. Theoretical Foundations

In optical sensors based on the principle of intermodal interference, the modification of one of the properties of the transmitted spectrum, caused by the interference between the modes that compose this spectrum, is related to the physical magnitude to be measured. For this relationship to be possible, some of these modes must travel in different optical paths, either on the same fiber or on different fibers. In addition, one of the optical paths must be subjected to interference from the external medium with the physical parameter that one wishes to measure [3,8]. For this to occur, this type of optical sensor requires components that provide for the division and re-coupling of these modes. The construction of a taper on the optical fiber is one of the ways to produce a sensor based on intermodal interference.

The TSNCF is formed from a square rod of pure silica and can be considered a square wave optical waveguide that can be inserted between two standard single-mode fiber (SMF) segments, forming the basic structure of the sensor using the TSNCF. In this structure, SMF-TSNCF-SMF, when the light that propagates through the single-mode fiber reaches the TSNCF, modes classified as  $E_{mn}^x$  and  $E_{mn}^y$  are excited and propagate through this segment, where  $mn$  is the modes order. Upon reaching the taper region, part of these excited modes is coupled to the external medium and continues to propagate through it, while another part continues to propagate through the tapered portion of the TSNCF. When the modes propagating through the external environment are re-coupled to the TSNCF structure, they produce intermodal interference with the modes that continued to propagate through TSNCF [8], as shown in Fig. 1.

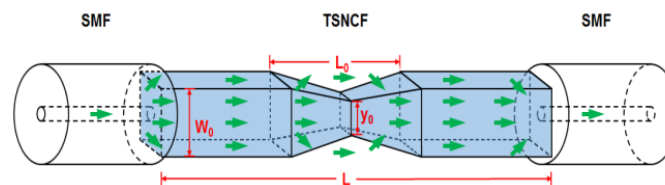


Fig. 1 - Structure of the SMF-TSNCF-SMF sensor.

The intermodal interference condition between  $mn$ -order and  $uv$ -order modes for spectral notches generate can be expressed as:

$$\varphi_{mn} - \varphi_{uv} = (2p + 1)\pi \quad (1)$$

Where  $\varphi_{mn}$  and  $\varphi_{uv}$ , are the  $mn$ -order and  $uv$ -order modes phases, respectively.

Thus, the variation in the wavelength that can be described by Eq. (2), considering that the tapering is linear and that the total length of the TSNCF ( $L$ ) is much larger than the taper length ( $L_0$ ) [8].

$$\lambda \approx \frac{(2p+1)n_0}{\frac{L[(m+1)^2-(u+1)^2]}{4W(1)^2} + \frac{L[(n+1)^2-(v+1)^2]}{4W(0)^2} + \frac{(W_0-y_0)[(m+1)^2-(u+1)^2]}{2k[W(1)^2-(W_0-y_0)W(0)]} + \frac{(W_0-y_0)[(n+1)^2-(v+1)^2]}{2k[W(0)^2-(W_0-y_0)W(1)]}} \quad (2)$$

Where  $p$  is an integer,  $n_0$  is the refractive index of the TSNCF,  $y_0$  is the minimum width of the taper,  $W(0)$  and  $W(1)$  are the effective widths of the  $mn$ -order modes along the  $x$  and  $y$  directions, respectively, and can be set by [8]:

$$W(\sigma) \approx W_0 - \left(\frac{\lambda_0}{\pi}\right) \left(\frac{n_{ext}}{n_0}\right)^{2\sigma} \frac{1}{\sqrt{n_0^2 - n_{ext}^2}} \quad (3)$$

Where  $n_{ext}$  is the refractive index of the external medium,  $\lambda_0$  is the peak wavelength of the Gaussian optical beam from the SMF and  $\sigma$  is equal to 1 or 0 depending on whether the modes are  $E_{mn}^x$  or  $E_{mn}^y$ . For the modes  $E_{mn}^x$ , we have  $W_{xm}^{eff} = W(1)$  and  $W_{ym}^{eff} = W(0)$ . For the modes  $E_{mn}^y$ , we have  $W_{ym}^{eff} = W(1)$  and  $W_{xm}^{eff} = W(0)$  [8].

In the magnetic field sensor analyzed in [8], the section of the TSNCF sensor is immersed in a MF. This magnetic fluid is basically a kind of stable colloidal dispersion of ferromagnetic nanoparticles in a suitable liquid carrier. A magnetic field perpendicular to the fiber axis is applied to the fiber region where the TSNCF is located. The refractive index of the MF is modified according to the intensity and direction of the applied magnetic field. The variation of the refractive index of the MF, which constitutes the external medium, will lead to a variation on the effective width of the  $mn$  order modes that propagate through the TSNCF and therefore a variation in the wavelength of the transmitted spectrum. In this way, the measured wavelength variation can be related to the variation of the external magnetic field. When the external magnetic field is applied parallel to the axis of the optical fiber, in the same direction of light propagation, the MF refractive index will increase with increasing the magnetic field strength. When the external magnetic field is applied perpendicular to the fiber axis, the MF refractive index decreases with increasing the magnetic field strength. This will result in the spatial anisotropy of MF, which makes MF exhibit optical birefringence under a magnetic field [9].

For an external magnetic field applied parallel to the fiber axis, the variation of the refractive index of the magnetic fluid as a function of the intensity of the external magnetic field can be described by the function of Langevin [10], which is expressed by:

$$n_{MF}(H, T) = (n_s - n_{MF}) \left[ \coth\left(\alpha \frac{H - H_{c,n}}{T}\right) - \frac{T}{\alpha(H - H_{c,n})} \right]; \quad H > H_{c,n} \quad (4)$$

Where  $n_s$  is the saturation value of the refractive index, from which there is no more significant variation in the refractive index with the increase of the intensity of the external magnetic field,  $n_{MF}$  is the refractive index of the MF under a magnetic field with less intensity than  $H_{c,n}$ , that is the critical intensity of the magnetic field, for which a variation in the refractive index of the MF begins to be observed,  $H$  is the intensity of the applied external magnetic field,  $T$  is the temperature and  $\alpha$  is a curve adjustment parameter.

### 3. Results

All simulations were performed using a code implemented in MATLAB from the equations described in section 2 for modeling the sensor [8]. As the code was developed from the analytical solutions presented, the simulations did not require a great computational effort, as it was not necessary to use numerical solutions.

In the experiment performed in [8] two spectral notches called Dip 1 and Dip 2 are monitored, where Dip 1 is located at 902.6 nm and Dip 2 at 1291.1 nm. Firstly, simulations were performed with the objective of reproducing the experimental results obtained in [8], in order to validate the implemented computational model. In this work the magnetic field is applied perpendicular to the axis of the optical fiber, different from the experiment carried out in [10], so that when the intensity of this field increases, the refractive index of the MF decreases. The result of the simulation using the Langevin function, is shown in Fig. 2.

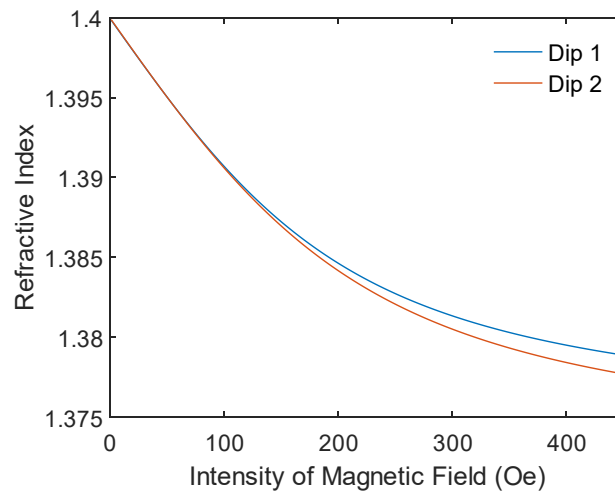


Fig. 2. Simulation response: variation of the refractive index of Dips 1 and Dip 2.

The result of the simulation of the wavelength variation as a function of the magnetic field intensity for Dip 1 and Dip 2 are shown in Fig. 3 (a) and (b), respectively.

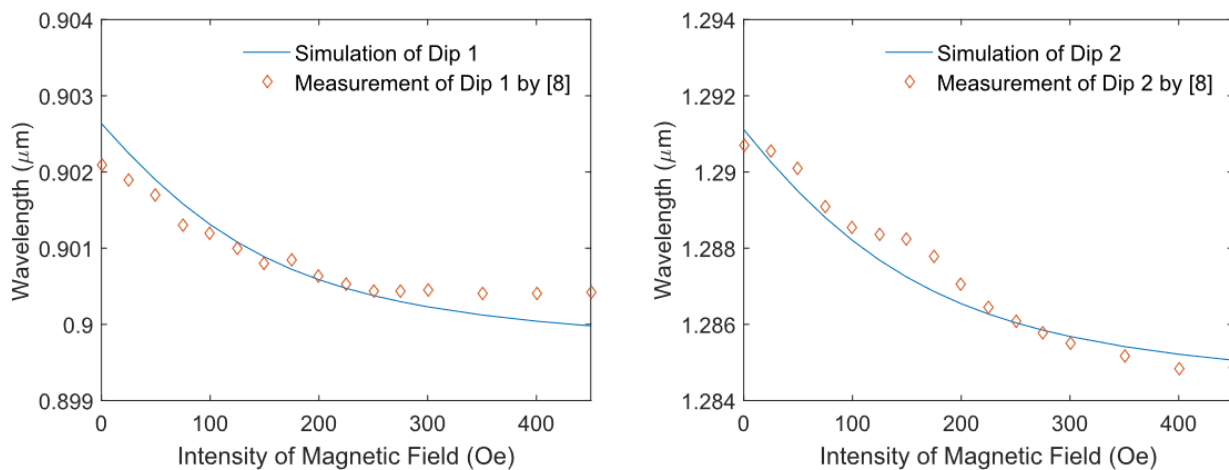


Fig. 3. Simulation response: (a) variation of the wavelength of Dip 1 and (b) variation of the wavelength of Dip 2. All of them as a function of the magnetic field intensity.

The Fig. 3(a)-(b) show that the computational model satisfactorily describes the results obtained experimentally in [8], presenting a coefficient of determination ( $R^2$ ) equal to 0.91 for Dip 1 and 0.94 for the Dip 2, with this the model was considered validated.

Once the model of the sensor was validated, an analysis was carried out by individually varying  $W_0$ ,  $y_0$ ,  $L$  and  $L_0$  in order to verify how these variations affect the performance of the sensor and what limit these variables can assume in order to keep the model mathematically valid. Fig. 4(a)-(d) present the results of the simulations of the wavelength variation as a function of the magnetic field strength when the dimensions  $W_0$ ,  $y_0$ ,  $L$  and  $L_0$ , respectively, were varied.

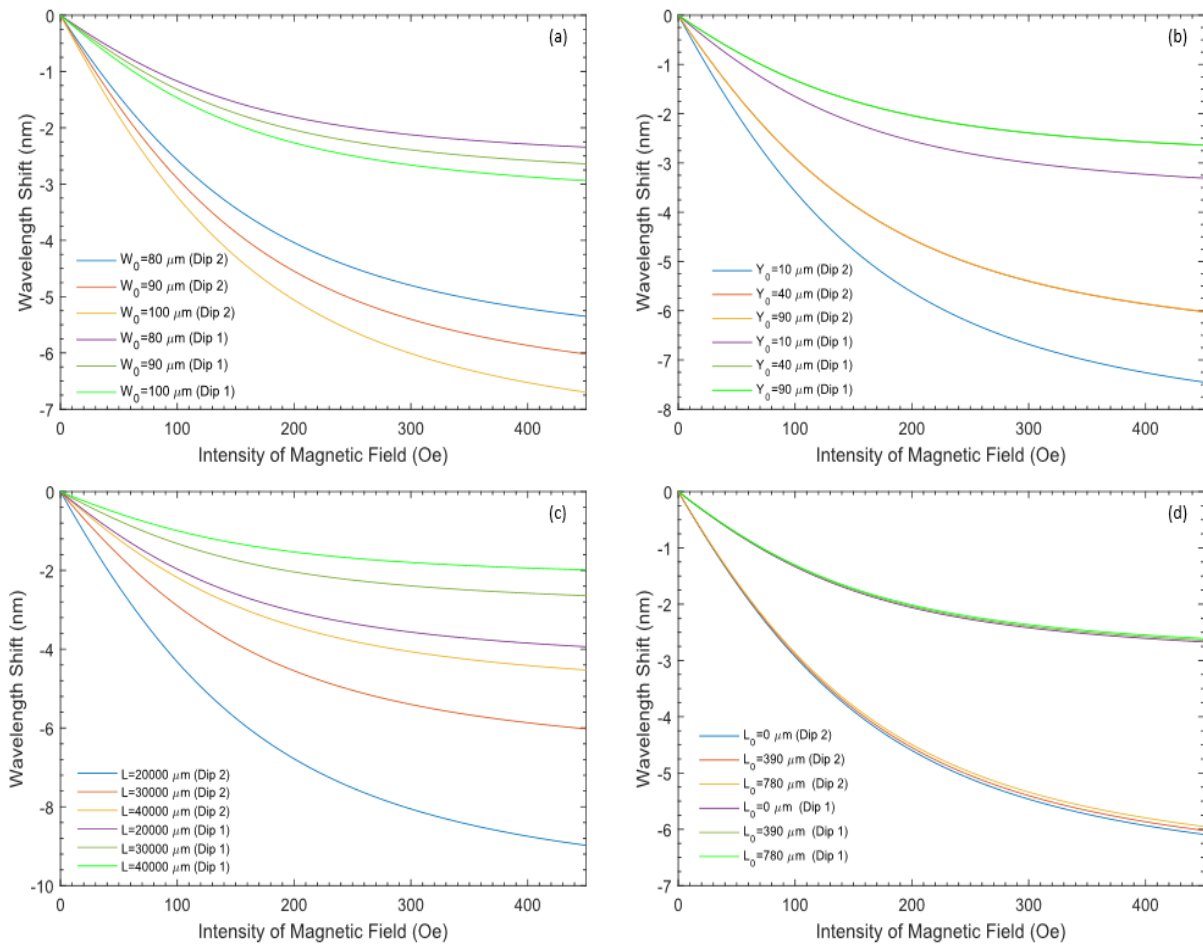


Fig. 4 – Response of the simulation of the wavelength variation as a function of the magnetic field strength for Dip 1 and Dip 2 when (a)  $W_0$ , (b)  $y_0$ , (c)  $L$  and (d)  $L_0$  we're varied.

Table 1 shows the sensitivities obtained in the simulations for the results presented in Fig. 4 (a) - (d). It can be observed how the variations in the TSNCf structure dimensions affect the sensitivity of the device. The sensitivity in each simulation was calculated by dividing the maximum wavelength shift by the total variation of the magnetic field intensity.

The highest sensitivity values were obtained when the length  $L$  is reduced to a minimum value of 2000  $\mu\text{m}$  and when the minimum width of the taper ( $y_0$ ) is equal to 10  $\mu\text{m}$ , which is the same order of magnitude of the core diameter of a single-mode fiber. In all simulations, Dip 2 presented a higher sensitivity than Dip 1.

Table 1. Summary of the sensitivities obtained for Dips 1 and Dip 2 varying the dimensions of the TSNCf.  
All sizes in  $\mu\text{m}$  and all sensitivities in  $\text{pm/Oe}$ .

Dimension	$W_0$			$y_0$			$L$			$L_0$		
	Min.	Mid.	Max.									
Size	80	90	100	10	40	90	20000	30000	40000	0	390	780
Sensitivity Dip 1	5.21	5.86	6.53	7.35	5.87	5.86	8.75	5.87	4.41	5.93	5.87	5.80
Sensitivity Dip 2	11.89	13.38	14.86	16.56	13.38	13.36	19.95	13.38	10.06	13.53	13.38	13.22

#### 4. Conclusions

The computational model implemented to relate the wavelength variation as a function of the magnetic field strength was compatible with the data presented in [8], within the established considerations, and in this way can constitute as an initial tool for the analysis of magnetic field strength sensors based on a SMF-TSNCf-SMF structure. In general, variations in TSNCf dimensions caused only minor changes in the sensitivity of the sensor. The dimensions that most affect the sensitivity of the sensor are  $W_0$  and  $L$ . Removal of the taper ( $y_0 = 90 \mu\text{m}$  and  $L_0 = 0 \mu\text{m}$ ) did not cause significant loss in sensor sensitivity. In addition, the value of the monitored wavelength also affects the sensitivity of the sensor, and the higher the wavelength, the higher the observed sensitivity.

#### 5. Acknowledgments

Authors would like to thank Farmanguinhos/Fiocruz, CAPES and CNPq for partially supporting this work.

#### 6. References

- [1] J. E. Antonio-Lopez, A. Castillo-Guzman, D. A. May-Arrijo, R. SelvasAguilar, and P. LiKamWa, "Tunable multimode-interference bandpass fiber filter," *Optical Letters*, vol. 35, no. 3, pp. 324–326, Feb. 2010.
- [2] E. B. Li, X. L. Wang, and C. Zhang, "Fiber-optic temperature sensor based on interference of selective higher-order modes," *Applied Physics Letters*, vol. 89, no. 9, pp. 091119-1–091119-3, Aug. 2006.
- [3] Y. Miao, X. Maa, Y. He, H. Zhang, K.L. Zhang, B. Song, B. Liu, J. Yao, "Low-temperature-sensitive relative humidity sensor based on tapered square no-core fiber coated with SiO<sub>2</sub> nanoparticles". *Optical Fiber Technology*. v. 29, p. 59–64, 2016.
- [4] Q. Wang and G. Farrell, "All-fiber multimode-interference-based refractometer sensor: Proposal and design," *Optical Letters*, vol. 31, no. 3, pp. 317–319, Feb. 2006.
- [5] S. Silva, E. G. P. Pachon, M. A. R. Franco, P. Jorge, J. L. Santos, F. X. Malcata, C. M. B. Cordeiro, and O. Frazao, "Curvature and temperature discrimination using multimode interference fiber optic structures-a proof of concept," *Journal of Lightwave Technology*, vol. 30, no. 23, pp. 3569–3575, Dec. 2012..
- [6] S. Y. Yang, H. E. Hornga, Y. T. Shiao, C.-Y. Hongb, and H. C. Yang, "Photonic-crystal resonant effect using self-assembly ordered structures in magnetic fluid films under external magnetic fields," *Journal of Magnetism and Magnetic Materials*, vol. 307, pp. 43–47, Feb. 2006.
- [7] J. J. Chieh, S. Y. Yang, Y. H. Chao, and H. E. Horng, "Dynamic response of optical-fiber modulator by using magnetic fluid as a cladding layer," *Journal of Applied Physics*, vol. 97, no. 4, pp. 043104-1–043104-4, Feb. 2005.
- [8] Y.P. Miao, J.X. Wu, W. Lin, B.B. Song, H. Zhang, K.L. Zhang, B. Liu, J.Q. Yao, "Magnetic field tunability of square tapered no-core fibers based on magnetic fluid". *Journal of Lightwave Technology*, v. 32, n. 23, p. 3998–4003, 2014.
- [9] Y. Zhao, X. Liu, R. Lv, Y. Zhang and Q. Wang, "Review on Optical Fiber Sensors Based on the Refractive Index Tunability of Ferrofluid," *Journal of Lightwave Technology*, v. 35, n. 16, 2017.
- [10] Y. F. Chen, S. Y. Yang, W. S. Tse, C.-Y. Hong, and H. C. Yang, "Thermal effect on the field-dependent refractive index of the magnetic fluid film," *Applied Physics Letters*, v. 82, n. 20, p. 3481–3483, 2003.

# Electromagnetic Contactor Core Temperature and Dynamic Strain Evaluation Using Fiber Bragg Gratings

<sup>a</sup>Cesar Caytairo Tapia, <sup>a</sup>Jorge Luis Roel Ortiz, <sup>b</sup>Uilian José Dreyer, <sup>a</sup>Kleitton de Moraes Sousa

<sup>a</sup>Federal University of Technology – Paraná, Pato Branco 85503-390, Brazil

<sup>b</sup>Federal University of Technology – Paraná, Curitiba 80230-901, Brazil

E-mail: kleitonsousa@utfpr.edu.br

**Abstract:** This paper presents the dynamic strain and temperature measurements of the contactor core using the Fiber Bragg Grating (FBG). These measurements are used to predict future preventative maintenance of this device. The temperature variation is approximately 76 °C. In the steady state, for dynamic strain measurement, the fundamental frequency is 120 Hz.

**Keywords:** Fiber Bragg Grating, contactor core, dynamic strain, temperature.

## 1. INTRODUCTION

The electromagnetic contactor is one of the most used electrical devices in industrial power systems. They can be integrated with other important circuits to perform more complex functions such as motor start, factory automation controller and protection. Electromagnetic contactor is composed by a magnetic circuit and a set of springs. When a voltage is applied to the solenoid coil, electromagnetic force attracts the mobile core toward the fixed core in order to close the main contacts of the device. There is the possibility of the contactor being operated remotely using control elements, such as the inner solenoid, consuming lower current than the load itself [1,2].

There are two types of problems related to an electromagnetic contactor. The first problem is the voltage sag. The most frequent reasons for voltage sag are the starting of industrial machinery, pumps and motor with high power consumption. When voltage sags occur to the contactor, it can cause problems resulting in the shutdown during restarting motors. The second problem is related to the closure of the contactors which is called contact bounce. The bounce occurs when the first touch of the electromagnetic core does not close the contactors due to excess of energy during the closing process. Thus, because of bouncing, the contactor makes and breaks their contacts several times before they reach a permanent state of contact. They are exposed to rebound damage due to this phenomenon [3,4]. It is important to analyze and determine the behavior of the electromagnetic contactor during adverse situations.

The strain and temperature measurements on the contactor core have some challenges. Among them is that the reduced space inside the contactor makes sensor installation difficult. Another problem is the electromagnetic interference due to the field generated by the contactor's coil. Their operation involves making or breaking electrical contacts leading to radiated electromagnetic noise. Because of this, Fiber Bragg Grating (FBG) temperature and strain sensors are suitable for these applications [5]. The FBG are used to investigate the temperature and strain on the fixed core of the electromagnetic contactor.

In previous papers, FBG applications were presented on electromagnetic devices for temperature and strain measurement. In [6] the strain measurement on the contactor core was presented, which is a continuation of the present paper. The temperature measurement on the surface of a high power generator stator was reported in [7] using FBG sensors. In [8] the dynamic strain induced by mechanical and electrical forces was reported by using FBG, installed inside the motor. FBG was used for the dynamic strain measurement of a four-pole induction motor stator to detect a broken rotor bar in [9].

This paper presents the use of FBGs to measure the dynamic strain and temperature on the core of an electromagnetic contactor. For the strain measurement, the sensing technique used for the dynamic strain measurement is through the indirect measurement of the electromagnetic force, which is obtained from the voltage and current.

## 2. EXPERIMENTAL SETUP

The tests were performed with a commercial contactor of 50 A/AC3. The solenoid coil is powered with 220 VCA, it is turned on and turned off through a power switch. For strain measurement is used a fiber optic cable with an FBG sensor recorded at its end, with 1542 nm of wavelength. For temperature measurement, fiber optic cable was used with another FBG. The acquisition is made using a Micronoptics optical interrogator with a sampling rate of

1 kHz for the strain and 5 Hz for the temperature measurement. An optical interrogator is an electronics optical instrument that allows the reading of FBG in static and dynamic monitoring application. Tests was carried out in a temperature-controlled environment, because of this the results do not present eternal temperature disturbing. The experimental setup is presented in Fig. 1. The acquisition system uses a Micronoptics optical interrogator along with a computer for data analysis.

Shading rings play an important role in the dynamic response of the electromagnetic contactor. Basically it is constructed by blades of ferromagnetic material and has two parts separated by mechanical action of springs. One of these parts of the core is coupled to the contacts and when there is movement of the core, the activation of the contacts of command and load of the contactor occurs. The magnetic fields generated by the solenoid coil produce a force that drops to zero twice each cycle (60Hz). This effect creates a vibration or undesired charter of the force contacts which can be canceled by shading rings.

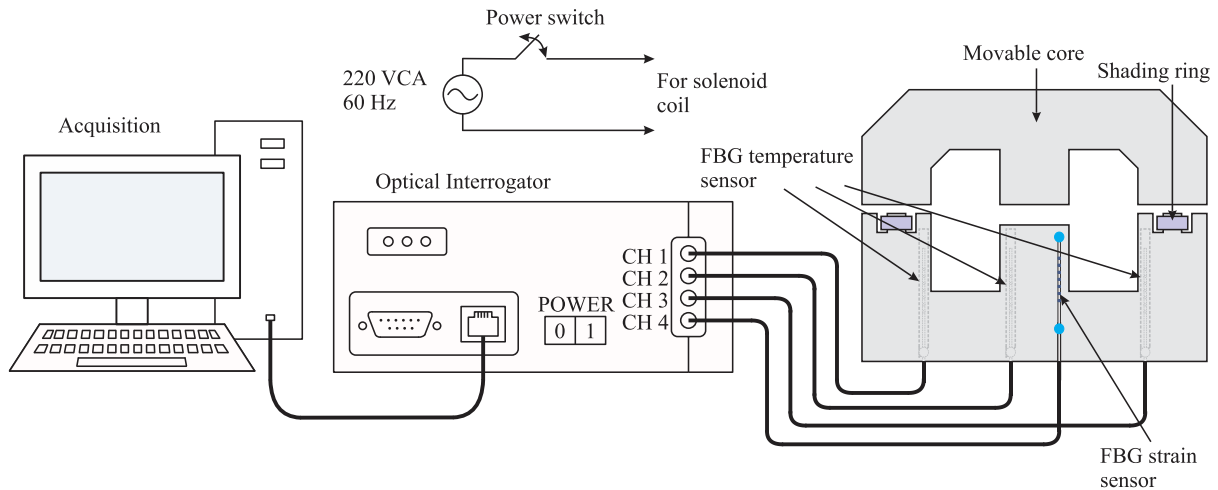


Fig. 1. Experimental setup for temperature and strain sensing.

To measure the fixed core strain, an FBG is fixed using cyanoacrylate glue directly on the fixed core. Fig.2 (a) present the schematic for the FBG strain sensor position. The core temperature is sensed using an FBG package using a stainless steel tube glued with epoxy glue just on one end of it, as shown in the Fig. 2 (b). The detail of how the FBG is placed inside the stainless steel tube is shown in Fig. 2 (c). It is necessary to glue only one side of the sensor, in order to avoid the tube thermal expansion effect on the FBG. The FBG thermal sensitivity used in the experiments is  $10 \text{ pm}/^\circ\text{C}$ , the value was obtained experimentally by calibrations. The experimental value can be found in [10,11]. For temperature sensors are obtained standard deviations, 1.155 pm for Sensor 1, 1.155 pm for Sensor 2 and 0.577 pm for Sensor 3. With these data can be obtained the measurement uncertainties, which are  $0.48 \text{ }^\circ\text{C}$  for Sensor 1,  $0.48 \text{ }^\circ\text{C}$  for Sensor 2 and  $0.41 \text{ }^\circ\text{C}$  for Sensor 3. The optical interrogator has a resolution of 1 pm.

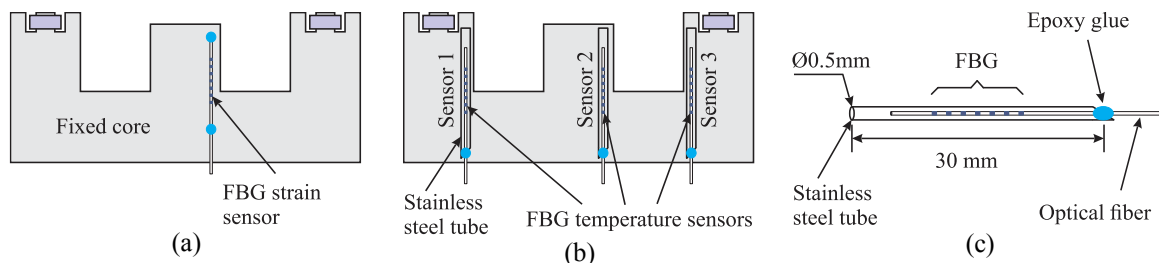


Fig. 2. (a) The FBG strain sensor placed on the fixed core. (b) Three FBGs temperature sensors inside the stainless steel tube placed on the fixed core. (c) Illustration of a FBG packaging with the stainless steel tube.

The experimental tests for the strain measurement, consist of turning on and turning off the excitation solenoid for three different circumstances to be analyzed. The first one is the core strain transient during the solenoid energization. The second is an oscillatory strain regime by the electromagnetic force. The last situation is the transient when the solenoid coil is turned off. In experimental tests for temperature measurement, two situations can be analyzed. The first one is the excitation solenoid turned off for about ten minutes and the second is turning

on the excitation solenoid coil and waiting for the core temperature to stabilize. These analyses are made separately, strain measurement and temperature measurement, since the variation in the Bragg wavelength peak due to temperature is slower than the dynamic strain.

### 3. RESULTS AND DISCUSSIONS

In Fig. 3 it is observed that the variation of the temperature on the fixed core is slower than strain variation. All sensors start at the same initial point of 27 °C and have the same behavior. The fixed core reaches thermal stability at  $t=160$  minutes. The temperature of Sensor 1 is 102.5 °C, Sensor 2 is 102.7 °C and Sensor 3 is 103.7 °C. The temperature variation is approximately 76 °C, which is the difference between stabilization temperature and ambient temperature. It can be seen that the temperature measurements of the three sensors are similar. The increase in temperature on the fixed core indicates that the joule losses in the solenoid coil and magnetic losses in the core lead to temperature rise.

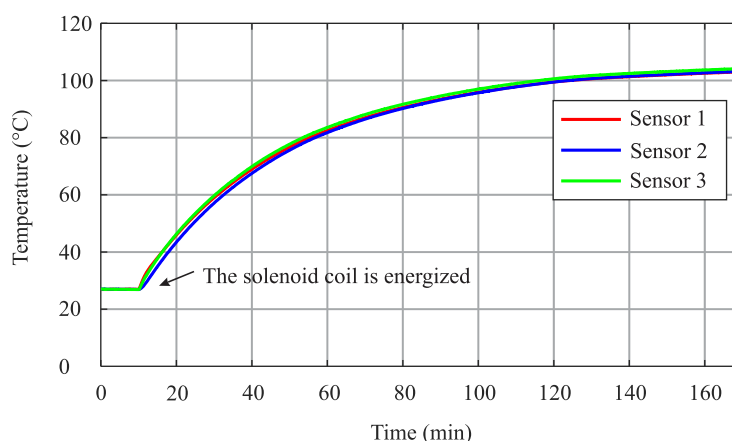


Fig. 3. Contactor core temperature variation over the test period.

For strain measurement the results were obtained by turning on and turning off the switch that supplies power to the solenoid coil. The Fig. 4 (a) presents the FBG wavelength variation for the strain measurement and the solenoid coil supply situation. It can be observed there is an inclination of the wavelength variation in the FBG, during the 16 s of measurement. This slow increase of the signal is due to the variation of the temperature and thermal expansion of the material inside the electromagnetic coil. The FBG wavelength variation due to temperature is slower than the variation due to dynamic strain.

The solenoid coil is turned on between the time  $t = 2s$  and  $t = 14.3s$ , outside that range the solenoid coil is turned off. At the time  $t = 2s$  there is a very rapid wavelength variation, which is due to the collision between the fixed core and the mobile core. The wavelength variation is negative when the fixed core is compressed and positive when it expands.

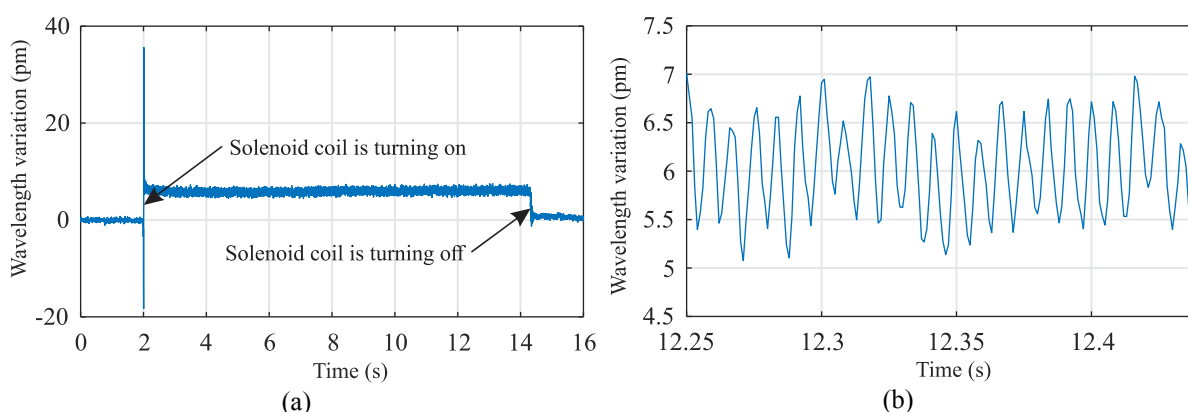


Fig. 4. The results of contactor's core deformation. (a) For  $t < 2s$  the solenoid coil is turning off, for  $2s < t < 14.3s$  the solenoid coil is turning on and for  $t > 14.3s$  the solenoid coil is turning off again. (b) The sinusoidal shape of the electromagnetic force for steady state.

In the steady state, the time in which solenoid coil remains turned on, (for  $2 < t < 14.3s$ ), it can be seen that the slope of the graph tends to rise, this is due to the fact that the FBG has a thermal sensitivity, which captures the

temperature increase in the contactor core. It can also be seen that the fixed core of the contactor experiences a deformation caused by the constant and sinusoidal electromagnetic force, as shown in Fig. 4 (b).

In Fig. 5 it is shown the Fourier Transform of the steady state dynamic strain deformation, where is possible to determinate the fundamental frequency of 120 Hz.

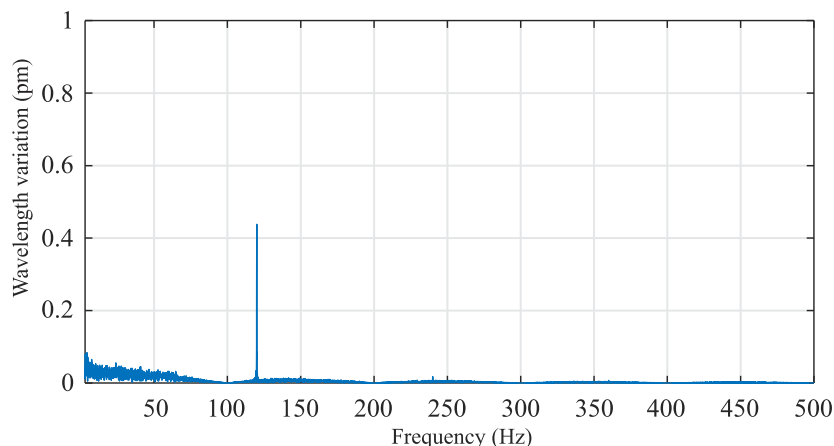


Fig. 5. Frequency response of the contactor core dynamic strain

#### 4. CONCLUSION

In this paper the measurement of the dynamic strain and the temperature using FBG sensors is presented. For dynamic strain, three situations can be observed: the transient state when the solenoid coil is turned on, the steady state and the transient when the solenoid coil is turned off. The use of FBG to measure strain made it possible to identify the sinusoidal electromagnetic force in the contactor core. In the permanent regime, the sinusoidal electromagnetic force has a fundamental frequency of 120 Hz, which is twice the frequency of the main supply. This fundamental frequency is obtained by applying a Fast Fourier Transform (FFT) of the signal in a steady state. For temperature measurement, three FBG are used, which start at the same initial point of 27 °C and have the same behavior. The fixed core reaches thermal stability at  $t=160$  minutes. The temperature of Sensor 1 is 102.5 °C, Sensor 2 is 102.7 °C and Sensor 3 is 103.7 °C. The temperature variation is approximately 76 °C. The increase in temperature on the fixed core indicates that the joule losses in the solenoid coil and magnetic losses in the core lead to temperature rise. The preliminary results in this document show a potential for applications of FBG deformation and temperature sensors in electromagnetic contactors. In future work, the appropriate instrumentation will be used to study the behavior of the deformation and temperature in the contactor core during a voltage drop.

#### ACKNOWLEDGMENTS

This study was financed in part by the Coordenação de Aperfeiçoamento de Pessoal de Nível Superior - Brasil (CAPES) - Finance Code 001", of Conselho Nacional de Desenvolvimento Científico e Tecnológico (CNPq), from Fundação Araucária (FA) and from Financiadora de Estudos e Projetos (FINEP).

#### REFERENCES

- [1] P. I. Koltermann, J. P. A. Bastos, and S. R. Arruda, "A model for dynamic analysis of AC contactor," *IEEE Trans. Magn.*, vol. 28, no. 2, pp. 1348–1350, Mar. 1992.
- [2] W. Kanokbannakorn, T. Saengsuwan, and S. Sirisukprasert, "The modeling of AC magnetic contactor for immunity studies and voltage sag assessment," in *The 8th Electrical Engineering/ Electronics, Computer, Telecommunications and Information Technology (ECTI) Association of Thailand - Conference 2011*, 2011, pp. 621–624.
- [3] S. W. Jeong, G. J. Lee, and J. H. Gim, "The study on the characteristics of operating limits of AC contactor during voltage sag," *Transm. Distrib. Conf. Expo. Asia Pacific, T D Asia 2009*, pp. 2–5, 2009.
- [4] A. G. Espinosa, J. R. R. Ruiz, J. Cusidó, and X. A. Morera, "Sensorless control and fault diagnosis of electromechanical contactors," *IEEE Trans. Ind. Electron.*, vol. 55, no. 10, pp. 3742–3750, 2008.
- [5] A. Othonos, "Fiber Bragg gratings," *Rev. Sci. Instrum.*, vol. 68, no. 12, pp. 4309–4341, 1997.
- [6] J. C. Galon, J. L. R. Ortiz and K. de M. Souza, "Electromechanical Contactor Core Strain Measurement Using Fiber Bragg Grating Sensors", *MOMAG 2018*.

- [7] C. Martelli, E. V. da Silva, K. M. Sousa, F. Mezzadri, J. Somenzi, M. Crespini, H. J. Kalinowski, and J. C. C. da Silva, "Temperature sensing in a 175mw power generator," pp. 8421 – 8421 – 4, 2012. [Online]. Available: <https://doi.org/10.1117/12.975308>.
- [8] K. M. Sousa, U. J. Dreyer, C. Martelli, and J. C. Cardozo da Silva, "Dynamic Eccentricity Induced in Induction Motor Detected by Optical Fiber Bragg Grating Strain Sensors," *IEEE Sens. J.*, vol. 16, no. 12, pp. 4786–4792, Jun. 2016.
- [9] K. M. Sousa, I. Brutkowski Vieira da Costa, E. S. Maciel, J. E. Rocha, C. Martelli, and J. C. Cardozo da Silva, "Broken Bar Fault Detection in Induction Motor by Using Optical Fiber Strain Sensors," *IEEE Sens. J.*, vol. 17, no. 12, pp. 3669–3676, Jun. 2017.
- [10] X. Jie, L. Zhi-Bin, H. Qi-Tao, and L. Chang, "A new packaged FBG sensor for underground cable temperature monitoring," *Proc. 2017 IEEE 2nd Adv. Inf. Technol. Electron. Autom. Control Conf. IAEAC 2017*, pp. 1789–1793, 2017.
- [11] X. Shen and Y. Lin, "Measurements of Temperature and Residual Strain during Fatigue of a CFRP Composite Using FBG Sensors," *2009 Int. Conf. Meas. Technol. Mechatronics Autom.*, vol. 1, no. 3, pp. 35–38, 2009.

# Influence of Gold Nanoparticles Film on the Sensitivity of Long Period Fiber Grating

Robsson Pereira Dias<sup>1</sup>, Carla Requena Klimpovuz<sup>2</sup>, Marcela Mohallem Oliveira<sup>3</sup>, José Luís Fabris<sup>1</sup>, Marcia Muller<sup>1</sup>

<sup>1</sup>Federal University of Technology-Paraná, 3165 Av. Sete de Setembro, Curitiba, Brazil, 80230-901;

<sup>2</sup>Federal University of Paraná, 100 Av. Cel. Francisco H. do Santos, Curitiba, Brazil, 81530-000;

<sup>3</sup>Federal University of Technology-Paraná, 5000 Dep. Heitor Alencar Furtado, Curitiba, Brazil, 81280-340.

robssonpdias@hotmail.com, carlaklimpovuz@yahoo.com.br, marcelam@utfpr.edu.br, fabris@utfpr.edu.br, mmuller@utfpr.edu.br

**Abstract:** The responses of three coated and uncoated long period gratings to the refractive index of the surroundings are compared. Gratings operate at the visible spectral range close to the plasmon resonance band of gold nanoparticles. Sensitivity increase up to 85.2% was achieved in water after coating the grating, making the device useful for environmental applications.

## 1. Introduction

Optical fiber sensors based on long period gratings (LPG) have been widely employed to detect chemical and biological agents. The key characteristic that enables the detection is the interaction between the light transmitted by the fiber and the surrounding medium. Such interaction relies on the coupling between the fundamental core mode and the  $m$ -th co-propagating cladding modes [1] provided by the grating. Such coupling results in attenuation bands centered at wavelengths  $\lambda_m$  given by  $\lambda_m = (n_{\text{core}}^{\text{eff}} - n_{\text{clad}(m)}^{\text{eff}})\Lambda$ , where  $n_{\text{core}}^{\text{eff}}$  and  $n_{\text{clad}(m)}^{\text{eff}}$  are the effective refractive indexes of fundamental core mode and the  $m$ -th cladding mode, respectively, and  $\Lambda$  is the grating pitch. As the  $n_{\text{clad}(m)}^{\text{eff}}$  depends on the refractive index of the medium surrounding the fiber, LPG is a very attractive refractive index sensor, however presenting low sensitivities in water environments. An effective method to increase the LPG sensitivity in such media is promoting the coupling between the evanescent fields of the cladding modes with localized surface plasmon resonances (LSPR) that can be produced on the fiber. In this sense, gold nanoparticles (AuNP) deposited on the fiber surface have been employed for this purpose [2,3]. In addition to the increased sensitivity, nanoparticles also opens the possibility for the devices functionalization, making the LPGs sensors selective to a specific analyte. Selective sensors using nanoparticles have been proposed for different purposes [4-6].

A chemical route is normally employed to reduce  $\text{Au}^{3+}$  to  $\text{Au}^0$  in order to grow the AuNP in a reaction between tetrachlorauric acid ( $\text{HAuCl}_4$ ) and sodium borohydride ( $\text{NaBH}_4$ ), resulting in a film which characteristics are critically dependent on the relative concentrations of the reagents. An alternative and promising method that discards the use of the reducing agent and results in a more homogeneous films with smaller AuNPs and increased crystallinity is the thermal route for the tetrachlorauric reduction [7].

In this work, the synthesis of AuNPs via thermal route was adapted in order to produce an AuNP film on the surface of an optical fiber with a previously inscribed LPG. The AuNPs films were produced on the surface of three LPGs using solutions with different concentrations of  $\text{HAuCl}_4$ . The effect of matching the resonances of several LPG modes and the localized surface plasmon band was analyzed as a function of the refractive index of the medium surrounding the device.

## 2. Methodology

The LPGs used in this work were produced in hydrogen-loaded optical fiber (Thorlabs SM-450,  $n_{\text{clad}} = 1.4616$  at 514 nm, cut-off @ 350-470 nm) at the Photorefractive Devices Unit of the Federal University of Technology – PR. The fiber was exposed to the light emitted by a UV laser (Coherent, Xantos XS, ArF at 193 nm, frequency of 300 Hz and energy per pulse of 5 mJ) producing gratings with periods of modulation (pitch) of 60  $\mu\text{m}$  (LPG1 and LPG2) and of 90  $\mu\text{m}$  (LPG3). The LPG writing parameters were chosen in order to obtain a highly sensitive grating with attenuation bands at the visible spectral range, close to the turning point. The LPG operation at the visible spectral range is a requirement to reach the resonance between a specific LPG mode and the gold nanoparticles LSPR band. On the other hand, the resonance mode splits in two bands at the turning point of the phase matching curve that represents the dependence between the resonance wavelength and the LPG periodicity [8]. These two bands at the normal and anomalous regions show the highest sensitivities to the external medium refractive index and shift in opposite directions when the surroundings change. LPGs responses to changes in the surroundings were measured before and after the deposition of the gold nanoparticles film over the fiber surface.

LPGs sensitivities were determined from their transmission spectra acquired using the light of a broadband source (FOSTEC, EKE 8375) and a UV-Vis spectrometer (Ocean Optics, HR4000 with resolution of 3.3 nm). Transmission was measured with the LPG kept under constant longitudinal strain on the surface of a glass slide. Liquid samples containing different proportions of water and glycerin were carefully poured over the LPG. During the experiments, realized to measure the samples refractive index and to acquire the LPG transmission spectra, a thermostatic bath (Lauda Staredition RE212) connected to an Abbe refractometer (Atago, DR-A1, 0.0001 resolution, 1.3000 – 1.7100 nD) was used to keep the temperature of the samples and the LPG at  $(20.0 \pm 0.2)$  °C. Proportions of water and glycerin in the samples as well as the measured refractive indexes are in Table 1.

Table 1. Characterization samples: water-glycerin content and refractive indexes.

Sample	Water (mL)	Glycerin (mL)	Refractive index
G0	30	0	$1.3322 \pm 0.0003$
G10	27	3	$1.3413 \pm 0.0001$
G20	24	6	$1.3611 \pm 0.0001$
G30	21	9	$1.3653 \pm 0.0002$
G60	12	18	$1.4125 \pm 0.0002$
G80	6	24	$1.4427 \pm 0.0002$
G100	0	30	$1.4681 \pm 0.0002$

A method based on the procedure proposed by [7] for the deposition of gold nanoparticles films on the silica surface was used to cover the fiber with a layer of nanoparticles. This procedure, in turn, is based on a method previously reported in the literature [2,3]. First, the silica surfaces are prepared to receive the nanoparticles film. The optical fiber, as well as cover slips and glass slides, are cleaned with detergent, rinsed with distilled water and acetone and dried at 200 °C. Then, they are immersed for 0.5 h in a piranha solution (2:1 mixture of sulfuric acid and hydrogen peroxide), washed with deionized water and dried at 200 °C. The amine groups that act as anchors for the gold nanoparticles are produced after immersing for 3 h the silica elements in an APTES solution ((3-Aminopropyl)triethoxysilane). Finally, the elements are exposed to the  $\text{HAuCl}_4$  solution for 3 h and heated at 200 °C to reduce the gold.  $\text{HAuCl}_4$  solutions with different concentrations ( $5 \times 10^{-3}$  mol.L<sup>-1</sup> for LPG1,  $5 \times 10^{-4}$  mol/L for LPG2 and  $5 \times 10^{-5}$  mol/L for LPG3), were used in order to determine the ideal concentration that should be used to produce an LPG with improved refractive index sensitivity in water environments. The LSPR bands of the films produced over the glass slides were measured with an UV-Vis spectrometer (Ocean Optics, HR4000 with resolution of 3.3 nm).

### 3. Results and Discussion

The LSPR bands of the AuNPs films obtained using  $\text{HAuCl}_4$  solutions with three different concentrations are shown in Figure 1. LSPR bands from 500 to 600 nm are characteristic of gold nanoparticles. The extinction magnitudes in the spectra of Figure 1 indicates that the films present different concentrations of nanoparticles and/or thicknesses. For  $\text{HAuCl}_4$  solution  $5 \times 10^{-5}$  mol.L<sup>-1</sup> (LPG3) the LSPR band is about 20 times less intense than the bands obtained with the other  $\text{HAuCl}_4$  solutions ( $5 \times 10^{-3}$  mol.L<sup>-1</sup> (LPG1) and  $5 \times 10^{-4}$  mol.L<sup>-1</sup> (LPG2)). Additionally, its peak wavelength is blue shifted, pointing out to a distinct size distribution. These differences should result from a lack of control in the production process and reflects on the LPG-AuNP spectra and sensitivity to the external medium refractive index.

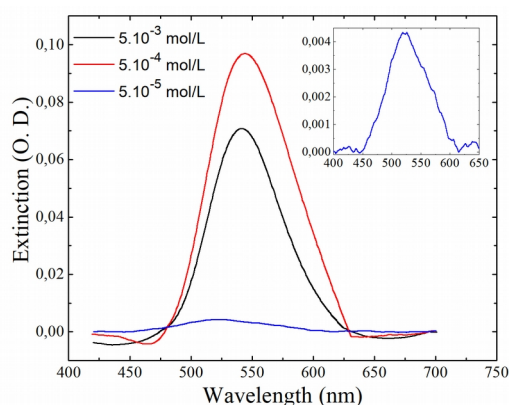


Fig. 1. Plasmon resonance bands obtained using  $\text{HAuCl}_4$  solutions with different concentrations.

LPGs transmission spectra measured before and after the formation of the gold nanoparticles film over the fiber surface are shown in Figure 2 for the gratings immersed in air. Spectral changes experienced by LPG1 and LPG2 are characterized by larger wavelength shifts and higher attenuation than those observed for LPG3. As expected, the metallic film increases the effective refractive index of the fiber cladding modes promoting the observed wavelength shifts of the LPG resonance bands. This statement is supported by the behavior of the LPGs bands in the presence of the water-glycerin samples, which is shown in Figure 3. For an LPG, when the surroundings refractive index increases, bands at the normal region are blue-shifted whereas bands at the anomalous region are red-shifted. Therefore, the bands responses allow identifying the turning point (TP) and bands at the normal or anomalous region. Mode coupling depends on the difference between the core and cladding effective refractive indexes and radius as well as on the grating periodicity. As the grating pitch is larger for LPG3, the turning point region is red-shifted when compared with LPG1 and LPG2.

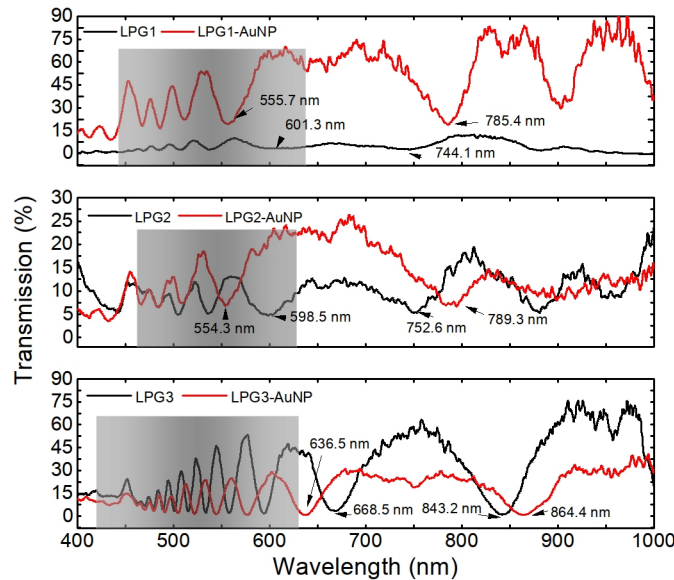


Fig. 2. LPGs transmission spectra in air, before and after coating the fiber with the gold nanoparticles film. The spectral region of the LSPR bands are represented by gray rectangles.

As can be seen from Figure 3, when the uncoated LPGs are immersed in glycerin (G100 sample,  $n=1.4681$ ) the surrounding refractive index approaches the fiber cladding refractive index, preventing the appearance of the resonances in the transmission spectra [9].

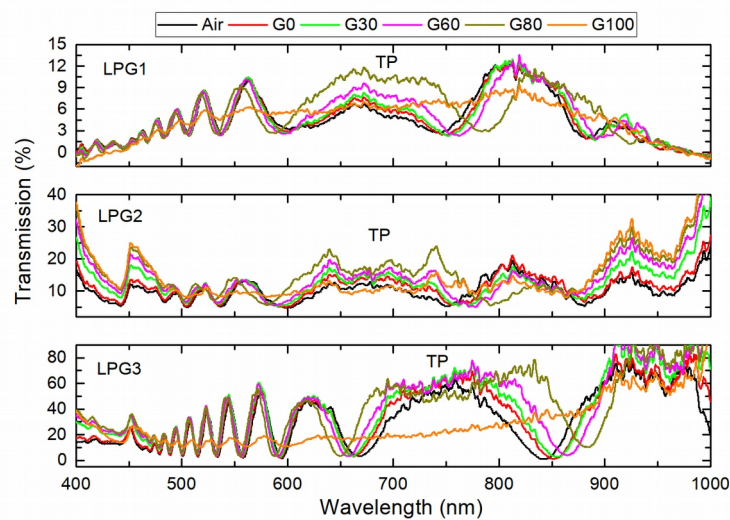


Figure 3. LPGs transmission spectra in air and in the presence of the water glycerin samples.

The fiber coating with gold nanoparticles also modifies the LPG response to the surroundings. Figure 4 shows transmission spectra obtained with the coated LPGs surrounded by different media. Gray rectangles

superposed to the spectra of Figures 2 and 4 indicate the approximate spectral ranges covered by the corresponding LSPR bands. LPG3-AuNP exhibits the characteristic wavelength shifts for the bands at the normal and anomalous regions. As the surroundings medium refractive index approaches the silica refractive index, the transmission spectrum of the coated LPG3 shows the same behavior observed in Figure 3 for the uncoated LPG3. Attenuation bands almost disappear from the spectrum when immersed in the G100 sample ( $n=1.4681$ ). However, this effect is less noticeable for the coated LPG as the cladding refractive index increases with the deposition of the gold nanoparticles on the fiber surface [2]. Unlike LPG3-AuNP, important spectral changes are not observed in the transmission spectra of LPG1-AuNP and LPG2-AuNP, even in the presence of the samples with the highest refractive indexes. Sensitivities of the coated and uncoated LPG3 are compared in Table 2 for six attenuation bands and surroundings with refractive indexes close to the pure water refractive index.

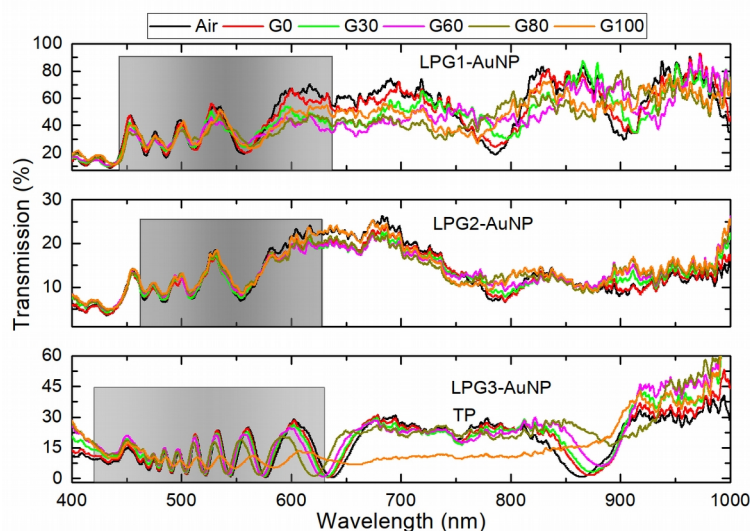


Figure 4. LPGs-AuNP transmission spectra in air and in the presence of the water glycerin samples.

Table 2. Refractive index sensitivities (nm/RIU) for attenuation bands of the coated and uncoated LPG3.

$\lambda$ (nm)	500.43	490.57		514.87	503.99		532.91	521.31	
n	Uncoated	Coated	Change (%)	Uncoated	Coated	Change (%)	Uncoated	Coated	Change (%)
1.3322	-1.67	-2.29	37.1	-1.87	-2.88	54.0	-2.38	-3.74	57.1
1.3413	-1.93	-2.62	35.8	-2.16	-3.29	52.3	-2.75	-4.28	55.6
1.3611	-2.75	-3.64	32.4	-3.11	-4.58	47.3	-3.95	-5.98	51.4
1.3653	-2.99	-3.93	31.4	-3.38	-4.95	46.5	-4.30	-6.47	50.5
$\lambda$ (nm)	556.87	543.60		592.22	575.02		667.53	634.15	
n	Uncoated	Coated	Change (%)	Uncoated	Coated	Change (%)	Uncoated	Coated	Change (%)
1.3322	-3.44	-6.37	85.2	-6.96	-9.48	36.2	-24.12	-28.36	17.6
1.3413	-3.98	-7.26	82.4	-8.04	-10.80	34.3	-27.81	-32.17	15.7
1.3611	-5.71	-10.00	75.1	-11.49	-14.88	29.5	-39.57	-43.87	10.9
1.3653	-6.21	-10.79	73.8	-12.51	-16.04	28.2	-43.00	-47.15	9.7

When the LPG3-AuNP attenuation bands and the LSPR band are resonant, an important increase of sensitivity was observed. A maximum increase of sensitivity of 85.2 % was measured for the attenuation band at 543.60 nm when the LPG is immersed in water. This attenuation band is resonant with the maximum of the gold nanoparticles LSPR band. Response, calibration and sensitivity curves for this resonance mode of the uncoated and coated LPG are show in Figure 5.

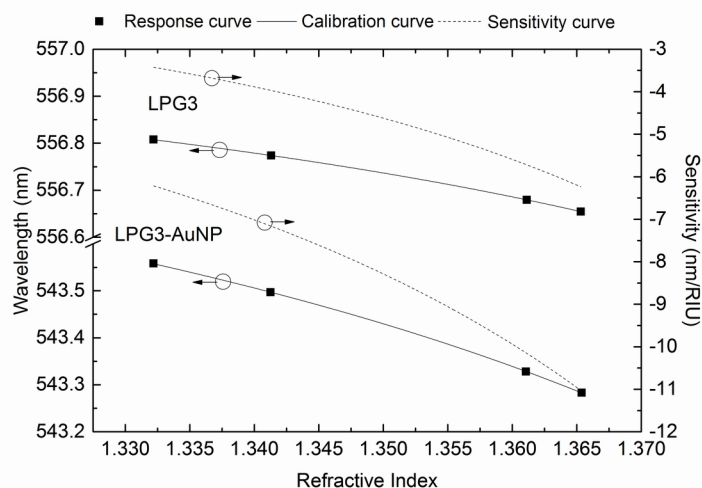


Figure 5. Calibration and sensitivity curves for the LPG3 band at 556.87 nm and LPG3-AuNP band at 543.60 nm for surroundings refractive indexes from 1.3322 to 1.3653. Error bars are less than the symbol size.

#### 4. Conclusions

In this work, the method adapted from [7] was successfully used for the optical fiber coating with gold nanoparticles. Due to the modified cladding effective refractive index as well as to the coupling between the LPG and LSPR resonances, an increase of up to 85% in the LPG sensitivity in water environment was achieved for the coated grating. Despite the resonance between the LPG attenuation and the LSPR band does not occur exactly at the turning point, this increase of sensitivity is larger than those previously reported in the literature of 50% [3] and 65% [10]. The increase in the effective refractive index of the cladding modes resulting from the use of  $\text{HAuCl}_4$  solutions  $5 \times 10^{-3}$  mol/L and  $5 \times 10^{-4}$  mol/L probably shifts the high sensitivity region to a range of refractive indexes higher than that of the G100 sample ( $1.4681 \pm 0.0002$ ). Tests are under way to prove this assumption. The methodology used for the nanoparticles deposition on the surface of the optical fiber have shown potential to optimize the performance of a nanostructured device already proposed in the literature for the detection of glyphosate in water [4]. Studies are under way in order to produce a reusable sensor with application extended to other water pollutants.

#### Acknowledgments

The authors acknowledge the financial support received from Coordenação de Aperfeiçoamento de Pessoal de Nível Superior - Brasil (CAPES) - Finance Code 001, CNPq, FINEP and Fundação Araucária.

#### References

- [1] S. W. James and R. P. Tatam, "Optical fibre long-period grating sensors: characteristics and application," *Meas. Sci. Technol.* **14** (5), R49-R61 (2003).
- [2] B. R. Heidemann, I. Chiamenti, M. M. Oliveira, M. Muller, and J. L. Fabris, "Plasmonic optical fiber sensors: enhanced sensitivity in water-based environments," *Appl. Opt.* **54** (27), 8192-8197 (2015).
- [3] B. R. Heidemann, J. D. C. Pereira, I. Chiamenti, M. M. Oliveira, M. Muller, and J. L. Fabris, "Matching long-period grating modes and localized plasmon resonances: effect on the sensitivity of the grating to the surrounding refractive index," *Appl. Opt.* **55** (32), 8979-8985 (2016).
- [4] B. R. Heidemann, I. Chiamenti, M. M. Oliveira, M. Muller, and J. L. Fabris, "Functionalized Long Period Grating-Plasmonic Fiber Sensor Applied to the Detection of Glyphosate in Water," *J. Light. Technol.* **36** (4), 863-870 (2018).
- [5] K. Chang, S. Wang, H. Zhang, Q. Guo, X. Hu, Z. Lin, H. Sun, M. Jiang, and J. Hu, "Colorimetric detection of melamine in milk by using gold nanoparticles-based LSPR via optical fibers," *PLoS One* **12** (5), 1-12 (2017).
- [6] S. Viswanathan, C. Rani, and C. Delerue-Matos, "Ultrasensitive detection of ovarian cancer marker using immunoliposomes and gold nanoelectrodes," *Anal. Chim. Acta* **726**, 79-84 (2012).
- [7] C. R. Klimpovuz, "Síntese de nanopartículas de ouro em substrato de sílica por diferentes rotas sintéticas, com posterior deposição de polímero luminescente para aplicação em sensores óticos," (undergraduate final project) Federal University of Technology-PR, 2017.
- [8] X. Shu, L. Zhang, and I. Bennion, "Sensitivity characteristics of long-period fiber gratings," *J. Light. Technol.* **20** (2), 255-266 (2002).
- [9] R. Hou, Z. Ghassemlooy, A. Hassan, C. Lu, and K. P. Dowker, "Modelling of long-period fibre grating response to refractive index higher than that of cladding," *Meas. Sci. Technol.* **12** (1), 1709-1713 (2001).
- [10] F. Tian, X. Li, J. Kanka, and H. Du, "Fiber optic index sensor enhanced by gold nanoparticle assembly on long period grating," *Optik (Stuttg.)* **132**, 445-449 (2017).

# D-Shaped Photonic Crystal Fiber Biosensor for Glucose Concentration Using a Graphene-Sheet

Romeiro, Amanda de Freitas<sup>1</sup> ; Gaia, Patrick Ferreira<sup>1</sup> ; Cardoso, Markos Paulo<sup>1</sup> ;  
Silva, Anderson Oliveira<sup>2</sup> ; Costa, João Crisostomo Weyl Albuquerque<sup>1</sup>

*Laboratory of Applied Electromagnetism - Federal University of Pará - Belém, Brazil.<sup>1</sup>*

*Department of Electronic Engineering – Federal Center for Technological Education Celso Suckow da Fonseca – Rio de Janeiro, Brazil.<sup>2</sup>*

*Romeiro, Amanda de Freitas - romeiro.amanda@gmail.com*

**Abstract:** We design a graphene-based D-shaped photonic crystal fiber refractive index sensor to detect changes in the levels of glucose concentration. Its sensing performance is theoretically analyzed using the Finite Element Method (FEM). The sensor has an average sensitivity of 2560.6 nm/RIU when we vary the glucose concentration from 0 to 200g/l.

## 1. Introduction

Highly accurate and non-invasive biosensing platforms are of major importance for a prompt detection and treatment of diseases. The sensors for the measurement of glucose concentration in blood are a remarkable example. Within this field, many promising alternatives rely on the development of optical sensing techniques [1, 2].

In this paper, a sensing platform based on a D-shaped photonic crystal fiber biosensor for glucose concentration is investigated. The Finite Element Method (FEM) was used to investigate the sensing properties of this glucose sensor. An average sensitivity of 2560.6 nm/RIU is obtained when the proposed configuration was applied to the detection of glucose concentration between 0 to 200 g/l in water. The average sensitivity increases to 2917.2 nm/RIU when we focus on the range 1 g/l to 6 g/l, which is of major clinical interest for diabetes diagnosis.

## 2. The D-shaped Photonic Crystal Fiber – Design and Modeling

The optical properties of silica-air photonic crystal fibers can be tailored by the size, position and shape of the air holes, which represents an advantage over conventional fibers for optical sensing applications [3]. In this work, we analyze the properties of a D-shaped photonic crystal fiber for the sensing of glucose concentration. The cross-section of the D-shaped PCF is depicted in Fig. 1. The configuration consists of a side polishing PCF with a hexagonal array of air holes on a matrix of fused silica. A thin graphene film above a gold layer is deposited on the flat surface of the cladding. The sample of glucose to be sensed can be dropped on the top of this coating. The contact area of the sample and graphene-gold film is increased and this interface is closer to the core, which provides a better coupling between the core-guided mode and the plasmonic mode. The total diameter of the fiber is  $D = 240 \mu\text{m}$  and the diameter of the air holes is designated by  $d$ . The distance between two adjacent air holes is fixed at  $\Lambda = 2 \mu\text{m}$ . The ratio between  $d$  and  $\Lambda$  is  $d/\Lambda=0.90$ .

The total thickness of the graphene layer is 5 nm. The refractive index of graphene is given by the relation:

$$n_g = 3 + iC_1\lambda/3, \quad (1)$$

where  $C_1 \approx 5.446\mu\text{m}^{-1}$  and  $\lambda$  is the vacuum wavelength [3]. The proposed structure is made up of silica, and all the holes are air-filled. The refractive index of silica can be determined using the Sellmeier equation [4].

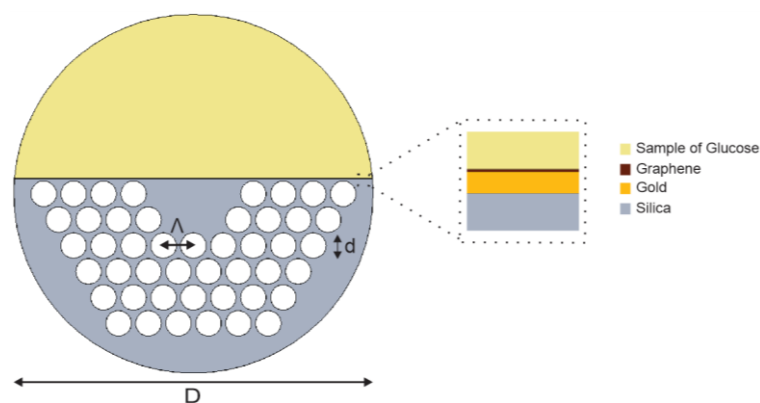


Fig. 1. Schematic design of the graphene-based D-shaped photonic crystal fiber.

In this work we used a 40 nm thick slab of gold (Au) as the conducting material in order to favor surface plasmon excitation and contribute with relatively low losses to the effective dielectric function of the flat layer. The dispersion of gold was obtained from the data tabulated in [5]. The numerical analysis of this work was made using a 2D simulation mode analysis assuming the cross section to be along XY plane and incident radiation at the Z axis. The electromagnetic mode of the sensor is solved by finite element method (FEM) using COMSOL Multiphysics software [6]. To evaluate properly the sensing properties of the D-shaped fiber we used a perfectly matched layer (PML) boundary condition with 10% of the fiber diameter for the truncation of the computational domain.

### 3. Results and Discussion

Fig. 2. presents the real and imaginary parts (blue and green curves, respectively) of the effective index and the electric field distribution at different wavelengths. The peak of the imaginary part (absorption peak) results from the coupling between the fundamental core-guided mode and the plasmonic mode. At this point a significant portion of energy is guided between the conducting film and the dielectric medium.

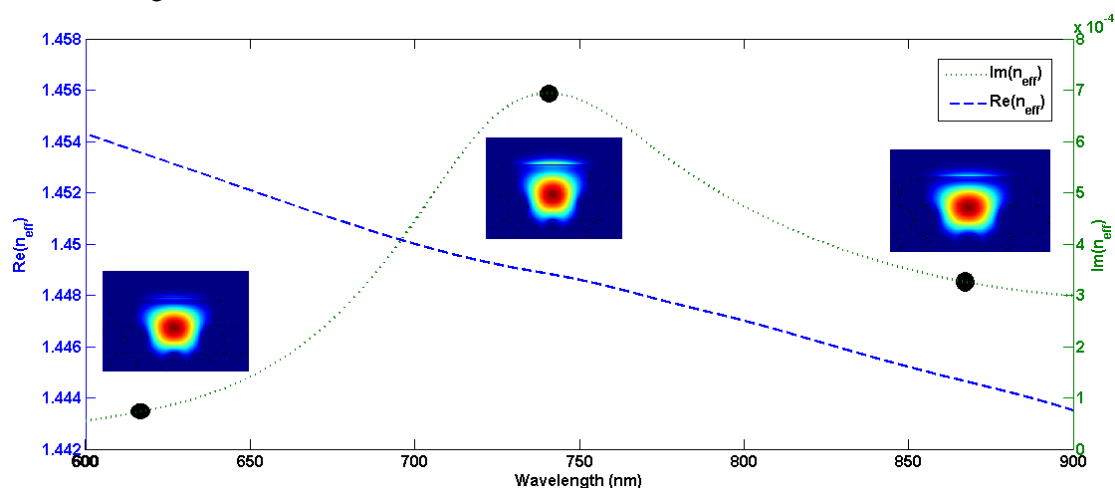


Fig. 2. Real and imaginary part of the effective refractive index for 200g/l of glucose concentration. The inset shows the mode field distribution in different wavelength of the proposed sensor. Conditions: gold film thickness of  $t_{Au} = 40$  nm, graphene layer depth  $t_{graphene} = 5$  nm and analyte refractive index  $n_{analyte} = 1.35497$ .

The sensor response of the structure shown in Fig. 1 is computed as the spectral shift of the absorption peak with the change in the refractive index of the analyte deposited on the flat surface.

In this work, the analyte corresponds to a solution of glucose in water. Therefore, the sensor response can also be considered the measurement of the spectral shift as function of the glucose concentration. Table 1 shows the relationship between the average refractive index of the sample with the glucose concentration [1]. This relation can also be approached by the equation.

$$n_{g/l} = 0.00011889C + 1.33230545 \quad (2)$$

where  $C$  is the glucose concentration (g/l) and the  $n_{g/l}$  is the average refractive index [1].

Table 1. Variation of the average refractive index with the glucose concentration. (Adapted from [1])

Average refractive index (n)	Glucose concentration (g/l)	Average refractive index (n)	Glucose concentration (g/l)
1.33128	0	1.34768	120
1.33469	20	1.34853	140
1.33698	40	1.35028	160
1.33985	60	1.35379	180
1.34273	80	1.35497	200
1.34446	100		

Fig. 3 depicts the spectral shift of the confinement losses for different values of glucose concentration in water. The Confinement loss is a suitable way to represent the imaginary part of the mode effective index and can be calculated by the equation [7]:

$$L = 8,686 \times \frac{2\pi}{\lambda} \text{Im}[n_{eff}] \times 10^4 (\text{dB/cm}), \quad (3)$$

where the  $\lambda$  represents the wavelength and  $\text{Im}[n_{eff}]$  is the imaginary part of the effective index. Based on the correspondence between glucose concentration and refractive index listed in table I, the sensitivity can be estimated by:

$$S_{\lambda} = \frac{\Delta\lambda_{peak}}{\Delta n_a} (\text{nm/RIU}), \quad (4)$$

where  $\Delta\lambda_{peak}$  is the wavelength resonance displacement and  $\Delta n_a$  is defined as the change in the analyte refractive index. The Table 2 exhibit the sensitivity for the variation of the refractive index of the sample and the corresponding glucose concentration.

The results listed in Table 2 show that the structure allows to reach an average sensitivity of 2560.6 nm/RIU, which is an improvement to the value of 1445.4 nm/RIU achieved when the graphene layer is removed. The resolution of the proposed structure with a graphene layer is  $3.9 \times 10^{-5}$  RIU for an optical spectrum analyzer with resolution of 0.1 nm.

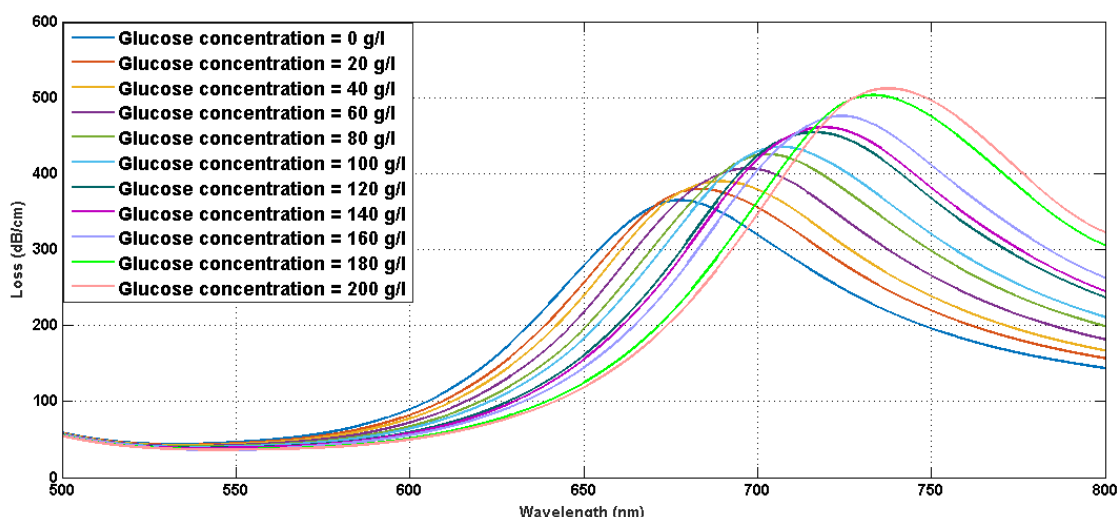


Fig. 3. Displacement of the resonance peak in confinement loss spectra under different glucose concentration. Conditions: gold film thickness of  $t_{Au} = 40$  nm, graphene layer depth  $t_{graphene} = 5$  nm.

Table 2. Sensitivity for the variation of refractive index.

Variation of glucose concentration (g/l)	Variation of refractive index (n)	Sensitivity (nm/RIU)
0-20	1.33128 - 1.33469	1759.53
20-40	1.33469 - 1.33698	2620.08
40-60	1.33698 - 1.33985	2613.24
60-80	1.33985 - 1.34273	1770.83
80-100	1.34273 - 1.34446	2601.15
100-120	1.34446 - 1.34768	3074.53
120-140	1.34768 - 1.34853	3529.41
140-160	1.34853 - 1.35028	2742.85
160-180	1.35028 - 1.35379	2478.63
180-200	1.35379 - 1.35497	3813.55
Average Sensitivity		2560.6

Additional computations have shown that the average sensitivity increases to 2917.2nm/RIU for the interval [1 g/l, 6 g/l], which is the typical range covered by commercially available glucose monitoring systems to assist the diagnosis and treatment of diabetes [8]. The resolution presented by the D-shaped PFC biosensor with a graphene sheet is  $3.4 \times 10^{-5}$  RIU. The corresponding results are summarized in Table 3.

Table 3. Sensitivity for the variation of refractive index in the range [1 g/l, 6 g/l]

Variation of glucose concentration (g/l)	Variation of refractive index (n)	Sensitivity (nm/RIU)
1-2	1.332424 – 1.332543	5882.35
2-3	1.332543 – 1.332662	4201.68
3-4	1.332662 – 1.332781	2100.84
4-5	1.332781 – 1.3329	420.16
5-6	1.3329 – 1.333019	3361.34
Average Sensitivity		2917.2

#### 4. Conclusion

A D-shaped photonic crystal fiber sensor for glucose concentration is described and analyzed. Its principle of operation relies on the coupling between the fundamental core fiber mode and the surface plasmon at the graphene-gold film and its spectral dependence upon the glucose solution deposited on the flat surface. The average sensitivity for values of glucose concentration in water ranging from 0 g/l up to 200 g/l is 2560.6 nm/RIU and particularly reaches 2917.2 nm/RIU over the range [1 g/l, 6 g/l], which covers the interval of conventional glucose biosensors. The results for sensitivity and resolution suggest the potential of the proposed structure as a sensing platform for the detection of glucose concentration.

#### 5. Acknowledgments

This study was financed in part by the Coordenação de Aperfeiçoamento de Pessoal de Nível Superior – Brasil (CAPES) – Finance code 001.

During the period of elaboration of this work, the authors have obtained support of the Conselho Nacional de Desenvolvimento Científico e Tecnológico (CNPq).

#### 6. References

- [1] Y.-L. Yeh (2008) Real-time measurement of glucose concentration and average refractive index using a laser interferometer, *Optics and Lasers in Engineering* 46 (2008) 666– 670.
- [2] C. J. Durango, J. M. Cardona, N. G. Cardona, E. R. Vera, B. H. Herrera, J. U. Restrepo, J. F. Restrepo, M. Váron (2018) Real-time measurement of glucose concentration and average refractive index using a laser interferometer, 2018 International Conference on Electromagnetics and Advanced Applications (ICEAA) 531– 534.
- [3] J. N. Dash, R. Ja (2015) On the performance of graphene-based Dshaped photonic crystal fibre biosensor using surface plasmon resonance. *Plasmonics* 10(5):1123–1131.
- [4] B.B. Shuai, X. Li, Y. Z. Zhang, D. M. Liu (2012) A multi-core holey fiber based plasmonic sensor with large detection range and high linearity. *Opt Express* 20(6):5900–5974.
- [5] P.B. Johson, R.W. Christy (1972) Optical Constants of the Noble Metals, *Physical Review*, 1972, Vol 6, Num 12.
- [6] <https://br.comsol.com>.
- [7] P. P. Zhang, J. Q. Yao, H. X. Cui, Y. Lu (2013) A surface plasmon resonance sensor based on a multi- core photonic crystal fiber. *Opt Lett* 35(6):1673–1905.
- [8] Dongmin Seo, Sung-Ho Paek, Sangwoo Oh, Sungkyu Seo and Se-Hwan Paek (2016) A Human Serum-based Enzyme-Free Continuous glucose monitoring technique using a needle-type bio-layer interference sensor. *Sensors* 2016, 16, 1581; doi:10.3390/s16101581.

# Plastic Fiber Optic for Ultrasensitive Gas Detector Applications

Meysam Keley<sup>1</sup>, Juan David Lopez<sup>2</sup>, Alex Dante<sup>1</sup>, Talitha Trovão<sup>1</sup>, Roberto Wu Mok<sup>1</sup>, Pedro Henrique Romualdo<sup>2</sup>, Fabricio Borghi<sup>3</sup>, Cesar Cosenza Carvalho<sup>1</sup>, Regina Celia da Silva Barros Allil<sup>1</sup> and Marcelo Martins Werneck<sup>1,2</sup>

<sup>1</sup>Photonics and Instrumentation Laboratory, Electric Engineering Program

<sup>2</sup>Photonics and Instrumentation Laboratory, Nanotechnology Engineering Program

<sup>3</sup>Magnetic Nanomaterials Laboratory, Physics Institute

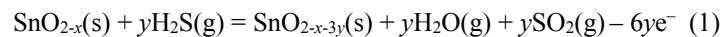
Federal University of Rio de Janeiro (UFRJ), RJ 21941-594, Brazil

<sup>1</sup>meysamkeley@hotmail.com

**Abstract:** In the present study, an ultrasensitive hydrogen sulfide sensor is developed via functionalization of U-shaped Plastic optical fiber. The results of the sensor demonstrate low response time and full recovery while exposed to a gas mixture containing 200 ppm concentration of measured.

## 1. Introduction

Plastic optical fibers (POFs) benefit from their higher mechanical strength, which makes them more flexible than glass fibers to use in toughness–demanded cases. The POFs also possess an extremely large core/cladding size ratio. This factor takes into account when the removal of cladding is required to fabricate a satisfactory sensor. Gas sensors are a subcategory of chemical detectors, which are designated to sense and/or quantify the concentration of one or more gaseous species. Highly increasing demand to detect gases in low concentrations inspires scientists to develop more precise and fast gas sensors. Carbon dioxide concentration, for example, is a good factor to evaluate the air freshness [1]. Taking into account the security issues, detection of inflammable and/or toxic gases, such as methane and hydrogen sulfide, turns a protection tactic against crew fatalities, explosion, and fire incidents on petroleum platforms[2]. Detection of some organic gases such as NO in exhaled breath is an approved pathological method of airway inflammations including asthma [3]. Polycrystalline SnO<sub>2</sub> is fundamental *n*-type semiconductor in gas sensing area principally for reducing gases such as H<sub>2</sub>, CH<sub>4</sub>, C<sub>4</sub>H<sub>10</sub>, CO, and H<sub>2</sub>S. Under ambient air conditions, (O<sub>2</sub><sup>-</sup>)<sub>ad.</sub> and (O<sup>-</sup>)<sub>ad.</sub> chemisorbed donors are present at the surface of SnO<sub>2</sub>. These species are involved in reversible catalytic oxidation of reducing gases [4]. The X-ray Photoelectron Spectroscopy (XPS) spectra gained from a tin oxide sample after exposure to H<sub>2</sub>S demonstrate a S(2s) core level peak at 161 eV binding energy. Consequently, the following reversible chemical reaction is proposed [5]:



The main disadvantages of SnO<sub>2</sub>, other than functional temperature of 400°C, are the poor selectivity and stability of the sensor signal. A SnO<sub>2</sub> sensor doped with 5 wt.% CuO becomes dramatically sensitive to H<sub>2</sub>S at temperatures lower than 200°C. Since H<sub>2</sub>S is an acidic (reducing) gas, its sensitivity increases using basic additives [5]. Like copper oxide, nickel oxide has an outstanding promotion effect in H<sub>2</sub>S sensitivity [6]. These behaviors are attributed to nickel and copper intrinsic affinity to sulfur [7]. Doped SnO<sub>2</sub> gas sensing mechanism can be explained based on semiconductors theory. Considering tin oxide as a matrix, copper oxide aggregations act as a dispersed phase. Oxygen deficient matrix (*n*-type semiconductor) and oxygen rich dispersed phase (*p*-type semiconductor) form a series of *n-p-n* semiconductor set. Consequently a depleted area is formed in matrix–dispersion interface and a potential barrier is established which increases the overall conductivity of the set. Once exposed to H<sub>2</sub>S or any other sulfur containing gas, copper oxide and sulfur undergo a reversible chemical reaction as follows:



Copper monosulfide (CuS) is a moderate conductor of electricity. Therefore, potential barrier which is the result of a *n-p-n* semiconductor set is removed. Moreover, the work function of CuS is several times lesser than SnO<sub>2</sub>. As a result, the bands bending downwards which facilitates the electron flow from CuS to SnO<sub>2</sub> and vice versa [10]. The same mechanism is proposed for NiO/SnO<sub>2</sub> Sensors. However, the point in NiO doping is the operation temperature range that falls in 0 to 150°C [8].

Partial removal of cladding enables the interaction between the light guided through an optical fiber and the surrounding media. The cladding can be either tapered, etched or even side–polished. In some cases, the sensing

procedure functions based on Evanescent Field (EF). As the proportion of light interacting with the surrounding depends on its refractive index, EF-operated sensors are more used with liquid samples (as liquids has more refractive index than gases due to their higher density) [9]. In a more advanced method, gas sensitive thin films substitute partially the cladding. Enabling the light to be influenced indirectly with the test gas [10]. A bent optical fiber sensor, working based on absorption or evanescent field, can achieve a sensitivity order of 70 times higher than a straight form [11]. In two successful works, a U-shaped POF receives sensitive films to detect glucose, ethyl alcohol, and milk quality [12, 13].

In the current study, a new generation of H<sub>2</sub>S gas sensors as developed with the aid of Refractive Index (RI) and Evanescent Field (EF) principles dominant in Plastic Optical Fibers (POF). The U-shaped POFs are functionalized receiving various Pulsed Laser Deposited (PLD) multilayer thin films of CuO and SnO<sub>2</sub>. During exposure to H<sub>2</sub>S, these metal oxides undergo a chemical reaction and/or a physico-chemical surface H<sub>2</sub>S adsorption. Consequently, their physical properties, in general, and optical behavior (refractive index, transmittance, etc), in particular, are altered. The U-shaped POF containing such thin film is coupled to an electro-optical set configured to retrieve signals depending on internal RI and EF. Therefore, any changes in the optical parameters of the thin film may interfere in the output of the fiber. The procedure of fabricating a U-shaped POF sensor through deposition of a thin film sensitive to desired measurand may function for wide range of chemical detection. Therefore, the challenge is to find a substance with affinity to measurand, which is also capable of being deposited on a POF. The optical sensing mechanism can be maintained the same.

## 2. Experimental Setup

The POFs are cut and their cladding is removed. Then, they are bent to gain dimensions reported in Fig. 1. This geometry makes a larger Evanescent Field (EF) in the curvature area. Each U-shaped POF is subjected to Pulsed Laser Deposition (PLD) in order to receive a thin film of SnO<sub>2</sub> and/or CuO. A light propagation (in this case LED) and detection (Photocell) system is used to analyze the behavior of studied optical sensor during H<sub>2</sub>S exposure.

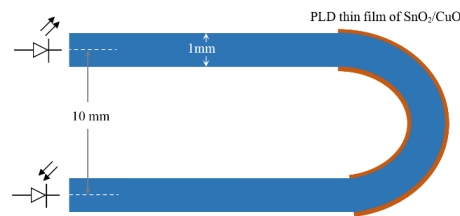


Fig. 1. The geometry of bent area in POF explored in the current work. The thin films of metal oxides are deposited on curved part of optical fiber equipped with light propagation (LED) and detection components (Photocell).

The laser used to perform PLD procedure has a pulse frequency of 10 Hz and a wavelength of 553 nm (2 $\Omega$  from Nd-YAG source). Its energy is adjusted to meet 50 mJ/cm<sup>2</sup> per pulse. The pressure of deposition chamber is kept to be 2.5 $\times 10^{-5}$  mbar (Fig. 2)

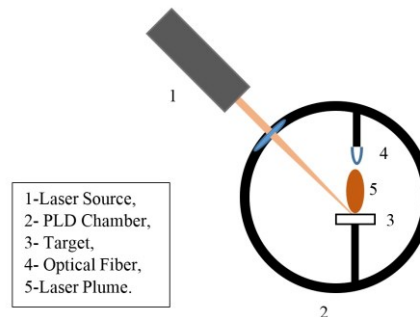


Fig. 2. Schematic of Pulsed Laser Deposition chamber.

A controlled atmosphere chamber capable of gas purge in controlled flow is developed to simulate the H<sub>2</sub>S exposure and record possible changes in optical energy transmitting through optical fiber-thin film set (Fig. 3).

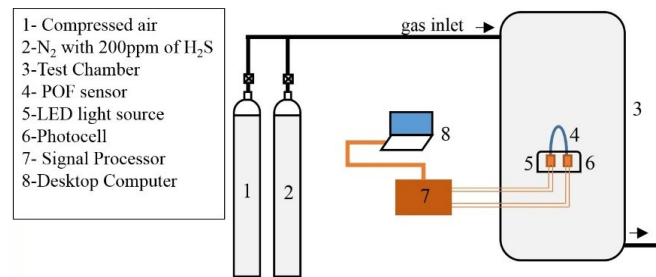


Fig. 3. Schematic exposure to hydrogen sulfide test chamber. The sensor is subjected to an atmosphere containing a maximum concentration of 200ppm H<sub>2</sub>S. Then the fresh air is injected to reset the procedure.

In order to have a reference film morphology free of POF roughness and curvature, a standard silicon wafer, with <100> crystal growth direction, is used as a substrate. The Si plate is cut in 1×1 cm<sup>2</sup> dimensions and subjected to PLD CuO deposition for 30 min. The sample then is analyzed using JPK<sup>®</sup>(NanoWizard<sup>®</sup>) Atomic Force Microscopy in “intermittent contact” mode and topography channel.

According to literature, SnO<sub>2</sub> doped with CuO demonstrates an excellent performance while the former has a matrix role and the latter forms a dispersed phase. Consequently, single layers of SnO<sub>2</sub> and CuO as well as SnO<sub>2</sub>/CuO hybrid thin films are deposited and tested. To fabricate the multilayer thin film, the POF is undergone through subsequent changing of the target (Pure SnO<sub>2</sub> and CuO disks) in a single PLD run. The best results are achieved in a deposition cycle containing a step of SnO<sub>2</sub> deposition for 55 seconds followed by a CuO deposition for 5 seconds. The mentioned cycle is repeated 10 times.

### 3. Results and Discussion

AFM images indicate that the PLD thin films produced containing a homogeneous structure accompanied with distinguishable circular droplets with diameter variety falling in 100 to 500 nm range (Fig. 4).

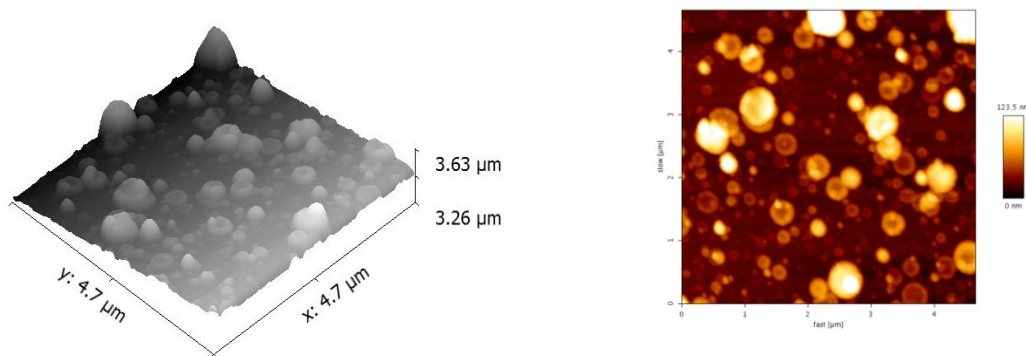


Fig. 4. AFM images of the PLD CuO thin film deposited on a standard Silicon substrate. Left) 3D and Right) 2D topography demonstration of the film. It contains a uniform ultrathin film underneath a set of nanometric sized isolated spherical-shaped islands (typical morphology of PLD films).

After receiving the thin film, each POF probe is mounted in H<sub>2</sub>S testing chamber at room temperature. the Infrared wavelength LED light source connected to one end of the fiber emits a constant light quantity and the Photocell connected to another side (see the Fig. 1) transforms it to voltage (in mV). Any attenuation during exposure to H<sub>2</sub>S is attributed to refractive index modification in the sensitive thin film. In order to normalize the intensity of transmitted light and relate it to the effect of H<sub>2</sub>S on the Refractive Index of the thin film and Evanescent Field of the POF, the following equation is used:

$$signal (\%) = \frac{y_0 - y_t}{y_0} \times 100 \quad (3)$$

Where:

$y_0$  is the steady state light transmitted and detected by photocell through the POF called as yield (in mV);

$y_t$  is the yield in time  $t$  while the test is running.

A common testing procedure for this class of sensors involves a set of cycles including purging of Nitrogen with a 200ppm concentration of  $H_2S$  and fresh air, respectively. These cycles simulate the occurrence of  $H_2S$  leakage in, for example, refinery plant. The POF containing a straight  $SnO_2$  thin film demonstrates no sensibility to measurand. This observation may be attributed to the fact that the functional temperature of undoped  $SnO_2$  is higher than  $400^\circ C$ . The U-shaped POF which receives a thin film of  $CuO$  demonstrates excellent sensitivity with high signal. However, poor reversibility. Actually the sensor functions for only two cycles (Fig. 5). The phenomenon can be related to intrinsic affinity of copper to sulfur and an irreversible reaction transforms it permanently to  $CuS$  (see equation 2).

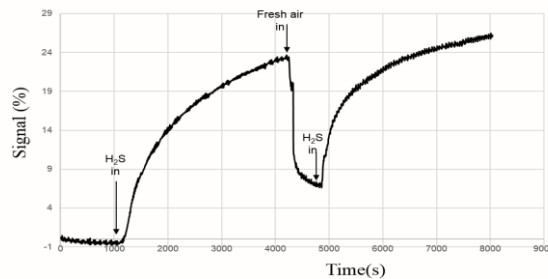


Fig. 5. The graph of a partially reversible sensor.

Finally, the U-shaped POF functionalized with the hybrid  $SnO_2/CuO$  multilayer thin film is tested in which the sensor undergoes three cycles and its response is recorded (Fig. 6). According to this test, the response time of the developed sensor falls in 80-100 seconds. It also demonstrates that the maximum signal is about 2%. The sensor demonstrates total reversibility after 3 cycles.

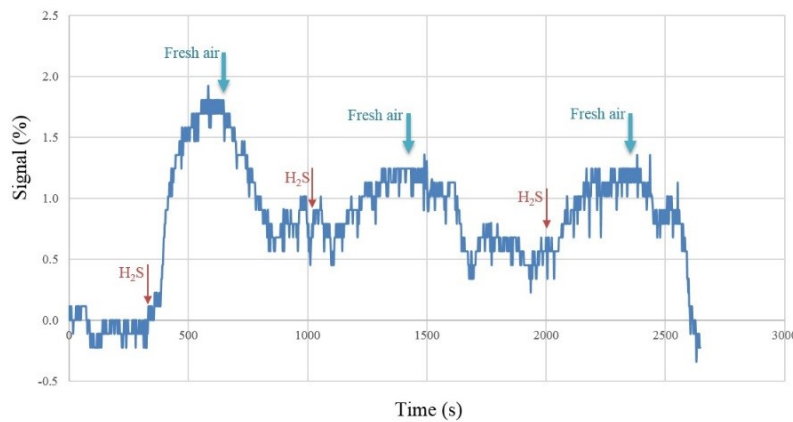


Fig. 6. The signal vs. time curve of developed sensor during a  $H_2S$  leakage simulation. The red arrows mark the moment of measurand (200ppm of  $H_2S$  in  $N_2$ ) injection to chamber. While the blue ones are marking fresh air purging.

#### 4. Conclusions

A new generation of  $H_2S$  gas sensors is developed and tested successfully at room temperature. Being an optic appliance, the sensing part is free of electrical charge. Consequently, it can be installed in sites at which there is a large demand of security against explosion. Thanks to its operational temperature, the sensor is free of any heating apparatus that used to be mandatory in conventional  $H_2S$  sensing setups. Its confirmed sensibility falls in orders of 100 ppm of the mentioned gas. The experiment revealed that the POF functionalized with hybrid  $SnO_2/CuO$  multilayer thin film undergoes a remarkable change in signal as it is exposed to  $H_2S$  in ppm concentration orders.

More studies are needed to measure exact reversible exposure limit of the sensor. Additionally another hybrid thin films may be studied, as well as other geometries than U-shape.

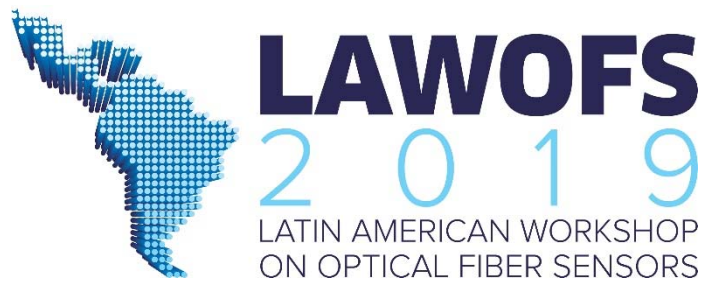
## Acknowledgements

The authors acknowledge support from Coordenação de Aperfeiçoamento de Pessoal de Nível Superior (CAPES) through the post-doctorate fellowship. This work was also financially supported by PETROBRAS, whose guidance and assistance are gratefully acknowledged.

## 5. References

- [1] A. Schieweck, *et. al.*, “Smart home and the control of indoor air quality”, *Renewable and Sustainable Energy Reviews* 94, 705–718 (2018).
- [2] K. V. D. Ambeth, “Human security from death defying gases using an intelligent sensor system”, *Sensing and Bio-Sensing Research* 7, 107–114 (2016).
- [3] R. A. Dweik, *et. al.*, “An official ATS clinical practice guideline: interpretation of exhaled nitric oxide levels (FENO) for clinical applications”, *American Journal of Respiratory and Critical Care Medicine* 184(5), 602–615 (2011).
- [4] C. E. Simons, O. G. Florea, A. Stanoiu, “Gas sensing mechanism involved in H<sub>2</sub>S detection with NiO loaded SnO<sub>2</sub> gas sensors”, *Romanian Journal of Information Science and Technology* 20, 415–425 (2017).
- [5] T. W. Capehart, S. C. Chang, “The interaction of tin oxide films with O<sub>2</sub>, H<sub>2</sub>, H<sub>2</sub>S”, *Journal of Vacuum Science and Technology* 18, 393–397 (1981).
- [6] J. Liu, X. Huang, *et. al.*, “H<sub>2</sub>S detection sensing characteristics of CuO/SnO<sub>2</sub> sensor”, *Sensors* 3, 110–118 (2003).
- [7] W. G. Davenport, M. King, M. Schlesinger, A. K. Biswas, “Extractive metallurgy of copper” 4<sup>th</sup> edition, 2002, Pergamon.
- [8] M. Kaur, *et. al.*, “RF sputtered SnO<sub>2</sub>:NiO thin films as sub-ppm H<sub>2</sub>S sensor operable at room temperature”, *Sensors and Actuators B*, 242, 389–403 (2017).
- [9] H. Waechter, *et. al.*, “Chemical sensing using fiber cavity ring-down spectroscopy”, *Sensors (Basel)*, 10(3) 1716–1742 (2010).
- [10] L. Bilro, *et. al.*, “Optical sensors based on plastic fibers”, *Sensors*, 12184–12207 (2012).
- [11] S. Tao, L. Xu, J. C. Fanguy, “Optical fiber ammonia sensing probes using reagent immobilized porous silica coating as transducers”, *Sensors and Actuators B* 115, 158–163 (2006).
- [12] C. Zhang, *et. al.*, “U-bent fiber optic SPR sensor based on graphene/AgNPs”, *Sensors and Actuators B: Chemical* 251, 127–133 (2017).
- [13] G. Annasamy, *et. al.*, “U-bent plastic optical fiber probes as refractive index based fat sensor for milk quality monitoring”, *Optical Fiber Technology* 47, 15–20 (2019).

**Page left in blank due to paper no-show at the workshop.**



# Etched Fiber Bragg Gratings Functionalized with PCDTBT:PDI Thin Film for Ammonia Detection

Jean F. Kuhne<sup>1</sup>, Anderson E. X. Gavim<sup>1</sup>, Paula C. Rodrigues<sup>1</sup>, Bruno B. M. Torres<sup>2</sup>, Andréia G. Macedo<sup>1</sup>, Jeferson F. de Deus<sup>1</sup>, Ricardo C. Kamikawachi<sup>1</sup>

<sup>1</sup>Federal University of Technology-Paraná, Av. Sete de Setembro, 3165, Curitiba-PR, Postal Code 80.230-901-Brazil

<sup>2</sup>Instituto de Física-Universidade de São Paulo-Av. Trab. São-Carlense, 400-Parque Arnold Schmidt, 13566-590, São Carlos-SP-Brazil  
e-mail address: canute@utfpr.edu.br

**Abstract:** The functionalization of an etched fiber Bragg grating with a drop casted thin film improved the sensor sensitivity to ammonia vapors. The film was obtained from a solution of a perylene derivative along with the copolymer PCDTBT, in chlorobenzene. The resulting sensor detects ammonia vapors ranging from 27 to 6954 ppm, at room temperature.

## 1. Introduction

Ammonia is a natural gas that can be found in the air, soil, and water. At the beginning of the 20<sup>th</sup> century, ammonia diffusion to the environment could be attributed to the nitrogen cycle, thunders and volcanoes activity. Nowadays, the majority of ammonia released in the atmosphere has its origin in human activities. Ammonia is one of the largest volume synthetic chemical produced in the world [1], with more than 80% of its production destined for the nitrogen-based fertilizers industry. Ammonia losses during production and fertilizer spreading correspond to more than 95% of the anthropogenic ammonia emissions [2]. At high concentrations or in the long term, it becomes a hazard to the local environment [3] and to human health [4]. Its vapor or liquefied forms are both corrosive and toxic, making its monitoring essential. Ammonia is colorless, with a characteristic pungent smell. Regular ammonia perception by smell is given by 25 ppm, and human exposure to such concentration is not recommended for periods longer than 8 hours. At 35 ppm, the recommended exposure limit drops to 15 minutes [5]. Concentrations above 100 ppm are uncomfortable to most people. In despite the upper respiratory tract irritation and eyes tearing, concentrations up to 500 ppm do not represent life-threatening health effects for short period exposure. Above 500 ppm, the protective response to inhaling irritant vapors known as reflex glottis closure is verified. Concentrations above 5000 ppm are potentially lethal [6]. Once that ammonia is very soluble in water, it forms ammonium hydroxide and produces heat when in contact with moist surfaces, such as mucous membranes. The corrosive and exothermic properties of ammonia can result in immediate damage to the eyes, skin, and severe damage at all levels of the respiratory system.

Several technologies can be applied to ammonia detection such as metal-oxide [7], the reactivity of catalytic metals [8] and conductive polymers [9]. Sensors parameters like flexibility, low weight, fast response and low cost of production are desirable in any measurement system. In this sense, fiber Bragg gratings (FBG) sensors are suitable candidates. Even though FBGs are inherently sensitive to strain and temperature [10], they become sensitive to the surrounding environment after their cladding portion had been functionalized or partially/completely removed [11]. The cladding portion removal can be easily accomplished by chemical etching in hydrofluoric acid (HF). The etched FBG (EFBG) sensor relies on the interaction of the evanescent field of the propagating core mode with the fiber surroundings [11]. Additionally, the sensor response can be improved with the application of conjugated films into the EFBG. The ammonia vapor interaction with these films is given by chemical reactions or charge transfers, resulting in changes in the film optical absorbance or in the film refraction index [12]. As a result, the propagating light in the optical fiber has its amplitude modulated or its wavelength shifted. Few publications report the use of fiber gratings for ammonia gas sensing [13-15].

In our previous work, we reported that PCDTBT:PDI thin films can be used to functionalize EFBGs sensors, improving their sensitivity to ammonia [16]. The copolymer PCDTBT was applied as a matrix to the perylene derivative PDI, which behaved as the sensing element. In this work we report that a greater sensitivity is achieved by lowering the compounds concentration. The new film has a  $(23.44 \pm 1.38)$  nm thickness and the prepared calibration curve allows ammonia detection with concentration ranging from 27 to 6954 ppm.

## 2. Materials and Methods

### 2.1. Chemicals

The perylene-3,4,9,10-tetracarboxylic dianhydride (PTCDA), the poly[[9-(1-octylnonyl)-9H-carbazole-2,7-diyl]-2,5-thiophenediyl-2,1,3-benzothiadiazole-4,7-diyl-2,5-thiophenediyl] (PCDTBT), the decylamine and the

zinc acetate were purchased from Sigma-Aldrich and they were used without any further purification. The imidazole was purchased from Alfa Aesar. Spectroscopic grade solvents were used for all the experiments.

### 2.2. Film Preparation, Characterization and Sensor fabrication

Individual solutions of PCDTBT and PDI were prepared, both adopting chlorobenzene as a solvent. The PCDTBT solution was prepared by the addition of 1 mg of the polymer in 1 ml of the solvent. The solution was magnetically stirred for 1 hour at room temperature. Solvent was added to the resulting solution of 1 mg.ml<sup>-1</sup> until a concentration of 0.125 mg.ml<sup>-1</sup> was verified.

The soluble symmetrically N,N'-substituted perylene derivative (PDI) was obtained by the condensation reaction of PTCDA with aliphatic primary amines, in molten imidazole solvent with zinc acetate as a catalyst, according to the standard condensation methods [17,18]. The PDI solution was prepared by the addition of 1 mg of the PDI molecule in 1 ml of the solvent. The solution was magnetically stirred for 1 hour at room temperature. The solvent was added to the resulting solution of 1 mg.ml<sup>-1</sup> until a concentration of 0.25 mg.ml<sup>-1</sup> was verified.

The 0.125 mg.ml<sup>-1</sup> PCDTBT solution and the 0.25 mg.ml<sup>-1</sup> PDI solution were magnetically stirred for 1 hour at room temperature. Both solutions were then mixed at a 1:1 volume ratio, remaining upon magnetic stirring for another extra hour at room temperature, resulting in a PCDTBT:PDI-0.187 mg.ml<sup>-1</sup> 1:2 solution. A thin film control sample was created by drop casting the volume of 20  $\mu$ l of the solution over a 1x2 cm glass substrate, made from a microscope slide.

Topography images of the PCDTBT:PDI-0.187 mg.ml<sup>-1</sup> 1:2 film control sample were acquired using the atomic force microscope (AFM) SPM-9700 (Shimadzu). The AFM operated in dynamic mode, using a NCR-10 (Nano World) silicon tip, with a frequency of 285 kHz and force constant of 42 N.m<sup>-1</sup>. The thickness of the PCDTBT:PDI 0.187 mg.ml<sup>-1</sup> 1:2 film control sample was measured with the non-contact 3D profiler Talysurf CCI Lite (Taylor Hobson), which has a 10 pm vertical resolution, with a 20x magnification lens.

The FBG was inscribed in a Draka Comteq single mode fiber with the phase mask technique. An ArF excimer laser (Xantos XS, Coherent®) was used, emitting at 193 nm, with 250 Hz and 2.5 mJ energy per pulse. The fiber cladding was removed by chemical etching (40 % HF) until a 4 nm blue wavelength shift had been observed. The etching process was neutralized in NaOH. A volume of 20  $\mu$ l of the PCDTBT:PDI-0.187 mg.ml<sup>-1</sup> 1:2 was drop casted over the EFBG and the sensor was kept light sheltered for 24 hours, at room temperature.

The Bragg wavelength shift was monitored with the SM-125 optical interrogator (Micron Optics), at a 2 Hz scan rate and wavelength accuracy of 1 pm. The curves were smoothed adopting the Savitzky Golay method (50 points of window and second polynomial order).

### 2.3. Sensor Characterization

The measurement setup is composed of a platform that lifts a chamber containing ammonia vapor to the sensor that is fixed at the top of a rod, as presented in Figure 1. The sensor is kept exposed to the ammonia vapor within the chamber for 15 minutes. Afterward, the platform is lowered and the sensor is exposed to the environmental air for the same amount of time. A 3-liter flask was used as a vapor chamber. In order to create ammonia vapor, a fixed volume of 50  $\mu$ l of ammonium hydroxide (NH<sub>4</sub>OH), under different concentrations, was pipetted into the chamber. Each NH<sub>4</sub>OH concentration had its own chamber. After the NH<sub>4</sub>OH had been placed inside the chamber, it was immediately closed and kept sealed for 10 minutes, until the measurement took place.

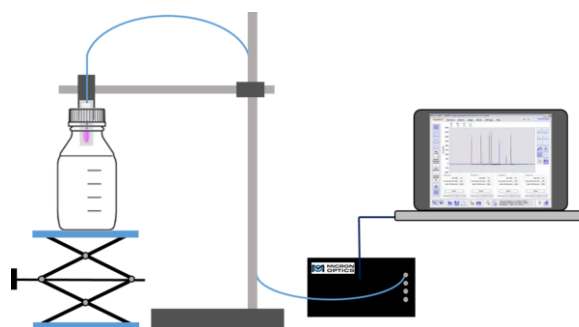


Fig. 1. A platform lifts an NH<sub>3</sub> chamber up to the sensor. The Bragg wavelength shift is registered by the optical interrogator.

### 3. Results and discussions

Figure 2 presents the height and phase AFM images acquired from PCDTBT:PDI-0.187 mg.ml<sup>-1</sup> 1:2 films using highly diluted chlorobenzene solution. This film is composed of fibers that may arise from the columnar aggregation of PDI. Moreover, the phase image pointed out the PDI aggregation resulting in isolated microsized domains with size ranging from 1 μm up to 2 μm. The profilometer measurement evaluated the thickness of the PCDTBT:PDI-0.187 mg.ml<sup>-1</sup> film, and the value of (23.44 ± 1.38) nm was found.

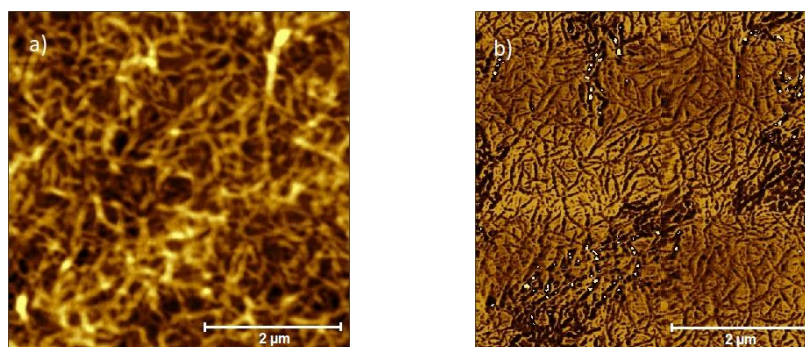


Fig. 2. a) Height and b) phase AFM images from PCDTBT: PDI 0.187 mg.ml<sup>-1</sup> 1:2 thin films.

Figure 3 presents the performance of the coated sensor for ammonia concentrations ranging from 27 to 6954 ppm, at room temperature. A red wavelength shift can be observed when the sensor is exposed to the ammonia within the chamber. A blue wavelength shift can be observed when the sensor is exposed to environmental air, indicating the sensor reversibility. The solid red line represents the exponential fit to each individual concentration, and their convergence values are plotted as calibration points in Figure 4(a). The sensor behavior could be explained by the charge transfer between the ammonia (electron donor) and the PDI molecule (electron acceptor). The charge transfer could change the film optical properties, like the refractive index, that could be detected by the EFBG. The full comprehension of the sense mechanism is under investigation.

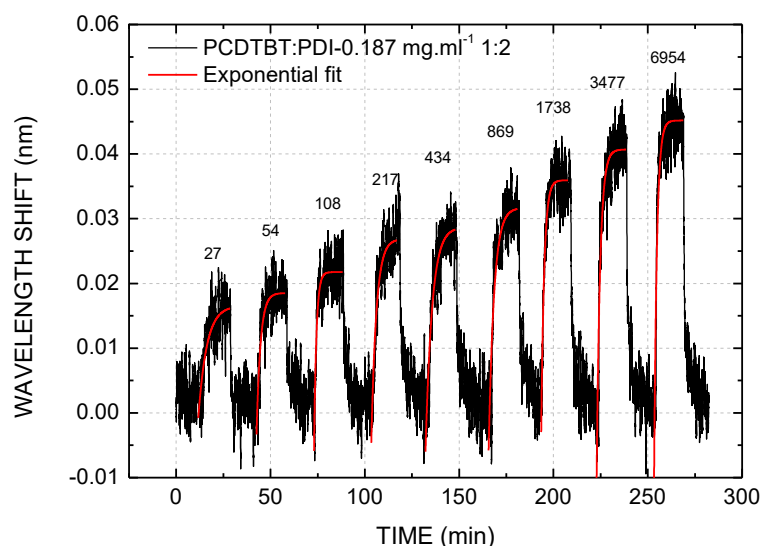


Fig. 3. PCDTBT:PDI-0.187 mg.ml<sup>-1</sup> 1:2 sensor wavelength shift versus time for ammonia exposure.

The exponential fit of the calibration points allowed to plot the calibration curve of the coated sensor, plotted in solid red line in Figure 4(a). The PCDTBT:PDI-0.187 mg.ml<sup>-1</sup> 1:2 sensor sensitivity and resolution are plotted in the Figure 4(b). The sensor sensitivity, plotted in solid black line, was obtained by the derivative of the calibration curve. The sensor resolution, plotted in the solid blue line, was obtained by the division of the SM-125 resolution by the sensitivity curve.

At 27 ppm, which is close to the lower limit of human nose ammonia perception, the sensor presents a sensitivity of  $0.019 \text{ pm.ppm}^{-1}$  and a resolution of 50.307 ppm. Around 100 ppm, a concentration that is very unpleasant to humans, the sensor sensitivity is  $0.018 \text{ pm.ppm}^{-1}$  and the resolution is 53.503 ppm. Around 500 ppm, a concentration where reflex glottis closure is verified, the sensitivity is  $0.013 \text{ pm.ppm}^{-1}$  and the resolution is 74.764 ppm.

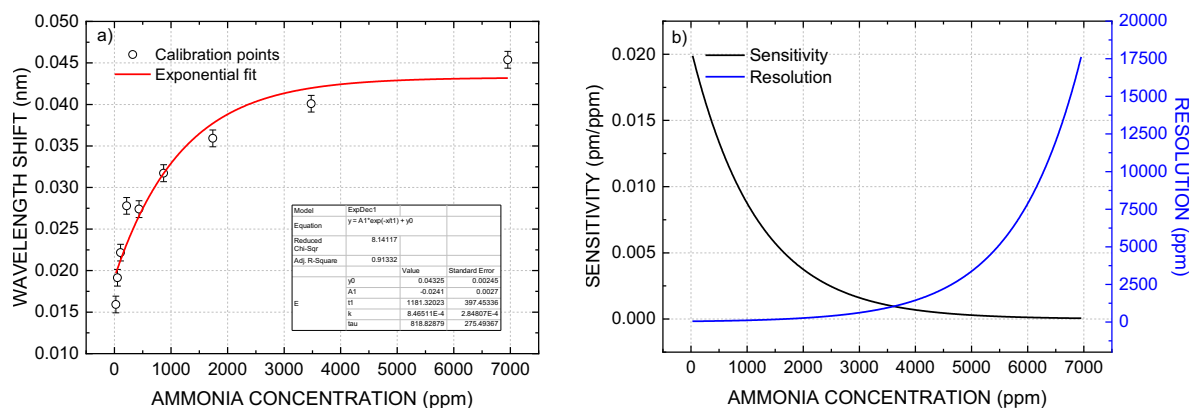


Fig. 4. a) Calibration curve and b) sensitivity and resolution curve of the ammonia sensor.

#### 4. Conclusions

An EFBG ammonia gas sensor, functionalized with a PCDTBT:PDI-0.187  $\text{mg.ml}^{-1}$  1:2 thin film was described. The sensor is reversible and allows the detection of an ammonia concentration down to 27 ppm, which is close to the average human nose perception limit. The sensor presents a dynamical range higher than a similar sensor showed in our previous work, allowing the detection of an ammonia concentration up to 6954 ppm, which can be lethal for long period exposure. A calibration curve was plotted, and its derivative allowed to plot the sensor sensitivity curve. The division of the interrogation system resolution (1 pm) by the sensitivity curve allowed to plot the resolution curve. At 27 ppm, which is close to the lower limit of human nose ammonia perception, the sensor presents a sensitivity of  $0.019 \text{ pm.ppm}^{-1}$  and a resolution of 50.307 ppm.

#### Acknowledgments

This work was supported by the Brazilian Agencies CNPq, CAPES Finance Code 001, SETI, FINEP, INCT-INEO, and Fundação Araucária.

#### References

- [1] V. Pattabathula, J. Richardson, "Introduction to Ammonia Production", *Chemical Engineering Progress*, pp. 69-75 (Sep. 2016).
- [2] J. R. Ista, R. Borger, L. Temmerman, Guns, K. Meeus-Verdinne, A. Ronse, P. Scokart, and M. Termoniad, "Effect of Ammonia on the Acidification of the Environment", Stationery Office Books (Dec. 1988).
- [3] S. V. Krupa, "Effects of atmospheric ammonia ( $\text{NH}_3$ ) on terrestrial vegetation: A review," *Environmental pollution* (Barking, Essex : 1987), vol. 124, pp. 179-221 (Aug. 2003).
- [4] B. Timmer, W. Olthuis, and A. van den Berg, "Ammonia sensors and their applications - a review," *Sensors and actuators. B: Chemical*, **107**, no. 2, pp. 666-677 (2005).
- [5] ATSDR, "Toxicological profile for ammonia", Atlanta, GA: Agency for Toxic Substances and Disease Registry. U.S. Department of Health and Human Services, Public Health Service, NTIS PB2004-107331 (2004).
- [6] N. R. Council, "Acute Exposure Guideline Levels for Selected Airborne Chemicals", Washington, DC: The National Academies Press, Volume 6 (2008).
- [7] A. Pathak, S. K. Mishra, and B. D. Gupta, "Fiber-optic ammonia sensor using Ag/SnO<sub>2</sub> thin films: optimization of thickness of SnO<sub>2</sub> film using electric field distribution and reaction factor," *Applied Optics*, **54**, 8712-8721 (2015).
- [8] I. Lundstrom, A. Spetz, F. Winquist, U. Ackelid, and H. Sundgren, "Catalytic metals and field-effect devices - a useful combination," *Sensors and Actuators B: Chemical*, vol. **1**, no. 1, pp. 15 - 20 (1990).

- [9] L. Kumar, I. Rawal, A. Kaur, and S. Annapoorni, "Flexible room temperature ammonia sensor based on polyaniline," *Sensors and Actuators B: Chemical*, **240**, 408 – 416 (2017).
- [10] K. O. Hill and G. Meltz, "Fiber Bragg grating technology fundamentals and overview," *Journal of Lightwave Technology*, **15**, 1263–1276 (1.997).
- [11] L. Dong, J. L. Cruz, L. Reekie, and L. Archambault, "Tuning and chirping fiber Bragg gratings by deep etching," *IEEE Photonics Technology Letters*, **7**, 1433–1435 (1.995).
- [12] S. Zhang, X. Wang, Y. Huang, H. Zhai, and Z. Liu, "Ammonia sensing properties of perylene diimides: Effects of core-substituted chiral groups," *Sensors and Actuators B: Chemical*, **254**, 805 – 810 (2018).
- [13] T. Wang, W. Yasukochi, S. Korposh, S. W. James, R. P. Tatam, and S. W. Lee, "A long period grating optical fiber sensor with nano-assembled porphyrin layers for detecting ammonia gas," *Sensors and Actuators B: Chemical*, **228**, 573 – 580 (2016).
- [14] G. B. Tait, G. C. Tepper, D. Pestov, and P. M. Boland, "Fiber Bragg grating multi-functional chemical sensor," in *SPIE Proceedings*, (international society for optics and photonics, 2005), **5279**, pp. 5994 – 5994 (2005).
- [15] H. Fu, J. Zhang, J. Ding, Q. Wang, H. Li, M. Shao, Y. Liu, Q. Liu, M. Zhang, Y. Zhu, and C. Yang, "Ultra sensitive nh3 gas detection using microfiber Bragg grating," *Optics Communications*, **427**, 331 – 334 (2018).
- [16] J. Kuhne, A. E. X. Gavim, A. G. Macedo, P. C. Rodrigues, B. B. M. Torres, J. F. Deus, and R.C. Kamikawachi, "Optical gas sensor for amines produced with etched fiber Bragg grating coated with PCDTBT:PDI thin films," in *OSA Conference Proceedings*, (Optical Society of America, 2018), Vol. 1985, paper WF9.
- [17] G. Türkmen, S. Erten-Ela, S. Icli, "Highly soluble perylene dyes: Synthesis, photophysical and electrochemical characterizations", *Dyes and Pigments*, **83**(3), pp. 297-30 (2009).
- [18] Th.B. Singh, S. Erten, S. Günes, C. Zafer, Turkmen, Kuban, Y. Teoman, N.S. Sariciftci, S. Icli, "Soluble derivatives of perylene and naphthalene diimide for n-channel organic field-effect transistors", *Organic Electronics*, **7**(6), pp 480-489 (2006).

# Hole-Assisted Helically Twisted Twin-Core Fiber Coupler

Juan Esteban Úsuga Restrepo<sup>1,2</sup>, William M. Guimarães<sup>1,2</sup>, Marcos A.R. Franco<sup>1,2</sup>

<sup>1</sup>Instituto Tecnológico de Aeronáutica, São Jose dos Campos SP 12228-900, Brazil.

<sup>2</sup>Divisão de Física Aplicada, Instituto de Estudos Avançados, São Jose dos Campos SP 12228-001, Brazil.  
jeur@ita.br

**Abstract:** Coupling characteristics of helically twisted twin-core fibers with hole-assisted structure were numerically evaluated. It was observed the increase of coupling length with the increase of twist rate, and it was confirmed the effectiveness of hole-assisted guidance to loss reduction. The proposed twisted fiber, with 66 mm length, works as a circular polarization splitter.

## 1. INTRODUCTION

Conventional optical fibers are structures formed by a high index core surrounded by low index cladding. These optical structures can guide the light due the well-known total internal reflection effect (TIR). The development of specialty optical fibers has demonstrated the possibility to support optical guidance by many other physical effects, such as: photonic bandgap and antiresonant effect [1,2]. Recent advances in fiber optic technology has demonstrated a new physical effect able to support optical guidance in helically twisted coreless Photonic Crystal Fibers (PCF) [3]. The helically twisted structure creates a topological channel that increases the optical confinement at the twisting axis [3,4]. This effect occurs both because the longitudinal twist rate and the quadratic increase of the optical path as function of radial coordinates [3,4].

In recent years the interest in developing optical platforms, based on helically twisted optical fibers, have grown [3,5,6] and applications in optical fiber sensing have been demonstrated [5,7]. Twisting optical fibers induces chiral properties that allows controlling the polarization state, generates modes with total angular momentum and induces optical activity [3,6]. In this paper, for the first time, are presented numerical characterization of helically twisted twin-core couplers (HTTC) as function of twist rate. Its main contribution is to reveals the influence of twist rate in the characteristics of twin-core couplers. To control the confinement losses in the proposed device, we explore a new design with the inclusion of a ring of air-holes to obtain a hole-assisted helically twisted twin-core fiber coupler (HTTC-HALF) [8].

## 2. HELICALLY TWISTED TWIN-CORE FIBER COUPLER

Twin-core fiber couplers are structures based on identical cores for which coupling length is dependent of the distance between cores, the wavelength and the refractive index contrast between cores and cladding. The proposed helically twisted twin-core fiber couplers (HTTC) are shown in Fig.1 (a) and Fig. 1(c). The simplest structure (Fig. 1(a)) consists of a step index twin-core with a small gap between them. The more complex structure (Fig. 1(c)) is similar to the first design with the inclusion of air-holes surrounding the fiber's cores. The air-hole ring increases the optical confinement acting as a hole assisted lightguide fiber (HALF) [8]. The new coupler design will be named HTTC-HALF.

The geometric models are presented in Figs. 1(a) and 1(c). The couplers consist of two step index solid cores with diameter  $D = 8.2 \mu\text{m}$  and gap between cores of  $1.0 \mu\text{m}$ . The refractive index contrast between core and cladding is  $\sim 0.357\%$  considering a cladding refractive index of 1.444024 at 1550 nm. The hole-assisted fiber coupler includes a ring of air-holes with diameter  $d = 0.4 * D$  (Fig. 1 (c)).

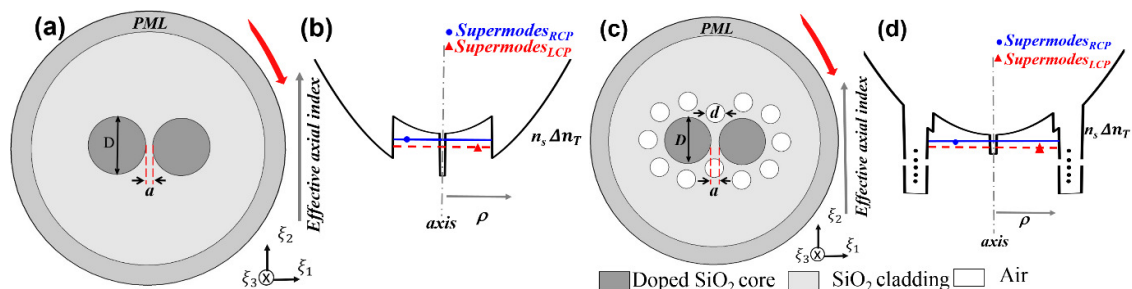


Fig.1. Helically twisted twin-core fiber couplers (HTTC). (a) Geometric model of HTTC. (b) Refractive index profile of HTTC along x axis. (c) Geometric model of HTTC-HALF. (d) Refractive index profile of HTTC-HALF along x axis. Arrow shows the rotation direction.

In this paper both fiber couplers are helically twisted what causes a change in the optical path as function of radial coordinate and twist rate. This increase in optical path can be properly represented mapping Cartesian to helical coordinates where helically twisted optical fibers are represented by a geometric model independent of longitudinal coordinate [9]. In this case, the optical path changes are represented by equivalent non-homogeneous material properties (electrical permittivity and magnetic permeability) with full anisotropy [3,9].

Figs. 1(b) and 1(d) present the equivalent refractive index values along symmetry horizontal axis after the space mapping from Cartesian to helical coordinates. It is possible to observe a quadratic index change as function of radial coordinate. Because fiber's cores are symmetrically fixed at a distance from fiber center, the increase of optical path is identical for both core regions ensuring a high coupling factor. However, high twist rates cause changes in the coupling factor infringing changes in coupling length.

For special optical fibers with helically twisted structures it is not possible to establish an accurate analytical approach capable to describe the whole characteristics of electromagnetic wave propagation. However, it is possible to use a numerical approach to solve the wave equations in all its complexity. A space mapping from Cartesian to helical coordinates allows using a 2D geometric model to represent the transversal cross section of twisted optical fibers. This is possible because helically mapped geometry is invariant along  $z$  axis. The helically twisted twin-core fiber couplers were numerically modeled with a commercial finite element software (COMSOL<sup>®</sup>) considering space mapped coordinates as an equivalent material with properties  $(\epsilon, \mu)$  that take into account the increase in optical path as function of radial coordinate and twist rate.

The space mapping from Cartesian  $(x,y,z)$  to helical  $(\xi_1, \xi_2, \xi_3)$  coordinates can be represented by:

$$\begin{aligned} x &= \xi_1 \cos(\alpha \xi_3) + \xi_2 \sin(\alpha \xi_3), \\ y &= -\xi_1 \sin(\alpha \xi_3) + \xi_2 \cos(\alpha \xi_3), \\ z &= \xi_3, \end{aligned} \quad (1)$$

where  $\alpha$  is the twist rate  $(2\pi/\Lambda_h)$  and  $\Lambda_h$  is the helical period.

Maxwell's equations are invariant under space mapping and independent of  $z$  axis for mapping to helical coordinates, when material properties  $(\epsilon, \mu)$  are represented into the helical frame [10]. The relative electrical permittivity  $\epsilon_r$  and relative magnetic permeability  $\mu_r$  tensors can be obtained in helical frame as  $\epsilon_h = \epsilon_r T^{-1}$  and  $\mu_h = \mu_r T^{-1}$ , where  $T = J^T J / \det(J)$  and  $J$  is the Jacobian matrix of the space mapping. The inverse transformation matrix is [9]:

$$T^{-1}(\xi_1, \xi_2) = \begin{bmatrix} 1 + \alpha^2 \xi_2^2 & -\alpha^2 \xi_1 \xi_2 & -\alpha \xi_2 \\ -\alpha^2 \xi_1 \xi_2 & 1 + \alpha^2 \xi_1^2 & \alpha \xi_1 \\ -\alpha \xi_2 & \alpha \xi_1 & 1 \end{bmatrix}. \quad (2)$$

### 3. RESULTS AND DISCUSSION

The numerical analysis of the structures was carried out using the full-vector finite element method. A twisted cylindrical perfectly matched layer was applied to avoid reflections at external boundaries and accurately evaluate the confinement losses [4].

In helically twisted optical fibers a linearly polarized optical mode is splitted into two circularly polarized modes, rotating to right (RCP) and left (LCP) directions. When these modes have different phase velocities, a linear combination of them results in total angular momentum. On the other hand, the helical twist affects the propagation modes creating a topological increase in optical path and in the effective index of circularly polarized modes at helical frame, that are dependent of twist rate and total angular momentum  $(l + s)$ . The effective index mode can be obtained at Cartesian frame by:

$$n_c = n_h + (l + s) \frac{\alpha}{\kappa_0}, \quad (3)$$

where  $n_h$  is the effective refractive index in the helical frame,  $l$  is the orbital angular momentum (optical vortex),  $s$  is the spin-angular momentum (circular polarization),  $\alpha$  is the twist rate, and  $\kappa_0$  is free space propagation constant. It was assigned  $s = +1$  for LCP and  $s = -1$  for RCP and  $l = 0$ . Optical activity is present when helically twisted optical fibers have different propagation constants for LCP and RCP modes. When LCP and RCP modes have a high difference on propagation losses occurs a circular dichroism.

Twin-core fiber coupler allows coupling optical signal from one core to another with a coupling coefficient-dependent coupling length. The coupling modes overlap in a linear combination of even and odd supermodes. In helically twisted twin-core fiber couplers, both the linearly polarized supermodes are splitted into RCP and LCP circular polarizations (RCP<sub>even</sub>, and RCP<sub>odd</sub>, LCP<sub>even</sub>, LCP<sub>odd</sub>). The coupler device characteristics can be evaluated using theory of coupled supermodes. This analysis requires simultaneous excitation of both even and odd modes. As usual, the coupling length ( $L_c$ ) can be evaluated as  $L_c = \lambda/2|n_{even} - n_{odd}|$ . For twisted optical fibers we combine RCP<sub>even</sub>, and LCP<sub>odd</sub> or LCP<sub>even</sub> and RCP<sub>odd</sub> to respectively evaluate  $L_{c\_LCP}$  or  $L_{c\_RCP}$ . The coupling length

of twisted devices can be evaluated following the same procedure, however using the circular polarization modes  $L_c^i = \lambda/2 |n_{c\_RCP}^{even} - n_{c\_LCP}^{odd}|$ , where  $n_{c\_RCP}^{even}$  is the effective index of RCP even supermode and  $n_{c\_LCP}^{odd}$  is the effective index of LCP odd supermode at Cartesian frame, and the index  $i$  represents the circular polarized modes (right and left).

The Figs. 2(a) and 2(b) present the effective index of  $LCP_{even}$ ,  $LCP_{odd}$ ,  $RCP_{even}$ , and  $RCP_{odd}$  modes, respectively to HTTC and HTTC-HALF fiber coupler as function of twist rate. It is observed that the effective index increases for RCP modes (odd and even) and decreases for LCP modes (odd and even) as function of twist rate, consequently generating circular birefringence. At Cartesian frame, the modal effective index difference  $|n_{c\_RCP}^{even} - n_{c\_LCP}^{odd}|$  decreases for higher twist rates, leading to longer coupling length.

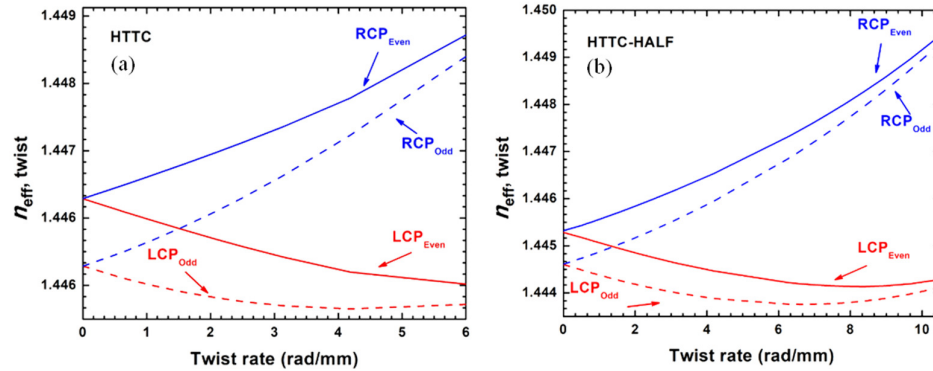


Fig.2. Modal effective index, at helical frame, of helically twisted twin-core fibers as function of twist rate. (a) HTTC. (b) HTTC-HALF.

The Figs 3(a) and 3(b) present the coupling length as function of twist rate for HTTC and HTTC-HALF. The untwisted twin-core couplers have coupling length of about 1000  $\mu\text{m}$ . Increasing the twist rate allowing longer coupling lengths to be reached. Higher twist rate causes a deformation in the optical field profile shifting the mode to peripheral region of the fiber's cores reducing the coupling factor and consequently increasing the coupling length. This mechanism is, for the first time, demonstrated for helically twisted twin-core fiber couplers.

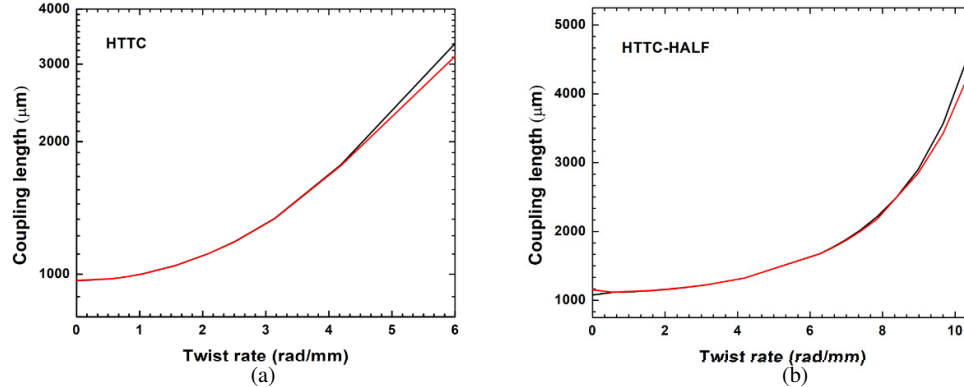


Fig.3. Coupling length of helically twisted twin-core fiber couplers as function of twist rate. (a) HTTC and (b) HTTC-HALF with gap of 1  $\mu\text{m}$ . The lines black and red represent the hand-coupled modes  $L_{c\_LCP}$  and  $L_{c\_RCP}$ .

Helically twisted fiber optic devices have larger confinement losses as the twist rate increases. To control this effect in HTTC fiber couplers it was proposed the HTTC-HALF design that includes hole-assisted guidance. The Fig. 4(a) and 4(b) show the confinement loss as function of twist rate for both configurations (HTTC and HTTC-HALF). It is evident that the structure with hole-assisted guidance presents very small confinement losses as compared to the regular structure without extra air-holes. The hole-assisted fiber coupler allows to reach a high twist rate (10.5 rad/mm) with fewer losses (0.008 dB/mm).

To analyze the possibility of obtaining a circular polarization separation it was evaluated the normalized power variation of the two circular polarization states along the propagation distance. It was considered a wavelength of 1550 nm, twist rates of 4.2 rad/mm and 10.5 rad/mm and both fiber coupler configurations (HTTC and HTTC-HALF). The Fig. 5(a) shows the power evolution at HTTC fiber's cores along propagation axis. It is possible to observe the effect of high confinement loss reducing the optical power along the fiber. The Fig. 5(b) presents the power evolution along the propagation axis of HTTC-HALF with 4.2 rad/mm twist rate. In this case the fiber coupler works fine without power reduction, however there is not circular polarization separation. The

Fig. 5(c) presents the optical power evolution of HTTC-HALF with 10.5 rad/mm twist rate. For the higher twist rate the fiber coupler is able to separate the circular polarizations at 66 mm distance.

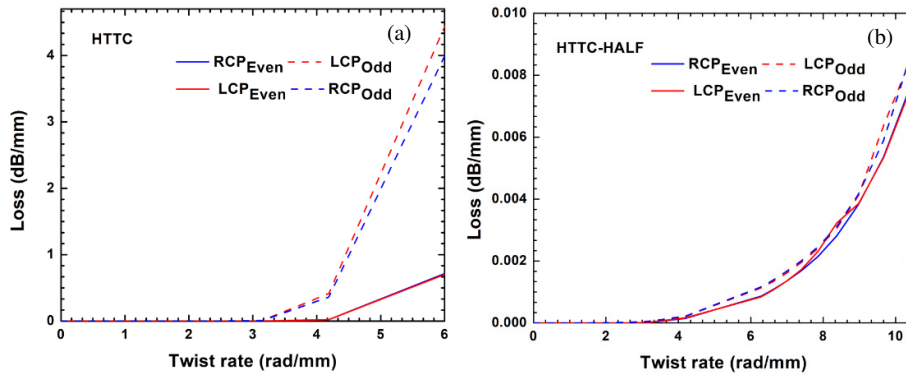


Fig.4. Confinement loss of the RCP (blue) and LCP (red) supermodes as function of twist rate. (a) HTTC. (b) HTTC-HALF.

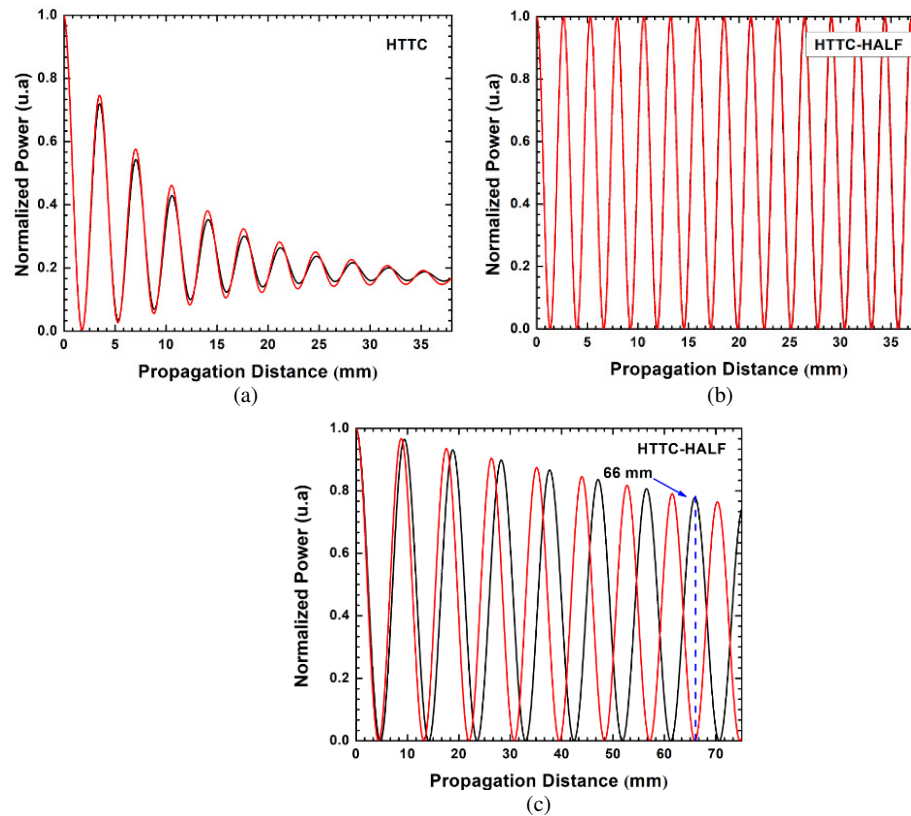


Fig.5. Normalized power of modes along propagation axis. HTTC with  $\alpha = 4.2$  rad/mm. (b) HTTC-HALF with  $\alpha = 4.2$  rad/mm. (c) HTTC-HALF with  $\alpha = 10.5$  rad/mm. The lines black and red represent the circular polarization modes  $L_{c\_LCP}$  and  $L_{c\_RCP}$ .

#### 4. CONCLUSION

In this work, for the first time, the coupling characteristics of helically twisted twin-core couplers were analyzed, demonstrating the increase of coupling length with twist rate. The first analyzed structure contains two solid waveguide cores, while the second only differs by the insertion of an air holes ring. The results show that the air holes reduce confinement losses and suppress the device's optical dichroism as twist rate increases. Lower losses allow to achieve a higher twist rate (10.5 rad/mm) obtaining a 66 mm length circular polarization splitter that has potential applications in optical information processing, routing, sensing and imaging systems. Due to the structural simplicity of the proposed coupler and circular polarization splitter, it could be useful in optical communication systems.

This study was financed in part by the Coordenação de Aperfeiçoamento de Pessoal de Nível Superior-Brasil (CAPES)-Finance code 001.

## 5. REFERENCES

- [1]. Méndez, A. and Morse, T. F., "Specialty Optical Fibers Handbook, Elsevier", (2007). ISBN 10:0-12-369406-X.
- [2]. P. Rugeland, C. Sterner, and W. Margulis, "Visible Light Guidance in Silica Capillaries by Antiresonant Reflection," *Opt. Express*. 21, 29217-29222, (2013).
- [3]. X. M. Xi, G. K. L. Wong, and T. Weiss, "Helically Twisted Solid-Core Photonic Crystal Fibers," 1–2 (2013).
- [4]. T. Fujisawa and K. Saitoh, "Off-axis core transmission characteristics of helically twisted photonic crystal fibers," *Opt. Lett.* 43, 4935-4938 (2018).
- [5]. L. Chen, W.-G. Zhang, T.-Y. Yan, L. Wang, J. Sieg, B. Wang, Q. Zhou, and L.-Y. Zhang, "Photonic crystal fiber polarization rotator based on the topological Zeeman effect," *Opt. Lett.* 40, 3448-3451 (2015).
- [6]. G. K. L. Wong, M. S. Kang, H. W. Lee, F. Biancalana, C. Conti, T. Weiss, and P. St J Russell, "Excitation of orbital angular momentum resonances in helically twisted photonic crystal fiber," *Science* 337, 446–449 (2012).
- [7]. Bai, Z. et al, "Torsion Sensor with Rotation Direction Discrimination Based on a Pre-twisted In-Fiber Mach-Zehnder Interferometer", *IEEE Photon. Lett.* Vol. 9, 7103708, (2017).
- [8]. M. Onishi, M. Nishimura, T. Hasegawa, E. Sasaoka, Y. Tsuji, and M. Koshiha, "Hole-assisted lightguide fiber for large anomalous dispersion and low optical loss," *Opt. Express* 9, 681-686 (2009).
- [9]. A. Nicolet, F. Zolla, Y. O. Agha, and S. Guenneau, "Geometrical transformations and equivalent materials in computational electromagnetism," *COMPEL* 27, 806–819 (2008).
- [10] A. J. Ward & J. B. Pendry Refraction and geometry in Maxwell's equations, *J. Mod. Opt.*, 43:4, 773-793 (1996).

# Fiber Specklegram Analysis for Monitoring Evaporation Inside a Capillary-like Optical Fiber

Thiago D. Cabral<sup>1,2</sup>, Luiz E. da Silva<sup>1</sup>, Eric Fujiwara<sup>2</sup>, Cristiano M. B. Cordeiro<sup>1</sup>

<sup>1</sup>Laboratory of Specialty Fibers and Photonic Materials - "Gleb Wataghin" Institute of Physics, University of Campinas, Rua Sérgio Buarque de Holanda 777, Campinas, 13083-860, Brazil. <sup>2</sup>Laboratory of Photonic Materials and Devices - School of Mechanical Engineering, University of Campinas, Rua Mendeleev 200, Campinas, 13083-860, Brazil.

tdcabral@ifi.unicamp.br, luiz-evaristo@hotmail.com, fujiwara@fem.unicamp.br, cmbc@ifi.unicamp.br

**Abstract:** A liquid filled capillary-like fiber sensor for monitoring the evaporation rate of the filling liquid through fiber specklegram analysis is proposed and evaluated. Experimental data shows a clear relation between the specklegram shift over time and evaporation, prospectively allowing the assessment of multiple parameters of the liquid by modeling evaporation in a capillary.

## 1. Introduction

The measurement of fluid evaporation in microchannels and capillary structures is important to several applications, such as in evaporative cooling devices and porous coating technologies [1,2]. Optical fibers can be used as a medium for carrying and analyzing fluids via microchannels intrinsic to the fiber. Even though liquid sensing with fiber devices such as Photonic Crystal Fibers is a prolific research topic [3], a simpler approach based on capillary-like fibers can be used [4,5]. In this paper, a new approach for monitoring the evaporation of a liquid inside a capillary-like fiber is reported. The fiber is filled with the fluid sample and light is launched into the capillary wall, the light traveling down the capillary interacts with the fluid and the resulting output speckle field is processed in order to retrieve the displacement of the air/liquid interface in a sensitive way.

## 2. Methodology

### 2.1. Sensor Design and Experimental Setup

The sensor consists of a hollow glass tube with outer and inner diameters of  $\sim 250$   $\mu\text{m}$  and  $\sim 200$   $\mu\text{m}$ , respectively. It was drawn from a  $6 \times 3$  mm industrial grade fused silica tube preform by setting furnace temperature to  $1902^\circ\text{C}$ , preform feeding speed to 1.5 mm/min, drawing speed to 0.80 m/min, and maintaining a constant manometric pressure of 0.4 kPa inside the tube by injecting inert gas to prevent the walls from collapsing.

A small length ( $\sim 55$  mm) of the fabricated capillary tube is filled with fluid by attaching it to a hypodermic needle and syringe containing the fluid of interest. To avoid unwanted loss of fluid by leakage or evaporation both sides of the capillary piece are sealed by injecting and hardening photocurable resin, remaining this way until the start of experiments. Fig. 1 (a) shows optical microscopy images of the tip of a resin sealed liquid filled capillary.

A schematic of the experimental setup is depicted in Fig. 1 (b). Light from a He-Ne laser source passes through a neutral density filter (NDF) and is directed to the sensing fiber by the mirrors M1 and M2. Objective lenses (L1 and L2) mounted on precision translation stages launch the light into the sensing fiber and focus the output speckle pattern into the exposed CCD of a webcam. A microscope is used to monitor the movement of the liquid inside the sensing fiber. Both the webcam and the microscope camera are connected to a computer via USB cables for data acquisition. A digital thermo hygrometer is placed near the setup to monitor temperature and relative humidity.

With an average wall thickness of 25  $\mu\text{m}$  and proper choice of the filling fluid, the capillary tube is expected to behave as a highly multimode waveguide for the light from the He-Ne source ( $\lambda = 632.8$  nm). As coherent light propagates through a multimode fiber, interference between the propagating modes creates a complex output speckle pattern. This speckle pattern, or specklegram, is sensitive to the waveguide conditions. In addition to that, the evanescent field from higher order modes interact with the surroundings of the capillary walls, making the output specklegram also sensitive to the refractive index of the surrounding mediums [6].

As the fluid inside the capillary evaporates, the output specklegram is affected by the changes in the air and liquid filling fractions. The development of the specklegram  $I(x, y)$  as the liquid evaporates was quantified by evaluating the zero-mean normalized cross-correlation (ZNCC) defined as follows [7]:

$$ZNCC = \frac{\iint (I_0 - \bar{I}_0)(I_n - \bar{I}_n) dx dy}{\left[ \iint (I_0 - \bar{I}_0)^2 dx dy \right]^{1/2} \left[ \iint (I_n - \bar{I}_n)^2 dx dy \right]^{1/2}} \quad (1)$$

Where  $I_0(x, y)$  is the reference specklegram (specklegram of the first video frame),  $I_n(x, y)$  is the specklegram for the n-th video frame,  $\bar{I}_0$  is the average intensity of  $I_0(x, y)$ ,  $\bar{I}_n$  is the average intensity of  $I_n(x, y)$ , and  $(x, y)$  are pixel coordinates in the digital specklegrams. ZNCC was chosen for its property of suppressing variations in the image brightness, providing results more robust than a conventional normalized correlation coefficient [7,8].

ZNCC data reported in this work was calculated from a  $200 \times 200$  pixels square window in the specklegram videos centered at mid-height and slightly off-centered towards the inner wall, to analyze the speckle closer to the filling fluid. This region of interest is shown as a dashed yellow square on the inset to the right of Fig. 1 (b).

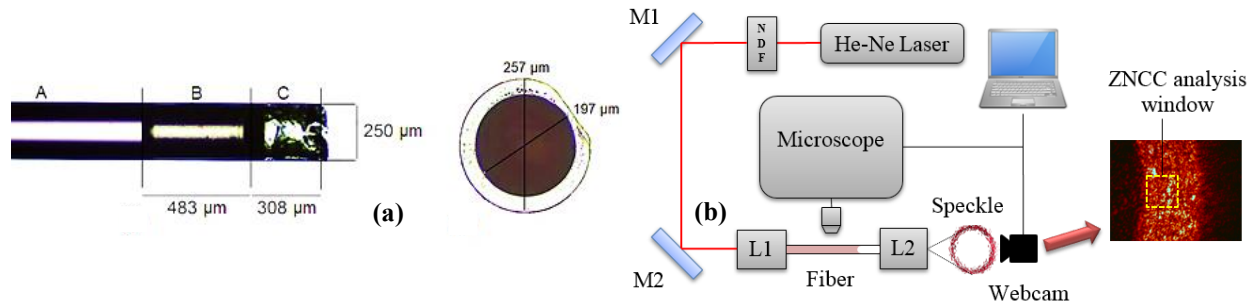


Fig. 1. (a): Microscopy images of a sealed capillary filled with water; left = front view showing the water filled section “A”, photocurable resin seal “B” and a free tip “C”; right = top view with inner and outer diameter measurements. (b): Schematic of the experimental setup, a frame of the captured specklegram video is shown to the right along with a representation of the analysis window for the calculation of ZNCC.

For the best results with the ZNCC analysis a good speckle contrast is desirable. Speckle contrast increases as the optical power from the laser source shifts from fundamental modes to higher-order modes in the waveguide [9]. Since higher-order modes have bigger modal area and higher evanescent field contribution, the aim is to excite a high number of higher-order modes, as this is important to enhance the device sensitivity. This can be achieved by using the precision translation stage in which the input lens L1 is mounted to introduce a misalignment of the incident beam in relation to the capillary-like fiber glass walls [9].

## 2.2. Experimental Procedure and Data Acquisition

Prior to starting the experiments, the He-Ne laser is turned on and let stabilize for about 1 hour. One of the sealed extremities of the sensing fiber containing a liquid of interest (water with red coloring in this study) is cleaved out and the fiber is carefully placed between the objective lenses, open side directed towards the webcam.

A LabVIEW routine was used to capture and save images of the meniscus with the microscope camera. Overlays for image count and a reference scale for measuring the movement of the meniscus can be toggled on and off using the LabVIEW implementation. Fig. 2 (a) shows a schematic of the meniscus observed with the microscope at an arbitrary time  $t = t_0$ , while Fig. 2 (b) shows the meniscus displaced by  $\Delta x$  due to the evaporation of the fluid after a period of time  $\Delta t$  has passed. The microscope is used as a reference for observing the movement of the meniscus and determine when the displacement reaches the target  $\Delta x$  since the start of a speckle recording session.

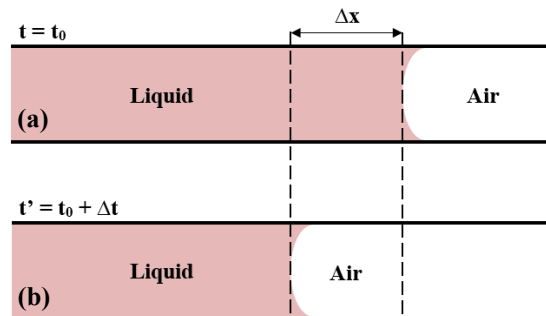


Fig. 2. Schematic drawing of the liquid/air interface meniscus inside the sensing fiber as observed under the microscope: at an arbitrary time  $t = t_0$  (a); at a time  $t' = t_0 + \Delta t$  in which  $\Delta t$  is the time interval for the meniscus to move  $\Delta x$   $\mu\text{m}$  to the left.

The speckle is recorded using a free video capture software application at 15 fps, 800×600 pixels resolution, by the webcam as it shifts due to the change of the air filling fraction in the sensing fiber as the liquid evaporate.

### 3. Results and Discussion

First it is important to compare the temporal evolution of the ZNCC for a capillary filled with air and one filled with fluid, to determine if the presence of an evaporating liquid changes the behavior of the ZNCC curve. This comparison is shown in Fig. 3 (a). Without the liquid filling ZNCC is very stable and remains very close to 1. The general behavior of ZNCC in relation to the displacement of the liquid/air interface can be observed by plotting both ZNCC and Displacement over time in the same graphic. This is shown in Fig. 3 (b) for a  $\Delta x$  of 40  $\mu\text{m}$  over 450 seconds. ZNCC seems to vary fairly linearly over time with good correspondence to the observed displacement.

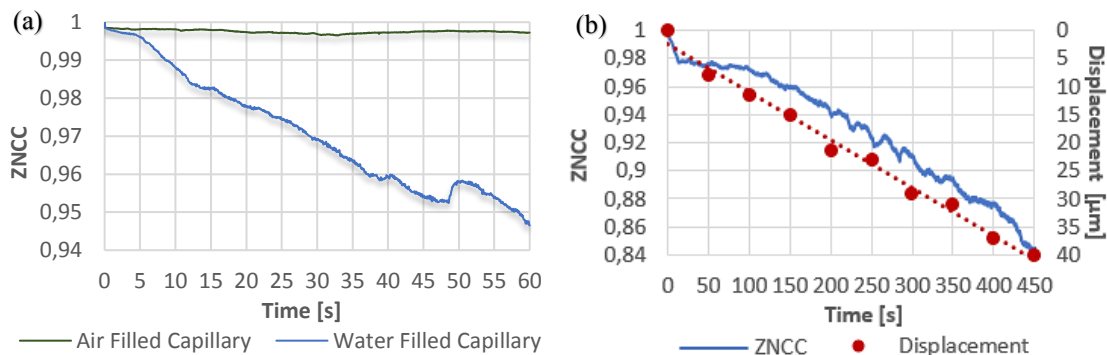


Fig. 3. Comparison of the ZNCC curve over time for an air-filled capillary and a water filled capillary (a). Combined displacement and ZNCC data over time up to a maximum displacement of 40  $\mu\text{m}$  (b).

To determine if the behavior of ZNCC is stable over time eight more tests were performed in sequence. Displacement ( $\Delta x$ ) values of 20, 30, 40 and 50  $\mu\text{m}$  were selected for testing and two tests were recorded for each  $\Delta x$  value to access the repeatability of the measurements. The results are presented in Fig. 4.

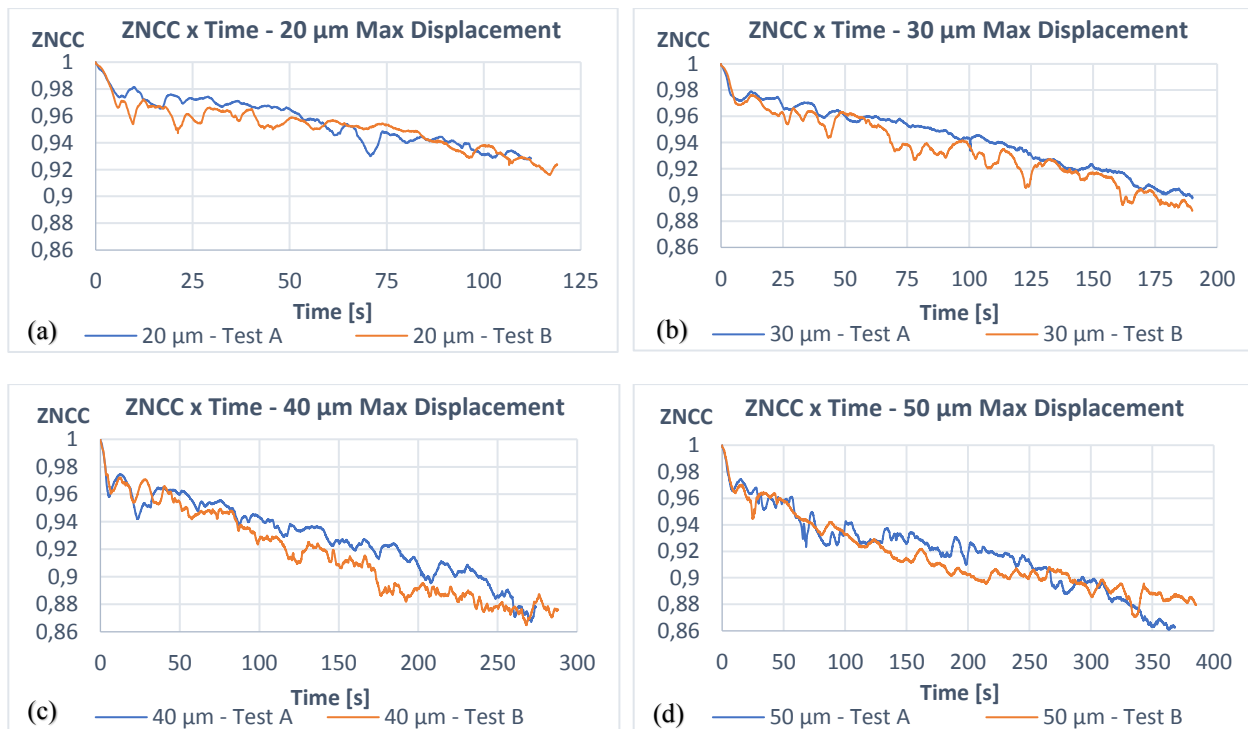


Fig. 4. ZNCC over time data for liquid/air interface displacements up to 20  $\mu\text{m}$  (a), 30  $\mu\text{m}$  (b), 40  $\mu\text{m}$  (c) and 50  $\mu\text{m}$  (d).

Finally, by taking the average final ZNCC value for each set of tests in Fig. 4 it is possible to plot ZNCC as a function of  $\Delta x$  (Fig. 5).

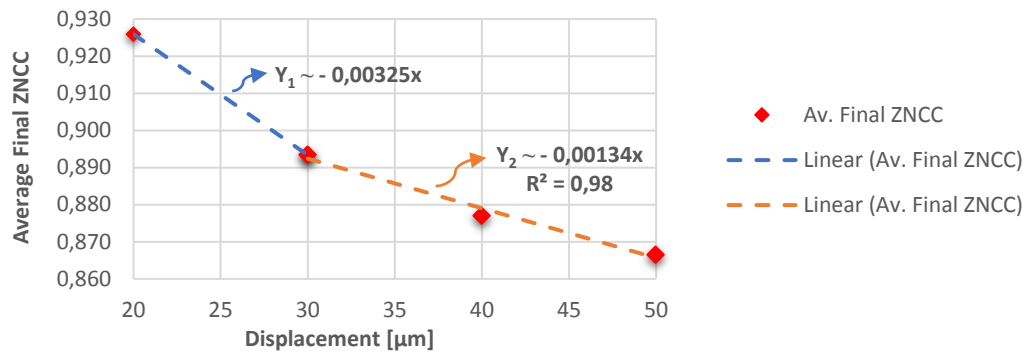


Fig. 5. Average Final ZNCC as a function of displacement. Dashed lines are data fittings for the dynamic ranges of 20-30  $\mu\text{m}$  and 30-50  $\mu\text{m}$ .

To better access the non-linear data in Fig. 5 the data was divided in two linear dynamic ranges. For the 20-30  $\mu\text{m}$  range the sensitivity is  $-3.25 \times 10^{-3} \mu\text{m}^{-1}$  and resolution 1.54  $\mu\text{m}$  considering a minimum detectable  $\Delta\text{ZNCC}$  of  $5 \times 10^{-3}$ , while for the 30-50  $\mu\text{m}$  range the sensitivity is  $-1.34 \times 10^{-3} \mu\text{m}^{-1}$  and resolution 3.73  $\mu\text{m}$ . There is a clear relationship between the change of ZNCC over time and the displacement of the air/liquid interface due to evaporation, which strongly suggests that the mechanism of multimodal interferometry inside the sensing capillary walls can be exploited for the purposes detailed in this work. Displacement information can be fed into a mathematical model for evaporation in a capillary as a mean to quickly evaluate many properties of the filling liquid such as viscosity and effective diffusivity.

Further investigation is needed to improve the linearity of the sensor to capitalize on the higher sensitivity observed in the 20-30  $\mu\text{m}$  range. We believe that the deviation from linearity observed between individual tests and the Average Final ZNCC can be reduced by minimizing the temporal drift of the room temperature and relative humidity. While during an individual test temperature and relative humidity shifts were typically lower than 0.3  $^{\circ}\text{C}$  and 5%, over the span of all tests reported in Fig. 5 temperature and humidity drifted in excess of 4  $^{\circ}\text{C}$  and 25%. Single measurements for practical applications are rather quick (2 to 7 minutes depending on  $\Delta x$ ), so no significant thermal noise due to temperature fluctuations is expected under reasonable operating conditions.

Changes in temperature produce small deviations of the refractive indexes of the glass walls and filler fluid through the thermo-optic effect, modifying the index contrast between the core and the cladding of the capillary-like fiber [10]. Not only the number of propagating modes is directly related to the refractive index contrast [11], each propagating mode experiences a slightly different effective refractive index that is also affected by the thermo-optical effect, leading to a change in the phase delay between propagating modes [11]. The combination of these temperature-induced effects result in a shift in the output speckle pattern that is superposed to the evaporation signal.

The effects of relative humidity fluctuations are not as direct. Ideally the relative humidity value only affects the evaporation rate of the water filling, making tests slightly longer or shorter, but in the presence of non-constant temperature increased testing times may aggravate the long-term thermo-optical noise described in the previous paragraphs.

#### 4. Conclusion

A capillary-like fiber specklegram sensor capable of monitoring evaporation of a filling liquid was demonstrated. The sensor presents maximum sensitivity and resolution of  $-3.25 \times 10^{-3} \mu\text{m}^{-1}$  and 1.54  $\mu\text{m}$ , respectively, for the  $20 \mu\text{m} \leq \Delta x \leq 30 \mu\text{m}$  range. A non-linear response was observed when seemingly linear data from multiple test was compiled, warranting further investigation on external disturbances (temperature related effects in particular). Future improvements to this research includes investigating the behavior of the evaporation signal produced by filling liquids with faster or slower evaporation rates, investigating the evaporation signal for filling liquids with refractive index higher than glass (light guided in the liquid core as opposed to in the glass walls), and revising sensor design for enhanced sensitivity by introducing microstructures in order to increase the interaction between the propagating light and the filling fluid.

## 5. References

- [1] R. H. Nilson, S. K. Griffiths, S. W. Tchikanda, "Axially Tapered Microchannels of High Aspect Ratio for Evaporative Cooling Devices", *Journal of Heat Transfer ASME*, Vol. 126, 453-462 (2004).
- [2] O. D. Velev, S. Gupta, "Materials Fabricated by Micro-and Nanoparticle Assembly – The Challenging Path from Science to Engineering", *Advanced Materials* **21**(10), 1897-1905 (2009).
- [3] M. F. H. Arif, M. M. Hossain, N. Islam, S. M. Khaled, "A nonlinear photonic crystal fiber for liquid sensing application with high birefringence and low confinement loss", *Sensing and Bio-Sensing Research*, Vol. 2 (2019).
- [4] J. H. Osório et al, "Simplifying the design of microstructured optical fibre pressure sensors", *Scientific Reports* **7** (2017).
- [5] M. A. Gouveia et al, "Morphology dependent polymeric capillary optical resonator hydrostatic pressure sensor" **23**(8), 10643-10652 (2015).
- [6] F. T. S. Yu, "Fiber specklegram sensors" in *Fiber Optic Sensors*, S. Yin, F. T. S. Yu, eds. (Marcel Dekker Inc, New York, 2002).
- [7] E. Fujiwara et al, "Evaluation of image matching techniques for optical fiber specklegram analysis", *App. Opt.* **57**(33), 9845-9854 (2018).
- [8] F. T. S. Yu et al., "Submicrometer displacement sensing using inner-product multimode fiber speckle fields," *Appl. Opt.* **35**, 4685-4689 (1993).
- [9] T. Tsuji, T. Asakura, H. Fujii, "Variation of the speckle contrast in a graded-index fibre by misalignment of the incident beam", *Optical and Quantum Electronics* **16**, 9-18 (1984).
- [10] Gorachand Ghosh (editor), "Handbook of Optical Constants of Solids". Volume V, Chapter 3 – Thermo-Optic Coefficients (Academic Press, 1997) – DOI 10.1016/B978-012544415-6.50150-3.
- [11] Gerd Keiser, "Optical Fiber Communications", 4th Edition (McGraw-Hill, 2008).

# Fibre Bragg grating based sensor system for pantograph – overhead line interface condition monitoring during electrified train operation

<sup>a</sup>Miodrag Vidakovic, <sup>a</sup>Ye Chen, <sup>a</sup>Matthias Fabian, <sup>b</sup>Matthew Askill, <sup>b</sup>Lee Brun, <sup>c</sup>Rod Fawcett, <sup>c</sup>Peter Dearman, <sup>c</sup>Simon Warren, <sup>a</sup>Tong Sun and <sup>a</sup>Kenneth T. V. Grattan

<sup>a</sup>City, University of London, EC1V 0HB, 10 Northampton Square, London, UK; <sup>b</sup>Faiveley Brecknell Willis, TA20 2DA, Chard, UK; <sup>c</sup>Network Rail, Transfer Bridge Industrial Estate, County Rd, SN1 2EL, Swindon, UK.  
Miodrag.Vidakovic.1@city.ac.uk

**Abstract:** Efficient current collection and monitoring railway current-collecting pantographs is one of the key challenges for railway sector in electrical train operation. Fibre Bragg grating (FBG) sensors integrated into a pantograph are used to provide accurate contact force and contact location measurements at the crucial pantograph-overhead line (OHL) interface. Data collected during field trials are reported in the paper.

## 1. Introduction

Fibre Bragg Grating (FBG) based optical sensors are very important as key sensing elements for the measurement of strain, temperature, and a wide range of other parameters in many industrial and field applications, and their use has significantly increased over the last decade [1]. Their intrinsic immunity to electromagnetic interference, ease of multiplexing, small size and light weight have often made them more suitable than their electrical counterparts for measurements under harsh and indeed extreme conditions [2]. The application described in this paper is one such extreme condition, involving the integration of number of FBGs into a railway current-collecting pantograph for remote condition monitoring. Under normal use a railway pantograph is exposed to all-weather conditions, with the overhead line at 25,000 Volts during train operation, at high speeds of up to 350 km/h. The immunity of optical fibre based sensors to such high voltages and their ruggedness and lightness in use *in situ* in a pantograph enable them to be used in this monitoring situation where electrical sensors have not been shown suitable [3].

An important consideration when using FBG-based techniques either in laboratory-controlled environment or field applications is providing compensation for the well-known cross-sensitivity to both strain and temperature [2]. There are number of techniques that have been applied to compensate for the temperature effect when strain is being monitored, such as the use of two single FBGs in separate fibres [3], FBG sensors packaged in aluminum boxes instrumented on the carbon strips [4] and the integration of FBG sensors between the carbon and the aluminum parts of the pantograph, as reported by Schroder *et al* [5]. All the techniques reported add complexity to the whole system by using additional hardware and are based on the erroneous assumption that the temperature is uniform under operational conditions along the carbon strip. The consequence of this is a limitation on their use in the field and critically in real time train operation. The successful temperature compensation mechanism demonstrated in a previous paper by some of the authors [6] has enabled on-going field testing on railway tracks across the UK.

## 2. FBG-based sensor system integrated in railway pantograph

The sensor system design reported in previous work [6] has been used for *in situ* pantograph instrumentation, giving confidence that this design can provide accurate real-time, simultaneous measurement of both contact force and contact location during train operation, and at various train operational speeds.

Figure 1 shows the optical setup used in this work, this being essentially similar to what was reported in our previous work [6]. Here nine FBGs have been integrated into each carbon strip, using a package-based design which enables the data from the sensors to be captured by a commercial FBG interrogator, prior to processing of the data from the individual sensors using an appropriate algorithm built in the software developed to achieve the required information. Three FBG-based sensor packages are integrated, at three different locations, into each carbon strip of the pantograph, as indicated in Figure 2(b), to achieve simultaneous measurement of contact force and contact location, coupled with temperature compensation.

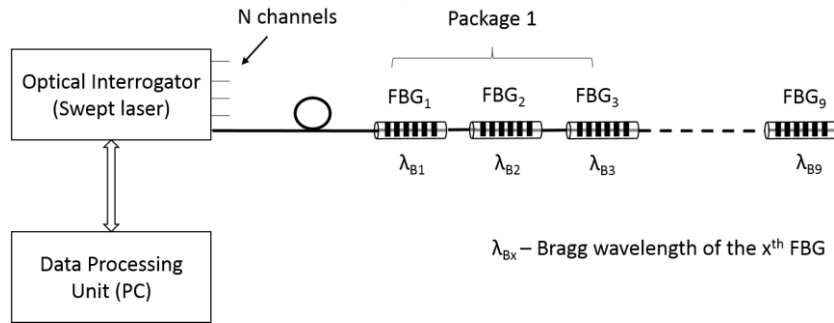


Figure 1. Schematic of the FBG package-based design sensor system used in this work

The train used for field testing was provided by Network Rail and is known as the High Output Plant System (HOPs). Figure 2(a) shows a photograph of this HOPs train, with FBG sensor system-instrumented pantograph installed.

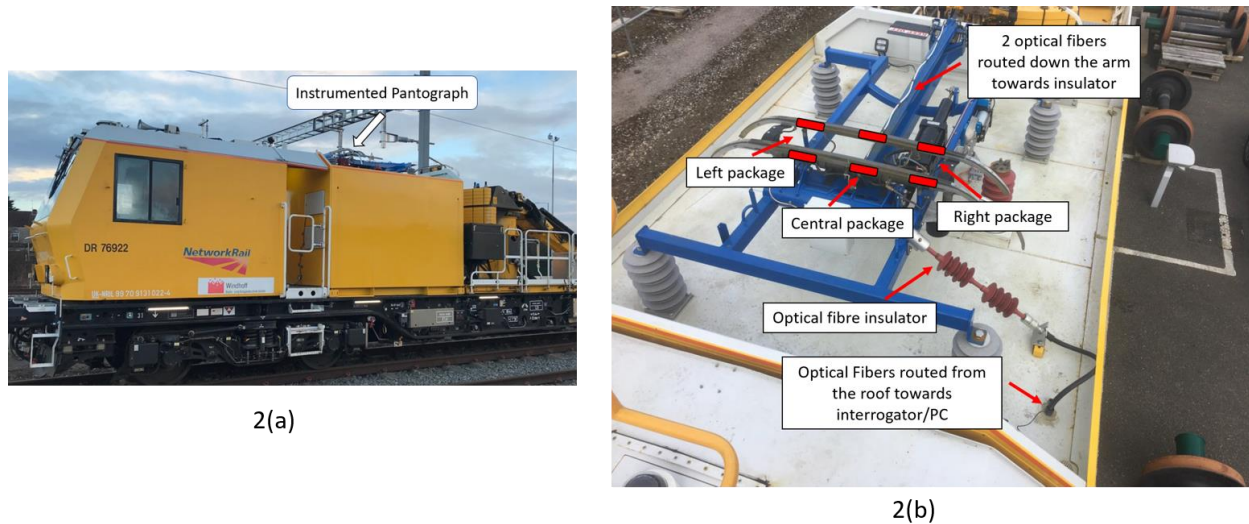


Figure 2. High Output Plant System (HOPs) train with the FBG-based sensor system instrumented pantograph installed (a), detailed instrumentation and fiber routing (b)

The HOPs train, equipped with the FBG-based sensor system instrumentation has been used on the part of UK network, between two stations, to verify the operation of the sensor system designed. The data obtained show that the measured static contact force at the beginning of the run was 107 N, while the maximum train speed during that run was 60 mph (96 km/h) and the distance travelled was 12.4 miles (19.9 km). During this run, two railway switches or turnouts were tested and evaluated.

### 3. Contact force and contact location measurement during train operation

Figure 3 shows overall the data obtained from the instrumented pantograph system, indicating the contact force measured for this ~20 km journey, as well as change of the speed during the field test, as well as the overall distance travelled.

Once the static force is applied to the pantograph pan-head when in use, the fully temperature-compensated contact force was measured, combining data from each of FBGs forming each of the three sensor packages. The contact force measured by each three-FBG package, is linearly proportional to its distance from the centre position of the package to the location of the applied force where the pan-head touches the overhead wire. For example, when the contact force is applied directly above the left-hand package, the maximum force will be the force measured by the left package. The measurement of force made by the other two packages will be linearly reduced

moving towards the right sensor package. Knowing precisely the locations of each package as fitted to the pan-head allows a simple calculation to be made of the location of the maximum force applied corresponding to the position of the pan-head on the overhead wire. Prior to their use on the train itself, the pan-head with the FBG-based sensor packages incorporated has been calibrated in the laboratory environment, using accurately known values of strains achieved using known weights being applied. The calibration coefficients thus obtained are then used to create the algorithm to allow the contact force and location measurements, reported in both Figure 3 and Figure 4, to be obtained.

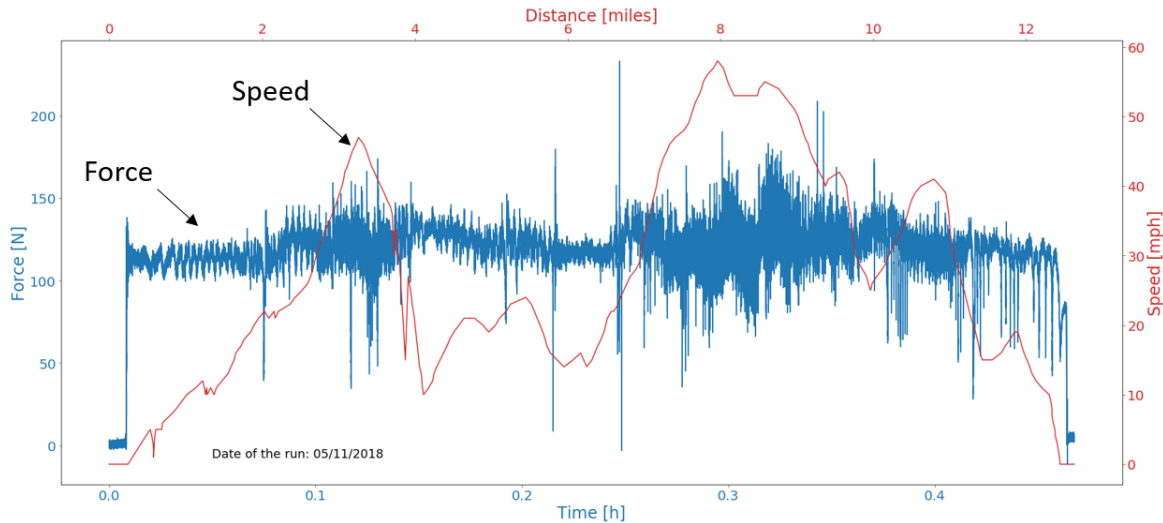


Figure 3. Contact force measured using the FBG-based sensor system integrated into the railway pantograph

Figure 3 shows the data obtained on the contact location (or so called ‘horizontal stagger’) data, collected using the instrumented pantograph during this trial. This allows the lateral movement of the over-head line in relation to pantograph pan head to be monitored. Knowing the location of the wire, with respect to the pantograph is necessary to avoid incidents that can occur when the contact wire goes ‘out of the range’ (which is within 40 cm of the middle of the pantograph).

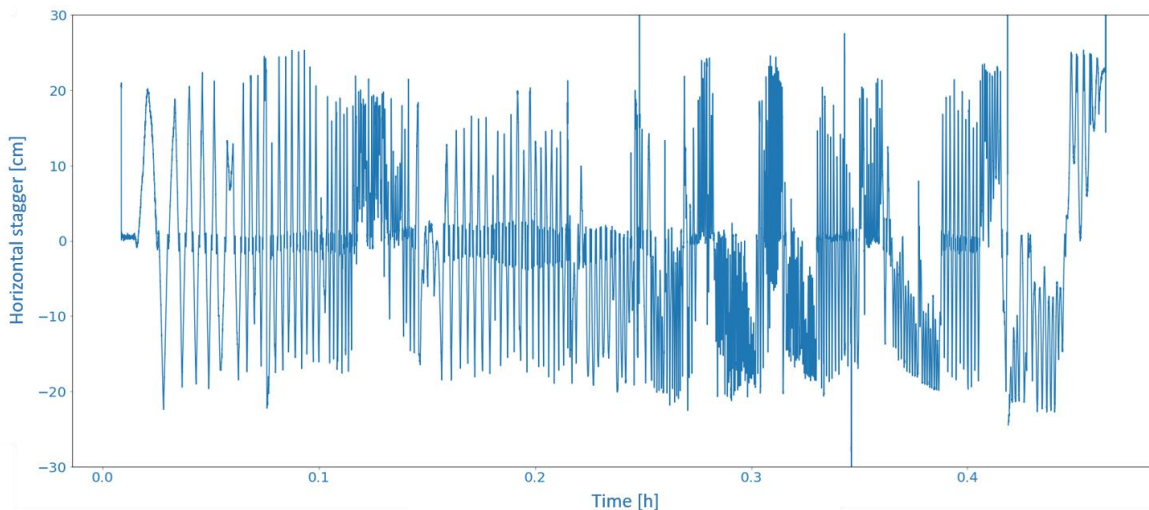


Figure 4. ‘Horizontal stagger’ measurement data obtained using the FBG-based sensor system developed

As discussed previously, the detection of high peak (over 200 N) forces and low peak (under 50 N) forces is important in order to ensure both a longer lifetime of the carbon strips, as well as to provide optimal current collection and therefore reduce the cost of strip replacement and the train being out of service. Figure 5 shows the

range of peak forces detected during the train operation – including the high and low forces experienced – while going through one of the ‘turnouts’ on the route (where the train speed was approximately 20 mph (36 km/h)).

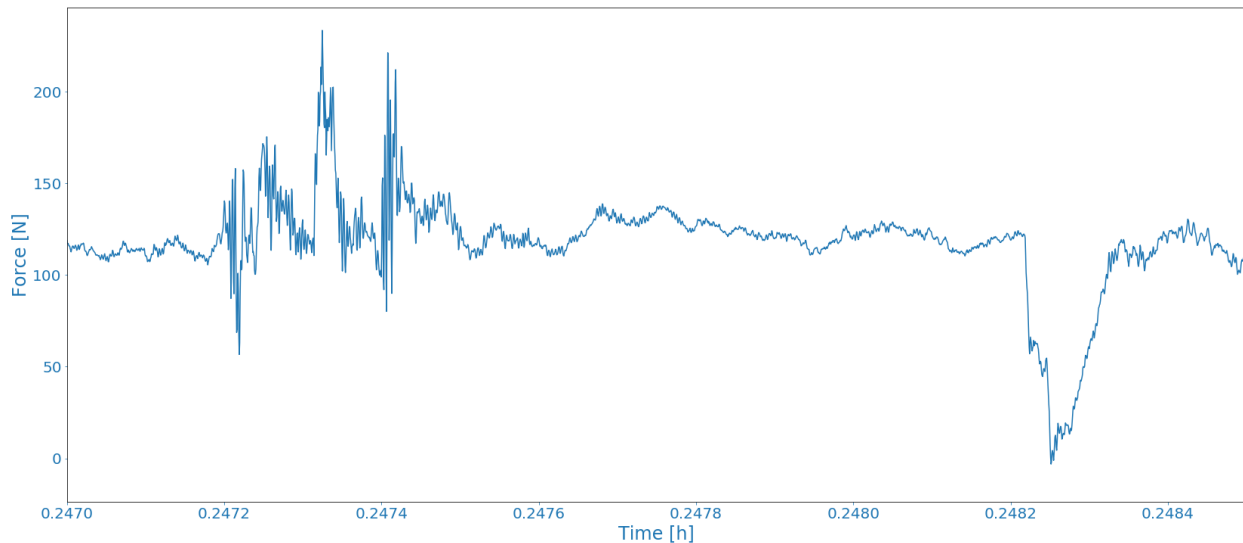


Figure 5. Railway ‘turnout’ examination showing the high and low peak forces experienced

The highest peak force measured was 233 N, at the beginning of the turnout section on the route, with the lowest peak force seen at the end of this part of the infrastructure, as is evident from Figure 5. This figure represents a snapshot of a short period of measurement, showing a detail taken from Figure 3. The design contact force that should be maintained during the electrified train operation is  $\sim 90$  N, this allowing a longer lifetime of both the pan-head and the associated infrastructure. However, the contact force set for this run was 107 N, this being slightly higher than the nominal 90N due to the speed limitation of the HOPs train. The high peak force normally indicates that there is potential defect on the network – one that could cause damage to the pantograph and thus significantly reduce its service lifetime. Equally, a low peak force (under 50 N) is also problematic in that it causes arcing in electrified train operation, a phenomenon that also leads to a shortened life time of the pantograph and inefficient current collection. This arcing also causes interference to traction power and signaling systems, with consequences for both safety and train scheduling and punctuality. As a result, setting and maintaining the desired contact force between the pan-head and the overhead wire is important and this new sensor system provides an effective means to do that in routine operation.

#### 4. Conclusions

This paper has reported the successful use of a new type of fibre optic instrumented pantograph in actual train operation and a stream of data collected in-the-field. The tests done have shown that accurate contact force and contact location measurements, up to a maximum train speed of 60 mph (96 km/h) have been obtained and are valuable to show issues with the train operation. The positive outcomes obtained from these field trials carried out have confirmed that the sensor design created for this application is highly effective and well suited to successful remote condition monitoring of the critically important pantograph-OHL interface. The research and system design work is still on-going, with plans for more sensors to be added to the pantograph to ensure successful implementation of a condition-based maintenance (CBM) system which will be far more efficient and cost effective than the traditional maintenance approach used.

#### 5. Acknowledgments

The authors would like to thank the RSSB (Rail Safety and Standards Board) in the UK, EPSRC (Engineering and Physical Science Research Council) and Innovate UK for the funding support to enable this collaborative research undertaken between City, University of London and Faiveley Brecknell Willis in the UK. The support of the Royal Academy of Engineering is also much appreciated. In addition, the authors would like to thank to Network Rail for the opportunity to use HOPs as well as railway tracks in the UK for this technology development study.

## 6. References

- [1] Grattan, K. T. V. and Sun, T., "Fiber optic sensor technology: An overview", *Sens. Actuators A: Phys.*, vol. 82, no. 1–3, pp. 40–61, (2000).
- [2] Kersey, A., Davis, M., Patrick, H., et al. "Fiber grating sensors", *Journal of Lightwave Technology* 15(8): 1442–1463, (1997).
- [3] Comolli, L., Bucca, G., Boccione, M. and Collina, A., "First results from in-line strain measurements with FBG sensors on the pantograph collector of underground trains", *Proceeding of SPIE*. Vol.7726., (2008).
- [4] Wagner, R., Maicz, D., Viel, W., Saliger, F., Saliger, C., Horak, R., and Noack, T., "A fibre optic sensor instrumented pantograph as part of a continuous structural health monitoring system for railway overhead lines", *7th European Workshop on Structural Health Monitoring*, (2014).
- [5] Schroder, K., Ecke, W., Kautz, M., Willett, S., Jenzer M., and Bosselmann, T., "An approach to continuous on-site monitoring of contact forces in current collectors by a fiber optic sensing system", *Optics and Lasers in Engineering*. Vol. 51, (2013).
- [6] Chen, Y., Vidakovic, M., Fabian, M., Swift, M., Brun, L., Sun, T. and Grattan, K.T.V., "A temperature compensated fibre Bragg grating (FBG)-based sensor system for condition monitoring of electrified railway pantograph", *The 25<sup>th</sup> International Conference on Optical Fiber Sensors, Jeju, South Korea (2017)*.

# Optical Current Transducer Metrological Characterization for Current Transformer on-Site Calibration

Marcelo Melo da Costa<sup>1</sup>, Ângela Costa Santa Brígida<sup>2</sup>, Cledson Santana Lopes Gonçalves<sup>2</sup>, João Crisóstomo Weyl Albuquerque da Costa<sup>2</sup>

*<sup>1</sup> Eletrobras Eletronorte, <sup>2</sup> Universidade Federal do Pará*

*marcelo.melo@eletronorte.gov.br, acsbrigida@ufpa.br, cledsonslg@ufpa.br, jweyl@ufpa.br*

**Abstract:** This paper presents metrological characterization of an optical current transducer solution for high voltage current transformers on-site calibration. In metrological evaluation, from 150 A to 1700 A, ratio errors were between  $\pm 0.1\%$  and phase errors were between  $\pm 5'$ . Although the good results, some strategies are suggested for uncertainty improvement in field application.

## 1. Introduction

Instrument transformers [1] play important role in high voltage electrical power measurement systems, as they accurately step down voltage and current levels for measurement, protection and other purposes. Different accuracy classes instrument transformers are used, depending on their applications. For example, current and voltage transformers with 0.3% accuracy are used in billing measurement systems, as well as 0.6% accuracy transformers are used for supervisory and control measurements [1, 2].

Due to the heavy and large instrument transformers involved, their calibrations have to be preferably performed on site, using standards based on some sensors technologies, as optical sensors and Rogowski coils [3,4]. In the case of current transformers (CTs) calibration, optical current sensors bring the significant advantages that they are non-conductive and lightweight, which can allow for much simpler insulation and mounting designs.

The calibration system presented in this paper is based on an optical current transducer (OCT). The sensor is fitted with a flexible fiber optic cable that is connected directly to the live line up to 550 kV. The system performance obtained in laboratory and field application results are presented.

## 2. Onsite CT Calibration System

The complete CT calibration system is divided in two parts: Optical current transducer (OCT) – Electronics and optical sensor (Figure 1a), and power system comparator (Fig. 1b). The OCT is the NXCT-F3 from NXPPhase (now GE Grid): it is based on the magneto-optic Faraday Effect. The NXCT uses the in-line Sagnac design shown in Fig. 2 and is described in detail in J. Blake, et. al., [5], [6]. These interferometric Sagnac sensors are stabilized with a phase modulator. The phase modulator allows the sensor to heterodyne the signal away from low frequency noise during the signal processing. The modulator also allows the interrogation of the sensor response function, which contains information about the health of the optical path and the impact of the optical path on the sensor scale factor [7]. The sensor has a flexible fiber optic cable that is wrapped around the conductor where the current measurement is desired. Its accuracy is 0,1% according to manufacturer's specification, and the output is a configurable current signal. The power system comparator is the Arbiter 933A and it is responsible for current comparison. Also, a clamp meter should be used to measure the CT under calibration current output. Fig. 3 shows the measurement diagram for the CT calibration system.



Fig. 1: Complete CT calibration system: (a) OCT: Electronics and optical sensor and (b) power system comparator.

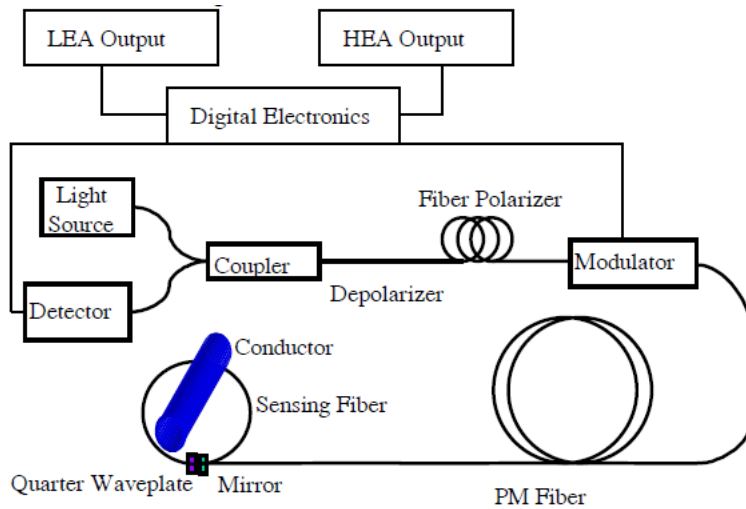


Fig. 2: schematic of the NXCT [7]

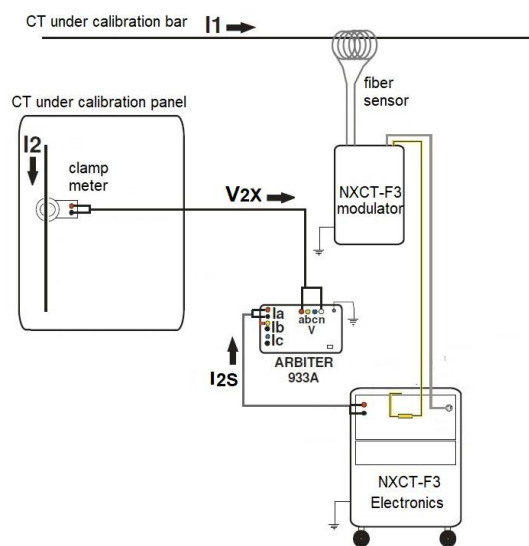


Fig. 3: CT calibration system measurement diagram.

### 3. Laboratory Testing

After some insulation tests performed at a high voltage laboratory, the OCT was calibrated at a metrology laboratory, using a reference standard, Tettex type 4764. Figure 4 shows calibration results for ratio and phase measurements, for test currents from 150 A up to 1700 A. As it can be seen, ratio errors lied between  $\pm 0.1\%$  while phase errors were between  $\pm 5'$ . These results comply with a classe 0.3 CT. Figure 5 shows a OCT 5-day short-term stability evaluation, for some current amplitudes.

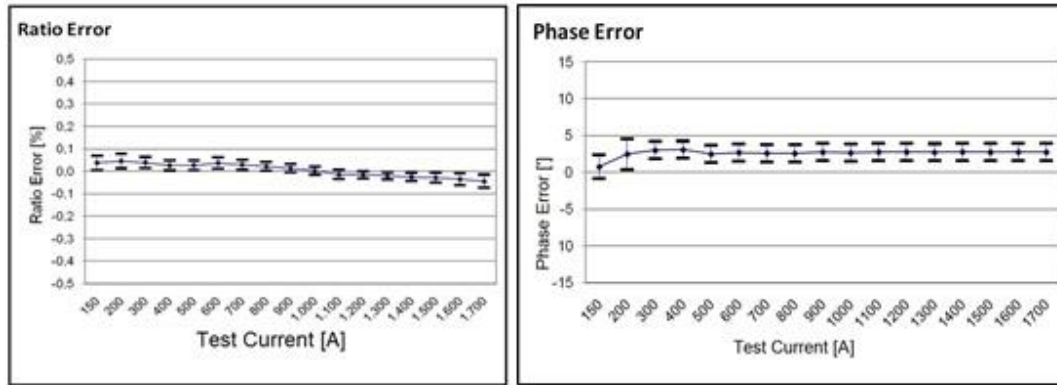


Fig. 4: OCT calibration results.

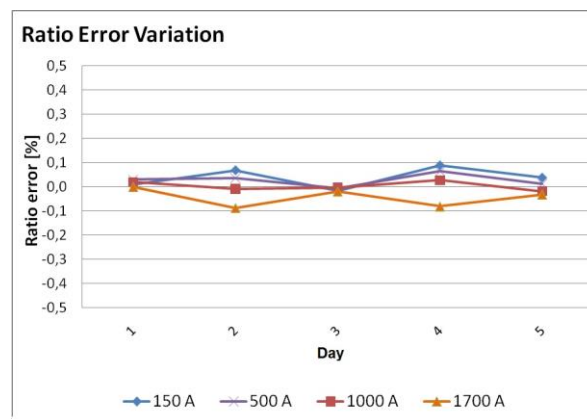


Fig. 5: OCT short-term stability evaluation

### 4. Field Application

The CT calibration system was applied on two HV substations, in Belém, northern Brazil. Table 1 shows the uncertainty budget for the CT ratio calibration results [8].

Table 1: Uncertainty budget for CT ratio calibration

Quantity ( $X_i$ )	Probability Distribution	Contribution to the standard uncertainty (%) $u_i(y)$
NXCT-F3 manufacturer's specification	Rectangular	0.05
NXCT-F3 calibration	Normal	0.015
Clamp meter manufacturer's specification	Rectangular	0.5
933A comparator manufacturer's specification (input $V_{AN}$ )	Rectangular	>1
933A comparator (input $V_{AN}$ ) + clamp meter calibration	Normal	0.02
933A comparator manufacturer's specification (input $I_A$ )	Rectangular	0.025
933A comparator (input $I_A$ ) calibration	Normal	0.015
933A comparator readings repeatability	Normal	<0.01
Standard uncertainty ( $1\sigma$ )		>1,1

As it can be seen in Table 1, measurement uncertainty is not adequate for 0.3 or 0.6 class CTs calibration. The main contributions to the standard uncertainty do not come from the OCT but are due to clamp meter and comparator manufacturer's specifications. Thus, some strategies can be used to obtain lower uncertainty: (1) Calibrate the clamp meter and the comparator twice, just before and just after their utilization on site; (2) use a current shunt instead of a clamp meter (limited by the power system architecture); and (3) Calibrate the optical current sensor twice, just before and just after their utilization on site. In cases (1) and (3), uncertainty due to manufacturer's specification can be replaced by instruments short-term stability and the temperature dependence. Moreover, other significant influences should be considered.

## 5. Conclusion

This paper demonstrated metrological characterization and evaluation of an on-site calibration system of current transformers that used an optical current transducer (OCT). Metrology laboratory calibration of the OCT presented ratio errors between  $\pm 0.1\%$  while phase errors lied between  $\pm 5'$ . The complete calibration system has large uncertainty considering classes 0.3 and 0.6 CTs calibration, not due to the OCT but due to the other components of the calibration system. Some strategies were proposed for uncertainty improvement.

## 6. References

- [1] IEEE Standard C57.13, "Requirements for Instrument Transformers", 2016.
- [2] L. J. A. Kojovic, "Impact of current transformer saturation on overcurrent protection operation", Power Engineering Society Summer Meeting 2002 IEEE Volume 3, vol. 3, pp. 1078-1083, 2002.
- [3] M. M. Costa, J. C. D. Carvalho, D. B. Dahlke and P. H. M. Santos, "System for high voltage current transformers onsite verification", in *Proceedings of 2011 IEEE International Workshop on Applied Measurements for Power Systems (AMPS)*, (Institute of Electrical and Electronics Engineers, Aachen, 2011), pp. 58-61.
- [4] E. Suomalainen, J. K. Hällström, "Onsite Calibration of a current transformer using a rogowski coil", in *Transactions on Instrumentation and Measurement*, (Institute of Electrical and Electronics Engineers, 2008), V. 58, n. 4, pp.1054-1058.
- [5] G. A. Sanders, J. N. Blake, et al, "Commercialization of fiber-optic current and voltage sensors at NxtPhase", in *Transactions of 15th Optical Fiber Sensors Conference*, (Institute of Electrical and Electronics Engineers, 2002), pp. 31-34.
- [6] J. Blake, P. Tantaswadi, R. T. de Carvalho, "In-Line Sagnac Interferometer Current Sensor", in *Transaction on Power Delivery*, (Institute of Electrical and Electronics Engineers, 1996), V. 11, pp. 116-121.
- [7] J. N. Blake, A. H. Rose, "Fiber-optic current transducer optimized for power metering applications", in *Transactions on PES Transmission and Distribution Conference and Exposition*, (Institute of Electrical and Electronics Engineers, 2003), V. 1, pp.405-408.
- [8] EA-4/02 M:2013, "Evaluation of the uncertainty of measurement in calibration", Rev. 01, 2013.

# Evaluation of Coupling to Symmetric and Asymmetric Cladding Modes in Long-Period Fiber Gratings

F. Delgado, Renato Luiz Faraco, Daniel Silveira and Alexandre Bessa

Federal University of Juiz de Fora, Electrical Engineering Department, Juiz de Fora - MG, Brazil, 36036-330  
felipe.souza@engenharia.ufff.br

**Abstract:** We analyze the influence of coupling to symmetric and asymmetric cladding modes in arc-induced Long-Period Fiber Gratings for temperature and strain sensing. The origin of this difference in energy coupling is related to the fabrication process of these gratings and depends on the electric arc discharge conditions, which modulates the refractive index and geometry of the optical fiber. Finally, results demonstrate the performance of different cladding modes excited in arc-induced LPFGs to temperature and strain applications and, in addition, indicate which coupling might be appropriate to certain sensing applications.

## 1. Introduction

Long Period Fiber Gratings (LPFGs) are optical devices extremely versatile in sensing applications [1,2]. Normally, these devices are based upon the periodic perturbation of the refractive index and geometry of the optical fiber, which usually is of the order of hundreds of micrometers [3]. Furthermore, the energy from the fundamental core mode couples to different co-propagating cladding modes and, therefore, the transmission spectrum of the LPFG contains different resonance peaks. Each energy coupling is located at a specific resonance wavelength ( $\lambda_i$ ) and satisfies the phase-matching condition [3]:

$$\lambda_j = (n_{co} - n_{j,clad})\Lambda \quad (1)$$

where  $\Lambda$  is the period of the grating,  $n_{co}$  and  $n_{j,clad}$  are the effective refractive indices of the fundamental core and cladding modes, respectively. For the specific case of LPFGs based solely upon electric arc discharges, it was demonstrated that LPFGs could promote energy coupling to cladding modes of different symmetries and, in addition, some authors discussed on the conditions leading to symmetric and asymmetric energy coupling [5,6]. Rego [4] reported a particular LPFG fabrication setup, where the arc discharge is directional, to produced gratings considering Ge-doped fibers such as the SMF-28 from Corning with coupling to asymmetric cladding modes. Recently, Yin [7] also reported the asymmetry of cladding modes involved in the coupling mechanism by developing an automatic arc discharge technology using a commercial fusion splicer system to inscribe LPFGs. On the other hand, some authors reported arc-induced LPFGs in conventional silica fiber with energy coupling to symmetric cladding modes using commercial fusion splicer machines [8] or by developing their own fabrication setup [9]. Therefore, the investigation of the influence of different mode symmetry involved in LPFGs is important for sensing applications.

In this work, we report a comparative study of LPFGs with energy coupling to symmetric and asymmetric cladding modes in order to investigate the impact of different energy coupling on the sensor performance for temperature and strain measurements. Therefore, the results of the study may be of impact on the prospects of tailoring the projects of grating sensors.

## 2. Methodology

We made LPFGs with period of 470  $\mu\text{m}$  and different arc discharge power, which allowed us to observe energy coupling to symmetric and asymmetric cladding modes. In order to observe energy coupling to symmetric cladding modes, we produced LPFGs with low arc power of 30 bits (manufacturer unit) and exposure time of 500 ms. Therefore, it was possible to observe coupling into the first four circularly symmetric cladding modes (LP<sub>02</sub>-LP<sub>05</sub>). On the other hand, to observe asymmetric mode excitation, we produced LPFGs with higher arc power discharge, for example, electric arc discharges of 100 bits and duration of 500 ms. Thus, it was possible to observe energy coupling to the LP<sub>11</sub>-LP<sub>14</sub> cladding modes. Figure 1 shows the transmitted spectra, which is observed using a broadband light source, of two arc-induced gratings fabricated with the same grating period, however, with different cladding modes excited. In order to identify the cladding modes of resonant wavelengths observed in Fig. 1, we have simulated the phase-

matching curves for the produced arc-induced LPFGs. In our simulations, we have used the modified phase matching condition, which allow us to identify the resonance wavelengths with an error lower than 0.1% [10]:

$$\beta_{01}(\lambda) + s_0 \zeta_{01,01}(\lambda) - \left( \beta_{0j}(\lambda) + s_0 \zeta_{0j,0j}(\lambda) \right) = \frac{2\pi N}{\Lambda} \quad (2)$$

where  $\beta_{01}$  and  $\beta_{0j}$  are the propagation constants of the core and the  $j^{\text{th}}$  cladding modes, respectively.  $\Lambda$  is the period of the grating,  $\zeta_{01,01}$  and  $\zeta_{0j,0j}$  are the self-coupling coefficients of the core and the  $j^{\text{th}}$  cladding modes, respectively. Finally,  $s_0$  is the coefficient of the first Fourier component of the grating and  $N$  is the diffraction order. It is important to mention that for the asymmetric energy coupling analysis, ( $LP_{1j}$ ;  $j \geq 1$ ) modes must be considered. Therefore, the propagation constants  $\beta_{1j}$  and self-coupling coefficients  $\zeta_{1j,1j}$  of these cladding modes must be considered in (2). We have considered the refractive index of the optical fiber as stated in Corning SMF-28 specifications, refractive index difference of  $\Delta n = 0.0036$  and core and cladding diameter of  $8.2 \mu\text{m}$  and  $125 \mu\text{m}$ , respectively. Furthermore, we have considered an increase in the cladding refractive index induced by the electric arc discharges to optimize the results [10]. The phase-matching curves in Fig. 2 illustrate the dependence between the grating modulation period and the resonant wavelengths of the different cladding modes and the black dots correspond to the experimental data from the produced LPFGs with  $\Lambda = 470 \mu\text{m}$ . Therefore, the phase-matching curves in Fig. 2(a) confirm that the symmetric transmission spectrum observed in Fig. 1 contains the attenuation dips corresponding to the  $LP_{02}$ - $LP_{05}$  modes. Whereas the phase-matching curves in Fig. 2(b) identify the four attenuation dips observed in the asymmetric spectrum in Fig. 1, correspond to the energy coupling of the fundamental core mode to asymmetric cladding modes.

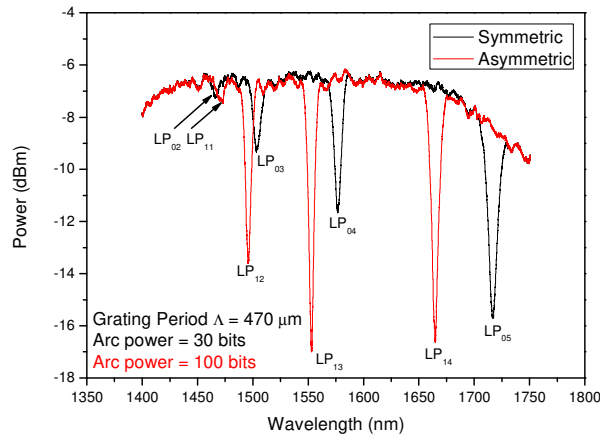


Fig. 1. Transmitted spectra for LPFGs with energy coupling to symmetric and asymmetric cladding modes.

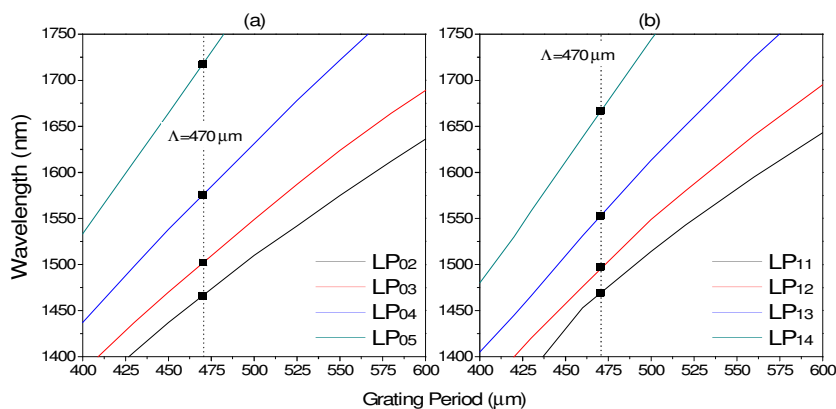


Fig. 2. Resonant wavelengths versus period of cladding modes excited by arc-induced LPFG (a) symmetric and (b) asymmetric.

### 3. Results

To investigate the characteristics of the cladding modes of the LPFG, observed in Fig. 2, we interrogated different modes for temperature and strain-sensing applications, as shown in Figs. 3-6. The characterization of the spectral response of the LPFGs to external perturbations of temperature and strain variations are responsible for removing the resonance condition to different wavelengths. Initially, the LP<sub>02</sub>, LP<sub>03</sub>, LP<sub>04</sub> and LP<sub>05</sub> modes were located at 1467, 1503, 1576 and 1716 nm in the optical spectrum, respectively. Whereas, the modes LP<sub>11</sub>, LP<sub>12</sub>, LP<sub>13</sub> and LP<sub>14</sub> were located at 1470, 1496, 1553 and 1664 nm, respectively. Thus, it is possible to estimate sensitivity coefficients for each mode under investigation, which are defined by the slope of the fitted curve of the results for temperature and strain measurements.

The values of temperature and strain sensitivity of each mode were estimated as linear coefficients through a fitting process of the results considering the LPFGs response varying from 25 to 100 °C and to strain ranging from 0 to 2000 µε. We can observe in Figs. 3 and 4 that the resonance wavelength of both symmetric and asymmetric cladding modes shift continuously in the direction of higher wavelengths of the spectrum as the temperature increases. On the other hand, for strain measurements, the resonance wavelength of both symmetric and asymmetric modes shifted towards shorter wavelengths of the spectrum as strain increased, as seen in Figs. 5 and 6.

Moreover, we can note that asymmetric cladding modes are more sensitive to external perturbations, such as temperature and strain, than the symmetric modes. For example, the asymmetric mode LP<sub>14</sub> showed a temperature sensitivity of 0.43304 nm/°C, which is higher than the resulting sensitivity of 0.32036 nm/°C of the LP<sub>04</sub> symmetric mode. A similar behavior can be observed during the strain analysis and thus, we note that the asymmetric modes are more sensitive to strain variations than the symmetric cladding modes. This behavior is confirmed by contrasting the strain sensitivity of the LP<sub>14</sub> mode of 0.00545 nm/µε against the sensitivity of the LP<sub>04</sub> mode of 0.00433 nm/µε. Finally, it is worth noting that the higher sensitivity to temperature and strain observed in asymmetric cladding modes could be mainly attributed to the modal field distribution of these cladding modes inside the optical fiber.

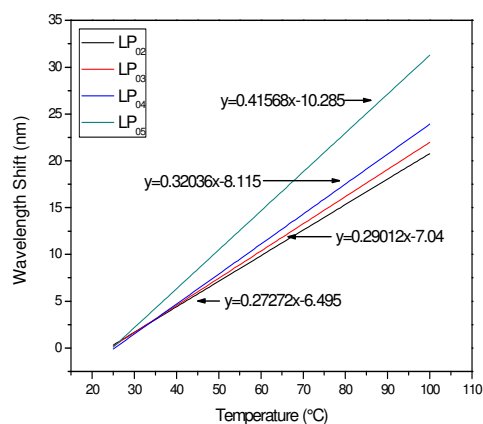


Fig. 3. Temperature sensitivity of symmetric cladding modes.

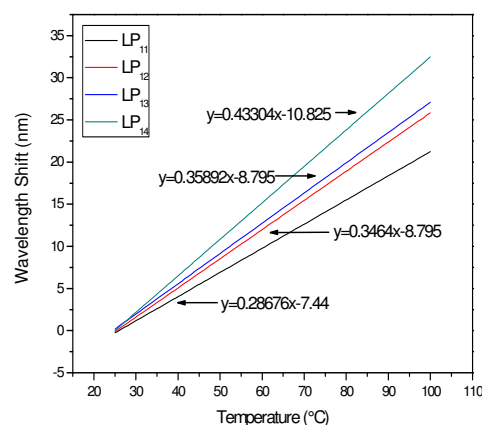


Fig. 4. Temperature sensitivity of asymmetric cladding modes.

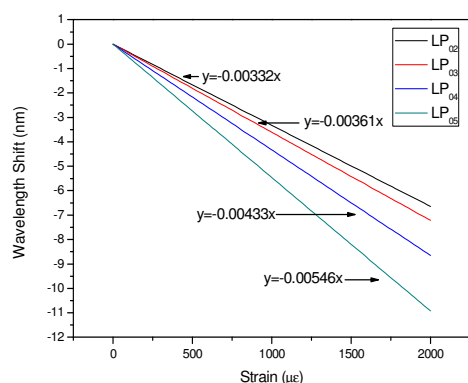


Fig. 5. Strain sensitivity of symmetric cladding modes.

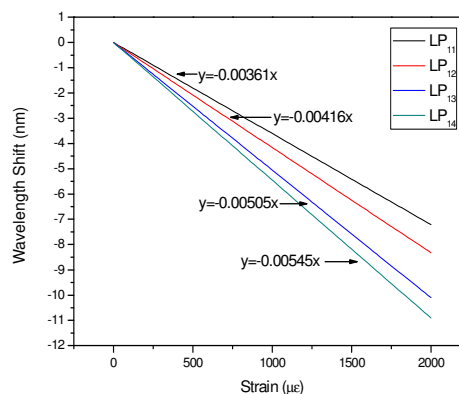


Fig. 6. Strain sensitivity of asymmetric cladding modes.

#### 4. Conclusion

We reported a comparative study between arc-induced LPFGs with energy coupling to symmetric and asymmetric cladding modes. LPFGs fabricated with higher arc power excites asymmetric modes, which are more sensitive to external perturbations such as temperature and strain. Furthermore, it is possible to obtain gratings with strong energy coupling with reduced grating period number and, therefore, allowing the fabrication of shorter gratings. The results of the study may be of impact on the prospects of tailoring the projects of grating sensors.

#### 5. Acknowledgements

This work was supported by CAPES, INERGE, CPFL Energia and CNPq.

#### 6. References

- [1] Delgado, F.S.; Carvalho, J.P.; Coelho, T.V.N.; Dos Santos, A.B. An Optical Fiber Sensor and Its Application in UAVs for Current Measurements. *Sensors* 2016, 16, 1800.
- [2] Lars Glavind, John Canning, Shaorui Gao, Kevin J. Cook, Gang-Ding Peng, Yanhua Luo, Bjarne Funch Skipper, Martin V. Kristensen, "Long-period gratings in special geometry fibers for high-resolution and selective sensors," *Opt. Eng.* 53(6) 066109 (25 June 2014).
- [3] Stephen, W.J.; Ralph, P.T. Optical Fiber Long Period Grating Sensors: Characteristics and Application. *Meas. Sci. Technol.* 2003, 14, 49–61.
- [4] Gaspar Rego, "Arc-Induced Long Period Fiber Gratings," *Journal of Sensors*, vol. 2016, Article ID 3598634, 14 pages, 2016.
- [5] C. Rego, O. V. Ivanov, and P. V. S. Marques, "Demonstration of coupling to symmetric and antisymmetric cladding modes in arc-induced long-period fiber gratings," *Optics Express*, vol. 14, no. 21, pp. 9594–9599, 2006.
- [6] O. V. Ivanov and G. Rego, "Origin of coupling to antisymmetric modes in arc-induced long-period fiber gratings," *Opt. Express*, vol. 15, pp. 13936–13941, 2007.
- [7] Guolu Yin, Jian Tang, Changrui Liao, and Yiping Wang, "Automatic arc discharge technology for inscribing long period fiber gratings," *Appl. Opt.* 55, 3873–3878 (2016).
- [8] R. Ranjan, F. Esposito, A. Iadicicco, A. Stăncălie, D. Sporea and S. Campopiano, "Comparative Study of Long-Period Gratings Written in Standard and Fluorine-Doped Fibers by Electric Arc Discharge," in *IEEE Sensors Journal*, vol. 16, no. 11, pp. 4265–4273, June 1, 2016.
- [9] M. W. Kim, D. W. Lee, B. I. Hong, and H. Y. Chung, "Performance characteristics of long-period fiber-gratings made from periodic tapers induced by electric-arc discharge," *Journal of the Korean Physical Society*, vol. 40, no. 2, pp. 369–373, 2002.
- [10] Celso Colaço, Paulo Caldas, Ignacio Del Villar, Rui Chibante, and Gaspar Rego, "Arc-Induced Long-Period Fiber Gratings in the Dispersion Turning Points," *J. Lightwave Technol.* 34, 4584–4590 (2016).

# Inertial Compensation in an Electrified Railway Pantograph Condition Monitoring System Using FBG-based Accelerometers

Ye Chen<sup>1</sup>, Miodrag Vidakovic<sup>1</sup>, Matthias Fabian<sup>1</sup>, Matthew Askill<sup>2</sup>, Lee Brun<sup>2</sup>,  
Tong Sun<sup>1</sup> and Kenneth T. V. Grattan<sup>1</sup>

<sup>1</sup>School of Mathematics, Computer Sciences and Engineering, City University London, London, EC1V 0HB, UK;

<sup>2</sup>Faiveley Brecknell Willis, Millfield, Chard TA20 2DA, UK  
ye.chen@city.ac.uk

**Abstract:** This paper presents the results from an assessment of dynamic force inertial compensation, obtained using two Fibre Bragg Grating (FBG)-based accelerometers integrated into a railway current-collecting pantograph, allowing more accurate measurement of contact force and contact location are presented. In the tests carried out, a high level of transfer function accuracy in the monitoring of dynamic contact force was achieved.

## 1. Introduction

The pantograph is the familiar power collection device in electrified train systems across the world. In a moving electric train, the contact force between the pantograph and the overhead wire needs to be kept stable to ensure minimal losses, limiting ‘wear and tear’ and offering a reduced risk of disruption of the current collection by the electric vehicle [1]. Due to the high voltage (typically 25kV) environment of the overhead line, measuring systems based on conventional electronic techniques have shown some limitations from, for example, the added mass of the sensor system and added wind resistance, in spite of efforts to add the electrical isolation needed.

Fibre Bragg Grating (FBG)-based optical sensors have attracted considerable interest to create better sensing systems for the measurement of strain, temperature, and a wide range of other parameters, *in situ*, in a number of industrial applications [2, 3]. The advantages of immunity to electromagnetic interference, the ease of multiplexing, the small size and their lightness have made them well-suited for measurements under a range of harsh and often extreme conditions. A number of researchers have investigated the application of FBG-based sensor systems into a railway pantograph to allow remote condition monitoring [4–10]. Previous work has been reported showing the performance of an FBG-based accelerometer on a pantograph panhead [11], however, the transfer function test of inertial compensation through the integration of a system of FBG-based strain sensors and accelerometers has not yet been successfully demonstrated.

In this work, test results on transfer function of active inertial compensation, using a FBG-based accelerometer are reported. The results indicate that an optical fibre based dynamic contact force measurement can be made with high transfer function accuracy (in this case achieving 96% averaged accuracy) when compared with an uncompensated system over the frequency range from 10Hz–20Hz.

## 2. Theoretical background

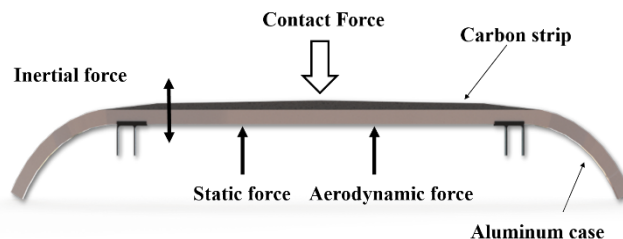


Figure 1. Typical structure of a pantograph, with schematic illustration of forces experienced in use.

Figure 1 shows the structure of a typical pantograph, illustrating the forces on the carbon strip which is combined with the aluminum case. The contact force,  $F_{contact}$ , between the overhead wire and pantograph combines the following components: the static force,  $F_{static}$ , the inertial force,  $F_{inertial}$  and the aerodynamic force,  $F_{aerodynamic}$ , as follows in equation (1) [12]

$$F_{contact} = F_{static} + F_{inertial} + F_{aerodynamic} \quad (1)$$

The static force can be measured by using a FBG-based strain sensor, using a design discussed in a previous paper [9]; the aerodynamic force is speed-related and can be measured by using a flowmeter. The inertial force can best be measured by the use of accelerometers and here a new fibre optic based design is proposed and its performance discussed as equation (2)

$$F_{inertial} = \frac{m_{above}}{k_a} \sum_{i=1}^{k_a} a_{sensor,i} \quad (2)$$

Where the  $a_{sensor,i}$  is the measured accelerometer at sensor  $i$ ,  $k_a$  is the number of acceleration sensors, and  $m_{above}$  is the mass of panhead located above the force sensors.

### 3. Experimental set up and results of the system evaluation

Figure 2 illustrates the experimental setup used in the laboratory to investigate the inertial compensation of the pantograph. The test facility comprises a large frame on which the pantograph is mounted, with an electrical shaker fitted above the pantograph to provide a variable vibration signal. The shaker is connected to a signal generator to allow a known, but variable frequency vibration to be applied to the pantograph. The panhead with two accelerometers mounted on it is lifted to make contact with the shaker using compressed air from a compressor, creating typically a 90N static contact force between the shaker and the panhead.

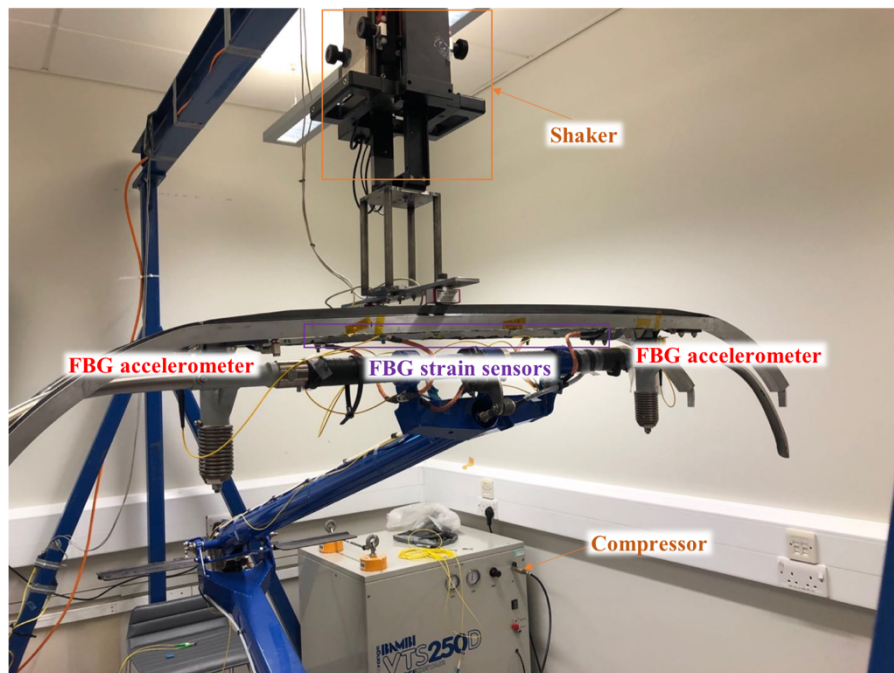


Figure 2. Experiment setup for the inertial compensation tests carried out showing the pantograph panhead (with FBG-based strain sensors), the shaker and the FBG-based accelerometer.

The optical FBG-based strain sensors and accelerometers (diaphragm structure) used in this work are connected to a high speed FBG interrogator (Hyperion si155 from Micron Optics; sampling rate 1kHz). The optical and electronic sensing system thus set up is connected to a high performance PC for data acquisition and its analysis .

The experimental investigation carried out comprises the following steps. Initially, the shaker was moved to the center of the panhead, which was lifted to contact with the shaker to offer a 90N static force. The shaker was then activated using a sinusoidal periodic signal, lasting for 30s, following which the frequency was increased in 1Hz steps from 10Hz to 20Hz and for each step, the data obtained were recorded and analyzed.

The measured contact force are calculated by following equation:

$$F_{measured} = F_{static} + \frac{m_{above}}{k_a} \sum_{i=1}^{k_a} a_{sensor,i} \quad (3)$$

The static force was measured by using FBG-based strain sensors array with temperature compensation built in, using the design discussed in a previous paper [9]. The accelerations  $a_{sensor,i}$  were obtained by the FBG based accelerometers on both side of the panhead.

The accuracy of the transfer function shall be calculated by using following formula [12]:

$$A = \left( 1 - \frac{1}{(f_n - f_1)} \sum_{i=1}^{n-1} \left( (f_{i+1} - f_i) \left[ 1 - \frac{F_{measured}}{F_{applied}} \right] \right) \right) \cdot 100\% \quad (4)$$

where  $A$  is the measured accuracy of the transfer function,  $f$  is the frequency,  $F_{measured}$  and  $F_{applied}$  are the measured and applied contact force, respectively.

Figure 3(a) shows a graph of the applied dynamic excitation contact force, the measured uncompensated dynamic contact force (using the FBG-based strain sensors) and the inertial compensated dynamic contact force (measured by use of the strain sensors and accelerometers based on FBGs). Figure 3(b) shows the achieved measurement accuracies, before and after the inertial compensation is applied.

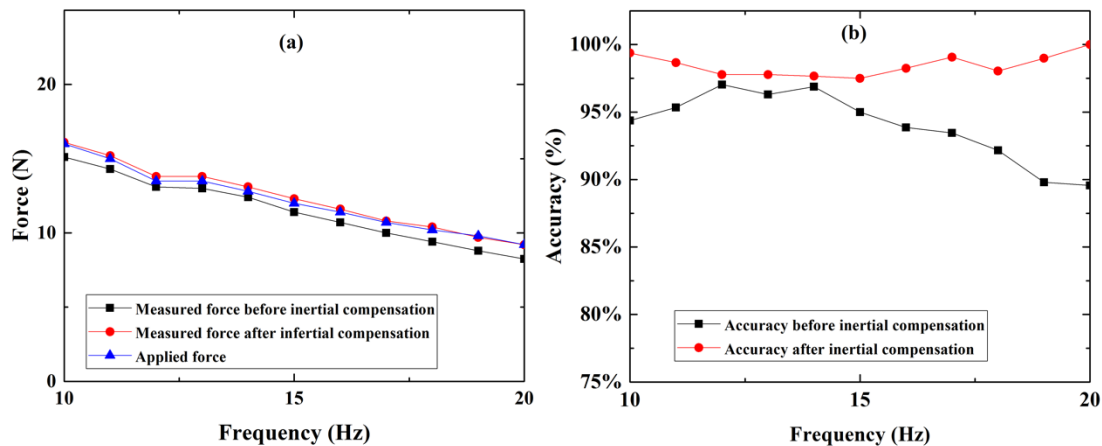


Figure 3. Comparison of (a) RMS of the measured dynamic contact force and (b) the accuracy achieved before and after inertial compensation, over the frequency range from 10Hz to 20Hz.

From the results obtained, it can be seen that the accuracy of the measurement of the total contact force has been improved through the application of inertial compensation. The results show that the accuracy of the transfer function of the measured contact force before the inertial compensation was applied was ~92.5% and the transfer function accuracy after the inertial compensation increases to ~96.3%, which shows a ~ 4 percentage point increase in the accuracy of the transfer function. From Fig. 3(b) we can see the inertia force varies with the frequency change which is small compare with the static force, as the applied dynamic force is ~10% percent of the static one. However during the real train operation, there are shock vibrations causing acceleration as large as 20g, when the inertia force should not be neglected.

#### 4. Conclusion

An inertial compensation approach, based on the use of FBG-based accelerometers mounted on both sides of the pantograph panhead is reported, using test frequencies covering the range 10-20Hz. High

quality contact force measurement results have been achieved, showing a  $\sim 4$  percentage point improvement in the transfer function accuracy achieved. The results show the potential of this optical fibre based sensing technique to be directly applied to many electrified railway systems, in that way allowing better real-time monitoring of this important parameter.

## 5. Acknowledgements

The authors would like to thank Innovate UK for funding this JIANGSU-UK Industrial Challenge Programme. The support of the Royal Academy of Engineering is much appreciated.

## 6. References

- [1] S. Kusumi, T. Fukutani, and K. Nezu, "Diagnosis of Overhead Contact Line based on Contact Force," *QR of RTRI* **47**, 39–45 (2006).
- [2] K. T. V. Grattan and T. Sun, "Fiber optic sensor technology: an overview," *Sensors and Actuators A: Physical* **82**, 40–61 (2000).
- [3] S. J. Mihailov, "Fiber Bragg Grating Sensors for Harsh Environments," *Sensors* **12**, 1898–1918 (2012).
- [4] L. Comolli, G. Bucca, M. Bocciolone, and A. Collina, "First results from in line strain measurements with FBG sensors on the pantograph collector of underground trains," in *SPIE Photonics Europe*, (Brussels, Belgium, 2010), vol. 7726, p. 772605.
- [5] M. Bocciolone, G. Bucca, A. Collina, and L. Comolli, "An approach to monitor railway pantograph-catenary interaction with fiber optic sensors," in *Fourth European Workshop on Optical Fibre Sensors*, (Porto, Portugal, 2010), vol. 7653, p. 76533Q.
- [6] K. Schröder, W. Ecke, M. Kautz, S. Willett, M. Jenzer, and T. Bosselmann, "An approach to continuous on-site monitoring of contact forces in current collectors by a fiber optic sensing system," *Optics and Lasers in Engineering* **51**, 172–179 (2013).
- [7] R. Wagner *et al.*, "A Fibre Optic Sensor Instrumented Pantograph As Part of a Continuous Structural Health Monitoring System for Railway Overhead Lines," presented at the *EWSHM - 7th European Workshop on Structural Health Monitoring*, (Nantes, France, 2014).
- [8] K. Schröder, M. Rothhardt, W. Ecke, U. Richter, A. Sonntag, and H. Bartelt, "Fibre optic sensing system for monitoring of current collectors and overhead contact lines of railways," *Journal of Sensors and Sensor Systems* **6**, 77–85 (2017).
- [9] Y. Chen *et al.*, "A temperature compensated fibre Bragg grating (FBG)-based sensor system for condition monitoring of electrified railway pantograph," in *25th International Conference on Optical Fiber Sensors*, (Jeju, Korea, 2017), vol. 10323, p. 103236T.
- [10] M. Tan, N. Zhou, Y. Cheng, J. Wang, W. Zhang, and D. Zou, "A temperature-compensated fiber Bragg grating sensor system based on digital filtering for monitoring the pantograph-catenary contact force," *Proceedings of the Institution of Mechanical Engineers, Part F: Journal of Rail and Rapid Transit* **233**, 187–200 (2019).
- [11] M. Bocciolone, G. Bucca, A. Cigada, A. Collina, and L. Comolli, "An application of FBG accelerometers for monitoring pantographs of underground trains," in *Fourth European Workshop on Optical Fibre Sensors*, (Porto, Portugal, 2010), vol. 7653, p. 765341.
- [12] BS EN 50317:2012. Railway applications. Current collection systems. Requirements for and validation of measurements of the dynamic interaction between pantograph and overhead contact line. *CENELEC*, (2012).

# Optical Fiber Sensor for Carbon Dioxide Measurement Using Tapered Long Period Grating

**Manuella Cruz de Oliveira, Felipe Souza Delgado, Marco Aurélio Jucá, Renato Luiz Faraco Filho, Daniel Discini Silveira, Thiago Vieira Coelho and Alexandre Bessa dos Santos**

*Federal University of Juiz de Fora, Rua José Lourenço Kelmer, s/n, São Pedro, 36036-900, Juiz de Fora, Minas Gerais, Brazil.  
manuella.oliveira@engenharia.ufjf.br; felipe.souza@engenharia.ufjf.br; thiago81uffj@gmail.com; alexandre.bessa@engenharia.ufjf.br*

**Abstract:** This paper presents the development of a refractive index (RI) sensing methodology for measuring CO<sub>2</sub> concentration in environments considering the temperature effect. We propose and demonstrate the modulated tapered Long Period Gratings to enhance the RI sensitivity of the sensor. The results showed that the CO<sub>2</sub> measurement considering the temperature cross-sensitivity effect can be reliable.

## 1. Introduction

Carbon dioxide (CO<sub>2</sub>) monitoring techniques based on optical fiber sensors have acquired growing importance in the field of sensor technologies [1-2]. These devices are lightweight, immune to electromagnetic interferences (EMI) and resistant to harsh environments [3], which are key features required for gas detection systems. Therefore, several researchers have proposed and demonstrated different applications using optical fiber sensors to detect gaseous species [4-5]. Among the different types of optical fiber sensors, Long Period Gratings (LPGs) have been widely used for the measurement of the external refractive index [6].

LPGs consist of a periodic modulation along the core of an optical fiber, which usually has a period of modulation ranging from tens to hundreds of micrometers. Furthermore, these devices promote the coupling of the co-propagating fundamental guided mode and the cladding modes according to the phase-matching condition, which results in a series of attenuation peaks in the transmission spectrum. The phase-matching condition is given by the expression [7]:

$$\lambda^m = (n^{01}_{eff, core} - n^{0m}_{eff, clad}) \Lambda \quad (1)$$

Where  $\lambda^m$  is the resonant wavelength of the  $m^{\text{th}}$ -order cladding mode,  $n^{01}_{eff, core}$  and  $n^{0m}_{eff, clad}$  are the effective refractive indices of the fundamental core mode and the  $m^{\text{th}}$ -order cladding mode, respectively, and  $\Lambda$  is the period of the grating. Therefore, the raise of the external refractive index is responsible for shifting the wavelength condition to shorter wavelengths in the optical spectrum [8-9]. In this context, the presence of CO<sub>2</sub> in certain environments is rather difficult to identify due to its low refractive index. In this paper, we use a tapered LPG to enhance the refractive index sensitivity of the sensor in order to monitor different CO<sub>2</sub> concentrations. Moreover, the proposed method was based on the interrogation of two different cladding modes to perform a dual-peak resonant wavelength detection and allow the CO<sub>2</sub> sensing under the effect of cross-sensitivity arising from the temperature effect on the grating sensor.

## 2. Methodology

In order to analyze the concentration of CO<sub>2</sub> in the environment, it was used a tapered LPG sensor to monitor the refractive index variation. The taper effect modified a commercial single-mode fiber (SMF-28) in its period and both core and cladding radius. These modifications allow us to improve the response of the LPG to external refractive index variations and, therefore, to different CO<sub>2</sub> concentrations. Furthermore, it was adopted core and cladding radius of approximately 88% of their original values.

### 2.1. Fiber Tapering

The fiber tapering process occurs in practice by stretching and heating the optical fiber, which results in an enhanced evanescent field of the guided light and produces an LPG more sensitive to external influences [4]. After heated and stretched, the fiber will be composed of three regions: the central region or taper waist, the transition region and the region of the fiber with no alterations. We focused on the central region to produce the LPG.

Furthermore, the parameters of the fiber were described in Table 1 and the transmission spectrum of the produced LPG was showed in Fig. 1.

Table 1. LPG specifications.

LPG parameters	Core	Cladding
Radius	3.652 $\mu\text{m}$	51.348 $\mu\text{m}$
Refractive Index	1.44947	1.44411
Period	590 $\mu\text{m}$	

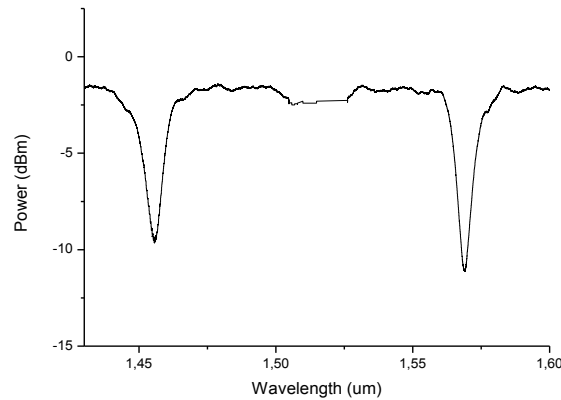


Fig. 1. Transmission spectrum of the LPG sensor.

### 3. Measurements

Firstly, the response of the long period grating was analyzed considering variations of the external refractive index (RI) and temperature individually. Then, it was investigated the response of the LPG sensor under the effects of the RI changes and temperature variations at the same time, therefore, taking into account the cross-sensitivity effect. In order to do this, it was characterized the LPG with respect to the external refractive index of the surrounding medium, which could be correlated to concentrations of CO<sub>2</sub> varying from 0-50%. However, this substance has a very low refractive index, so as discussed in [1] and [10], in order to identify the CO<sub>2</sub> presence, it is necessary to enhance the sensor's sensitivity by coating the original sensor with a CO<sub>2</sub> sensitive layer resulting in higher values of external refractive index, as represented in Table 2.

Moreover, the effect of the temperature cross-sensitivity was analyzed within the ranging from 22°C to 27°C (this range was chosen as a function of ambient temperature). Because of these perturbations on the LPG sensor, the wavelengths of two attenuation dips of the LPG shifted to different wavelengths. Thus, several measurements of the wavelength shift were performed to estimate when temperature and CO<sub>2</sub> concentration changes occurred.

Table 2. Refractive index relation for different CO<sub>2</sub> concentrations.

CO <sub>2</sub> [%]	Sensitivity - Refractive Index (RI)
0	1.3558
10	1.3567
20	1.3570
30	1.3571
40	1.3572
50	1.3573

#### 3.1. CO<sub>2</sub> Sensitivity

Here, it is shown the influence of the surrounding refractive index over the LPG sensor by focusing on the second attenuation dip of the transmission spectrum. Thus, the LPG was tested for the characterization of the

refractive index by placing it into different refractive indices of the external environment, ranging from 1 to 1.4, as the evidence of the applicability of this sensor for measurement of the CO<sub>2</sub> concentration. With these data, it is possible to analyze the wavelength shift related to the refractive index for the second dip of the LPG, as shown in Fig. 2.

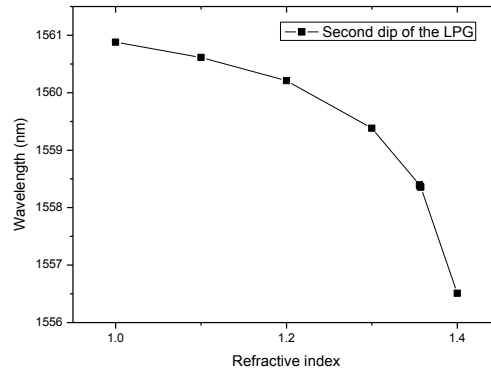


Fig. 2. Wavelength shift of the second attenuation dip of the LPG with respect to different refractive index values.

### 3.2. Temperature Sensitivity

It was also investigated the temperature effects on the LPG sensor in order to verify its effectiveness to measure temperature fluctuations of the external medium of the LPG. As mentioned before, the temperature ranged from 22°C to 27°C and because of that, the refractive index of the external environment has kept constant. In Fig. 3. It is possible to indicate the wavelength shift of the two different attenuation dips under investigation.

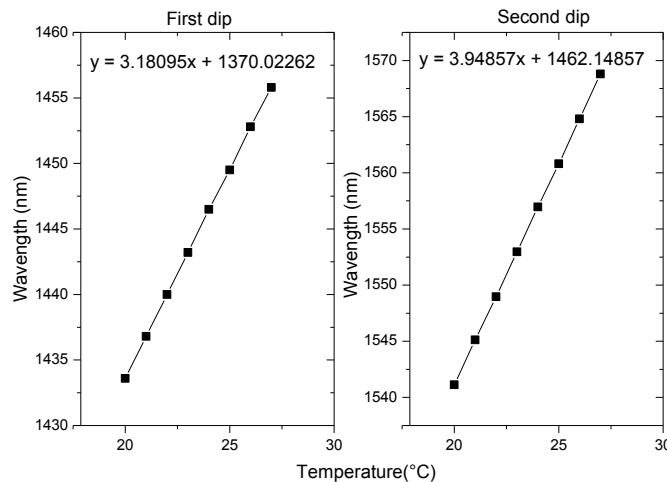


Fig. 3. Wavelength versus temperature for the first and second dip simultaneously.

### 3.3. CO<sub>2</sub> and Temperature Cross-sensitivity

In order to analyze the variations of CO<sub>2</sub> and temperature simultaneously, it was proposed a dual-peak sensing method based on the measurement of the differences between the wavelengths of the two different attenuation dips. First, it was realized variations of the temperature (22°C - 27°C) and refractive index of the LPG. After that, it was measured the differences of the central wavelength of both dips showed in Fig. 1.

Then, it was proposed mapping the differences of the central wavelength of the dips, which allow us to identify when the refractive index and the temperature acts on the sensor, the value of this index it is the CO<sub>2</sub> concentration. The methodology could be explained by the value of the difference of the central wavelength of both dips. Then, it

is possible to estimate the temperature effect on the LPG by (2). This equation was obtained through the measurement of the differences between both dips when the temperature is changed.

$$\text{temperature} = 1,2951 * \text{difference} - 116,8517 \quad (2)$$

Where difference is the difference between both dips.

After that, by considering the temperature effect we can define the refractive index value through the equations also indicated in Table 3. These equations were obtained through the simulation and measurement of the differences between both dips of LPG tapered sensitive to the refractive index and the temperature. The refractive index can be obtained by the difference of both dips; using the equation (2) is possible to get the temperature. The values of the temperature and Table 3 indicate how is it possible to find the respective equation to determine the index. It is important to mention that the temperature values indicated in Table 3 specified some temperature values, although the temperature has been measured with a variation of 0.3 °C in the ranging from 22°C to 27°C. For the equations indicated in Table 3, the x value is represented by the values of the refractive index and the y value is the difference of the wavelengths between the dips

Table 3. Relation of the variation ranges of the differences between both dips as a function of temperature.

$\Delta\lambda$ ( $\mu\text{m}$ ) (ranges)	Temperature (°C)	Characteristic Equation
107.21-107.24	22	$y = -18.39088 x + 132.17673$
107.97-107.99	23	$y = -18.13681 x + 132.58936$
108.73-108.77	24	$y = -18.46254 x + 133.79597$
109.04-109.08	24.4	$y = -18.54723 x + 134.21938$
109.27-109.31	24.7	$y = -18.28339 x + 134.09296$
109.5-109.54	25	$y = -18.5993 x + 134.7541$
109.74-109.78	25.3	$y = -18.95114 x + 135.46455$
109.97-110.1	25.6	$y = -20.20847 x + 137.40479$
110.20-110.24	25.9	$y = -19.25407 x + 136.34364$
110.44-110.48	26.2	$y = -18.87948 x + 136.07072$
110.68-110.71	26.5	$y = -18.70033 x + 136.06325$
110.91-110.95	26.8	$y = -19.25081 x + 137.04687$
111.07-111.11	27	$y = -21.06515 x + 139.6685$

#### 4. Conclusion

In this article, it was proposed an investigation of the variation of the external refractive index of the fiber. Firstly, measurements of the refractive index and temperature separately were performed. Then, it was possible to combine the refractive index and temperature measurements in order to analyze the effects of the temperature simultaneously with the RI sensing. As a result, it was observed that the variations of the external environment and temperature influenced on the LPG wavelengths because it is sensitive to variations of gases like CO<sub>2</sub>. After that, a methodology was proposed to perform dual-peak interrogation of the LPG based on the difference between two different resonant wavelengths, obtaining the information in Table 3. Therefore, it is possible to obtain the refractive index and temperature value acting on the fiber.

Although this paper focused on the measurement of CO<sub>2</sub> concentration in the environment and on the influence of the temperature, future researches can perform a larger range of temperature or different concentrations of substances on the external environment.

#### 5. Acknowledgments

The authors thank for the support of FAPEMIG, Inerge-UFJF, CNPq, Propesq-UFJF and Capes.

#### 6. References

- [1] F. S. Delgado, M. A. Jucá, D. D. Silveira, T. V. N. Coelho e A. B. Santos, "Investigation of Carbon Dioxide Sensitivity in Long Period Gratings," in: *12<sup>o</sup> CBMag - Congresso Brasileiro de Eletromagnetismo; 17<sup>o</sup> SBMO - Simpósio Brasileiro de Micro-ondas e Optoeletrônica e LAWOFS 2016 - Latin American Workshop on Optical Fiber Sensors* (Porto Alegre, 2016).

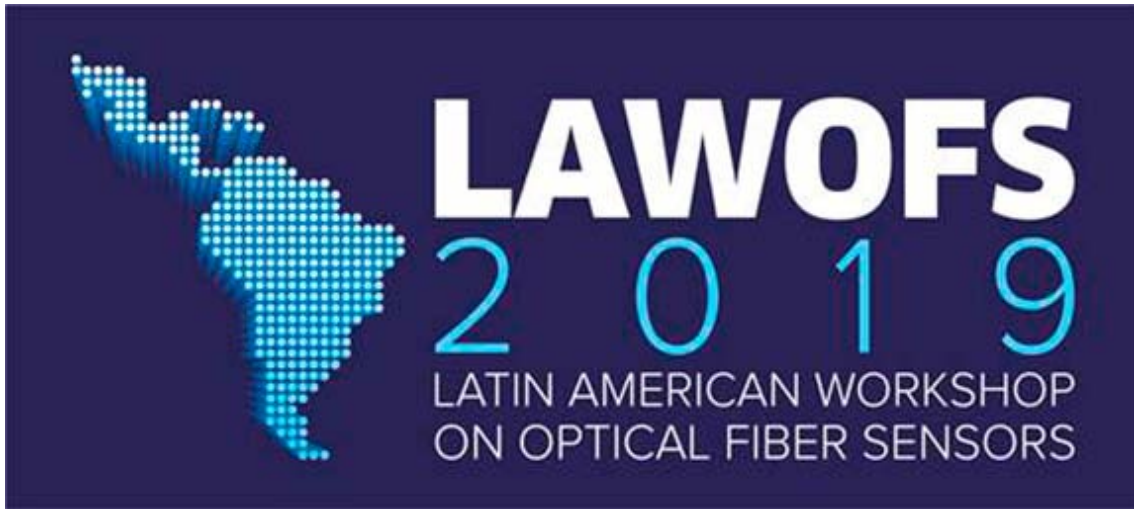
- [2] Mejia Quintero, S.M.; Guedes Valente, L.C.; De Paula Gomes, M.S.; Gomes da Silva, H.; Caroli de Souza, B.; Morikawa, S.R.K., "All-Fiber CO<sub>2</sub> Sensor Using Hollow Core PCF Operating in the 2  $\mu$ m Region," *Sensors* 2018, 18, 4393.
- [3] Ding, Z.; Du, Y.; Liu, T.; Liu, K.; Feng, B.; Jiang, J., "Distributed optical fiber current sensor based on magnetostriction in OFDR," in *IEEE Photon. Technol. Lett.* 2015, 27, 2055–2058.
- [4] Liu, J.; Sun, Y.; Fan, X., "Highly versatile fiber-based optical Fabry-Pérot gas sensor," *Opt. Express* 2009, 17, 2731.
- [5] Wu, Y.; Yao, B.; Zhang, A.; Rao, Y.; Wang, Z.; Cheng, Y.; Gong, Y.; Zhang, W.; Chen, Y.; Chiang, K.S., "Graphene-coated microfiber Bragg grating for high-sensitivity gas sensing". *Opt. Lett.* 2014, 39, 1235.
- [6] Zhengtian Gu, Xiuli Jiang, and Haiyun Chen, "High-sensitivity sensor design based on cascaded long-period fiber grating with film coating," *Optical Engineering* 53(2), 021104 (5 September 2013).
- [7] Smietana, M.; Bock, W.J.; Mikulic, P.; Chen, J., "Increasing sensitivity of arc-induced long-period gratings-pushing the fabrication technique toward its limits," *Meas. Sci. Technol.* 2011, 22, 015201.
- [8] Jian Yang, Li Yang, Chang-Qing Xu, Chenglin Xu, Weiping Huang, and Yingfu Li, "Long-period grating refractive index sensor with a modified cladding structure for large operational range and high sensitivity," *Appl. Opt.* 45, 6142-6147 (2006).
- [9] Tsuda, H.; Urabe, K.. "Characterization of Long-period Grating Refractive Index Sensors and Their Applications," *Sensors* 2009, 9, 4559-4571.
- [10] C. Gouveia, A. Markovics, J. M. Baptista, B. Kovacs, P. A. S. Jorge, "Measurement of CO<sub>2</sub> using refractometric fiber optic sensors", 3rd WSEAS International Conference on Advances in Sensors, Signals and Materials, p.169-173, 2010.



Sociedade Brasileira  
de Micro-ondas  
e Optoeletrônica

Printed in Brazil

São Caetano do Sul (SP) 2019



CEFET/RJ - Centro Federal de Educação Tecnológica Celso Sukow da Fonseca

Rio de Janeiro, Brazil